Dissertation zur Erlangung des Doktorgrades
der Fakultät für Chemie und Pharmazie
der Ludwig-Maximilians-Universität München

Towards Multifunctional Device Concepts Utilizing Light Absorption and Charge Storage in Carbon Nitrides

Andreas Thomas Gouder

aus

Karlsruhe, Deutschland

2023

Erklärung

Erklärung

Diese Dissertation wurde im Sinne von § 7 der Promotionsordnung vom 28. November 2011 von Frau Prof. Dr. Bettina V. Lotsch betreut.

Eidesstattliche Versicherung

Diese Dissertation wurde eigenständig und ohne unerlaubte Hilfe erarbeitet.

Stuttgart, den 13. April 2023

Andreas Thomas Gouder

Dissertation eingereicht am	13.04.2023
1. Gutachterin	Prof. Dr. Bettina V. Lotsch
2. Gutachterin	Prof. Dr. Jennifer Rupp
Mündliche Prüfung am	22.05.2023

"My candle burns at both ends;
It will not last the night;
But ah, my foes, and oh, my friends –
It gives a lovely light!"

- Edna St. Vincent Millay,
First Fig

Contents

Acknowledgements **1**

Summary **3**

I Description of the Thesis

1. Introduction **9**

1.1. Motivation: Global Warming and the Greenhouse Effect 10

1.1.1. Sustainable Energy 13

1.1.2. Sunlight as Renewable Energy Resource 15

1.1.3. The Challenge of Intermittency 15

1.2. An Introduction into Carbon Nitrides 16

1.2.1. Structural Composition and Synthesis 17

1.2.2. Photophysical Properties 19

1.2.3. Emerging Photoelectrochemical Applications 24

1.3. Energy Conversion *via* Solar Cells 28

1.3.1. Emerging Solar Cell Technologies: DSSCs 30

1.3.2. Emerging Solar Cell Technologies: OSCs 35

1.4. Energy Storage *via* Batteries and Capacitors 44

1.4.1. An Overview of Energy Storage Technologies 45

1.4.2. Electrical Energy Storage *via* Capacitors 45

1.4.3. Pseudocapacitive Energy Storage 49

1.4.4. Electrochemical Energy Storage *via* Batteries 54

1.5. Beyond Energy Storage 60

1.5.1. Resistance Switching 62

1.5.2. Materials for Resistance Switching 64

1.6. References 65

2. Fundamentals & Methods **81**

2.1. Fundamentals of the Photovoltaic Effect 82

2.1.1. Carrier Dynamics in Semiconductors 82

2.1.2. P-N Junctions 84
2.2. Fundamentals of Electrochemistry 87
2.2.1. The Electrochemical Cell 88
2.2.2. Interfacial Electron Transfer 91
2.2.3. Mass Transport and Diffusion Layers 94
2.3. Electrochemical Characterization Techniques 96
2.3.1. Voltammetry 96
2.3.2. Chrono Methods 104
2.3.3. Electrochemical Response of Devices 107
2.4. References 109

3. Research Objective 113
3.1. References 117

II Perspectives Towards Novel Photo Devices and Concepts

4. Optoionics 2.0: A toolkit to design novel applications for the post-Silicon age 121
4.1. A brief historical context of optoionics and photoionics 122
4.2. The optoionic mechanism 126
4.2.1. Extending the concept of intrinsic/extrinsic and 1-/2-phase optoionic systems 128
4.2.2. Experimental impact of the different field effects 130
4.3. References 131

5. Integrated Solar Batteries: Design and Device Concepts 135
5.1. The Solar Battery Experiment 139
5.2. A brief overview of current solar battery concepts 142
5.2.1. Three-electrode designs 142
5.2.2. Bifunctional electrodes *via* heterojunctions 144
5.2.3. Bifunctional electrodes *via* bifunctional materials 148
5.3. Design philosophy of solar batteries: Improving power or energy balance 151
5.4. References 158

III Research Publications

6. Bridging the Gap between Solar Cells and Batteries: Optical Design of Bifunctional Solar Batteries based on 2D Carbon Nitrides 165

6.1. Introduction 167

6.2. Results and discussion 169

6.2.1. Optical design 170

6.2.2. The device thickness paradigm 172

6.2.3. Efficiency limitations beyond optical engineering 178

6.2.4. Evaluating performance of solar batteries *via* Ragone plots . 179

6.3. Conclusion 182

6.4. References 184

7. An Integrated Solar Battery based on a Charge Storing 2D Carbon Nitride 189

7.1. Introduction 193

7.2. Results and discussion 195

7.2.1. Device design 195

7.2.2. Operation modes of the device 198

7.3. Conclusion 207

7.4. Experimental 210

7.5. References 212

8. Photomemristive sensing *via* charge storage in 2D carbon nitrides 217

8.1. Introduction 222

8.2. Results and discussion 224

8.2.1. PEC sensing interaction on K-PHI 224

8.2.2. Photomemristive sensing with K-PHI films 225

8.2.3. Photomemristive sensing with K-PHI wireless particles . . . 232

8.3. Conclusion 236

8.4. Experimental 237

8.5. References 240

IV Concluding Remarks

9. Conclusion & Outlook **247**
9.1. References 252

V Appendix

A. Supporting Information to chapter 6 **257**
A.1. Optical Characterization of Materials 258
A.1.1. Absorption profile 258
A.1.2. Refractive Index 259
A.2. Optical simulation methods 259
A.3. Charge collection layer 260
A.4. Battery performance in the dark 262
A.5. Further optical and electrochemical considerations 264
A.5.1. Dependence of charging state on photocurrent 264
A.5.2. Electrochromic behavior 268
A.6. Simulating discharging 269
A.6.1. Influence of decaying photocurrent on charging time 271
A.6.2. Performance data normalization 271
A.6.3. Input data for simulations / calculations 272
A.7. References 276

B. Supporting Information to chapter 7 **279**
B.1. Morphological characterization 280
B.2. Electrochemical study of HTM materials 280
B.3. Activation & reset of solar battery samples 281
B.4. Kinetic analysis of charge storage mechanism 283
B.5. Additional analysis: Light charging and electric discharging 285
B.6. Additional analysis: Scaling of Power and Energy with Discharge Current 287
B.7. Shape of GCD measurements & chosen voltage window 288
B.8. Charge retention for delayed discharge 290
B.9. Solar cell performance comparison 1 sun & 365 nm LED 292

B.10. Comparison of solar battery performance with literature 294
B.11. References 295

C. Supporting Information to chapter 8 **297**
C.1. Material and thin film analysis 298
C.1.1. Molecular structure and optical analysis 298
C.1.2. Structure Analysis of K-PHI Films 299
C.2. K-PHI as a direct amperometric PEC sensor 301
C.3. Electrochemical self-cleaning of thin films 303
C.4. Normalizing coulometric readout measurements 304
C.5. Fitting of the sensor curves 305
C.5.1. Potentiometric fitting 308
C.5.2. Impedimetric fitting 312
C.5.3. Coulometric fitting 315
C.5.4. Colorimetric fitting 318
C.5.5. Fluorometric fitting 320
C.6. Additional electrochemical analysis of memristive properties of K-PHI films 323
C.7. Additional optical analysis of memristive properties of K-PHI particles 324
C.7.1. Influence of particle size 324
C.7.2. Dependence on illumination time 327
C.7.3. Delayed sensor information readout 327
C.7.4. Negligible invasive nature of the memristive state readout . . 328
C.7.5. Schematic representation of the PL characterization process by the quenched PL emission 329
C.8. References 330

List of Publications **333**

List of Figures **337**

List of Acronyms **341**

Chemical Glossary **347**

Acknowledgements

The road to obtain this PhD was long and I am incredibly grateful for all the support of many people along the way! Let me first and foremost sincerely thank Prof. Dr. Bettina Lotsch for her supervision, enabling me to perform my PhD at the Max Planck Institute for Solid State Research, as well as for all of the very fruitful and supporting conversations throughout the last years. I have always left from our meetings incredibly inspired, motivated, and encouraged to embark on investigating the novel design concepts and ideas that will be presented in this thesis, and beyond.

Furthermore, I would like to thank the members of my PhD committee to evaluate this thesis and accept the invitation for the oral exam, namely Prof. Dr. Jennifer Rupp, Prof. Dr. Kristina Tschulik, Prof. Dr. Joost Wintterlin, Prof. Dr. Thomas Bein, and Prof. Dr. Achim Hartschuh.

I sincerely thank the fruitful day-to-day supervision and support of Dr. Alberto J.-S. and the many conversations we have shared over the years. I also thank Dr. Filip P. and Dr. Nella V.-B. for their day-to-day supervision and for introducing me into the realms of electrochemistry. I am very grateful for all of the discussions and career advice I had with Dr. Nella V.-B., Dr. Liang Y., Dr. Hugo V., Prof. Dr. Doris Grumelli, and many others.

Many thanks to all co-authors, of which I would like to accentuate Dr. Liang Y., Dr. Yang W., Dr. Julia K., Ksenia S. Rabinovich, Dr. Takayoshi O., and Dr. Sourav L., as well as Dr. Stefan Bette and Dr. Davide Moia for performing the internal review of the manuscripts. Thanks a lot to Dr. Liang Y., Dr. Tigmansu P., and Dr. Thomas G. for proof-reading this thesis. I also thank the master thesis students that I have supervised and co-supervised, namely Julia S. and Rachel W.

I would like to especially thank Viola D., Claudi C., Sigrid F., and Stefan H. for all of their scientific, technical and administrative support, as well as all the funny con-

versations we had throughout the years. Still confused about the Carnet document though! Many thanks also to Vera. H. for designing the beautiful journal cover artworks, that also decorate the front cover of this thesis!

I sincerely thank all the members of the Lotsch group, which have made this experience so memorable and where I have found many friends over the years and shared lots of funny moments and holidays. Thanks a lot to my office mates Lars G., Max P., Sebastian E., and Charli K. Many thanks also to Prof. Dr. R. Seshardi for hosting us for a research stay at the UCSB, as well as to Filip P., Julia K., Gökcen S., Prof. Dr. Bettina Lotsch, and Prof. Dr. Christian Ochsenfeld for the awesome time we spend in California, USA.

Vor allem und zu guter Letzt gilt mein größter Dank Ella und meiner Familie. Thanks, Ella, for your support during tough moments, inspiration, and love! Vielen Dank, Eva und Thomas, und meinen Brüdern, Matthias und Philip, für eure Unterstützung und den Rückhalt durch die letzten Jahre auf dem Weg zur Promotion!

Summary

This thesis comprises 5 parts. In Part I, we start in Chapter 1 by giving a general introduction which includes a motivation (Section 1.1), an introduction into carbon nitrides as the main material class we utilize (Section 1.2), and an overview of important concepts from the field of energy conversion, energy storage, and new device concepts beyond energy storage (respective Section 1.3, Section 1.4, and Section 1.5). Since solar batteries are a multidisciplinary research endeavor that require input from very different research field directions, it is important to have a broad understanding of key concepts. We underline important messages in grey boxes and then proceed in Chapter 2 to underline the fundamental physical and electrochemical background (Section 2.1 and Section 2.2) as well as electrochemical measurement techniques to characterize the devices (Section 2.3).

Part II consists of two perspective papers, which propose fundamental considerations and design guidelines for two emerging research fields: optoionic devices and solar batteries. In our perspective in Chapter 4, we explain the emerging concept of light-assisted ionic effects, which are generally termed *optoionic*. We start by giving a historical overview over the field and also over related light-ion interaction effects termed *photoionic* – a term which is used far more often, but only partially relates to *optoionics* as we understand it today. We then proceed to explain our current understanding of optoionic effects in layered compounds and propose an extension to the picture, that is, the impact of short- or long-range field effects *via* a case study in carbon nitrides.

Our perspective on solar batteries in Chapter 5 starts by explaining the fundamental *Solar Battery Experiment* and with this underline how light energy affects the energy and power density as well as operation modes of this new class of devices. We classify two main design routes for the devices: (1) Solar cell and battery can operate in parallel to the consumer and as such the light energy produces a photocurrent that increases the overall current output (Current Efficient Charging (IEC)). (2) Solar cell and battery can operate in series to the consumer and the photopotential reduces the overall required charging voltage (Voltage Efficient Charging (VEC)). We then continue to give an overview and classify all current solar battery designs in the respective category (two or one device designs, the latter with bifunctional electrodes or bifunctional materials) and explain how the respective

electrochemical signature of the devices can be understood.

We proceed in Part III to discuss the main three research projects associated to this thesis, namely optical design and proof-of-concept device of a solar battery and a photomemristive sensing concept. We start in Chapter 6 with a theoretical study of how to design an integrated solar battery with K-PHI acting as photoanode (*i.e.*, light absorber and electron storage electrode) and all-organic polymer hole transport and hole storage materials, with the hole transporter acting as battery electrolyte as well as performing photogenerated hole transfer *via* a rectified redox ladder-type charge transfer mechanism. We first design an optical model of the device and calculate optimized respective layer thicknesses and illumination geometries (front or rear illumination; light absorption with a high internal quantum efficiency occurring only in a small *collection layer* at the junction of K-PHI and hole transporter) by using charging time as a figure of merit. We conclude that rear illumination significantly reduces parasitic absorption of parts of K-PHI not participating in light absorption and thus increases the photocurrent. We then propose several optimization strategies to enhance light absorption in the collection layer: *via* scattering of a random textured surface, diffraction by quasi-random binary gratings, diffraction of arrays of dielectric nanoparticles, or excitation of localized surface plasmons in metal nanoparticles. We then simulate how light absorption improves energy and power density in a *Ragone plot* – up to $60\,\%$ increase in energy output. The latter is based on a study of photochromic effects as well as the effect of a charging state dependent photocurrent (*i.e.*, the more the battery is charged, the smaller the photocurrent gets) – the latter required an electrochemical study of the photoanode and cathode half cells.

We proceed in Chapter 7 to design a *proof-of-concept* device by using the knowledge gained from the previous chapter. We start by designing the multilayer configuration of the device, which required a thorough study of thick K-PHI film preparation *via* dip coating and hole transport / hole storage film fabrication *via* spin coating, as well as an electrochemical study to underline the material's suitability for the desired charge transfer and charge storage dynamics at respective junctions and in the bulk of the layers. We have then performed a study of charging solely *via* illumination, either when operated as a planar heterojunction solar cell (Open Circuit Potential (OCP) of $0.45\,\mathrm{V}$, maximum power of $0.326\,\mu\mathrm{W\,cm^{-1}}$, FF of 0.73), or when charged in open circuit conditions and subsequently discharged in the dark with an applied discharging current, *i.e.*, solar battery operation. We analyzed the latter in regard to charge, energy, and power output as a function of illumination

time (after illumination of $10\,000$ s: extracted charge of 1.5 mA h g^{-1} and energy of 0.60 W h kg^{-1}) and electric discharging current (most efficient operation at smallest current of 5.25 mA g^{-1}). We then proceeded to investigate further solar battery modes with an applied current during charging: (1) Both charging and discharging in the dark, (2) charging under illumination, or (3) charging and discharging under illumination. We concluded with looking at how light modifies charge output, electric coulombic efficiency, and *Ragone plots*. Illumination can yield an increase in extracted energy and charge by 94.1 % and 243 %, respectively.

In Chapter 8, we use knowledge gained throughout this thesis on light charging dynamics of K-PHI (*i.e.*, optoionic and optoelectronic properties) to modify the photogenerated hole extraction mechanism. Herein, we sacrificially oxidize organic electron donor molecules, which serve as the analyte in an electrolyte, and quantitatively relate the change in photophysical properties accompanying K-PHI charging to the amount of analyte. Thus, this device can be understood as a sensor, which senses *via* charge storage, and thereby imparting a memory function to this electrochemical sensor. Different operations occur: (1) Charging of the sensor "writes" the concentration information onto the device. (2) Reading is performed *via* different electrochemical and optical techniques. (3) Resetting occurs by quenching the charging state with the sacrificial electron acceptor oxygen. We term this sensor a photomemristive sensor, since electrochemical properties such as resistance depend on the charging history. Note that K-PHI acts simultaneously as receptor, transducer, and memristive amplifier. We start this work by underlining K-PHI's photoelectrochemical amperometric sensing ability with manifold analytes (sugars, alcohols, ascorbic acid, dopamine), with glucose showing a Limit Of Detection (LOD) of 11.4 µM. We then proceed to investigate charging as a function of illumination time and use glucose as a case study analyte. Readout is performed by evaluating the change in OCP (Potentiometric sensing), resistance (Impedimetric sensing), charge (Coulometric sensing), radiative emission (Fluorometric sensing), and change in color (Colorimetric sensing) – all readout methods showing different levels of invasiveness, readout times (instant to <300 s), and sensing over a wide range of concentrations (up to 50 µM to 50 mM).

In Part IV and Part V, we conclude with a conclusion and outlook towards new research/application directions as well as appendices consisting of the supporting information of Chapter 6, Chapter 7, and Chapter 8.

Part I

Description of the Thesis

1

Introduction

The first chapter sets the stage to understand this thesis. We motivate the research, discuss carbon nitrides as an exciting 2D polymer for photoelectrochemical devices, introduce energy storage and conversion technologies in light of renewable energy, and conclude by reporting on novel technology solutions, such as information storage.

Contents

1.1. Motivation: Global Warming and the Greenhouse Effect 10
1.1.1. Sustainable Energy 13
1.1.2. Sunlight as Renewable Energy Resource 15
1.1.3. The Challenge of Intermittency 15
1.2. An Introduction into Carbon Nitrides 16
1.2.1. Structural Composition and Synthesis 17
1.2.2. Photophysical Properties 19
1.2.3. Emerging Photoelectrochemical Applications 24
1.3. Energy Conversion *via* Solar Cells 28
1.3.1. Emerging Solar Cell Technologies: DSSCs 30
1.3.2. Emerging Solar Cell Technologies: OSCs 35
1.4. Energy Storage *via* Batteries and Capacitors 44
1.4.1. An Overview of Energy Storage Technologies 45
1.4.2. Electrical Energy Storage *via* Capacitors 45
1.4.3. Pseudocapacitive Energy Storage 49
1.4.4. Electrochemical Energy Storage *via* Batteries 54
1.5. Beyond Energy Storage 60
1.5.1. Resistance Switching 62
1.5.2. Materials for Resistance Switching 64
1.6. References 65

1

Preface of the Introduction

The device concepts that comprise the main research part of this thesis (Part III) are multifunctional (solar batteries, photomemristive sensors), which in return requires an understanding of manifold different concepts and research fields: Carbon nitrides are the main class of materials that we will discuss (Section 1.2). Light absorption and photocurrent generation is essential to enable light-assisted concepts (Section 1.3). Charge storage is the second pillar of multifunctionality of the devices discussed herein (Section 1.4). Understanding novel device concepts such as memristors may extend our understanding beyond traditional charge storage and are discussed in context of the photomemristive sensor (Section 1.5). Hence, multiple research fields need to be introduced.

In the following introduction, we summarize those fields towards key concepts that aid understanding of the perspectives in Part II and research publications in Part III. To guide the reader through this topic-wise rather extensive introduction and ensure understanding of the most important concepts, "Take Home" messages are marked in blue boxes.

1.1. Motivation: Global Warming and the Greenhouse Effect

Mitigating adverse effects of global warming (*i.e.*, the increase in the surface average temperature of the earth)[1] presents likely one of the greatest challenges to our modern society and requires a sudden and significant increase in pace of climate actions as recognized by the United Nations (UN) *via* the Paris Rulebook of the UN Climate Change Conference 2021 (COP26). The concept of terrestrial heat retention responsible for global warming was investigated as early as 1824 by Jean-Baptiste Joseph Fourier and we will briefly explain it in the following. Fourier reported calculations of an earth-size planet with a comparable distance to the sun, which should in theory be much colder when considering only sun's irradiation energy.[2] He concluded with proposing that the atmosphere acts as an insulating blanket. In 1856, Eunice Foote related changes in atmospheric composition to warming and thus, discovered that trapping of infrared radiation transmitted by the earth's surface *via* carbon dioxide and water vapor is likely responsible for this "atmosphere blanket" heating effect.[3]

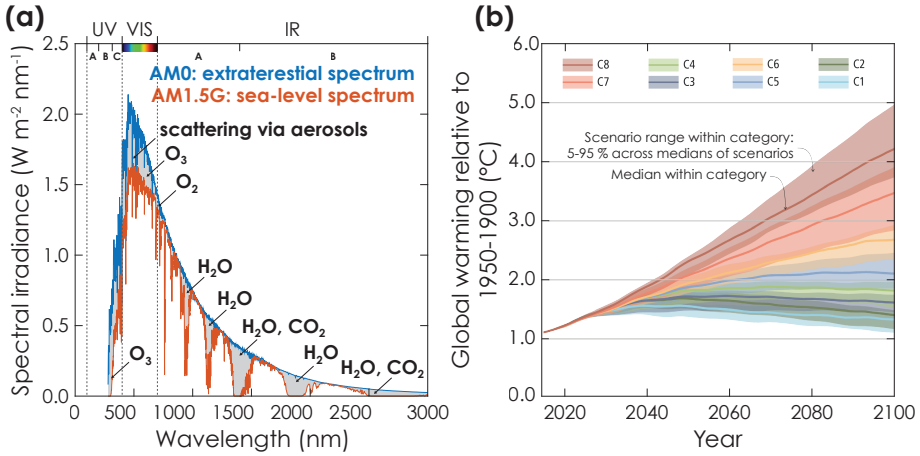

Figure 1.1. Global warming. (a) The extraterrestrial (blue) and terrestrial (orange) solar irradiance spectrum ((ASTM) G-173) at standard atmospheric conditions, given as distribution of power as a function of wavelength. The former is defined as irradiance through no air mass (AM0), the latter as irradiance through 1.5 reference air masses with scattering from the surrounding environment (AM1.5 Global). Absorption of the two GHGs water vapor and carbon dioxide is marked with respective arrows. Reproduced with permission.[4] Copyright 2002, Elsevier Ltd. **(b)** Ensemble of projected median warming across global modelled pathways within a climate category (C1-C8), with the category medians (lines). The categories are detailed in the IPCC report (Climate Change 2022: Mitigation of Climate Change. Contribution of Working Group III to the Sixth Assessment Report of the Intergovernmental Panel on Climate Change). Reproduced with permission from IPCC, 2022: Summary for Policymakers.[5] Cambridge University Press, Cambridge, UK and New York, NY, USA.

Today, we term this effect as *Greenhouse* effect and understand it as follows:[6] Earth's atmosphere consists mainly of oxygen (O_2), nitrogen, and argon, but also of the trace gases carbon dioxide, methane, nitrous oxides, and ozone. Unlike the main components of earth's atmosphere, these trace gases (also called greenhouse gases or GHGs) have the ability to absorb and re-emit parts of the solar irradiation *via* suitable internal vibrational modes: carbon dioxide and methane absorb in the infrared region, ozone absorbs in the ultraviolet region. Note that the absorption of water vapor and carbon dioxide GHGs is most significant in the IR-range of the solar spectrum and reduces the spectral irradiance at certain wavelengths to zero. This can be observed best when comparing the solar irradiance at sea-level (AM1.5 global spectrum) and extraterrestrial (AM0 spectrum) as shown in Figure 1.1 (a). Note that nearly $67.1\,\%$ and $62.5\,\%$ of incident solar photon flux (corresponding to the solar energy) at sea-level and extraterrestrial, respectively, occurs at wavelengths larger than $780\,\text{nm}$, defined by IUPAC as infrared radiation onset wavelength.[7]

Thus, upon irradiation parts of the incident solar light gets absorbed by GHGs and since emission is isotropic re-emitted towards both earth's surface and into space. At the same time, the major amount of solar irradiation transmits through the atmosphere and hits earth's surface, causing it to heat up accordingly. As a result of this temperature difference between earth and its surrounding environment, black body radiation gets emitted.[8] Due to the low temperature (on average in 2020: around $274\,\mathrm{K}$ or $0.77\,^{\circ}\mathrm{C}$), this radiation occurs at large wavelengths (short-wave IR radiation), since according to Wien's displacement law the wavelength is inversely proportional to the temperature of a black body if there is no net flow of energy or matter between the body and its environment. Analogous to incident solar light, this radiation gets absorbed by GHGs and portions are re-emitted back towards the surface, thus "trapping" it in the atmosphere.

The magnitude of the *Greenhouse* effect depends on the concentration of GHGs in the atmosphere. Both natural (*e.g.*, volcanic eruptions) and anthropogenic (*i.e.*, human) emissions govern the amount of both water vapor and carbon dioxide – however, while volcanos can have significant short term effects on temperature (both cooling *via e.g.*, volcanic ash and sulfuric gases, and warming *via* significant GHG emissions), their annual average GHG emissions (130 to 230 million tons of carbon dioxide) falls around two orders of magnitude shorter than the annual average human emissions (around 26 billion tons of carbon dioxide).[9] Other natural effects are either neglectable (*e.g.*, fluctuations in solar irradiation likely contribute to only $10\,\%$ of 20th century global warming[10]) or influence global warming on much longer timescales (*e.g.*, the *Milankovitch* cycle describing fluctuations in earth's orbit requires around $100\,000$ years, with considerable changes between extremes occurring at less than $10\,000$ years[11]).

Hence, one can draw a correlation between GHG emissions and the magnitude of the *Greenhouse* effect, which governs the temperature increase. In Figure 1.1 (b), we show the annual increase of global surface temperature in dependence of different predicted carbon dioxide emission scenarios. It becomes evident that the more carbon dioxide is emitted, the larger the temperature is expected to increase.[5] It is thus paramount to limit future carbon dioxide emissions. In fact, detrimental effects such as more extreme weather events[12] and more realistic climate "tipping" points (*e.g.*, cryosphere melting could cause a significant rise in sea-water level over centuries to millennia)[13,14] cause already to-date pressure on our society and dictate urgency in developing solutions to reduce GHG emissions that we can control, *i.e.*, from anthropogenic sources.[14]

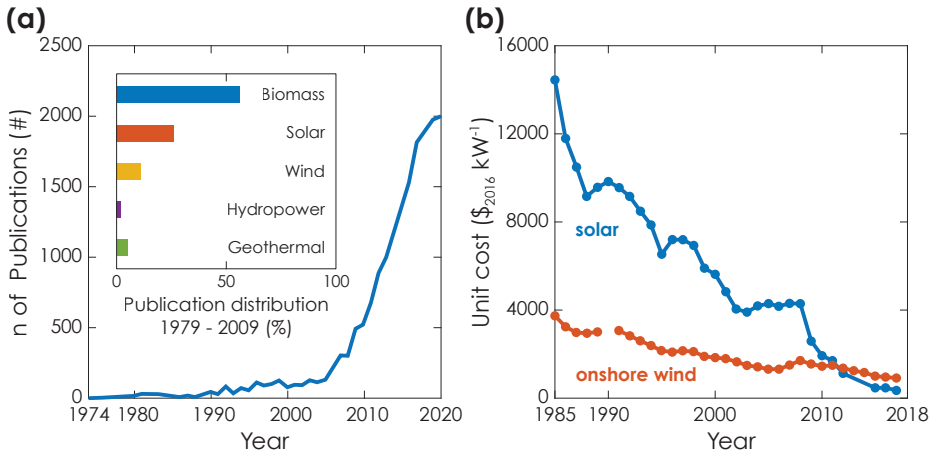

Figure 1.2. Sustainable energy research. (a) The amount of scientific papers published in the field of renewable energy from 1974 to 2020. Note that 51.7 % of papers were published between 2016 and 2020, underlining the recent significant increase in research interest. Adapted from O. Chygryn *et al.* under the terms of open access CC BY 4.0 license.[15] Copyright 2021, E3S Web of Conferences. The inset shows the share of renewable energy technologies in respective research papers. Adapted with permission.[16] Copyright 2013, Elsevier Ltd. **(b)** Development of cost of renewable energy device units for solar (blue) or onshore wind (red) harvest normalized to their respective power output from 1985 to 2018. The decrease in cost underlines growing maturity and implementation of renewable energy technologies. Reproduced under the terms of open access CC BY 4.0 license.[17] Copyright 2021, Elsevier Ltd.

1.1.1. Sustainable Energy

The Paris Climate Agreement of 2015 defined key goals to reduce global warming to a temperature increase of below 2 °C – preferably 1.5 °C – compared to pre-industrial levels. Commitment to this legal framework was renewed and implementation established during COP26, in which 190 countries have agreed to phase out fossil coal power plants, with a total reduction of new power plant projects by 76 %. At the same time, 34 countries and 5 public finance institutions agreed to end all public funding of fossil fuel energy related projects by the end of 2022.[18] While on the one hand the reduction of fossil energy usage is very good and important to reduce GHG emissions, on the other hand alternative renewable energy solutions are required to supply the growing energy demand. In fact, while in 2020 the global population consumed a total of 115 951 TWh, this number is expected to increase by 18 % to around 136 943 TWh in 2040.[19] This increase results from population growth, the high standards of energy requirement in developed nations, as well as socio-economic growth of developing nations. We will discuss renewable energy

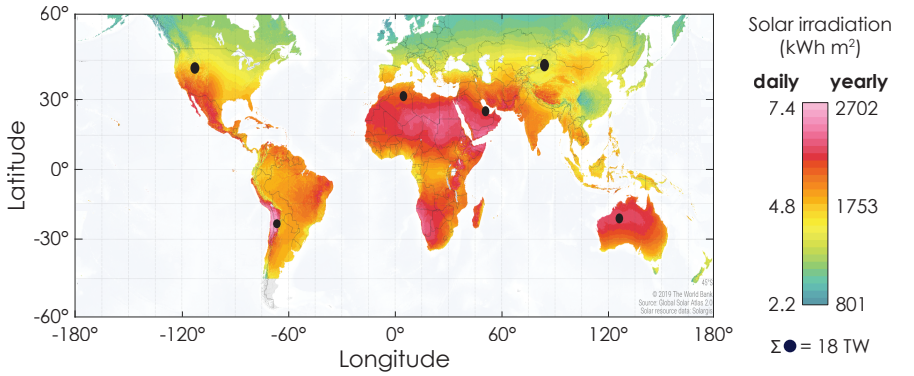

Figure 1.3. Potential of solar irradiation as renewable energy source. Average of solar absolute irradiation. The dots represent circular areas (radii of 100 km), which accumulated would produce sufficient energy to power human's energy requirements if covered with solar panels with an efficiency of 8 %. Solar irradiation map adapted under the terms of the open access CC BY 4.0 license.[21] Copyright 2020, The World Bank and Solargis. Irradiation area (black dots) adapted from M. Loster.[22]

solutions in the following.

Renewable energy is defined as transforming natural phenomena such as sunlight, wind, gravitational forces (*e.g.*, tides), or heat of the Earth's core (*i.e.*, geothermal) into usable energy.[20] While in theory this combined energy supply dwarfs equivalent fossil resources, it is traditionally difficult to access and thus, not cost efficient. The first development of renewable resources was kicked off by the 1950s oil crisis which saw huge increases in oil prices and thus, cheaper alternatives were required.[20] Since then, the growing environmental awareness has significantly increased research effort in the last decades and several technologies have reached maturity. The growing research interest is best visualized *via* a literature review, as shown in Figure 1.2 (a): The annual published literature on renewable energy related technologies has seen a huge increase to around 2000 publications per year in 2020.[15] At the same time, the maturity and implementation of these technologies increases their economic viability, thus decreasing the price which in return facilitates implementation. As an example, while in 1985 a typical solar cell unit had cost ca. $14\,000\,\$(2016)/\mathrm{kW}$, this price dropped to below $500\,\$(2016)/\mathrm{kW}$ in 2017 (Figure 1.2 (b)).[17] Wide implementation has led to a record amount of 256 TWh of electricity being produced in 2022 in Germany *via* renewable sources, which accounts to 46 % of consumed electricity.

1.1.2. Sunlight as Renewable Energy Resource

Let us compare the earth to a thermodynamically closed system with no mass transfer between the atmosphere and space. As such, the major energy influx is solar radiation (with a temperature of $T \approx 5760\,\mathrm{K}$), which far outmatches radiative emissions of earth (at $T \approx 276\,\mathrm{K}$ as mentioned above).[23] In fact, this energy influx is mainly responsible for all natural photochemical processes on earth, accounting to a total power of ca. $200\,\mathrm{TW}$ (for comparison: humanity requires a total average power of ca. $18\,\mathrm{TW}$).[22,24] Thus, both the abundance of solar irradiation energy and the fact that it is the only major energy influx to earth underline its suitability as – likely the most – viable renewable energy source. To name some numbers, the surface of the earth receives an average absolute irradiation of $343\,\mathrm{W\,m^{-2}}$. When including losses due to reflection (ca. $30\,\%$) and only area above sea-level (ca. $30\,\%$), we can calculate a total average absolute irradiance of $36\,000\,\mathrm{TW}$. Even when halving this number to account for impractical solar panel locations (*e.g.*, antarctica), the average human energy requirements are merely $0.1\,\%$ of solar irradiation power.[22] We visualize the theoretically required area of solar panels with an efficiency of $8\,\%$ in Figure 1.3. The black dots distributed over the map show circular areas with a diameter of $100\,\mathrm{km}$, which would have to be covered with solar cells to produce an average power of $18\,\mathrm{TW}$. This is more than the power requirement in 2018 and according to the International Energy Agency (IEA) only a bit less than the predicted power requirements of $19\,\mathrm{TW}$ in 2030, if current energy saving policies are implemented.[25]

1.1.3. The Challenge of Intermittency

While we have underlined the suitability of renewable energy sources as a viable solution to tackle the world's energy needs, there are also challenges associated to their implementation, mainly their intermittent availability. Sunlight, *e.g.*, is only available during the day and solar irradiation intensity is far larger in the summer than in the winter. Furthermore, cloud overcast can significantly influence the intraday irradiation intensity. Thus, stochastic fluctuations on timescales of months, days, hours, or even minutes exist.[27]

Since energy demand can also be very volatile, buffering the energy grid is essential for a stable operation. To illustrate this difficulty, we show in Figure 1.4 both electricity supply and demand of Germany for a week in the winter compared to one week in the summer. It becomes evident that matching electricity supply and

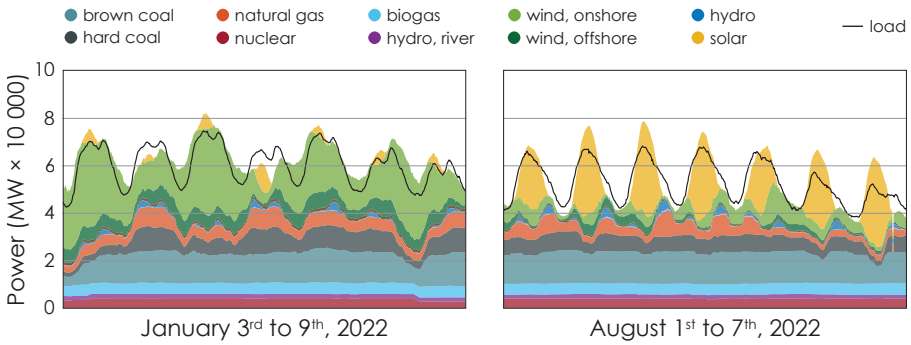

Figure 1.4. Germany's energy mix in 2022. Major electricity sources for a week in the winter and a week in the summer. The electricity load curve is shown *via* a black line. Significant fluctuations of electricity sources and a volatile load cause a partially unsuccessful matching of both curves, underlining the importance of balancing intermittent energy sources such as wind and solar. Adapted with permission from *energy-charts.info*.[26]

demand is not facile and nearly never fully achieved. Note that energy sources based on fossil (brown coal, hard coal, natural gas), nuclear energy, or hydro energy Figure 1.4 must adapt their power output when a surplus or not enough electricity is present. However, the buffer capability is far smaller than required.

While the climate crisis dictates an urgent rethink in sustainability and renewable energy show huge potential to shape our future's energy supply, energy storage is required. In this work, we will focus on this aspect and present first a conclusive introduction into solar cells and batteries and subsequently present a novel class of bifunctional devices, capable to both harvest solar irradiation and store its energy at the same time.

1.2. An Introduction into Carbon Nitrides

In the following, we will proceed to introduce carbon nitrides as an exciting material class, suitable for many applications in emerging device technologies for the "post-silicon electronics" age.[28] Carbon nitrides (CN_x) are a class of synthetic 1D or 2D polymeric materials with a backbone composed of strictly alternating carbon (C) and nitrogen (N) atoms, thus forming exclusively C-N and N-H bonds, but not of C-C or C-H bonds. Consequently, it is controversial whether to term them as or-

ganic or inorganic polymers, since the term organic would imply the latter C-C and C-H bonds. Since the fully condensed, binary structure resembles the structure of graphite, carbon nitrides are often termed *graphitic* carbon nitrides (or graphitic CN).[29] The main advantages of carbon nitrides lie in their optoelectronic and optoionic properties (Section 1.2.2), earth abundant nature, easy scalable synthesis, and low toxicity.

A brief History. Early research on this material class was performed in 1834 by Jacob Berzelius, who observed a self-propagating reaction of mercury(II) thiocyanate when ignited – thus fabricating the so-called *pharao's serpent* and making carbon nitrides one of the oldest reported synthetic polymers.[30] Justus von Liebig published in the same year a more systematic research on various precursor materials and byproducts of this novel compound, naming in *Melon* for no apparent reason.[31] It took until the second half of the 20st century for carbon nitride research to revive – fueled by theoretical structural investigations performed by Cohen and Liu who predicted that a three-dimensional interconnected carbon nitride (β-C_3N_4) should possess a larger hardness than diamond.[32,33] However, the most significant increase in research activity was fueled from a very different direction: X. Wang, K. Domen, M. Antonietti *et al.* published in 2009 an experimental study containing theoretical calculations for Melon's semiconducting properties, enabling photocatalytic water reduction and oxidation in presence of respective Sacrificial Electron Donor (SED) and Sacrificial Electron Acceptor (SEA).[34] He complemented his work by reporting a wavelength dependent photocatalytic hydrogen evolution rate of up to ca. $10.7\,\mu M\,h^{-1}$ when illuminated at 420 nm. This report pushed carbon nitrides back into the spotlight and triggered numerous publications, which proposed applications in various sustainable research fields. In this section, we will first discuss the material's chemical background and then develop an understanding for its exciting optoionic and optoelectronic properties, which enable a wide range of applications.

1.2.1. Structural Composition and Synthesis

The fundamental tectonic unit of all carbon nitride analogs are either triazine (1,3,5 - triazine, C_3N_3) or heptazine (1,3,4,6,7,9,9b - heptaazaphenalene, C_6N_7) building blocks, which are an aromatic alternating arrangement of sp^2-hybridized nitrogen and carbon atoms (Figure 1.5).[28,35–37] The most prominent triazine is melamine

– known for its applications as precursor for thermoset plastics and flame retardant materials.[38,39] Melamine can be synthesized from the precursors cyanamide or urea.[40] When heating melamine to temperatures above 317 °C, a cascade of condensation reactions occurs, accompanied by a release of ammonia, which eventually leads to the formation of the heptazine monomer melem. Melem can be used as precursor to form various polymeric carbon nitrides, based both on a triazine or heptazine backbone. For instance, heating melem to above 520 °C yields a yellow powder, the so-called 1D polymeric Liebig's Melon ($[C_6N_7(NH_2)NH]_n$). Melon has an optical bandgap of around 2.7 eV and thus, is a photoactive semiconductor (more details of photophysical properties are elucidated in Section 1.2.2).[34] Alternatively, 2D poly(triazine imide) (PTI) can be synthesized when heating melem to around 600 °C in an eutectic mixture of LiX/KX (with X = Cl or Br).[41,42] The pores of PTI are filled with the respective salt ions. Slightly lower synthesis temperatures of 550 °C in a salt melt with KCl results in 2D poly(heptazine imide) (PHI), with potassium ions (K^+) filling the pores of PHI (hence terming it K-PHI accordingly).[43] K^+ is located closer to the center of the pore channels.[44] Formation of this extended 2D network requires autogenous ammonia pressure, *e.g.*, by performing the reaction in a flow of inert gas.[45] It is possible to exchange the ions in K-PHI to Li^+, Na^+, Cs^+, Mg_2^+, Ba_2^+, Ru^+, Au^+, or NH_4^+.[46,47] An exchange with protons is also possible (H-PHI) and occurs upon reduction of the pH.[35,48] H-PHI shows a distinct color change from yellow to white. Both PHI and PTI are linked with imide bridges and sheets are stacked on top of each other *via* attractive van-der-Waals forces, forming a 3D structure (for K-PHI with a stacking distance of around 3.2 Å and an on-average neighbor layer offset of around 2.8 Å).[46,49] PHI is likely only delocalized within the heptazine structure. Analogous to Melon, both Li/K-PTI and K-PHI have optical bandgaps.[35,45,50,51] Fully condensed forms of both triazine and heptazine based carbon nitrides differ from the above-mentioned polymers by (covalently) filling the pores with a respective triazine or heptazine unit. They represent the most commonly referred to form of carbon nitrides and possess the stoichiometric formulas of g-C_3N_4 for triazine and heptazine, respectively, with "g" referring to their graphite-like structure as mentioned above.

It is worth mentioning that the correct structure of carbon nitride modifications is still controversial and a topic of ongoing research, which mainly results from the low crystallinity of the material.[57] In addition, according to a very recently published study by T. Jacob *et. al.*, thermochemical calculations suggest that mixed structures of different carbon nitride modifications such as Melon, PHI, and g-C_3N_4 may be stable at the same synthetic conditions.[58] Thus, small domains of more or less

condensed forms are likely always present when synthesizing carbon nitrides and govern photophysical properties. We will discuss this latter aspect in the next section.

1.2.2. Photophysical Properties

As mentioned in the previous section, polymeric carbon nitrides possess visible light bandgaps (2.7 eV for K-PHI). This bandgap is not only responsible for the characteristic yellow color, but also indicates photoresponsive semiconducting properties. In this section, we will dive into light absorption and photoinduced modification of conductivity as well as charge storage. We will discuss this in the context of band theory – as predominantly done for polymeric carbon nitrides – since it enables a discussion of charge-carrier behavior optimization.[59–61]

Light Absorption in View of Exciton Dynamics. Polymeric carbon nitrides have rather low dielectric properties (dielectric constant of around 3-8).[66,67] Consequently, when light absorption causes an electron to excite and rapidly thermalize into the CB, leaving behind a photogenerated hole in the VB, both photoexcited electron and hole experience a significant Coulomb interaction (Figure 1.6 (a)). This prevents both carriers to be free and causes the formation of an exciton. Due to the low dielectric constant, the binding energy (equivalent to the energy difference between a bound electron-hole pair and free electron and holes or energy released when photoexcited electron and hole recombine; termed *exciton binding energy*) is rather large and ranges from 0.1 to 1 eV. Such excitons are typically termed *Frenkel excitons* and produce strong excitonic effects, which in return influence electronic and optical properties. While the carbon nitride community still controversially discusses the extent to which excitonic effects govern electronic and optical prop-

Figure 1.5. Structural analogs and synthesis cascade of key carbon nitrides (next page). Melamine (synthesized from precursors such as urea, dicyandiamide, or cyandiamide) can condense to form 1D Melon polymers at a temperature of 500 to $600\,^{\circ}$C.[29,40] Melon can form K-PHI *via* a salt melt with potassium thiocyanate (KSCN) at $500\,^{\circ}$C.[35,37,52,53] K-PHI forms in a layered structure and with pores, in which mobile (hydrated) ions such as potassium (K^+) are coordinated.[46] Both Melon and K-PHI utilize heptazine units as key building blocks. Alternatively, heating melem in a salt melt to $600\,^{\circ}$C forms the triazine based poly (triazine imide).[54,55] The fully condensed forms are shown at the bottom of the figure. Adapted with permission[36] and under the terms of open access CC BY 4.0 license.[56] Copyright 2020, Springer Nature; Copyright 2021, Wiley-VCH.

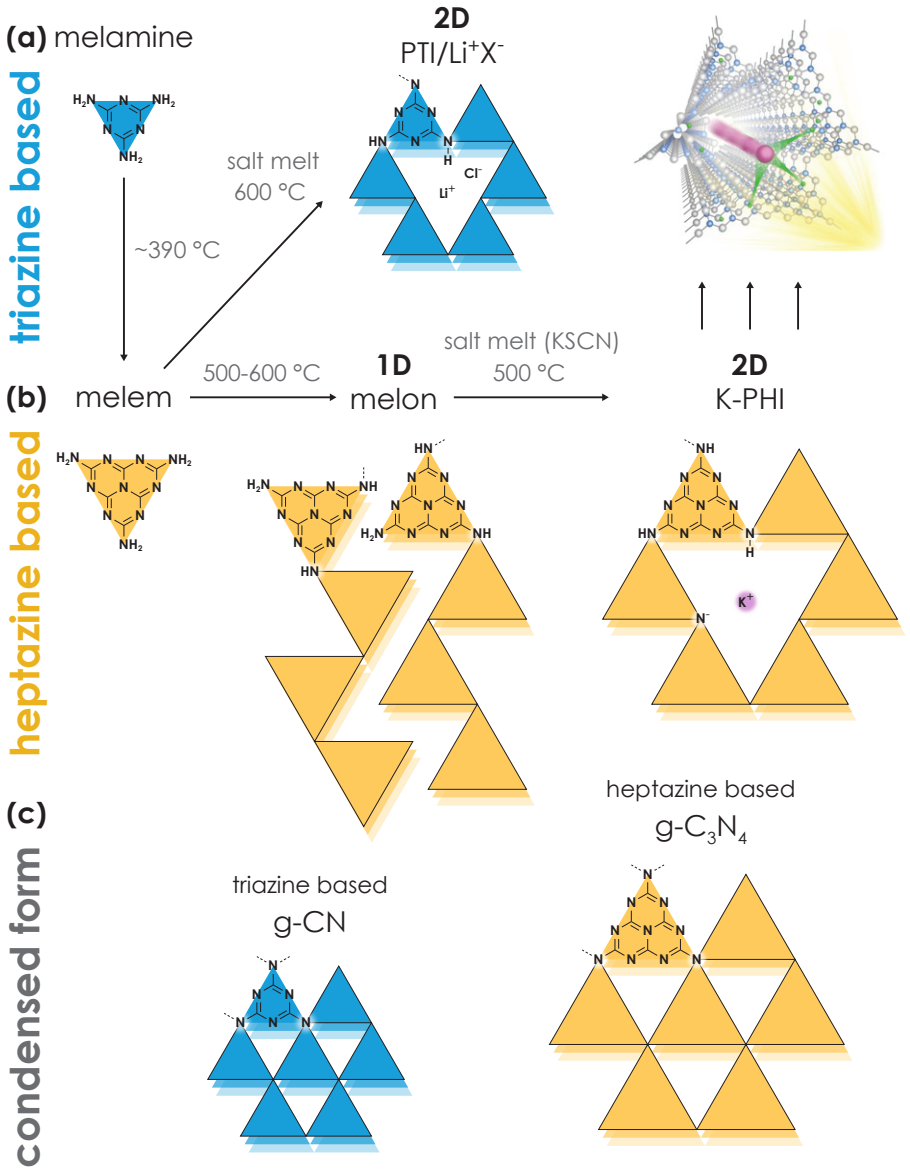

erties, we will base our discussion on these effects.[58,68–70] After light absorption and formation of the exciton, there are several different pathways to proceed:

(i) Exciton diffusion can occur but is rather limited in range (around 20 to 40 nm) and lifetime (for g-C_3N_4 reports range from several ns up to remarkably long 260 ns).[65,71,72]

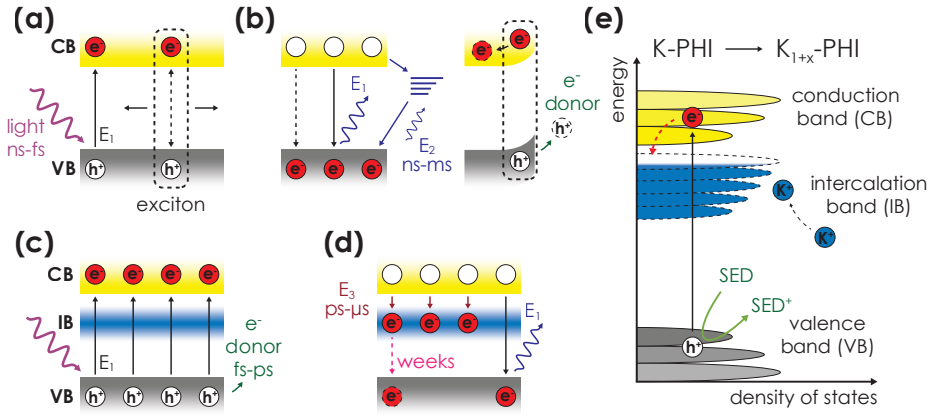

Figure 1.6. Light absorption and photocharging of carbon nitrides. (a) Incident light excites an electron from Valence Band (VB) into Conduction Band (CB). Attractive Coulomb forces between both charge carriers causes the formation of an exciton (dashed box), which can diffuse across the semiconductor. **(b)** Excitons can recombine (left). In carbon nitrides, this occurs non-radiatively, *via* a fluorescence (time range of ns) or phosphorescence mechanism (time range of ns to ms).[62,63] Alternatively, excitons can split in presence of sufficient energy to overcome the exciton binding energy (*e.g.*, at junctions; (b) right). **(c-d)** Certain 2D polymeric carbon nitrides have the ability to trap photoexcited electrons in an intercalation band, if photoexcited holes are extracted sufficiently fast (time scale of fs to ps). The trapped electrons state is stable over several days to weeks. **(e)** Summary of the charge trapping mechanism, which requires photointercalation of ions to stabilize the photoexcited electrons. Adapted under the terms of open access CC BY 4.0 license.[56] Copyright 2021, Wiley-VCH. Time ranges extracted *via* time-resolved ultra-fast spectroscopy.[64,65]

If excitonic effects are dominant, they likely also govern the charge conduction (or charge transfer) process, since the major photoinduced species are excitons and not free carriers. Energy transfer thus requires an exciton transfer process such as Förster-type energy transfer (FRET).[73] FRET is a radiation-free energy transfer, which works *via* dipole-dipole interactions between a donor and an acceptor molecule, and in theory has a higher efficiency than a carrier based charge transfer process.[74] However, the existence of this charge transfer mechanism has only received sporadic attention in carbon nitride research, likely since they are difficult to measure: carbon nitrides tend to aggregate in solution, which produces lots of scattering and thus complicates the spectroscopic investigation.[73,75,76]

(ii) Excitons can recombine, either through radiative or non-radiative pathways (Figure 1.6 (b), left). This process was tracked manifold times by means of spectroscopic studies. The polymeric carbon nitride absorption edge around

450 nm (corresponding to the bandgap of 2.7 eV) is followed by radiative decay of the excitonic states in the same wavelength range. A fluorescence lifetime of several ns was measured for g-C_3N_4.[65] The nature of the emission depends on both the specific type of carbon nitride polymer, but also on morphology and further chemical modifications such as the surface termination groups. For instance, S. Yang *et. al.* recently reported carbon nitride nanodots which resemble the g-C_3N_4 structure, but with oxygen surface termination.[63] The authors report two distinct lifetimes, 3.8 ns and 235 ms, which correspond to a respective fluorescence and phosphorescence process.

Note that reported Apparent Quantum Efficiency (AQE) for carbon nitride nanosheets utilized as photocatalysts range from 5 to 16 %.[77] The AQE is a measure of how efficient light (*i.e.*, incident photon flux) absorbs and produces a light driven effect, *e.g.*, a photocatalytic reaction or a photocurrent (in case of photocurrent and as a function of illumination wavelength, the AQE is also known as External Quantum Efficiency (EQE)).[78] The reported carbon nitride AQE is high for photocatalysts, but still underlines that most excitons recombine rather than producing free charge carriers.

(iii) The process desired for many applications is exciton separation, which results in respective free charge carriers, *i.e.*, an electron and a hole (Figure 1.6 (b), right). To achieve this, first sufficient energy is required to overcome the exciton binding energy – likely one of the major challenges for carbon nitride applications due to the large exciton binding energy.[67] Second, an electric field is required for effective charge carrier extraction. Exciton separation likely occurs at sites where energetic disorder occurs. For Melon, this was proposed to exist at order-disorder interfaces.[79] Dopants and additives can also induce exciton dissociation. W. Tu *et. al.* recently proposed cysteine units in g-C_3N_4 nanotubes for photocatalytic water splitting, achieving an AQE of 13.4 %.[80]

After exciton separation, electrons and holes can diffuse between nanosheets, in the case of Melon by hopping *via* overlapping π-π orbitals.[81] Since imide bridges between heptazine units are not conjugated and largely insulating as mentioned above, the electron/hole conduction mechanism is thus anisotropic. For PTI, M. J. Bojdys *et. al.* reported a 65 times lower electric conductivity along the basal plane than along the stacked plane.[82]

TRAPPING PHOTOGENERATED ELECTRONS. As detailed in the previous section, carbon nitrides can produce free charge carriers, if exciton separation occurs. These charge carriers can drive photoreactions, most prominently photocatalytic water splitting.[34] Remarkably, certain recently reported 2D polymeric carbon nitride modifications possess the capability to stabilize photogenerated charges after exciton separation and photogenerated hole extraction (*e.g.*, *via* a SED) in trap states close to the CB (Figure 1.6 (c) and (d)), as reported *via* time-resolved spectroscopic methods.[83,84] These states exhibit a very long stability of up to several weeks and can be accessed *via* catalytic or electrochemical methods that are discussed in the next section.[51,64,85–87]

While the 2D carbon nitride K-PHI supports charge storage, Melon does not show this feature.[87] The reason for this lies likely in the stabilization of stored charges, which likely occurs *via* mobile ions intercalated inside the pores of K-PHI (Figure 1.5). Thus, one commonly refers to "intercalative" electronic states inside the bandgap in an intercalation band (Figure 1.6 (e)).[56] Electronic charge carriers may couple to ionic charge carriers. Both are anisotropic and occur along the stacking order.[46] Since ion intercalation and motion is triggered by illumination, the effect is referred to as an *optoionic* process – a newly established research field which we will delineate in detail in Chapter 4. Both intrinsic (lattice constituents from synthesis, see Section 1.2.1) and extrinsic K^+ ions participate, the latter causing a stoichiometry change (Figure 1.6 (e)). Noteworthy, both intrinsic and extrinsic ions are hydrated, *i.e.*, possess a solvation shell, which either co-intercalates into the pores – the K-PHI pore radius of ca. $3.8\,\text{Å}$[35,87] is in the range of K^+ hydration shell hydrodynamic radii (around 2.8 to $3.3\,\text{Å}$, when around 5-7 water molecules coordinate around K^+ in an inner shell, as typically observed in crystallographic studies)[88,89] – or needs to partially decompose at the K-PHI / solution interface. The reported PHI ionic conductivity is highest for hydrated Na^+ ($(5.0 \pm 3.0) \times 10^{-6}\,\text{S cm}^{-1}$, compared to $(6.0 \pm 10.0) \times 10^{-8}\,\text{S cm}^{-1}$ for K-PHI and $(1.0 \pm 1.0) \times 10^{-7}\,\text{S cm}^{-1}$ for Li-PHI) at ambient conditions (humidity of around 30 to $40\,\%$, resulting in 9 to 15 wt% of water in PHI), likely since their solvation shell fits best into the pore size of PHI as a result of layer stacking.[46] Hydrated ion motion thus likely influences the charging kinetics of K-PHI, which has been described to possess a pseudocapacitive signature in the bulk and capacitive signature on the surface (for an explanation of the term pseudocapacitance please refer to Section 1.4.3).[87] Pseudocapacitance originates from reduction of the PHI backbone (trapping of electrons in the intercalation band) and connected (photoinduced) ion motion in the bulk. Capacitance results from ions

at the K-PHI / solution interface forming double layer capacitance.[56,90] We further discuss pseudocapacitance in Section 2.3 and throughout Part III.

A well-known feature of photoreduced (*i.e.*, charged) 2D polymeric carbon nitrides is their distinct photo (electro) chromic color change from yellow to blue.[35,51] The color change is caused by an additional absorption band at around 670 nm (see bottom-left inset in Figure 1.7 (b)), and quantitatively relates to the amount of photocharged trapped electrons (Chapter 8). The origin of this color change is still subject to ongoing investigation. One can draw a comparison to photocharging color change effects observed in inorganic 2D layered compounds, such as TiO_2 or ZnO, where the intervalence transitions (*e.g.*, metal-to-metal transitions) likely produce the effect.[49] While for TiO_2 these transitions occur between 595 to 780 nm – similar to the carbon nitride K-PHI and therefore also resulting in a blue color, for ZnO an absorption increase is observed around 3000 to 7000 nm.[92–94] One can also draw a comparison to metal halide F-centers, or stable radical molecular compounds.[56]

1.2.3. Emerging Photoelectrochemical Applications

The exciting photophysical properties have expressed themselves in the formation of manifold applications. We will mention key example applications herein. We will

Figure 1.7. Emerging applications of carbon nitrides (next page). (a) The carbon nitride compounds K-PHI and H-PHI are capable to perform photocatalytic water reduction under illumination with the cocatalyst Pt (here: 2 wt% for H-PHI and 8 wt% for K-PHI) and in presence of the SED methanol (here: 10 vol%). Particle morphology significantly influences hydrogen production yield, with an optimum particle size around 600 to 1000 nm for K-PHI and 180 to 500 nm for H-PHI. Reproduced under the terms of open access CC BY 4.0 license.[48] Copyright 2021, Wiley-VCH. **(b)** When illuminated without a water splitting cocatalyst, K-PHI accumulates photogenerated charges, accompanied by a new absorption band around 670 nm which changes K-PHI's color from yellow to blue (see bottom-left inset). Adapted under the terms of open access CC BY license.[35] Copyright 2019, American Chemical Society. Photocatalytic water reduction is subsequently triggered in the dark by adding the cocatalyst Pt. Reproduced with permission.[51] Copyright 2017, Wiley-VCH. **(c)** Design strategies to improve photocatalytic performance include forming a heterojunction with conductive polymers such as PEDOT:PSS. Reproduced under the terms of open access CC BY 4.0 license.[91] Copyright 2021, Wiley-VCH. **(d)** K-PHI nanoparticles can be used as microswimmers *via Janus particles*, that is, particles half coated with Pt. Upon photocharging, water oxidation and reduction only occur on the coated side of the particle, thus providing propulsion. Reproduced under the terms of open access CC BY-NC-ND 4.0 license.[85] Copyright 2020, PNAS. **(e)** The concept of microswimmers presented in (d) was extended to incorporate drug storage (doxorubicin (DOX)) in K-PHI, which is enabled by the highly porous structure. Controlled drug release can be triggered *via* illumination. Reprinted with permission.[86] Copyright 2022, AAAS.

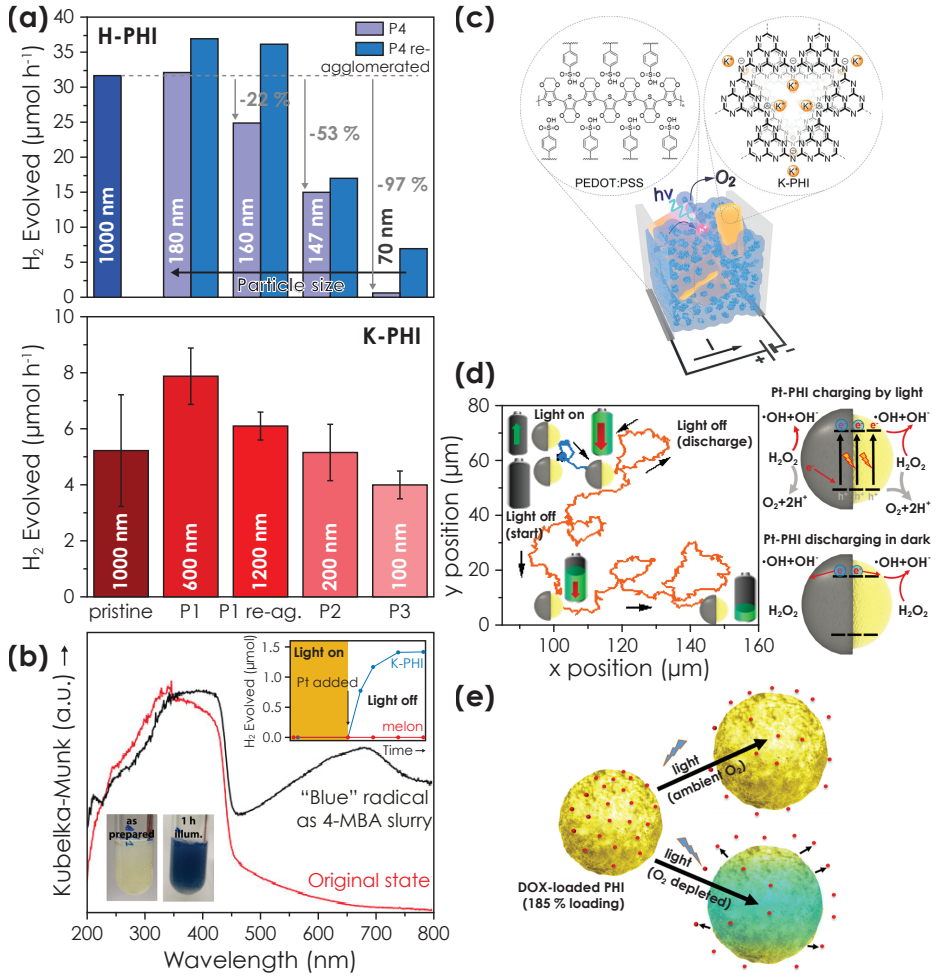

thereby focus on several application areas and discuss both more traditional carbon nitride applications as well as applications which incorporate the unusual ability of intrinsic charge storage.

PHOTOCATALYSIS WITH CARBON NITRIDES. The most prominent application field is likely photocatalysis, which – as detailed above – is also responsible of triggering the huge carbon nitride research boost that we experience today.[34] Most importantly, typical VB and CB band positions for carbon nitrides are located suitably to enable photocatalytic water splitting (*e.g.*, for K-PHI: CB $= -0.6$ V *vs.* NHE and VB $=$ 2.1 V *vs.* NHE), that is, -0.4 V *vs.* NHE for water reduction (H_2) and 0.8 V *vs.* NHE for water oxidation (O_2) at $pH = 7$.[36,87] Carbon nitrides possess a significant overpo-

tential for water reduction, which requires the addition of suitable cocatalysts such as Pt.[34,35,48,95]

For K-PHI and H-PHI a H_2 evolution rate up to $8\,\mu mol\,h^{-1}$ and $41\,\mu mol\,h^{-1}$, respectively, were reported by J. Kröger *et. al.* for optimized particle sizes.[48] The authors describe in the same study impact of morphology on photocatalytic activity and underline the impact of particle size on uniform Pt cocatalyst deposition, bandgap, suspension stability, exciton/charge transport, functional groups, and trap states – all parameters that govern the H_2 yield and require an advanced understanding (Figure 1.7 (a)).

Tuning routes to improve photocatalytic yields include functionalization. J. Kröger *et. al.* reported a postsynthetic modified 2D PHI with terminal melamine groups (Mel-PHI).[95] Its photocatalytic hydrogen production yield of $5570\,\mu mol\,h^{-1}\,g^{-1}$ outperforms other PHI-related carbon nitrides such as K-PHI (ca. $2200\,\mu mol\,h^{-1}\,g^{-1}$) or H-PHI (ca. $3500\,\mu mol\,h^{-1}\,g^{-1}$). The authors conclude that the covalent modification enhances catalyst-electron donor interaction and stabilizes the catalyst suspension. Other tuning routes suggest heterojunctions as a viable strategy to increase photocatalysis performance. For instance, A. Savateev *et. al.* reports on a composite heterojunction between K-PHI and the conductive polymer PEDOT:PSS, with PEDOT:PSS significantly increasing the electrical conductivity of the cell and its associated photocatalytic performance (Figure 1.7 (c)).[91]

A very different photocatalysis approach involves the charge storage capability of K-PHI. B. Lotsch *et. al.* reported in 2017 the concept of *dark photocatalysis*, wherein K-PHI is first charged *via* illumination and in presence of the SED 4-methylbenzyl alcohol (4-MBA).[51] A subsequent addition of Pt cocatalyst in the dark triggers the release of stored electrons, which then produce H_2 (Figure 1.7 (b)). A significant hydrogen yield can be achieved even when delaying Pt addition in the dark by $6\,h$.[35]

Besides water splitting, numerous further photocatalytic reactions have been investigated with carbon nitride photocatalysts. Photocatalytic CO_2 reduction into hydrocarbon fuels was demonstrated with PHI at a rate of $12.07\,\mu mol\,h^{-1}\,g^{-1}$.[96] Nitrogen monoxide reduction was demonstrated with a heterojunction of $BiOBr/C_3N_4$, albeit with the carbon nitride acting solely as photoabsorber.[97] Photodegradation of organic compounds is another substantial field, in which carbon nitrides found various applications. To name two examples: L. Huang *et. al.* reported $WO_3/g{-}C_3N_4$ for 4-chlorophenol and methylene blue degradation,[98] and S. Hong *et. al.* reported $CuO/g{-}C_3N_4$ for Rhodamine B degradation.[99]

Microswimmers and Drug Delivery. A novel and exciting application field for charge storing carbon nitrides are autonomous microswimmers, that is, a wireless particle which can produce a directed ballistic propulsion for a set amount of time by drawing energy from its surrounding environment. Two mechanisms are responsible for this effect: Self-diffusiophoresis results from convection caused by diffusion of a catalytically converted species. Self-electrophoresis is caused by charge carrier transfer between parts of the swimmer particle that produces an electric field which interacts with charged species generated *via* surface redox reactions.[100]

Applications for this system range from targeted drug delivery to micromachines in environmental remediation. A key requirement for such a particle is its directed propulsion, which in case of carbon nitrides was realized with their photocatalytic water splitting ability that we have discussed in the previous section. V. Sridhar *et. al.* have reported in 2020 a *Janus particle* that consists of a K-PHI microparticle.[85] One half of the particle was covered with a water splitting and oxygen reducing cocatalyst (performing the Oxygen Evolution Reaction (ORR)) such as Au or Pt (Figure 1.7 (d)). Upon illumination, K-PHI absorbs light and the photogenerated hole is quenched *via* the SED methanol or hydrogen peroxide. An asymmetric oxygen reduction rate occurs as a result of the better oxygen reduction performance of Pt. Thus, reduced oxygen species are mainly produced on only one side of the particle, which in return generates the propulsion. The authors also demonstrate swimming in the dark *via* stored electrons on K-PHI – a concept analogous to the idea of *Dark Photocatalysis* discussed in the previous section. This is possible, since under illumination and in presence of a SED parts of the photogenerated electrons charge K-PHI and can produce propulsion subsequently in the dark *via* ORR. The authors have termed this concept *solar battery swimming*.

In a follow-up work, the authors also reported on the ability of K-PHI and Melon to store the model cancer drug doxorubicin (DOX) with a high loading efficiency of $185\,\%$, produce propulsion, and subsequently release the drug on demand.[86] A different swimming mechanism was proposed: In the absence of a metal cap, directional swimming is induced by a shadowing effect and positive phototaxis of the particle is observed. Drug loading can occur within the volume in PHI and is likely assisted by the surface CNx groups, which enable hydrogen bonds with the drug and produce strong physisorption. After storing the drug, no passive release was observed for 30 days. Drug release can be subsequently triggered *via* illumination. The concept is visualized in Figure 1.7 (e).

FURTHER APPLICATIONS. The list of carbon nitride applications is vast.[101] We will introduce carbon nitride based sensors and further neuromorphic devices in Section 8.1 and charge storage devices such as batteries and solar batteries in Chapter 5, Section 7.1 and Section 6.1. We discuss solar cells with carbon nitrides in Section 1.3.1.

1.3. Energy Conversion *via* Solar Cells

As detailed in Section 1.1.1, sunlight is likely the most promising renewable energy source. In the following, we will introduce photovoltaic (Photo Voltaic (PV)) solar cell technology as a viable solution to access this energy source – both the historic context and current state of the art. Please refer to Chapter 2 for a fundamental discussion on the working principle of the photovoltaic effect as well as how to characterize solar cells and measure their respective performance.

A BRIEF HISTORY OF PHOTOVOLTAIC TECHNOLOGY. Around 175 years ago in 1839, Alexandre Edmond Becquerel discovered the photogalvanic effect when observing a small current developing between a silver and a platinum electrode immersed in an aqueous electrolyte solution und illumination.[102] These findings were advanced to selenium in 1873, when Willoughby Smith observed a modified light intensity dependent photoconductivity.[103] The first solar cell based on selenium was developed only four years later in 1877 by William Grylls Adams and his coworkers, which showed a Power Conversion Efficiency (PCE) of $0.5\,\%$.[104] Their work presents the first report on the photovoltaic effect in a solid-state material. A few years later in 1883, Charles Fritts developed a very early infant multilayer device, consisting if a thin layer of selenium deployed between two layers of gold.[105] He managed to double the PCE to $1\,\%$ and his device is often referred to as the first ever solar cell.

The fundamental theory of photophysics was significantly advanced by Albert Einstein, for which he was awarded the Nobel Prize in 1921. Einstein laid the foundations of photoelectric theory by describing the particle-wave duality for the very first time (see beginning of Section 2.1). The first of his four famous papers from 1905 details the description of the light quanta ($E = h \cdot \nu$).[107] This work is fundamental to explain light absorption in semiconductors that we have detailed in the previous Section.

In the following years, research effort significantly increased, leading to significantly enhanced efficiencies due to the discovery of n-doped and p-doped Si and

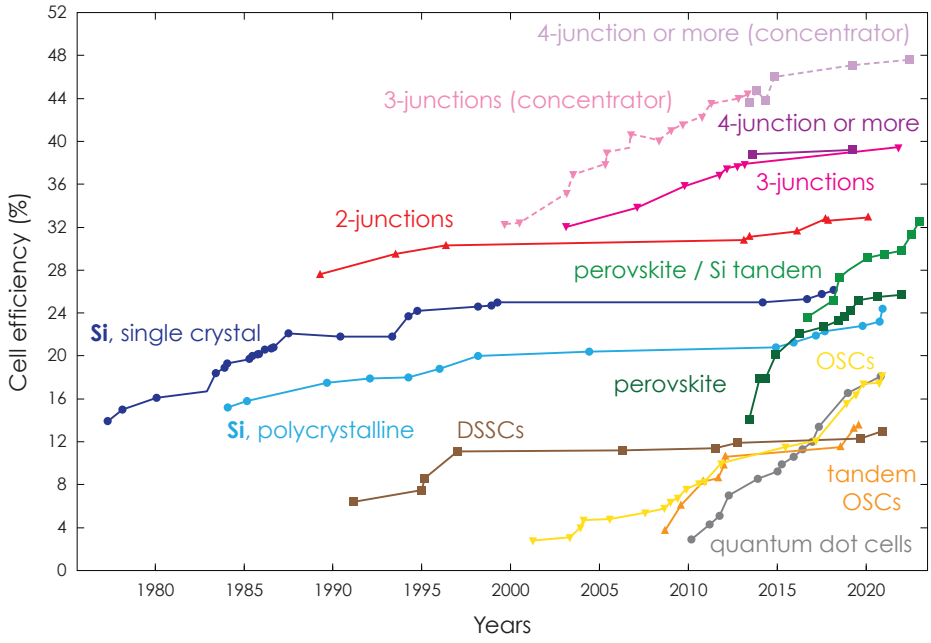

Figure 1.8. Progress in solar cell technology. Selection of reported solar cell devices according to their PCE. The devices are organized in 5 different categories: crystalline Si cells, Single-junction gallium arsenide cells, multijunction cells, thin films, and emerging photovoltaic technologies. This plot was adapted and is courtesy of the National Renewable Energy Laboratory, Golden, CO.[106]

their first implementation *via* a p-n junction (Section 2.1) geometry for the first time in 1939 and 1940 by Russell Ohl and Bell Labs.[108,109] This breakthrough paved the way for today's wide-spread application of high efficiency Si solar cells. However, back then the main foreseen applications were sensors, *e.g.*, a photography light sensor developed by Werner Siemens, who was the first to commercialize a devices based on a Si p-n junction.[105] The likely first commercially viable solar cell was developed by Daryl Chapin of Bell Labs in 1951, consisting of a Si p-n junction which was doped with boron and arsenic and achieved a PCE of already $6\,\%$.[110] Then in 1955, the first application of a solar cell came, when it powered a telecommunication network station in Georgia, USA.

The extraordinary development of solar cell technology in the last 50 years is best visualized by the best research-cell efficiency chart that the National Renewable Energy Laboratory (NREL) publishes and which is presented in Figure 1.8. The current top performing solar cell developed by the *Fraunhofer Institute for Solar Energy Systems* achieves an astonishing $47.6\,\%$ for a multijunction solar cell under 665 Sun

illumination.[111]

The current solar cell marked is dominated by thick ($\sim 100\,\mu$m) multicrystalline silicon (Si) with high efficiencies ($>20\,\%$), low cost ($<0.5\,\$/$W) and a sufficiently good reliability (<25 years).[112] Emerging solar cell technologies on the other hand promise a much higher level of sustainability by utilizing earth abundant materials and/or easier processability, thus transforming PV technology into the so-called *post silicon age*.[113] We will focus our brief introduction of solar cell technologies on the field of emerging solar cells, with a main focus on Dye Sensitized Solar Cells (DSSCs) and Organic Solar Cells (OSCs) (Figure 1.8). We will focus on them in the following, since the concepts behind emerging solar cell technologies will provide us with a suitable toolkit to understand photoactive device concepts, which we will discuss in Part III. In that context, we will use the following discussion as a guideline to highlight key relevant aspects for solar batteries and photomemristive sensors, *vide infra*.

1.3.1. Emerging Solar Cell Technologies: DSSCs

An Introduction into DSSCs. One of the most promising novel PV solar cell devices is the DSSC (Figure 1.9).[114] The fundamental working principle of a DSSC lies in the very efficient and tunable light absorption capability of dye molecules. The dye sensitizes a thin layer of a wide bandgap semiconductor such as TiO_2, ZnO, or SnO_2.[115] We show the working principle of a DSSC in Figure 1.9 (a). The dye S absorbs light, and the photogenerated exciton separates by injecting the electron into the anode coated with a respective semiconductor ($S + h\nu \longrightarrow S^{\bullet} \longrightarrow S^{+} + e^{-}(TiO_2)$).[116] Photooxidation of the dye and charge injection into the semiconductor occurs very fast – on the time scale of ~ 100 ps.[117] This fast electron extraction is key for efficient operation of the DSSC, since exciton recombination occurs on the range of $\sim$ ns.

> We can deduce that an efficient photogenerated charge carrier extraction is key to produce free charge carriers that can produce a photocurrent. At the same time, carrier extraction must occur faster than recombination of the exciton.

To prevent recombination of photogenerated electron and hole on the dye, a redox shuttle such as the triiodide/iodide (I_3^-/I^-) redox couple is required.[119] This process

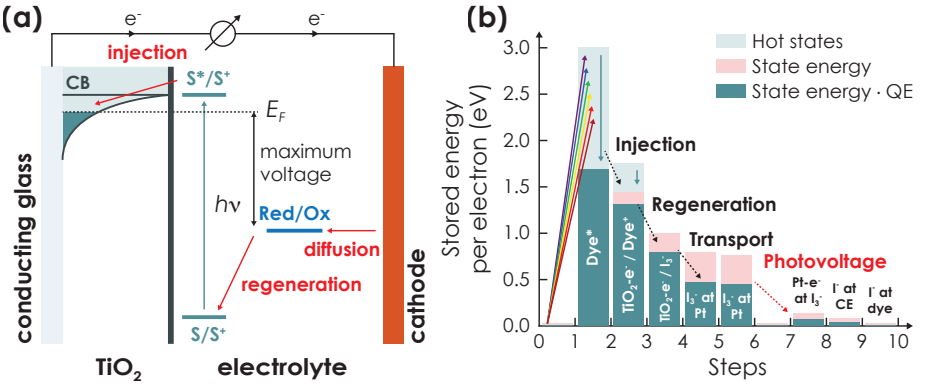

Figure 1.9. Operation and energy loss mechanism in DSSCs. (a) Scheme of the operation principle of a DSSC. A dye S absorbs light and injects the electron into a semiconductor such as TiO_2. The dye is subsequently regenerated by a redox shuttle, which in return transfers the photoexcited hole to a cathode. The operation voltage results from the CB of TiO_2 and redox potential of the redox shuttle. Adapted with permission.[117] Copyright 2011, American Chemical Society. **(b)** Different steps of energy loss in DSSC devices. Light absorption at wavelengths larger than the bandgap produces hot carrier injection, which thermalize into the CB of the dye. All subsequent charge transfer steps require a small potential difference to produce sufficient driving force, however in return cause a reduction in the overall cell voltage. Adapted with permission.[118] Copyright 2009, American Chemical Society.

is termed regeneration of the dye and typically occurs on the timescale of ~1 µs (*e.g.*, for I_3^-/I^- dye regeneration: $2\,S^+ + 3\,I^- \longrightarrow 2\,S + I_3^-$ and redox couple reaction at the counter electrode: $I_3^- + 2\,e^- \longrightarrow 3\,I^-$).[116] In comparison, recombination on the dye requires µs to ms.[117] The redox shuttle can subsequently transfer the photoexcited hole to the counter electrode (ms to s). This latter process is mainly governed by diffusion kinetics.

DYES FOR DSSCS. For efficient operation of DSSCs, dyes require suitable bandgaps to absorb visible light, high dye stability in ground, oxidized, and reduced state, suitable band positions to efficiently inject photoelectrons into the semiconducting layer and regenerate *via* electrons from a redox shuttle, and a high quantum efficiency.[115] The list of highly efficient dye candidates is vast. In fact, manifold natural plant-based dyes have proven their applicability, such as coffee (open circuit voltage $V_{oc} = 0.6\,V$; PCE $\eta = 0.33\,\%$), raspberries ($V_{oc} = 0.4\,V$; $\eta = 1.5\,\%$), or spinach ($V_{oc} = 0.6\,V$; $\eta = 0.1\,\%$).[120–122] Till date, the most efficient dye sensitizers are ruthenium based dyes ($\eta = 11.4\,\%$),[123] porphyrin dyes (D-π-A porphyrins with $\eta = 13\,\%$ and Zn(II) porphyrins with $\eta = 12.1\,\%$),[124,125] or manifold organic dyes

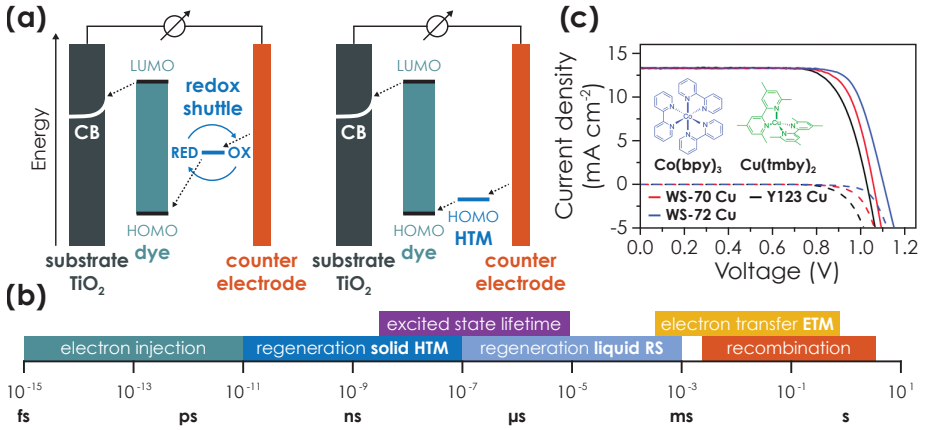

Figure 1.10. Hole Transport Materials (HTMs) as redox shuttle for solid-state DSSCs. (a) Scheme describing the difference between DSSCs based on liquid redox shuttles (left) and solid-state HTMs (right). The cell voltage is thereby governed by the redox potential of the redox shuttle, or by the VB (*i.e.*, Highest Occupied Molecular Orbital (HOMO)) of the HTM. Adapted under the terms of the open source CC BY-NC 3.0 license.[128] Copyright 2018, Royal Society of Chemistry. **(b)** Different time scales of processes occurring in solid-state and liquid DSSCs. While both undergo electron injection, electron transfer, recombination, and excited state lifetime, the time scale of dye regeneration differs in both devices quite significantly. Adapted under the terms of the open source CC BY-NC 3.0 license.[128] Copyright 2018, Royal Society of Chemistry. **(c)** The Current Voltage (measurement) (IV) characteristic of the solid-state DSSC with the highest PCE of 11.7 % to-date. Three different dyes were utilized, with all producing a similar short circuit photocurrent J_{sc} of ca. 14 mA cm^{-2} and open circuit voltages of 0.87 to 0.93 V. The solid-state HTMs are shown in the inset. Reproduced with permission.[129] Copyright 2018, Royal Society of Chemistry.

the most efficient of which are based on thiophenes (up to $\eta = 14.6\,\%$).[126,127]

Redox Shuttles for DSSCs. The redox shuttle was identified as a further key component that impacts both performance and longevity of the device.[119,130] Importantly, the redox shuttle sets the cell voltage of the DSSC, as the redox potential governs the potential at which re-reduction occurs at the counter electrode. Note that the overall DSSC cell voltage results from the redox potential and CB potential of the anode semiconductor (*e.g.*, TiO_2). Liquid redox shuttles have initiated DSSC research and still yield the highest performance. The list of liquid redox shuttles is huge. To list a few examples, commonly employed redox shuttles are I_3^-/I^-,[114] Br_3^-/Br^-,[131] various transition-metal complexes such as Fe_3^+/Fe_2^+,[132] Cu_2^+/Cu^+,[133] or organic redox shuttles such as TEMPO$^+$/TEMPO (2,2,6,6 - tetramethyl - 1 - piperidinyloxyl radical),[134] T_2/T^- (5-mercapto-1-methyltetrazole ion and

the dimer of that species).[135]

Solid-state redox shuttles have also been investigated in detail in the context of solid-state DSSCs.[128] In such a device, the task of the redox shuttle is performed by a solid-state HTM (Figure 1.10 (a)). Notably the main advantage of solid-state HTMs is the ultra-fast dye regeneration (Figure 1.10 (b)), which occurs on the same timescale as electron injection from dye into the semiconductor (that is, in the order of ms to ps). The range of kinetics is remarkably large, with ultra-fast hole injections being reported by Cappel *et. al.* for spiro-OMeTAD (around 1 ps – astonishingly likely faster than electron injection into TiO_2)[136] and ultra-slow hole injections being reported for PEDOT in the range of ms.[137]

However, despite a significant research effort solid HTM DSSC devices still lack behind their liquid counter parts, with the highest PCE of 11.7 % being reported by M. Grätzel *et. al.* for a device, which utilizes $Co(bpy)_3$ and $Cu(tmby)_2$ as HTMs (Figure 1.10 (c)).[129] The main reasons for this slightly worse efficiency are understood to originate from several sources: Relatively thin HTM layers are required, which in return limits the thickness of the porous semiconductor layer which is sensitized with dyes (ca. 2 µm). This thin layer in return cannot fully absorb incident light.[138,139] Further limitations arise from a smaller cell voltage due to a higher driving force for dye regeneration. Synthetic modifications can partially overcome this issue.[140,141] The Fill Factor (FF), which acts as an ideality criterium for solar cells and which is typically reduced by series resistance and shunt resistance,[142] suffers from recombination processes between the HTM and metal counter electrode, which produces dark currents as well as series resistances. Morphology engineering of the junction can improve this issue by reducing junction resistances.[143]

> A solid HTM effectively quenches photoexcited holes from an organic dye upon photoexcitation and transfers the holes to a counter electrode – analogous to a redox shuttle.

Carbon Nitrides in DSSCs. Several different carbon nitride modifications have been investigated as dye candidates for DSSCs.[144] The largest PCE of 8.07 % was reported for g-C_3N_4 by L. Yin *et. al.*[145] In this system, g-C_3N_4 was functionalized on top of TiO_2 and an I_3^-/I^- redox shuttle was utilized to transfer photoexcited holes to a counter electrode consisting of either Pt or Co_9S_8 nanotube arrays.

2D polymeric carbon nitrides were reported as dyes for DSSCs, with photoexcited electrons being injected into TiO_2 and photoexcited holes being extracted *via* the I_3^-/I^- redox couple.

Carbon nitrides (C_3N_4) have also been used to post-treat TiO_2 substrates by producing a type II heterojunction. G.-D. Li *et. al.* reported reduced recombination and improve photocurrent from a dye (N719 ruthenium dye) sensitized C_3N_4@TiO_2 by both providing additional light absorption and injecting photogenerated electrons from C_3N_4 into TiO_2 and simultaneously quenching photoexcited holes from TiO_2 UV light absorption.[146] A new film preparation technique was incorporated by the authors, who fabricated the carbon nitride C_3N_4 by dipping TiO_2 into a solution of urea and subsequently calcinating the sample at $500\,°C$ for $1\,h$. The authors achieved a PCE of $7.3\,\%$ and upon addition of C_3N_4 improved the PCE by $25\,\%$. Noteworthy, the reported carbon nitride is not particularly comparable to g-C_3N_4 that we discuss in Section 1.2 due to the different sample preparation routine and since it is not a 2D polymer.

Carbon nitrides were also employed at the counter electrode of DSSCs. Here, carbon nitrides are utilized to improve the efficiency of electrocatalytic I_3^-/I^- reduction. Blends with several additives have been reported, which improved counter electrode conductivity and by this reduced re-reduction of the redox shuttle at the dye or semiconductor (a process which occurs on similar time scales (ms to s) as dye diffusion and re-reduction at the counter electrode). For a g-C_3N_4 blend with graphene oxide, G. Wang *et. al.* reported an improved counter electrode resistance of $1.8\,\Omega\,cm^2$ compared to $70.1\,\Omega\,cm^2$ for g-C_3N_4, which improved the PCE from 7.13 to $7.37\,\%$.[147] M. M. Momeni *et. al.* reported on a g-C_3N_4/polyaniline nanocomposite as counter electrode, which improved electrocatalytic I_3^-/I^- re-reduction at the counter electrode. Using the N719 dye, the DSSC produced a comparably good PCE of $1.786\,\%$.[148]

Efficiency Limitations of DSSC Devices. We will conclude our discussion of DSSCs by looking more broadly onto how efficiency is limited *via* the photovoltage. Let us keep in mind that the theoretical PCE limit is given by the Shockley Queisser limit, which resides at around $30\,\%$ for a single absorbing material with an optimum bandgap of 1.1 eV.[149]

We will discuss major energy loss channels by looking at individual energy loss

processes illustrated in a state energy diagram in Figure 1.9 (b). In the Figure, we show energetics of a typical DSSC device with a PCE of $\sim 9.5\,\%$. Light absorption causes electron excitation into a hot state, since light is absorbed with slightly larger energies than the bandgap of the dye. The electron subsequently thermalizes into the CB (or Lowest Unoccupied Molecular Orbital (LUMO)) of the dye. Every subsequent step requires a certain amount of driving force which reduces the overall cell voltage, that is, injection of the electron into the semiconductor TiO_2, regeneration of the dye with the redox shuttle, transport of the redox shuttle to the counter electrode and subsequent re-reduction. For the exemplary device shown in Figure 1.10 (c), operation at the Maximum Power Point (MPP) (see Section 2.2.2 for an explanation of the MPP) should occur at a device voltage of $0.65\,\mathrm{V}$. With an internal quantum efficiency (Internal Quantum Efficiency (IQE); see Section 2.2.2 for an explanation of the IQE) of $70\,\%$, the resulting device extracts $0.46\,\mathrm{eV}$ per absorbed photon.

The overall cell voltage of a solar cell results mainly from the bandgap, but also from the efficiency of each individual charge transfer process required to complete the electric circuit.

1.3.2. Emerging Solar Cell Technologies: OSCs

In this section, we will give a short overview of relevant OSC technologies, which are connected to the work of this thesis. In OSC devices, light absorption in the active layer is performed by organic semiconductor polymers, small molecules, or a mixture of different materials.[150] In most cases, the active layer consists of a blend of two light absorbing organic materials in a heterojunction. The first material with energetically slightly lower CB and VB (or LUMO and HOMO) positions (when referenced against the vacuum energy level) injects photogenerated electrons into the second material, thus terming the first material as donor and the second material as acceptor (Figure 1.11 (a)). The photovoltage of both devices is thus governed by the VB of the donor and CB of the acceptor, provided that no significant voltage is lost when extracting photogenerated charge carriers from the active material.[151] Donor and acceptor materials can either occur in a Planar Heterojunction (PHJ) (*i.e.*, donor and acceptor material layers deposited on top of each other, Figure 1.11 (b) left) or in a Bulk Heterojunction (BHJ) (*i.e.*, a blend of donor and acceptor materials,

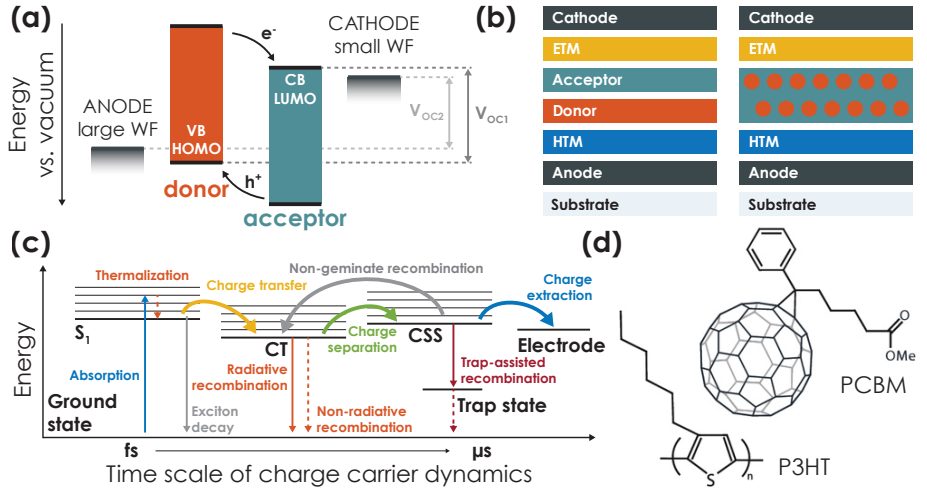

Figure 1.11. Concepts of OSC devices. (a) Generalized band diagram of the operation principle of an OSC device relying on a donor acceptor heterojunction for light absorption. Both donor and acceptor absorb light. The donor transfers photoexcited electrons to the acceptor, which in return injects photoexcited holes into the donor. The theoretical photovoltage (V_{oc1}) is governed by VB (or HOMO) of the donor and CB (or LUMO) of the acceptor. To extract the photoexcited carriers, current collectors with a high Work Function (WF) extract holes from the donor, and current collectors with a low WF extract electrons from the acceptor. Junction resistances can cause the photovoltage to reduce (V_{oc2}). **(b)** Schematic diagrams of PHJ OSCs (left) and BHJ OSCs (right). Both require a cathode with ETM and anode with HTM. However, in the PHJ and BHJ donor and acceptor occur in a layered structure and a blend, respectively. Adapted with permission.[150] Copyright 2022, Wiley-VCH. **(c)** Simplified Jablonski diagram of different states during photocurrent generation in OSCs. The different processes occur in timescales of fs to µs. Reproduced with permission.[152] Copyright 2022, Wiley-VCH. **(d)** The donor P3HT and acceptor PCBM form a very common BHJ active layer for OSC devices and are shown as an example. Reproduced with permission.[153] Copyright 2020, Wiley-VCH.

Figure 1.11 (b) right). To efficiently extract charge carriers from the active material preferably *via* only conductive ohmic junctions, several different layers are required (Figure 1.11 (b)): An electron transport layer (Electron Transport Material (ETM)) transfers electrons from the acceptor to the cathode current collector. A HTM transfers holes from the donor to the anode current collector. Both current collectors are deposited onto respective substrates.

The photocurrent generation process can be described *via* several distinct steps that are governed by distinct kinetics – analogous to our discussion on DSSC photocurrent generation (Figure 1.11 (c)):[154,155] The donor and acceptor absorb incident light and an exciton is formed. This occurs analogous to our discussion on excitons for carbon nitride materials in Section 1.2.2. Formation of excitons is an ultra-

fast process that occurs on the timescale of fs. Two states are associated with exciton separation and free charge carrier generation: The Charge Transfer State (CT) is energetically slightly lower and occurs from interaction between acceptor electrons and donor holes at the donor/acceptor junction – so called interfacial electron-hole pairs.[154] Upon injection of electrons and holes into acceptor and donor molecules, respectively, the system reaches the Charge Separated State (CSS). Both CT and CSS states occur in timescales of ps to ns. The subsequent extraction of free charge carriers requires µs.

Active Layer Materials. In the following paragraph, we will briefly dive into different key acceptor and donor materials that were investigated by researchers. For acceptor materials, prior to 2015 the predominant focus lied on fullerene derivatives. Fullerenes such as PC61BM (Figure 1.11 (d)) or PC71BM are strong electron acceptors that can accept up to a total of 6 electrons.[156] The first fullerene based OSC was published in 1995 by A. J. Heeger *et. al.* and consisted of a composite of PC61BM mixed with polymeric MEH-PPV (poly(2-methoxy-5-2'-ethylhexyloxy) - 1,4-phenylene vinylene).[157] The device achieved a PCE of $2.9\,\%$, two orders of magnitude larger than devices reported up to that time which relied only on MEH-PPV as photoactive material (*i.e.*, without an acceptor). The introduction of soluble fullerenes boosted their application in OSCs in the following years. Optimizing donor-fullerene morphology to thick, highly crystalline yet reasonably small domains of polymers produced a to-date for fullerene acceptors record high PCE of $10.4\,\%$ (V_{oc} of $0.77\,\mathrm{V}$ and J_{sc} of $18.2\,\mathrm{mA\,cm^{-2}}$).[158] However, despite the huge popularity as acceptors in OSCs, fullerenes possess several intrinsic limitations: limited tunability in terms of chemical and energetic structure, not a very strong absorption in both visible and near-infrared light, instability in morphology, as well as high synthetic costs.[159] These drawbacks have motivated OSC research in recent years to move to different non-fullerene acceptors (termed Non Fullerene Acceptors (NFAs)). OSCs based on small molecule acceptors achieved PCEs of above $18.6\,\%$.[160,161] Polymeric non-fullerene acceptors (*e.g.*, indanone-derived organic polymers such as PY-IT, PY-OT, or PY2F-T) are performing slightly lower, with top PCE devices performing in the range of $15\,\%$.[162,163]

The range of implemented donor materials on the other hand has always been far wider and can be divided into wide bandgap ($>1.8\,\mathrm{eV}$), medium bandgap (1.6 to $1.8\,\mathrm{eV}$), and low bandgap ($<1.6\,\mathrm{eV}$) donors.[164] OSC research started with wide bandgap phenylene vinylene derivative donors in 1995, as mentioned in the para-

graph above.[157] One of the most widely investigated polymeric donors is P3HT, which exhibits PCEs of up to 6.5 % (Figure 1.11 (d)).[165] Different low bandgap polymeric donors were reported based on thiophenes (PTB7-Th, achieving a PCE of 10.1 %)[166] or polymeric hydrocarbon derivatives (PffBT$_4$T-C$_9$C$_{13}$, reaching a PCE of 11.7 %).[167]

As a consequence of the weak absorption ability of fullerenes, low bandgap donors are favorable due to their good light absorption ability. Wider bandgap donors are rather utilized in conjunction with non-fullerene acceptors.[168] Champion efficiency OSC devices utilizing non-fullerene acceptors have been reported for conjugated polymer donors, *e.g.*, the fused-ring aromatic lactone derivative D18 reaching a PCE of 18.56 %, or polymers consisting of the backbone benzodithiophene, benzodithiophene dione, and thiophene carboxylate esters (PBDB-TF) reaching a PCE of 17.8 %.[169,170]

BHJ *vs.* PHJ. As mentioned above, active layers can be fabricated as BHJs or PHJs, when either mixing donor and acceptor molecules in a blend or fabricating two distinct layers, respectively. BHJs have emerged as a solution to prevent exciton recombination, which occurs when excitons are generated in parts of the donor or acceptor layer too far away from the junction. While exciton diffusion can occur in organic materials, the diffusion length is typically very short (in the range of 5 to 30 nm).[171,172] The much larger junction area in the BHJ blend compared to PHJ requires less exciton diffusion (order of tens of nanometers), thus reducing exciton recombination and increasing the photocurrent.[172] Larger PCEs are the result.

On the other hand, PHJ avoid complicated morphology control and morphology disorder as a result of the physical blending of both materials. In fact, the formation of a BHJ is a very complex process, which is strongly influenced by history of the blend solution, different vertical component distribution, and the crystallization of the donor and acceptor disturbing each other.[173] This can lead to traps and quenching centers for excitons.[174] For instance, Y. Lin *et. al.* underlined that an OSC with different fused-ring electron acceptors show a lower trap density (magnitude of 10×10^{15} cm^{-3}) in a PHJ configuration than in a BHJ configuration (magnitude of 10×10^{16} cm^{-3}).[175] This lead to improved stability of the device using a PHJ active layer. Charge extraction and transport are also highly dependent on the vertical component distribution.[173]

In the ideal active layer structure, one would produce a gradient structure which is donor enriched at the anode side, acceptor enriched at the cathode, and a bulk

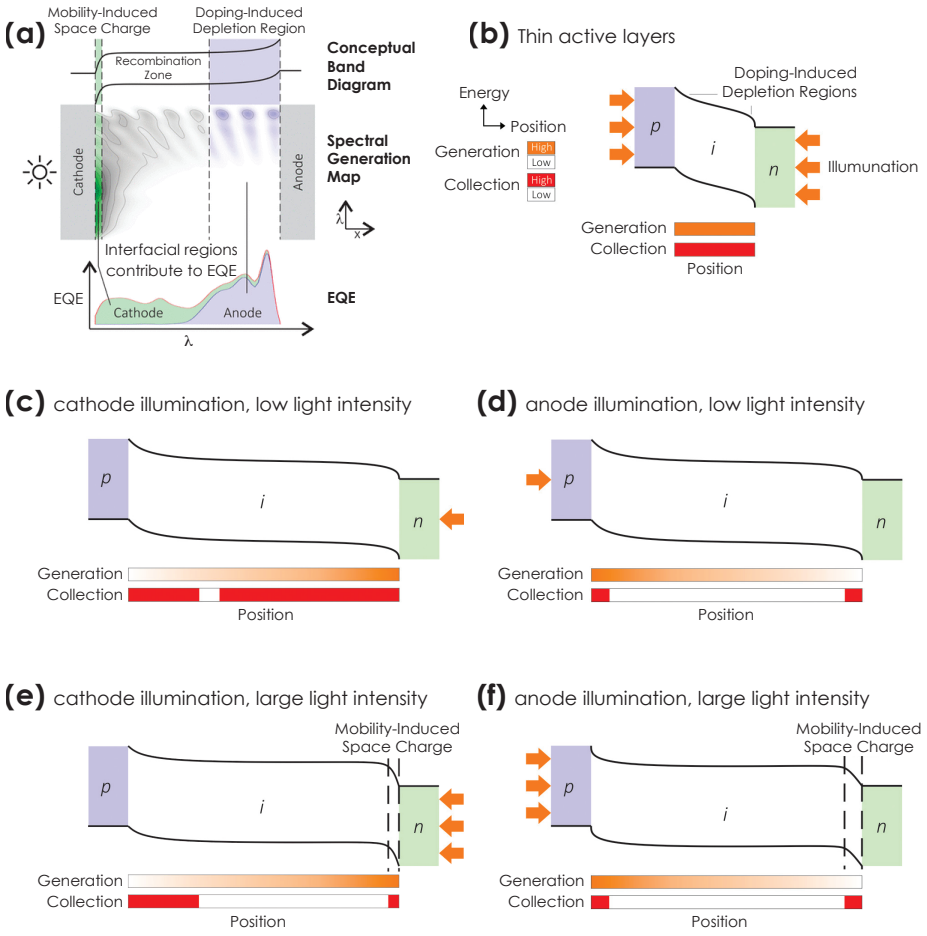

Figure 1.12. The effect of electric field distribution in BHJ OSC devices governed by Space Charge Limited Current (SCLC). The exemplary device has a smaller electron than hole diffusion mobility. **(a)** Scheme of different space charge regions affecting the band bending of a thick active layer and the resulting EQE. **(b)** Thin active layers under large light intensity show continuous charge generation and charge collection throughout the active layer. **(c-d)** In thick active layers, small light intensities are not sufficient to produce a large mobility-induced space charge region. Illuminating from the cathode direction (n) causes nearly continuous charge collection due to the fast hole diffusion. Illuminating from the anode direction (p) reduces charge collection in the bulk due to recombination of slow diffusing electrons. **(e-f)** Illuminating with large light intensities produce a significant mobility-induced space charge region. This in return significantly reduces the electric field gradient in the bulk, which reduces collection efficiency for both electrons and holes, however, more gravely electrons due to their lower mobility. Adapted with permission.[176] Copyright 2016, American Chemical Society.

heterojunction in the middle. Such a PHJ/BHJ mixture was recently reported by J. Hou *et. al.*[174] The authors used PBDB-TF as donor and BTP-eC9 as acceptor and

reached a huge PCE of 18.5 %. The PHJ/BHJ showed enhanced charge transport, improved charge extraction, and suppressed charge recombination.

While donor/acceptor BHJs decrease required exciton diffusion distances, PHJs offer a far simpler morphology, which reduces trap density and defects acting as exciton quenching centers. An ideal structure would consist of a PHJ at the anode and cathode current collectors and BHJ in the center of the film, *i.e.*, a PHJ/BHJ structure.

Space Charge Limited Photocurrent in Thick Active Layers. In the following subsection, we will touch the subject of active layer thickness and its impact on efficiency of the OSC – a further very relevant property when designing multifunctional photoactive devices. To-date, charge carrier dynamics and charge extraction in thin to moderately thick BHJ active layers can be described with the concept of SCLC. As the name SCLC implies, photocurrent extraction in OSCs is governed by electrostatic limitations, which are affected by the electric field within the active layer and the shape of the space charge region (please refer to Section 2.1 for an explanation on the concept of space charge).[177]

The reason for this is that organic materials typically have short carrier lifetimes and low carrier diffusion constants. Carrier extraction occurs due to drift along the electric field in the active layer that is formed by the donor and acceptor. If carrier mobilities of electrons and holes are different, high-mobility carriers will drift faster causing the lower-mobility carriers to accumulate. This accumulation causes depletion zones, which in return results in band bending. Note that this band bending is irrespective of doping or junction induced band bending discussed in Section 2.1.[176] Thus, the shape of the band structure within the BHJ depends on band bending and the gradient of band bending governs whether a carrier diffuses quickly to the extraction site (large gradients) or diffuses slowly which can result in recombination (slow gradients). In thicker active layers, this results in a recombination zone in the middle of the layer, where the light absorption efficiency is reduced, and extraction zones at the junctions. We visualize this concept in Figure 1.12 (a): External quantum efficiency (EQE, defines photocurrent collected per incident photon flux, as a function of illumination wavelength)[78] is lower in the middle of the active layer and larger at the junctions to anode and cathode.

Formation of a charge carrier does not automatically mean that it gets collected. Especially in thick BHJ active layers, a generated charge carrier is only collected, if the mobility and electric field gradient is large enough. This can significantly vary in different parts of the bulk of the film.

To understand the impact of this effect on light absorption and performance of the active layer, we must differentiate between spatial distribution of the charge carrier generation efficiency and collection efficiency (Figure 1.12 (b-e)). The former describes how many charge carriers are generated upon illumination, the latter describes how many of those charge carriers are collected and produce a photocurrent. We discuss this for a system, where the active layer has a larger mobility for holes than for electrons. In case of sufficient illumination intensity and thin active layers (Figure 1.12 (b)), the thin layer thickness produces a high enough electric field gradient to ensure fast carrier extraction. Illumination from both directions coupled to the thin active layer thickness inhibits formation of a mobility-induced space charge region.

However, the story changes completely when utilizing thick active layers. Here, the electric field gradient is far smaller and the carrier diffusion distance much greater. When illuminating from the cathode side with low light intensity (Figure 1.12 (c)), carrier generation occurs mainly close to the cathode. Holes diffuse quickly to the anode, and electrons are being extracted at the cathode. Due to the large mobility of holes, recombination in the bulk is minimal. Since light intensity is low, overall charge carrier generation is not large enough to produce significant amount of electron accumulation and thus a mobility-induced space charge region (as discussed above). When illuminating from the anode direction however (Figure 1.12 (d)), the lower electron mobility-inhibits a fast electron diffusion to the cathode, which in return significantly increases recombination in the bulk. Charge collection only occurs in parts of the active layer close to anode (hole collection) and cathode (electron collection) junction.

In thick active layers, where photophysical properties are governed by SCLC, it is very important to control illumination direction and intensity. Due to band bending, electric field gradients can become small enough to significantly inhibit charge collection.

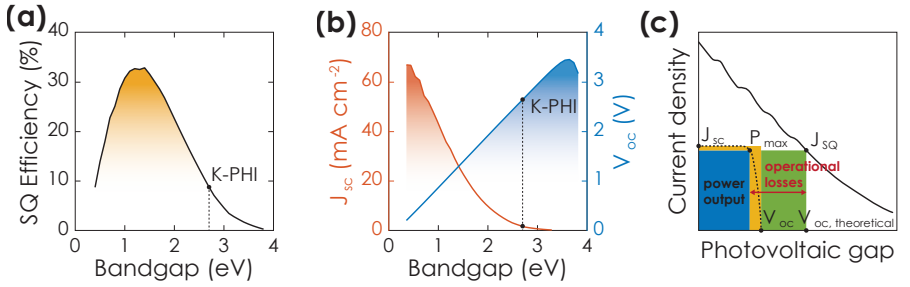

Figure 1.13. Solar cell performance and efficiency. (a) Maximum PCE as a function of the bandgap of the light absorber according to the Shockley-Queisser model. Data for the plot adapted from S. Rühle with permission.[178] Copyright 2016, Elsevier Ltd. **(b)** Short circuit current J_{sc} and open circuit voltage V_{oc} as a function of the bandgap of the light absorber. Data for the plot adapted from S. Rühle with permission.[178] Copyright 2016, Elsevier Ltd. Dashed lines in both (a) and (b) show the bandgap of the bifunctional solar battery carbon nitride material K-PHI (see Section 1.2.1). **(c)** The current density is plotted against the photovoltaic gap. The IV curve of a solar cell with a specific bandgap, J_{sc}, and V_{oc} is plotted with a dashed line. The blue area marks the effective power output, the yellow area marks efficiency losses due to operation at the maximum power point P_{max}, and the green area marks other efficiency losses due to the Shockley Queisser (SQ) efficiency and non-radiative recombination. Both yellow and green area produce operational losses, which are marked with the red arrow. Adapted with permission.[179] Copyright 2019, Springer Nature.

When increasing illumination intensity, the effect of mobility-induced space charge regions starts to affect the electric field gradient, since more charge carriers are generated and thus more charge carriers can also accumulate. When illuminating from the cathode direction (Figure 1.12 (e)), the lower mobility of electrons causes them to accumulate. This produces a mobility-induced space charge region, which increases band bending close to the cathode and by that decreases the electric field gradient in the bulk. This in return results in a reduced charge collection, since the larger mobility of holes is not sufficient anymore to ensure their extraction (compared to low illumination intensity from the cathode direction (Figure 1.12 (c)), where no mobility-induced band bending occurs). Illuminating from anode direction (Figure 1.12 (f)) worsens the charge collection further, as the slow electron diffusion through the active layer increases both mobility-induced space charge region hence, recombination in the bulk.

Further General Design Considerations. We conclude our introduction on solar cells by briefly discussing some further design guidelines relevant for Part III.

The maximum PCE of a single-junction solar cell was described by Shockley and Queisser in 1961 and is given as a function of the bandgap of the light absorber

for a solar cell operated at $T = 300\,\mathrm{K}$ in Figure 1.13.[178] The maximum theoretical photoconversion (or Shockley-Queisser (SQ)) efficiency of ca. $33\,\%$ is reached at a bandgap of ca. $1.3\,\mathrm{eV}$. The respective short circuit current J_{sc} and open circuit potential V_{oc} can be calculated and are shown in Figure 1.13.[178] Two trends become evident: While V_{oc} increases with larger bandgaps since the photovoltage depends directly on the bandgap, J_{sc} actually decreases. Two reasons explain this decrease: (1) The SQ efficiency of light absorption decreases for larger wavelengths (Figure 1.13 (a)). (2) The photon flux of the solar spectrum (AM1.5 G) decreases significantly at large photon energies (*i.e.*, low wavelengths). Several conclusions can be drawn for an active layer of the OSC:

> Large bandgaps increase the voltage of photogenerated charge carriers. Small bandgaps on the other hand generate a larger photocurrent, albeit at a smaller voltage.

In any case, the bandgap must be sufficiently large to supply photogenerated electrons to the anode and holes to the cathode. In case of the bifunctional 2D polymeric carbon nitride K-PHI that we introduce in Section 1.2.1, the bandgap of $2.7\,\mathrm{eV}$ produces a theoretical V_{oc} of $2.3\,\mathrm{V}$ and J_{sc} of $4\,\mathrm{mA\,cm^{-2}}$, which relates to a theoretical maximum SQ efficiency of $8.8\,\%$. However, while a large bandgap can be beneficial to produce a significant charging voltage, band alignment between light absorber, ETM, HTM, anode, and cathode is paramount for an efficient conversion of light energy.

It is also worth mentioning that in order to maximize effective photovoltage and photocurrent, operational losses of the solar cell need to be minimized. We show in Figure 1.13 (c) the theoretically achievable current density of a solar cell with a specific bandgap, $V_{oc,\,theoretical}$. The theoretical maximum current J_{sc} is not achieved due to losses, which can be summarized as follows: losses governed by the SQ efficiency and non-radiative recombination (Figure 1.13 (c), green), as well as both current and voltage losses due to operation at the maximum power point P_{max}, (Figure 1.13 (c), yellow), which occur due to non-ideal behavior of the solar cell, *e.g.*, due to series and shunt resistances.[179] We will give a more detailed explanation of how to characterize all these effects in Section 2.2.2.

To conclude our introduction into solar cells, we have discussed several key concepts and ideas that govern emerging solar cell technologies. The take-home messages that will become important throughout the experimental Part III of this thesis, are given in gray boxes.

1.4. Energy Storage *via* Batteries and Capacitors

In the last section of the introduction of this thesis, we will discuss several concepts of charge storage that will become relevant in Part III. We will not focus on traditional batteries or capacitors, but rather discuss fundamental concepts that will equip us to understand charge storage in carbon nitrides. Key messages will be outlined in gray boxes, as done in the previous section.

A brief History of Electrical and Electrochemical Energy Storage. Energy storage technologies govern our modern life, but also possess a quite fascinating history. We will very briefly mention key discoveries leading to the modern battery and capacitor. The earliest *prehistoric* battery in fact dates to the ancient Persians and was discovered in 1936 near Baghdad.[180] The so-called "Parthian Battery" consisted of an iron rod electrode and a copper steel cylinder as the second electrode. Both were immersed into a vinegar solution as the electrolyte. The battery produced a cell voltage of 1.1 to $2.0\,\mathrm{V}$ and was likely used for silver and gold plating. The first *modern* primary (*i.e.*, non-rechargeable) battery was developed around 1800 by Alessandro Volta and consisted of alternating discs of zinc and copper separated by pieces of cardboard, which were immersed in a brine solution as electrolyte.[181] The next milestones – rechargeable (*i.e.*, secondary) batteries – were achieved over the years by developing the lead-acid battery (1859), nickel-cadmium battery (1899), and nickel-metal hybrid batteries (*i.e.*, NiMH batteries; patented in 1986). Li-ion batteries were first reported in 1973 and patented 1977 by Michael S. Whittingham.[182] For this achievement, he received the 2019 Nobel Prize in Chemistry alongside John B. Goodenough and Akira Yoshino.[183] Breakthrough energy densities were achieved in 1980 by J. B. Goodenough and commercialization followed in the 1990s.

The phenomenon of rubbing amber with a cloth that then attracts small particles is reported manifold times in antiquity. This phenomenon inspired develop-

ment of the first *friction machine* capacitor in 1745 by Ewald Georg von Kleist. He termed it "Leyden jar" – a glass (dielectric) which was laminated on both sides with a thin metal foil (both electrodes), capable to be charged to $20\,000$ to $60\,000$ V.[184] Notable subsequent invented capacitors include paper capacitors in 1876 (rolled up sandwich of two metal foils separated with a wax-impregnated paper), "valve metal" capacitors (aluminum and tantalum that produce a passivation layer on the surface of the film (Al_2O_3 and Ta_2O_5) when immersed in an appropriate electrolyte. This layer acts as dielectric) patented in 1896, and a patent by *General Electric* filed in 1957, which described the concept of electric double-layer charge storage for the first time.[185,186] Since then, capacitor development proceeded rapidly, culminating in the first commercialized capacitor by *Nippon Electric* (1.0 F, 5.5 V).[187] The concept of pseudocapacitance was first introduced by S. Trasatti and G. Buzzanca in 1971 with ruthenium oxide (RuO_2) electrodes, opening up a new world of capacitor systems with enhanced performance.[188]

1.4.1. An Overview of Energy Storage Technologies

There are manifold different energy storage technologies, including chemical energy storage (*e.g.*, fuel cells, (photo)electrocatalytic water splitting, carbon dioxide reforming), thermal/thermochemical energy storage (*e.g.*, heat storage, solar thermal hydrogen, solar thermal energy) as well as different approaches for mechanical energy storage (*e.g.*, flywheels).[186,189] Let us focus on electrical and electrochemical energy storage technologies, that is, batteries and capacitors. These systems are the leading charge storage devices that are employed to-date but rely on different charge storage mechanisms that result in contrary performance parameters – notably contrary implying complementary rather than competing. The working principle of capacitors and batteries is illustrated in Figure 1.14 (a) and (b) and will be discussed in the following.

1.4.2. Electrical Energy Storage *via* Capacitors

Physical (or dielectric) capacitors are the simplest form of energy storage. They consist of two metal plates (electrodes), separated by an insulating material termed dielectric. Upon applying a current, both plates are polarized, *i.e.*, one plate is being charged negatively, and one plate is charged positively (see Figure 1.14 (a)). Charge is stored *via* electric potential energy between the electrodes. Note that thus, only the potential difference governs the cell voltage, rather than the poten-

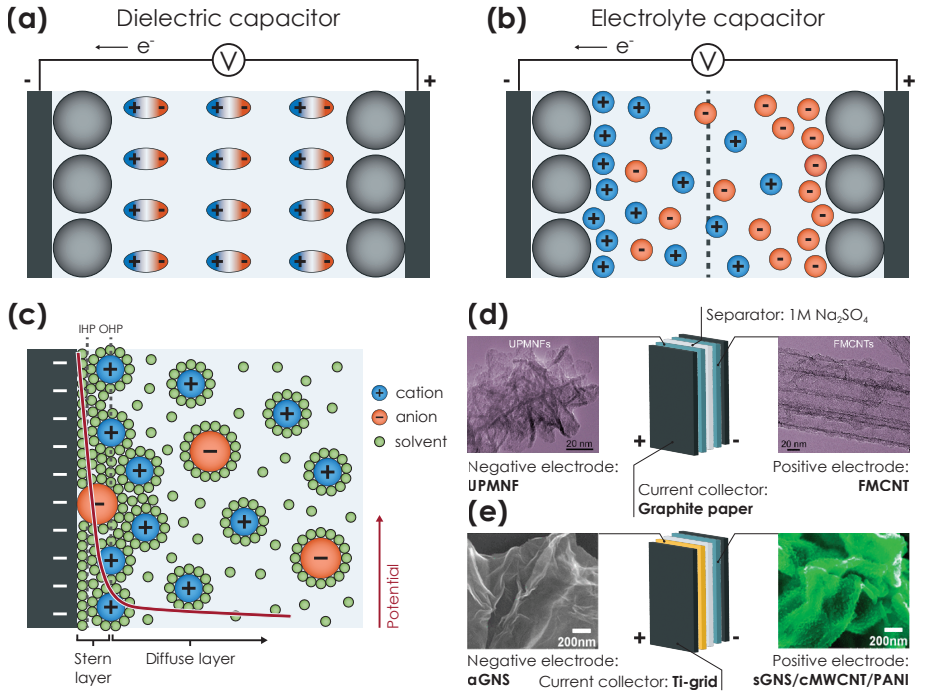

Figure 1.14. Capacitor energy storage. (a) A dielectric capacitor stores energy *via* polarization of two electrodes. **(b)** An electrolyte capacitor stores energy *via* formation of an Electric (Electrolyte) Double Layer (EDL) at the electrolyte junction with a high surface area electrode material. In both cases, electrons and holes are injected into the respective anode and cathode and their electric field is screened *via* the electrolyte. Both (a) and (b) are adapted with permission[190] and under the terms of open access CC BY-NC-ND license.[191] Copyright 2014, AAAS; Copyright 2013, Elsevier Ltd. **(c)** Formation of an EDL at a planar solid-liquid junction according to the Gouy-Chapman-Stern. The potential gradient is shown *via* the red line. Adapted with permission.[186] Copyright 2019, Royal Society of Chemistry. **(d)** Asymmetric supercapacitor, consisting of a MnO_2 and a carbon nanotube electrode. Adapted with permission.[192] Copyright 2012, Royal Society of Chemistry. **(e)** Asymmetric supercapacitor with a composite electrode consisting of polyaniline/graphene/carbon nanotube electrode and an activated graphene electrode. Adapted with permission.[193] Copyright 2013, American Chemical Society.

tial of the individual electrodes (referenced, *e.g.*, against vacuum energy). The dielectric prevents internal charge transfer between the electrodes and thus inhibits self-discharge.[186] However, the capacity of such a physical capacitor is limited by the rapidly developing potential between the electrodes and limited ability of the dipoles in the dielectric to screen charges at respective electrodes, which produces a huge electric field in the dielectric separator. If too large, the amount of charge carriers in the insulator dielectric can suddenly increase, causing an internal short

circuit. The required voltage is termed "breakdown voltage".

To increase capacitance, electrolyte capacitors were introduced, which exchange the dielectric with a liquid or solid ionic conducting (importantly not electronic conducting) electrolyte. Contrary to a dielectric capacitor where dipoles are stationary, ions in the electrolyte can move freely and upon charging cations accumulate at the interface between negatively charged electrode and electrolyte, and *vice versa* (see Figure 1.14 (b)).[191] A double layer (EDL) forms at both electrolyte solid-liquid interfaces (hence, these devices are often called electrolyte or electrochemical double layer capacitors (Electrolyte Double Layer Capacitors (EDLCs))). The capacitance scales with area of the EDL, hence a typical strategy to increase capacitance stems from maximizing the electrode area, *e.g.*, through nanostructuring (see next Section).

Formation of the EDL was described by different models. A recent mechanism was proposed by Gouy-Chapman-Stern, where ions are treated as point charges and ion concentration at the surface follows a Boltzmann distribution.[186] A multilayered structure develops, which consists of an inner and outer Helmholtz plane (termed Stern layer) and a diffuse layer (Figure 1.14 (c)). The electric field potential gradient grows slowly in the diffuse layer and significantly increases in the Stern Layer. Since inherently more mobile ions can accumulate in the EDL than stationary dipoles in a dielectric capacitor, the resulting capacitance is far larger.[186] Charge storage can also occur through Faradaic charge transfer *via* fast redox reactions (known as pseudocapacitance, see Section 1.4.3).[186,194–196] Since the capacitance of these systems is much larger (mF range compared to µF for dielectric capacitors), such capacitors are termed *supercapacitors* or *ultracapacitors*.[197] Note that this terminology in general refers to capacitors with a far enhanced capacitance compared to EDLCs. We will discuss further optimization routines to achieve *supercapacitance* in the following.

Improving Performance of Capacitors. The amount of ions electrostatically adsorbed onto the electrode surface is proportional to the capacity of the device. Hence, maximizing ion quantity is key, which can be achieved by increasing the highly accessible surface area. For instance, graphene electrodes with a huge active surface area (around $2630\,\mathrm{m^2\,g^{-1}}$[198]) can be used to achieve specific capacitances of up to $2585\,\mathrm{F\,g^{-1}}$.[199] In comparison, carbon-based EDLCs with a specific surface area of ca. $250\,\mathrm{m^2\,g^{-1}}$ only achieve a specific capacitance of ca. $15\,\mathrm{F\,g^{-1}}$.[200] Such microstructured EDLCs are thus also termed *supercapacitors* or *ultracapaci-*

tors. P. Simon *et. al.* investigated the relationship between pore size and electrolyte ion size by matching anions with different sizes to the pore size of carbon electrodes and found a maximized capacitance for the closest anion and pore size match.[201] One can understand this effect best by comparing specific capacitance normalized against mass (*i.e.*, gravimetric capacitance) with capacitance normalized against area (ratio between specific capacitance and surface area). For carbon-based electrodes, the latter stabilizes at around 5 µF at a specific surface area of 1500 m^2 g^{-1}.[200] Note that this value presents a limit and larger capacitances can only be achieved by optimizing the nanostructure of the electrode, *e.g.*, by preventing graphene sheet aggregation *via* laser reduction of graphene oxide growth. This approach was reported by R. B. Kaner *et. al.*, who improved the areal capacitance to 4.04 mF cm^{-2}.

A maximized specific capacitance requires matching of ions with electrode pore sizes. Larger ions do not or insignificantly contribute to the capacitance. In aqueous electrolytes, ions are hydrated – a partial desolvation may be required.

The electrolyte also plays a significant role in capacitor performance. While carbon-based aqueous systems can exceed 300 F g^{-1}, organic electrolytes only barely reach this value. This can be explained with our previous discussion on pore size and ion size matching: While pores <0.5 nm can still fit aqueous hydrated ions, organic electrolytes require pore sizes of >1.0 nm.[186] Furthermore, the electrolyte governs the maximum voltage *via* the Electrolyte (Electrochemically) Stable Window (ESW) (see Section 2.2.1) – note that for aqueous electrolytes this is 1.23 V. Requirements for the electrolyte can be summarized as follows: wide potential window and well matched with electrodes, high ionic conductivity, high (electro)chemical stability and inertness to electrode/casing components, wide operating temperature range, low volatility and flammability, environmentally friendly, and low cost.[202]

Electrolytes limit cell voltage through their electrochemical stability window. However, overpotentials can be employed to increase the electrode potential beyond the electrolyte decomposition redox potential (*e.g.*, for water: H_2 evolution at the anode, O_2 evolution at the cathode).

The issue of low theoretical potential window can be further engineered not on the

electrode and electrolyte level, but the device level: A capacitor device always requires two electrodes, one to store electrons and one to store the respective holes. Two types of devices exist: symmetric capacitors (both electrodes are composed of the same material) or asymmetric capacitors (electrodes have different material compositions). The former was developed first due to its more simple design – both electrodes require matching kinetics (see Section 2.2.3). However, this also means that the cell voltage is governed by the narrow potential window of the single type active material.[203] The idea of asymmetric capacitors tries to improve this low cell voltage problem by tuning both electrode sides independently.[197] For instance, when using water as electrolyte, a symmetric capacitor cell voltage is limited to $1.23\,\mathrm{V}$. However, in asymmetric configuration, electrodes with a very large overpotential for water oxidation (*e.g.*, MnO_2 or PbO_2) and water reduction (*e.g.*, carbon) can be chosen independently, which can extend the practical voltage limit to $2\,\mathrm{V}$ or $2.3\,\mathrm{V}$, respectively.[204]

Electrode Materials for Capacitors. The list of electrode materials is large. The by far most investigated class of electrode materials are nanostructured carbon materials, such as graphene derivatives,[205] activated carbons,[206] aerogels,[206] onion-like carbons,[206] different nanostructures (nanotubes,[207] nanocoils,[208] nanohorns,[209] or fibers[210]). All have been utilized as supercapacitors electrodes. Further electrode materials for capacitive supercapacitors include manganese oxide (MnO_2; specific capacitance and energy densities of $85.8\,\mathrm{F\,g^{-1}}$ and $47.4\,\mathrm{W\,h\,kg^{-1}}$ for MnO_2 and carbon nanotube asymmetric supercapacitors (Figure 1.14 (d))[192]) as well as composites of different materials (*e.g.*, a polyaniline/graphene/carbon nanotube composite electrode coupled with an activated graphene electrode, reaching energy densities of $20.5\,\mathrm{W\,h\,kg^{-1}}$ (Figure 1.14 (e))[193]).[197] We will discuss pseudocapacitive electrode materials more in the next section.

1.4.3. Pseudocapacitive Energy Storage

The concept of pseudocapacitance is to-date still very much debated in the electrochemistry community. In general, energy storage at a solid-liquid junction can occur (1) *via* formation of an EDL as discussed in the previous section, (2) *via* surface redox reactions, (3) *via* ion insertion analogous to electrochemical intercalation, or (4) *via* decomposition, alloying, or conversion reactions.[194] The latter three are faradaic processes – hence utilizing a different charge storage mechanism than

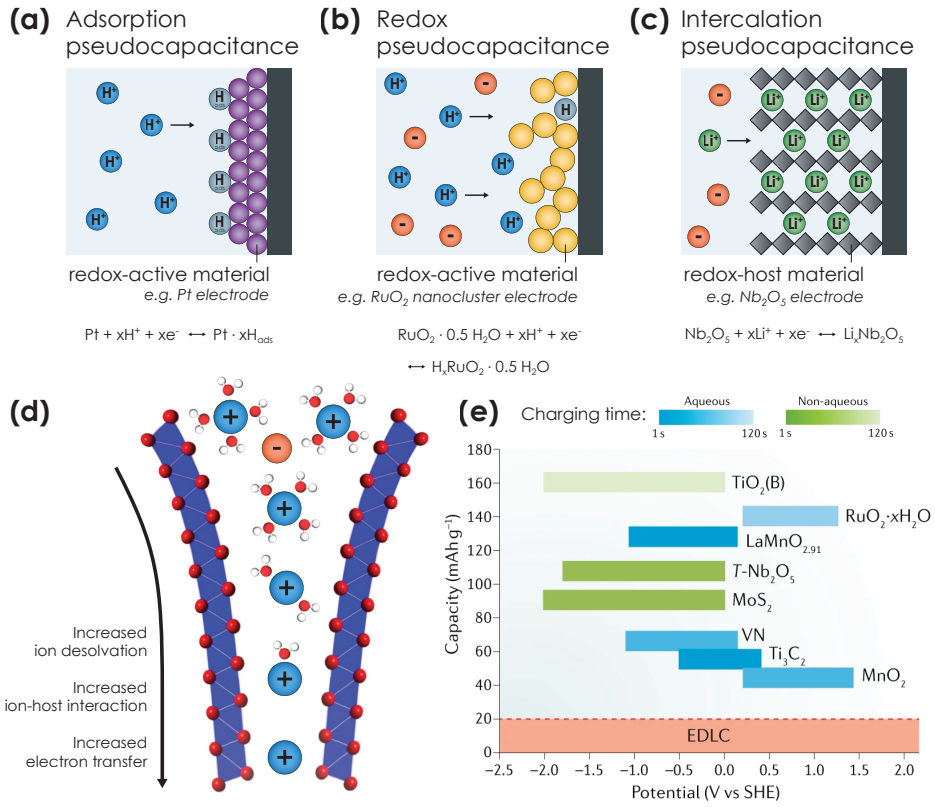

Figure 1.15. Pseudocapacitance. (a-c) Schemes depicting the mechanism of pseudocapacitance as defined by B. E. Conway in the 1970s for different exemplary systems. Adapted with permission.[190,195] Copyright 2014, AAAS; Copyright 2014, Royal Society of Chemistry. **(d)** Hydrated ion motion through different pore sizes during intercalation requires a partial desolvation of the hydration shell. Reproduced with permission.[211] Copyright 2022, Springer Nature. **(e)** Electrochemical performance shown for several exemplary pseudocapacitive materials – both aqueous (blue) and non-aqueous (green) – and referenced against EDLCs (red). Reproduced with permission.[212] Copyright 2019, Springer Nature.

capacitors discussed above. One can also classify these mechanisms by their time scale:[194] (1) $\leq$30 s: EDL formation. This surface process is very fast and EDLC devices rely on it (see previous Section). (2) $>$10 min to hours: conversion/alloying or intercalation with accompanied phase change. Note that contrary to EDL these processes are not necessarily occurring only at the surface anymore. Batteries can utilize such mechanisms (see next Section). (3) 10 s to 10 min: Redox surface or near-surface intercalation processes occur in this intermediate time range. Since the kinetics of these processes is still close to EDLs and hence their electrochemical signature is related (see Section 2.2.3) but the mechanism clearly has a faradaic

nature, one terms them *pseudocapacitive* processes.

> Pseudocapacitive processes show the kinetics close to EDL, but the capacity of a faradaic mechanism. Thus, while obtaining high power output, the specific capacitance is ca. 1-2 orders of magnitude greater than in EDLCs.

Pseudocapacitance can be described *via* several distinct mechanisms. We depict more traditional mechanisms defined by B. E. Conway *et. al.* in the 1970s in Figure 1.15 (a-c) and discuss them in the following:[186,212]

(i) **Adsorption pseudocapacitance** (Figure 1.15 (a)) – also sometimes referred to as underpotential deposition pseudocapacitance – occurs, when metal ions or hydrogen form an adsorbed monolayer on the surface of a noble metal electrode (for Pt and H: $Pt + H^+ + e^- \rightleftharpoons Pt - H_{ads}$).[213] Note that the electrosorption/desorption process that stores the energy occurs at respective potentials more negative or positive of the redox potential of the adsorbent, depending on whether it is a reduction or oxidation reaction.

(ii) **Redox pseudocapacitance** (Figure 1.15 (b)) requires a faradaic charge transfer reaction occurring at or close to the surface – here in contrast to (i) at the redox potential.[214] The process is accompanied by ion adsorption. Since ions adsorb at or near the surface, the diffusion distances and times are short.

The prototypical pseudocapacitive material – RuO_2 – was first reported in 1971 *via* a mechanism involving protonation of the RuO_2 surface in mildly acidic aqueous conditions.[215] The redox reaction involves reduction of H^+, which can subsequently easily diffuse through the hydrous boundaries in the nanoporous RuO_2.

(iii) **Intercalation pseudocapacitance** (Figure 1.15 (c)) is caused by reversible ion intercalation into ion-conduction channels or layers of a host material, accompanied by a redox charge transfer, but importantly not a phase transformation of the host material.[216] This causes the ion diffusion to occur much faster, thus reducing the diffusion time.

Since development of these early pseudocapacitance definitions around 50 years ago, the field has proceeded to incorporate the behavior of various further pseudocapacitance effects. Different definitions were proposed – both from a mechanistic

and an electrochemical characterization level. We will discuss the most noteworthy definitions and exceptions in the following that assemble to the current interpretation of pseudocapacitance.

Brousse, Bélanger, and Long proposed in 2015 a stricter definition *via* the electrochemical signature, requiring a constant capacitance response over the entire charge storage voltage range – a typical phenomenon of an EDLC (Section 2.2.3).[217] This definition is very application oriented and was intended to discourage the growing trend of reports of materials, which showed high specific capacities albeit lacking the typical pseudocapacitive features (*e.g.*, redox behavior of $Ni(OH)_2$ in alkaline electrolytes).[194]

Dunn, Conway, and others proposed around the same time the terminology of "extrinsic" *vs.* "intrinsic" pseudocapacitance, that is, pseudocapacitance which results from morphology (*e.g.*, through microstructuring) and pseudocapacitance according to the more traditional definition discussed above.[190,217] Microstructuring can significantly reduce the diffusion length I of an intercalation species. According to the authors, pseudocapacitance occurs in this case, if $I \lll \sqrt{D \cdot t_d}$, with D being the diffusion coefficient and t_d giving the diffusion time. Besides faster intercalation, a larger fraction of the redox sites are located at the electrode-electrolyte interface, further increasing the charge storage kinetics (*e.g.*, for hierarchical, nanoporous anatase TiO_2).[218]

Dis-charging in conductive polymers shows a behavior similar to the pseudocapacitance response.[219] This mechanism – first investigated in the late 1980s for PANI[220] – is termed *Doping Pseudocapacitance* and results from reversible electrochemical de-doping.[186] The process involves oxidation (p-doping) or reduction (n-doping) of the conjugated backbone of the conductive polymer inducing a polaron or bipolaron, which is accompanied by the concurrent insertion of an anion or cation from the electrolyte, respectively. This effect has been shown to occur for many different conductive polymers, including PANI, PPY, and derivatives of PEDOT.[194,219] Note that the theoretical capacity is limited by the number of dopants per monomer unit, defined by the reversibly accessible doping level γ (ranging typically from 0.3 to 0.5). This determines the closest proximity of charge carriers on the polymer backbone.[221] To name some examples with respective theoretical capacities: PANI $\gamma = 0.5$ ($146\,\mathrm{mA\,h\,g^{-1}}$), PPY $\gamma = 0.33$ ($132\,\mathrm{mA\,h\,g^{-1}}$), and PEDOT $\gamma = 0.33$ ($62\,\mathrm{mA\,h\,g^{-1}}$).[194] Note that kinetics of the dis-charging process are mainly limited by the diffusion of counterions to doping sites in the bulk of the polymer electrode.

One must underline that definition of pseudocapacitance is in major parts still blurry and not very clear. For instance, C. Costentin and J.-M. Savéant analyzed pseudocapacitive effects in MnO_2 and hydrous RuO_2 and argued that previous interpretation of an ensemble of overlapping redox potential might not be correct, but rather an EDL formation or combination of surface Faradaic and EDL processes might explain the behavior – but failed to explain chemical changes occurring during discharging.[222]

> Conductive polymers show doping pseudocapacitance resulting from doping of the conjugated backbone accompanied by ion de-insertion. The resulting capacity is significant – 62 mA h g^{-1} for PEDOT.

Furthermore, the differentiation between intercalation pseudocapacitance in nanostructured materials and faradaic processes occurring in batteries is not very clear, since intercalation requires in any case only very minimal structural transformations.[194] Recent studies have also challenged the differentiation between pseudocapacitance and EDL capacitance.[222,223] For instance, a recent theoretical Density Functional Theory (DFT) study by M. Ontani *et. al.* reported that the only difference between pseudocapacitance and EDL capacitance in MXene was whether the ions had a hydration shell and had to intercalate into an already-hydrated interlayer.[224] In aqueous environments MXene shows capacitive behavior (rectangular CV shape, see Section 2.3.1.2). However, in non-aqueous environments shows pseudocapacitive behavior with a highly distorted CV shape. The authors rationalize that a hydration shell (present in aqueous electrolyte conditions) can inhibit orbital coupling between the intercalated ion and MXene, which gives rise to the pseudocapacitive behavior. V. Augustyn *et. al.* recently published a perspective on confined hydrated ion motion in pores of the host materials, which do, do not, or do not fully support the size of the hydration shell. The consequence is a necessary partial ion dehydration (that is, partial decomposition of the hydration shell) prior or during intercalation (Figure 1.15 (d)). Electrolyte confinement can thus govern the electrochemical response of the host material. The authors illustrate this concept by comparing the electrochemical response of Li^+ intercalation into single graphene sheets with multi-stacked graphene sheets reported by J. Rodríguez-López *et. al.*[225] While single sheets showed the expected EDL capacitance, for samples with more than 4 sheets redox signals started to appear, indicating a possibly pseudocapacitive response.

The authors hypothesize that the small interlayer distance in graphite (~ 0.33 nm) caused sufficient confinement so that the Li^+-ion has to dehydrate. This in return causes a more significant interaction between Li^+ and host, modifying the charge storage behavior.

> Hydrated ion motion in confined spaces can produce pseudocapacitive effects in intercalation charge storage materials, which modifies the charge storage behavior, which can result in a pseudocapacitive charge storage behavior.

The main advantages of pseudocapacitive materials however is the much higher capacity compared to charge storage *via* EDLCs due to the faradaic charge storage mechanism, but at the same time fast kinetics that enables high power output (see Section 2.2.3). For instance, surface redox pseudocapacitance in MnO_2 thin films in an aqueous electrolyte reached capacities of $263\,mA\,h\,g^{-1}$ at a cell voltage of $1.2\,V$.[226] Intercalation pseudocapacitance in TiO_2(B) cathodes was shown to reach $230\,mA\,h\,g^{-1}$ at a cell voltage of 1 to $3\,V$ *vs.* Li/Li^+.[227] Extrinsic pseudocapacitance in non-aqueous MoO_3 and MoO_{3-x} yielded energy densities of $250\,mA\,h\,g^{-1}$ and $270\,mA\,h\,g^{-1}$, respectively, at a cell voltage of 1.5 to $3.5\,V$ *vs.* Li/Li^+.[228] We show a comparison of capacity of further pseudocapacitive materials at different redox potential and referenced against typical performance of EDLCs in Figure 1.15 (e).

1.4.4. Electrochemical Energy Storage *via* Batteries

We will continue our discussion on energy storage devices with introducing batteries, however, will dive only briefly into this vast research field and mainly focus on Li-ion batteries. In comparison to EDLCs which store electrical energy directly as discussed before, batteries store energy *via* chemical bonds inside the electrode which form during a *faradaic* charge transfer, *i.e.*, they store "chemical energy". The process of charging and discharging is thus the process of transforming chemical to electrical energy through electrochemical reactions, and *vice versa*. Note that while EDLCs rely on a sole surface process, batteries store charges in the bulk of the material. Note also that pseudocapacitors are in the middle – they can store charges *via* a faradaic mechanism but show electrochemical reactions more according to a capacitive signature.[229]

We will discuss the charge storage mechanism through the discharging process

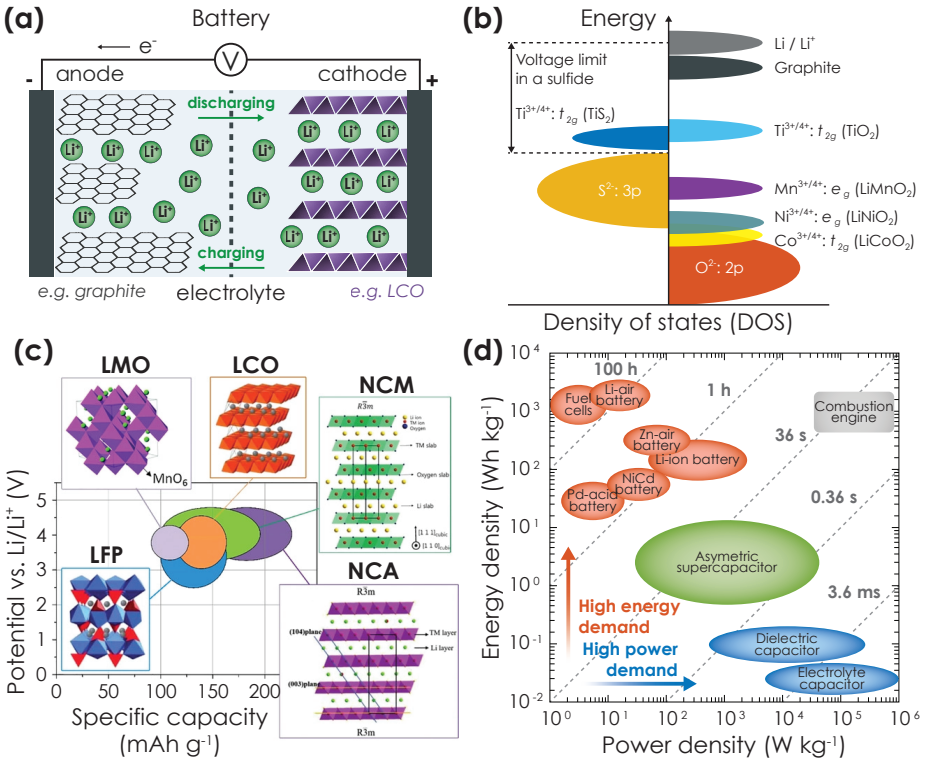

Figure 1.16. Battery energy storage and intercalation. (a) A battery consists of a porous conductive anode (*e.g.*, graphite), which is reduced upon Li^+ intercalation ($Li^+ + C_6 + e^- \rightleftharpoons LiC_6$).[230] At the same time, the cathode releases intercalated Li^+ ions and oxidizes the backbone. Adapted with permission.[186,190] Copyright 2019, Royal Society of Chemistry; Copyright 2014, AAAS. **(b)** Relative redox energy position referenced to the top of the anion p band of the cathode material. Sulfide based cathodes have a smaller cell voltage due to the higher energy limit of the S^{2-}:3p band compared to oxide-based cathodes. Reproduced under the terms of open access CC BY 4.0 license.[231] Copyright 2020, Springer Nature. **(c)** Approximate range of average discharge voltage of different cathode materials in dependance of their specific capacity. Reproduced with permission.[232] Copyright 2021, Wiley-VCH. **(d)** Ragone plot comparing performance of energy storage devices in terms of specific energy and specific power. The dashed lines give the respective times that a full discharging requires. Reproduced with permission.[197] Copyright 2018, American Chemical Society.

of a Li-ion battery. Here, the reaction at the negative electrode (anode) produces electrons *via* oxidation of the electrode, the positive electrode (cathode) accepts electrons (or produces holes) by reducing the electrode, and the electrolyte shuttles ions between the electrodes, which intercalate into the electrodes and provide electrostatic compensation (Figure 1.16 (a)). The cell voltage results from the difference between redox potentials of anode and cathode. To maximize energy and

power, this voltage should be as large as possible. This explains why Li-ion batteries achieve such a high performance: The Li^+/Li couple has an extremely negative standard potential (-3.04 V *vs.* NHE).[183] Reactions at the individual components during discharging are described in the following:

(i) **At the anode:** In case of Li metal anodes, Li is oxidized, injecting electrons into the external circuit and Li^+ ions into the electrolyte. In case of graphite anodes, graphite C_6 is oxidized, releasing intercalated Li^+ ions into the electrolyte. In theory, a Li metal anode can be used, but in reality is rarely employed, except for all-solid-state batteries (see next paragraph).

For Li metal anodes: $\mathrm{Li} \rightleftharpoons \mathrm{Li^+ + e^-}$

For graphite anodes: $\mathrm{LiC_6} \rightleftharpoons \mathrm{C_6 + Li^+ + e^-}$

(ii) **At the cathode:** The cathode material backbone is being reduced, accompanied by Li^+ intercalation. To produce a large device voltage, the reduction potential should be as positive as possible, since the cell voltage results directly from the difference of anode and cathode redox potentials. We discuss different cathode materials and abbreviations in the paragraph following the next, but give some exemplary cathodes in the following:

For LCO ($LiCoO_2$) cathodes:[233] $\mathrm{Li_{m-n}CoO_2 + nLi^+ + ne^- \rightleftharpoons Li_mCoO_2}$

For LMO ($LiMn_2O_4$) cathodes:[234] $\mathrm{Li_{m-n}Mn_2O_4 + nLi^+ + ne^- \rightleftharpoons Li_mMn_2O_4}$

(iii) **In the electrolyte:** Ions (*e.g.*, Li^+) are shuttled between anode and cathode. Hence, a good bulk ionic conductivity is required, but no electronic conductivity should be present, since this would produce an internal short circuit.

Anode Materials. Li metal electrodes are the simplest form of anodes in a Lithium Battery (LiB). However, they are rarely employed due to three major drawbacks: (1) Stripping of Li metal during charging/discharging causes a huge change in its volume, which causes internal pressure. (2) Higher rate of decomposition side reactions. (3) Dendrite formation on the Li metal electrode. Dendrites result from plating of Li^+ ions on top of the metal electrode as a result of the electrode not being able to reduce Li^+ fast enough during charging. Dendrites are detrimental in several ways: (a) Larger specific surface area of the electrode, resulting in more decomposition side reactions with the electrolyte and Li metal detachment forming ”dead” Li and reducing the capacity. (b) Internal short circuiting of the battery, when dendrites penetrate the separator.[235]

Hence, different anode materials were investigated which are capable to store Li metal but at the same time do not reduce the oxidation potential too much. Graphite is a straight-forward solution and widely employed, but suffers from poorer capacity and is associated with safety concerns.[236] The anode material lithium titanate ($Li_4Ti_5O_{12}$, LTO) has in recent years become the second most employed anode material after graphite due to its good cycling stability ($>10\,000$ *vs.* >1000 for graphite), rate capability, safety, and sufficiently good performance compared to the graphite reference (energy: ~ 100 *vs.* $\sim 200\,\mathrm{W\,h\,kg^{-1}}$; power: 10 *vs.* $5\,\mathrm{kW\,kg^{-1}}$).[237]

Cathode Materials. The most popular class of cathode materials are oxides, that were developed in the early 1980s. As mentioned above, a large battery voltage necessitates a cathode potential as positive as possible (electrochemical scale). This requires the stabilization of higher oxidation states in a low-lying energy band.[231] The question of how to access these states was investigated in detail in the latter half of the 20st century. Goodenough's group established in 1980 that the cell voltage will be always limited by the top of the S^{2-}:3p band (see Figure 1.16 (b)), based on knowledge that the top of the S^{2-}:3p lies at higher energies than the top of the O^{2-}:2p. In fact, sulfide cathodes limit the cell voltage to <2.5 V whereas oxide cathodes can achieve cell voltages of up to ~ 4 V.[231] Hence, they started to investigate oxides as cathode candidate materials. Today, most cathode materials are typically based on $LiMO_2$ (M = Co (abbreviated as LCO), Ni, Mn (abbreviated as LMO)), $LiMn_2O_4$, or $LiMPO_4$ (M = Fe (abbreviated as LFP), Co, Ni, Mn).[186]

However, the materials come with drawbacks: LCO is costly and capacity fading occurs during deep cycling. LMO possesses low cycling performance due to structure modifications upon Li de-intercalation and Mn leaching. LFP has poor electrical and ionic conductivity, producing low energy and power density.[238] Hence, doping of the pure phases is performed, leading to many advanced high-performance cathode materials. Some examples are given in the following: $Li[Ni_{1-x-y}Co_xMn_y]O_2$ (abbreviated with $LiNiMnCoO_2$ (battery cathode material) (NMC)) incorporate elements, to which one can associate their traits of high capacity (nickel), better rate capability (cobalt), and improved safety (manganese).[239] $Li[Mn_{1-x-y}Fe_xCo_y]PO_4$ utilizes the much better electrochemical activity and reversibility of the Fe^{3+}/Fe^{2+} redox couple and Co^{3+}/Co^{2+} couple compared to the Mn^{3+}/Mn^{2+} redox couple.[240] The material $Li[Ni_xCo_yAl_{1-x-y}]$ (abbreviated with NCA) adds small amounts of Co and Al to stabilize the structure and improve thermal stability.

Consequently, high performance and low-cost motivated *Tesla* to use NMC and

NCA as their main cathode materials. The company also investigates LFP as a possible future cathode candidate due to the resource scarcity of Co and Ni, albeit with a slightly lower specific capacity. We show specific capacitance of various cathode compounds in Figure 1.16 (c).

Key to a good performance *via* a large battery voltage is a large potential difference between anode and cathode.

Classification of Batteries. One can classify batteries generally into two categories: non-rechargeable batteries (primary cells; type I) or rechargeable batteries (secondary cells; type II). However, this very broad classification falls short of describing more intricate details of different sub-genres of batteries. It is important to obtain an overview of different battery types in order to understand the new field of solar batteries better, which often cannot be associated with one specific type of battery, but rather a convolution of battery concepts and solar cell concepts (we will discuss this in detail in Chapter 5). In the following, we will thus briefly summarize different battery concepts:[186]

(i) **Stationary *vs.* flow batteries.** Compared to a conventional battery, a flow battery contains two different types of electrolytes separated by an ion permeable membrane. Redox couples in the electrolytes store the charges in the liquid phase (hence, they are termed *anolyte* and *catholyte*). The main advantage of this type of battery is its scalable capacity, since implementing a larger tank is far more feasible than a thicker electrode, *i.e.*, the device decouples scaling of energy density from power density. The most common redox couples are Zn-Br_2 and V^{2+}/V^{3+}.[186,241]

(ii) **Dissolution / deposition-based *vs.* intercalation / de-intercalation-based batteries.** This differentiation results from the charge storage mechanism at the electrodes: Dissolution/deposition-based batteries store energy *via* chemical reactions occurring inside of the cell that dissolve the electrode (*e.g.*, Li^+ metal anodes). De-intercalation on the other hand only requires ion de-interca- lation and reduction/oxidation of the backbone (*e.g.*, graphite anodes).[186]

(iii) **Closed *vs.* open batteries.** Whereas a closed battery contains all active material within the battery and is sealed off, an open battery exchanges parts of

the active material with its surrounding. Examples are Li-air batteries, which require O_2 from air at the cathode during discharging. Aqueous Li-air batteries form LiOH ($2\,Li^+ + 2\,e^- + 0.5\,O_2 \rightleftharpoons 2\,LiOH$), non-aqueous Li-air batteries produce Li_2O_2 ($2\,Li^+ + 2\,e^- + O_2 \rightleftharpoons Li_2O_2$). Note that Li-air batteries possess the highest specific energy density of rechargeable batteries (500 to $900\,W\,h\,kg^{-1}$), but are challenging to implement as we discuss in Chapter 5.[242]

(iv) **Solid electrolyte *vs.* liquid electrolyte (or dry *vs.* wet) batteries.** All-solid-state batteries exchange the liquid electrolyte with a solid electrolyte, which brings a number of advantages: A possibly larger voltage operation window (when using Li or Si anodes) and less spacious electrolyte can lead to a higher gravimetric and volumetric energy density, only one mobile ion species occurs (leading to higher transference numbers) and diffusion of unwanted species is inhibited which reduces side reactions (with this, reducing Mixed Conducting Interphase (MCI) formation), higher thermal stability, and a more flexible cell design (*e.g.*, bipolar stacking or flexible devices).[243,244] Examples for solid-state battery electrolytes include Ag_4RbI_5 for silver-ion and LiI/Al_2O_3 for LiB batteries.[186]

(v) **Acidic *vs.* alkaline batteries.** The pH value of the electrolyte determines this battery type. One differentiates between acidic (*e.g.*, lead-acid batteries), near neutral (*e.g.*, zinc-air batteries), or alkaline (*e.g.*, NiCd or ZnMn batteries). While alkaline batteries typically have a longer shelf life and energy densities, neutral batteries may be less toxic.

(vi) **Aqueous *vs.* non-aqueous batteries.** Liquid electrolytes can be aqueous or non-aqueous. The former is commonly used as salt solutions in lead-acid, NiCd, or nickel-metal hybrid batteries. Li-ion batteries use lithium salts such as $LiPF_6$, $LiAsF_6$, $LiN(SO_2CF_3)_2$, or $LiSO_3CF_3$ in combination with solvents such as acetonitrile, ethylene carbonate, diethyl carbonate, propylene carbonate, 1,2-dimethoxyethane, DMSO, THF, their binary/ternary combinations, etc.[186] Aqueous electrolytes are thus less toxic and more environmentally friendly.

Performance Metrics of Batteries & Capacitors. Performance can be classified *via* energy density or power density. Energy density is the energy (that is, amount of power performed over a certain amount of time) normalized with respect to mass or volume of the active material ($W\,h\,kg^{-1}$ or $W\,h\,L^{-1}$). Power density describes the normalized power (*i.e.*, work being performed) on active mate-

rial mass ($\mathrm{W\,kg^{-1}}$). We describe these concepts in more detail as well as how to measure them in Section 2.2.3. Importantly, while a device can have a high energy output, it must not necessarily also produce a significant power output.

Ragone plots compare performance of energy storage devices in terms of specific energy and specific power output (Figure 1.16 (d)). A trend becomes evident: Batteries possess high energy densities (Li-ion batteries approach $180\,\mathrm{W\,h\,kg^{-1}}$), but rather low power output due to the slower kinetics of the discharging process, as discussed throughout this Section. Capacitors on the other hand show significant power density (EDLCs reach $100\,000\,\mathrm{W\,kg^{-1}}$) but lack energy densities. Asymmetric supercapacitors and pseudocapacitors show both medium energy and power densities, thus pushing energy storage devices a bit closer towards the desired "combustion engine performance" with high energy and power densities.[197] A different way of how to understand performance metrics lies in looking at discharge times, when discharged with the maximum power density. Batteries require on average several hours, whereas dielectric and EDL capacitors discharge $<0.4\,\mathrm{s}$.

1.5. Beyond Energy Storage

We will conclude our discussion on energy storage materials with a brief excursion into the world of memristors and resistance switching concepts. Let us start by explaining what a memristor is and how it relates to energy storage. The origin of memristors dates back to 1971, when Leon Chua postulated that due to symmetry requirements a fourth fundamental electrical component should exist besides capacitors (defined *via* capacitance C; links charge q with voltage V: $C = \frac{\mathrm{d}q}{\mathrm{d}V}$), resistors (defined *via* resistance R, links current i with V: $R = \frac{\mathrm{d}V}{\mathrm{d}i}$), and inductors (defined *via* inductance L; links magnetic flux ϕ and i: $L = \frac{\mathrm{d}\phi}{\mathrm{d}i}$).[245] As such, memristors should give the missing linkage of q with ϕ. Importantly, the magnetic flux ϕ should not be understood as representing a magnetic field, but rather describe generalized electric circuit characteristics of an inductor. An ideal memristor is hence characterized by its memristance M. Utilizing the time dependent relationships between q, V, i, and ϕ, we can define M as follows:

$$M\left(q\left(t\right)\right) = \frac{\mathrm{d}\phi\left(t\right)}{\mathrm{d}q\left(t\right)} = \frac{V\left(t\right)\cdot\mathrm{d}t}{i\left(t\right)\cdot\mathrm{d}t} = \frac{V\left(t\right)}{i\left(t\right)} \tag{1.1}$$

From this equation, we can infer that M is in fact a "charge-dependent resistance": In case of constant M, we obtain R according to Ohm's law ($R = \frac{U}{I}$). However, M

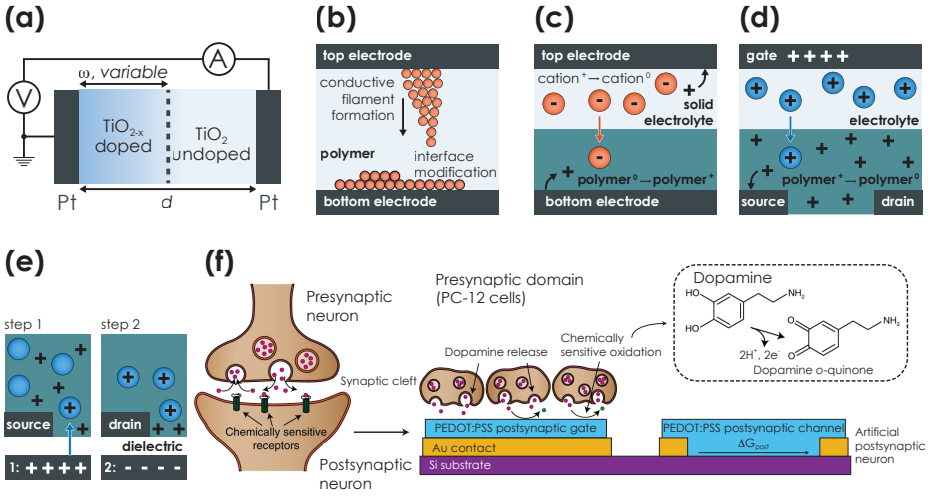

Figure 1.17. Memristors and resistance switching devices. **(a)** Scheme showing the operation of the prototype memristor, consisting of a doped and an undoped TiO_2 layer that upon applying a voltage or current modify their thickness through movement of mobile oxygen vacancies and thus change the overall conductivity. Adapted with permission.[246] Copyright 2008, Springer Nature. Different resistance switching mechanisms are shown in the next panels, namely **(b)** voltage-dependent interface modification, **(c)** two-terminal redox-based switching, **(d)** organic electrochemical redox-based switching, and **(e)** charge-trapping based switching. Adapted with permission.[247] Copyright 2018, Springer Nature. **(f)** Schematic comparison of a biological synapse (left) with an artificial synapse based on a PEDOT:PSS neuromorphic device that incorporates a dopamine recycling process. Reproduced with permission.[248] Copyright 2020, Springer Nature.

depends on q, which in return is time dependent. Solving Equation 1.1 for voltage reveals:

$$V(t) = M(q(t))\, I(t) \tag{1.2}$$

For Direct Current (DC) current and in case of constant memristance, the voltage-current dependence is linear. However, if charge is modified – prior or during the measurement – the dependence deviates from linear behavior, *i.e.*, memristors are non-linear circuit elements. The concept of resistance of the device depending on its *charging state history* becomes evident.

While this concept of the ideal memristor is rather straight-forward, an experimental demonstration of a proof-of-concept device is far from it and reported devices are to this date controversial.[249–252] The first proof-of-concept device was reported by R. S. Williams *et. al.* of *Hewlett Packard laboratory* in 2008, initiating this exciting new research field.[246] The authors report a two-terminal device consist-

ing of a layer of undoped TiO_2 on top of a layer of doped TiO_{2-x}, which both are sandwiched between Pt current collectors (Figure 1.17 (a)). While TiO_2 in its undoped state is insulating, upon doping with oxygen vacancies the material (TiO_{2-x}) becomes conductive. The oxygen vacancies are mobile and can drift along an external applied electric field. Thus, upon applying a potential to the device, the size of the doped and undoped layers change (Figure 1.17 (a), ω and d, respectively). The overall resistance results from the sum of resistances of the two individual layers, which are a function of the thickness of the layers. Applying an electric field pushing dopants into the undoped layer prior to the measurement produces a device with a lower overall resistance, and *vice versa*. Hence, the device's resistance is variable (depending on history of applied voltage and current), but importantly not volatile. The resulting electrochemical signature and its implications are explained in Section 2.3.1.3. The potential that such novel devices unravel is fascinating and ranges from non-volatile memory applications and resistive switching to artificial synapses, photomemristive sensing (Chapter 8), and neural networks for neuromorphic computing.[247,249]

1.5.1. Resistance Switching

The abovementioned memristance mechanism can be classified as a resistive switching method, since resistance holds the applied voltage and/or current history. Since the early report of the first memristor, more resistive switching mechanisms have been reported for manifold materials.[249,253–255] Let us focus on organic designs in the following and only briefly mention example inorganic counterparts. Four distinct mechanisms can be defined:[247]

(i) **Voltage-dependent interface modification.** (Figure 1.17 (b)) Applying a bias causes formation of a localized conductive filament in the electrolyte and modifies the junction interface.

(ii) **Two-terminal redox-based switching.** (Figure 1.17 (c)) Voltage-induced redox reactions occur in both a polymer and adjacent solid electrolyte, modifying the resistance of both layers.

(iii) **Organic electrochemical redox-based switching.** (Figure 1.17 (d)) This concept resembles the mechanism of an electrochemical transistor, with the respective nomenclature (that is, source and drain terminals act as the resistance switch interfaces and gate is the terminal, which controls the switch).[256]

Applying a bias voltage to the gate drives ions from an electrolyte into the adjacent polymer, modifying its redox state and thus resistance.

(iv) **Charge-trapping based switching.** (Figure 1.17 (e)) Conductivity of a host conductive polymer (*e.g.*, pentacene or poly(methyl methacrylate)) is modified by adding metallic (*e.g.*, Au)[257] or non-metallic (*e.g.*, ZnO)[258] nanoparticles. These nanoparticles act as nanoscale capacitors that charge (*i.e.*, "trap" charges) when applying a positive or negative bias potential to a conductive electrode in contact with the polymer. The nanoparticles then attract or repel mobile holes in the conductive polymer, thus modifying its conductivity.[247]

All resistive switching mechanisms have in common that they provide many non-volatile addressable states. Memory applications seem like a straight-forward powerful application as an alternative or extension to the currently employed resistive random-access memory (Random Access Memory (RRAM)) based on a binary system (*i.e.*, two addressable states: "1" and "0").[254] Typically the one-transistor-one-resistor (1T1R) architecture is implemented, which consists of one transistor and one resistor. Disadvantages of this architecture include a large required area and a significant thermal budget producing larger energy requirements as well as incompatibility with a 3D cell structure.[254] Memristors hold promise for the next generation memory devices due to their many individually addressable states in one single device. In fact, their charge/ion accumulation mechanism resembles synaptic functionality, and the advanced 3D and more volume optimized structures enable

Table 1.1. Key metrics of organic neuromorphic devices. This list defines key requirements that a memristive device should fulfill to be implemented for neuromorphic computing. Key metrics reproduced from A. Salleo *et. al.*[247]

Parameter	Value
Size for integration	$<1\ \mu m^2$ for dense/compact arrays
Number of states	$\sim$100 separable states, or $\sim$6 bit
Switching energy	1 pJ per switching events
Write/read speed	$<1\ \mu s$
State retention	1×10^3 to 1×10^8 s
Write endurance (cycles)	$\sim 1 \times 10^9$

development of neural network arrays, which are reminiscent of parallel operations in the brain, *i.e.*, neuromorphic computing.[259] Y. van de Burgt *et. al.* defined a list of key requirements that a memristive device should fulfill for neuromorphic computing and that we show in Table 1.1.

1.5.2. Materials for Resistance Switching

Manifold materials have been reported as resistance switches. To name some examples, inorganic materials include layered 2D materials (graphene,[260] boron nitrides (BN)[261]), Li battery anode and solid electrolyte materials (LTO,[262] Ag_2Se nanoparticles),[263] or conventional oxides (alumina,[264] SiO_2[265]). Organic materials include polymers (*e.g.*, PEO (programming speeds >1 µs, retention time >1 week),[266] PEDOT:PSS (512 different accessible states, 100 s retention time),[267] P3HT (>2 accessible states, <10 s retention time),[268] or light-assisted P3HT (256 accessible states, >500 days retention time)[269]), small molecules (*e.g.*, pentacene[270]), donor-acceptor complexes (*e.g.*, with 3 - nitrobenzal malonitrile (NBMN) and 1,4 - phenylenediamine (pDA)[271]), or ferroelectric materials (*e.g.*, polyvinylidene fluoride (PVDF)[272]).

> Memory can be stored in voltage/current dependent non-volatile memristance states *via* two different electrochemical doping processes – reminiscent of pseudocapacitive and faradaic processes discussed in Section 1.4.

Let us conclude this section with an exemplary artificial synapse reported recently by Y. van de Burgt, where the authors employ a PEDOT:PSS based neuromorphic device (as postsynaptic domains) with dopaminergic cells (PC-12 cells; as presynaptic domains) (Figure 1.17 (f)).[248] This device imitates a synapse to a new level by mimicking the dopamine recycling process: Dopamine is released by the PC-12 cells and oxidized by the PEDOT:PSS postsynaptic gate *via* a bias voltage pulse (0.3 V for 2 s). The oxidation generates an ion flow in the aqueous electrolyte, which modifies the conductance of the PEDOT:PSS postsynaptic channel. This change can be measured quantitatively, thus emulating the neurotransmitter.

1.6. References

(1) Ravishankara, A. R.; Rudich, Y.; Wuebbles, D. J. *Chem. Rev.* **2015**, *115*, 3682–3703.

(2) Fourier, J.-B. J. *Mémoires D L'académie R. Sci. L'institute Fr.* **1827**, *VII*, 570–604.

(3) Ortiz, J. D.; Jackson, R. *Notes Rec. R. Soc. J. Hist. Sci.* **2022**, *76*, 67–84.

(4) Gueymard, C.; Myers, D.; Emery, K. *Sol. Energy* **2002**, *73*, 443–467.

(5) Shukla, P. R.; Skea, J.; Slade, R.; Al Khourdajie, A.; van Diemen, R.; McCollum, D.; Pathak, M.; Some, S.; Vyas, P.; Fradera, R.; Belkacemi, M.; Hasija, A.; Lisboa, G.; Luz, S.; Malley, J., *Climate Change 2022: Mitigation of Climate Change. Contribution of Working Group III to the Sixth Assessment Report of the Intergovernmental Panel on Climate Change (DOI: 10.1017/9781009157926.001)*; IPCC 2022; Cambridge University Press: Cambridge, UK and New York, NY, USA, 2022.

(6) Al-Ghussain, L. *Environ. Prog. Sustainable Energy* **2019**, *38*, 13–21.

(7) Braslavsky, S. E. *Pure Appl. Chem.* **2007**, *79*, 293–465.

(8) Khandekar, M. L.; Murty, T. S.; Chittibabu, P. *Pure Appl. Geophys.* **2005**, *162*, 1557–1586.

(9) Houghton, J. T.; Ding, Y.; Griggs, D. J.; Noguer, M.; van der Linden, P. J.; Dao, X.; Maskell, K.; Johnson, C. A., *Climate Change 2001: The Scientific Basis*; Contribution of Working Group I to the Third Assessment Report of the Intergovernmental Panel on Climate Change; Cambridge University Press: Cambridge, UK, 2001.

(10) Lockwood, M. *Proc. R. Soc. A: Math. Phys. Eng. Sci.* **2010**, *466*, 303–329.

(11) Berger, A. *Rev. Geophys.* **1988**, *26*, 624–657.

(12) Xiong, M.; Rong, Q.; Meng, H.-m.; Zhang, X.-b. *Biosens. Bioelectron.* **2017**, *89*, 212–223.

(13) Lenton, T. M.; Rockström, J.; Gaffney, O.; Rahmstorf, S.; Richardson, K.; Steffen, W.; Schellnhuber, H. J. *Nature* **2019**, *575*, 592–595.

(14) Wang, S.; Foster, A.; Lenz, E. A.; Kessler, J. D.; Stroeve, J. C.; Anderson, L. O.; Turetsky, M.; Betts, R.; Zou, S.; Liu, W.; Boos, W. R.; Hausfather, Z. *Rev. Geophys.* **2023**, *61*, e2021RG000757.

(15) Rosokhata, A.; Minchenko, M.; Khomenko, L.; Chygryn, O. *E3s Web Conf.* **2021**, *250*, 03002.

(16) Manzano-Agugliaro, F.; Alcayde, A.; Montoya, F.; Zapata-Sierra, A.; Gil, C. *Renewable Sustainable Energy Rev.* **2013**, *18*, 134–143.

(17) Elia, A.; Kamidelivand, M.; Rogan, F.; ó Gallachóir, B. *Renewable Sustainable Energy Rev.* **2021**, *138*, 110488.

(18) *Un Clim. Chang. Conf. Uk 2021* **2021**.

(19) Ahmad, T.; Zhang, D. *Energy Rep.* **2020**, *6*, 1973–1991.

(20) Dincer, I. *Renewable Sustainable Energy Rev.* **2000**, *4*, 157–175.

(21) Solargis; ESMAP; Group, W. B. Solar Resource Map. Global Horizontal Irradiation `https://solargis.com/maps-and-gis-data/download/world` (accessed 03/10/2023).

(22) Loster, M. Total Primary Energy Supply - From Sunlight `https://www.ez2c.de/ml/solar_land_area/` (accessed 03/10/2023).

(23) Kleidon, A. *Philos. Trans. R. Soc. B: Biol. Sci.* **2010**, *365*, 1303–1315.

(24) Kleidon, A. *Philos. Trans. R. Soc. A: Math. Phys. Eng. Sci.* **2012**, *370*, 1012–1040.

(25) None, N., *Key World Energy Statistics 2009*; OECD: 2009.

(26) Fraunhofer Institute for Solar Energy Systems (ISE), Public net current production in Germany `https://www.energy-charts.info/charts/power/chart.htm?c=DE` (accessed 04/06/2023).

(27) Brunner, C.; Deac, G.; Braun, S.; Zöphel, C. *Renew. Energy* **2020**, *149*, 1314–1324.

(28) Kessler, F. K.; Zheng, Y.; Schwarz, D.; Merschjann, C.; Schnick, W.; Wang, X.; Bojdys, M. J. *Nat. Rev. Mater.* **2017**, *2*, 17030.

(29) Seyfarth, L.; Seyfarth, J.; Lotsch, B. V.; Schnick, W.; Senker, J. *Phys. Chem. Chem. Phys.* **2010**, *12*, 2227.

(30) Miller, T. S.; d'Aleo, A.; Suter, T.; Aliev, A. E.; Sella, A.; McMillan, P. F. *Z. Für Anorg. Allg. Chem.* **2017**, *643*, 1572–1580.

(31) LIEBIG, J. *Annalen Der Pharm.* **1834**, *10*, 1–47.

(32) Liu, A. Y.; Cohen, M. L. *Science* **1989**, *245*, 841–842.

(33) Riedel, R. *Adv. Mater.* **1992**, *4*, 759–761.

(34) Wang, X.; Maeda, K.; Thomas, A.; Takanabe, K.; Xin, G.; Carlsson, J. M.; Domen, K.; Antonietti, M. *Nat. Mater.* **2009**, *8*, 76–80.

(35) Schlomberg, H.; Kröger, J.; Savasci, G.; Terban, M. W.; Bette, S.; Moudrakovski, I.; Duppel, V.; Podjaski, F.; Siegel, R.; Senker, J.; Dinnebier, R. E.; Ochsenfeld, C.; Lotsch, B. V. *Chem. Mater.* **2019**, *31*, 7478–7486.

(36) Banerjee, T.; Podjaski, F.; Kröger, J.; Biswal, B. P.; Lotsch, B. V. *Nat. Rev. Mater.* **2020**, *6*, 168–190.

(37) Lau, V. W.-h.; Moudrakovski, I.; Botari, T.; Weinberger, S.; Mesch, M. B.; Duppel, V.; Senker, J.; Blum, V.; Lotsch, B. V. *Nat. Commun.* **2016**, *7*, 12165.

(38) Lotsch, B. V.; Schnick, W. *New J. Chem.* **2004**, *28*, 1129–1136.

(39) Weil, E. D. *J. Fire Sci.* **2011**, *29*, 259–296.

(40) Lotsch, B.; Döblinger, M.; Sehnert, J.; Seyfarth, L.; Senker, J.; Oeckler, O.; Schnick, W. *Chem. _ A Eur. J.* **2007**, *13*, 4969–4980.

(41) Chong, S. Y.; Jones, J. T. A.; Khimyak, Y. Z.; Cooper, A. I.; Thomas, A.; Antonietti, M.; Bojdys, M. J. *J. Mater. Chem. A* **2013**, *1*, 1102–1107.

(42) McDermott, E. J.; Wirnhier, E.; Schnick, W.; Virdi, K. S.; Scheu, C.; Kauffmann, Y.; Kaplan, W. D.; Kurmaev, E. Z.; Moewes, A. *J. Phys. Chem. C* **2013**, *117*, 8806–8812.

(43) Savateev, A.; Pronkin, S.; Willinger, M. G.; Antonietti, M.; Dontsova, D. *Chem. _ An Asian J.* **2017**, *12*, 1517–1522.

(44) Savateev, A.; Tarakina, N. V.; Strauss, V.; Hussain, T.; Brummelhuis, K.; Sánchez Vadillo, J. M.; Markushyna, Y.; Mazzanti, S.; Tyutyunnik, A. P.; Walczak, R.; Oschatz, M.; Guldi, D. M.; Karton, A.; Antonietti, M. *Angew. Chem. Int. Ed.* **2020**, *59*, 15061–15068.

(45) Döblinger, M.; Lotsch, B. V.; Wack, J.; Thun, J.; Senker, J.; Schnick, W. *Chem. Commun.* **2009**, 1541.

(46) Kröger, J.; Podjaski, F.; Savasci, G.; Moudrakovski, I.; Jiménez-Solano, A.; Terban, M. W.; Bette, S.; Duppel, V.; Joos, M.; Senocrate, A.; Dinnebier, R.; Ochsenfeld, C.; Lotsch, B. V. *Adv. Mater.* **2022**, *34*, 2107061.

(47) Sahoo, S. K.; Teixeira, I. F.; Naik, A.; Heske, J.; Cruz, D.; Antonietti, M.; Savateev, A.; Kühne, T. D. *J. Phys. Chem. C* **2021**, *125*, 13749–13758.

(48) Kröger, J.; Jiménez-Solano, A.; Savasci, G.; Lau, V. W. h.; Duppel, V.; Moudrakovski, I.; Küster, K.; Scholz, T.; Gouder, A.; Schreiber, M.-L.; Podjaski, F.; Ochsenfeld, C.; Lotsch, B. V. *Adv. Funct. Mater.* **2021**, *31*, 2102468.

(49) Savateev, O. *Adv. Energy Mater.* **2022**, *12*, 2200352.

(50) Schwinghammer, K.; Tuffy, B.; Mesch, M. B.; Wirnhier, E.; Martineau, C.; Taulelle, F.; Schnick, W.; Senker, J.; Lotsch, B. V. *Angew. Chem. Int. Ed.* **2013**, *52*, 2435–2439.

(51) Lau, V. W.-h.; Klose, D.; Kasap, H.; Podjaski, F.; Pignié, M.-C.; Reisner, E.; Jeschke, G.; Lotsch, B. V. *Angew. Chem. Int. Ed.* **2017**, *56*, 510–514.

(52) Savateev, A.; Pronkin, S.; Epping, J. D.; Willinger, M. G.; Wolff, C.; Neher, D.; Antonietti, M.; Dontsova, D. *ChemCatChem* **2017**, *9*, 167–174.

(53) Kurpil, B.; Otte, K.; Mishchenko, A.; Lamagni, P.; Lipiński, W.; Lock, N.; Antonietti, M.; Savateev, A. *Nat. Commun.* **2019**, *10*, 945.

(54) Wirnhier, E.; Döblinger, M.; Gunzelmann, D.; Senker, J.; Lotsch, B. V.; Schnick, W. *Chem. – A Eur. J.* **2011**, *17*, 3213–3221.

(55) Lin, L.; Wang, C.; Ren, W.; Ou, H.; Zhang, Y.; Wang, X. *Chem. Sci.* **2017**, *8*, 5506–5511.

(56) Podjaski, F.; Lotsch, B. V. *Adv. Energy Mater.* **2021**, *11*, 2003049.

(57) Teixeira, I. F.; Barbosa, E. C. M.; Tsang, S. C. E.; Camargo, P. H. C. *Chem. Soc. Rev.* **2018**, *47*, 7783–7817.

(58) Im, C.; Kirchhoff, B.; Krivtsov, I.; Mitoraj, D.; Beranek, R.; Jacob, T. *Chem. Mater.* **2023**, *35*, 1547–1556.

(59) Ong, W.-J.; Tan, L.-L.; Ng, Y. H.; Yong, S.-T.; Chai, S.-P. *Chem. Rev.* **2016**, *116*, 7159–7329.

(60) Cao, S.; Low, J.; Yu, J.; Jaroniec, M. *Adv. Mater.* **2015**, *27*, 2150–2176.

(61) Wang, X.; Blechert, S.; Antonietti, M. *ACS Catal.* **2012**, *2*, 1596–1606.

(62) Gouder, A.; Jiménez-Solano, A.; Vargas-Barbosa, N. M.; Podjaski, F.; Lotsch, B. V. *Mater. Horiz.* **2022**, *9*, 1866–1877.

(63) Yuan, T.; Yuan, F.; Li, X.; Li, Y.; Fan, L.; Yang, S. *Chem. Sci.* **2019**, *10*, 9801–9806.

(64) Yang, W.; Godin, R.; Kasap, H.; Moss, B.; Dong, Y.; Hillman, S. A. J.; Steier, L.; Reisner, E.; Durrant, J. R. *J. Am. Chem. Soc.* **2019**, *141*, 11219–11229.

(65) Corp, K. L.; Schlenker, C. W. *J. Am. Chem. Soc.* **2017**, *139*, 7904–7912.

(66) Patra, P. C.; Mohapatra, Y. N. *Appl. Phys. Lett.* **2021**, *118*, 103501.

(67) Li, Y.; Jin, S.; Xu, X.; Wang, H.; Zhang, X. *J. Appl. Phys.* **2020**, *127*, 170903.

(68) Wei, W.; Jacob, T. *Phys. Rev. B* **2013**, *87*, 085202.

(69) Wang, H.; Jin, S.; Zhang, X.; Xie, Y. *Angew. Chem.* **2020**, *132*, 23024–23035.

(70) Zhang, G.; Li, G.; Lan, Z.-A.; Lin, L.; Savateev, A.; Heil, T.; Zafeiratos, S.; Wang, X.; Antonietti, M. *Angew. Chem. Int. Ed.* **2017**, *56*, 13445–13449.

(71) Merschjann, C.; Tyborski, T.; Orthmann, S.; Yang, F.; Schwarzburg, K.; Lublow, M.; Lux-Steiner, M.-C.; Schedel-Niedrig, T. *Phys. Rev. B* **2013**, *87*, 205204.

(72) Re Fiorentin, M.; Risplendi, F.; Palummo, M.; Cicero, G. *ACS Appl. Nano Mater.* **2021**, *4*, 1985–1993.

(73) Wang, H.; Jiang, S.; Chen, S.; Li, D.; Zhang, X.; Shao, W.; Sun, X.; Xie, J.; Zhao, Z.; Zhang, Q.; Tian, Y.; Xie, Y. *Adv. Mater.* **2016**, *28*, 6940–6945.

(74) Jares-Erijman, E. A.; Jovin, T. M. *Nat. Biotechnol.* **2003**, *21*, 1387–1395.

(75) Li, F.; Yue, X.; Zhang, D.; Fan, J.; Xiang, Q. *Appl. Catal. B: Environ.* **2021**, *292*, 120179.

(76) Elbanna, O.; Fujitsuka, M.; Majima, T. *ACS Appl. Mater. Interfaces* **2017**, *9*, 34844–34854.

(77) Rahman, M. Z.; Davey, K.; Mullins, C. B. *Adv. Sci.* **2018**, *5*, 1800820.

(78) Qureshi, M.; Takanabe, K. *Chem. Mater.* **2017**, *29*, 158–167.

(79) Wang, H.; Sun, X.; Li, D.; Zhang, X.; Chen, S.; Shao, W.; Tian, Y.; Xie, Y. *J. Am. Chem. Soc.* **2017**, *139*, 2468–2473.

(80) Xing, W.; Ma, F.; Li, Z.; Wang, A.; Liu, M.; Han, J.; Wu, G.; Tu, W. *J. Mater. Chem. A* **2022**, *10*, 18333–18342.

(81) Merschjann, C.; Tschierlei, S.; Tyborski, T.; Kailasam, K.; Orthmann, S.; Hollmann, D.; Schedel-Niedrig, T.; Thomas, A.; Lochbrunner, S. *Adv. Mater.* **2015**, *27*, 7993–7999.

(82) Noda, Y.; Merschjann, C.; Tarábek, J.; Amsalem, P.; Koch, N.; Bojdys, M. J. *Angew. Chem.* **2019**, *131*, 9494–9498.

(83) Kasap, H.; Caputo, C. A.; Martindale, B. C. M.; Godin, R.; Lau, V. W.-h.; Lotsch, B. V.; Durrant, J. R.; Reisner, E. *J. Am. Chem. Soc.* **2016**, *138*, 9183–9192.

(84) Godin, R.; Wang, Y.; Zwijnenburg, M. A.; Tang, J.; Durrant, J. R. *J. Am. Chem. Soc.* **2017**, *139*, 5216–5224.

(85) Sridhar, V.; Podjaski, F.; Kröger, J.; Jiménez-Solano, A.; Park, B.-W.; Lotsch, B. V.; Sitti, M. *Proc. National Acad. Sci.* **2020**, *117*, 24748–24756.

(86) Sridhar, V.; Podjaski, F.; Alapan, Y.; Kröger, J.; Grunenberg, L.; Kishore, V.; Lotsch, B. V.; Sitti, M. *Sci. Robot.* **2022**, *7*, 62.

(87) Podjaski, F.; Kröger, J.; Lotsch, B. V. *Adv. Mater.* **2018**, *30*, 1705477.

(88) Nightingale, E. R. *J. Phys. Chem.* **1959**, *63*, 1381–1387.

(89) Mähler, J.; Persson, I. *Inorg. Chem.* **2012**, *51*, 425–438.

(90) Ashritha, M.; Hareesh, K. *J. Energy Storage* **2020**, *32*, 101840.

(91) Savateev, A.; Markushyna, Y.; Schüßlbauer, C. M.; Ullrich, T.; Guldi, D. M.; Antonietti, M. *Angew. Chem. Int. Ed.* **2021**, *60*, 7436–7443.

(92) Hartmann, H.; Schläfer, H. L.; Hansen, K. H. *Z. Für Anorg. Allg. Chem.* **1956**, *284*, 153–161.

(93) Koelle, U.; Moser, J.; Graetzel, M. *Inorg. Chem.* **1985**, *24*, 2253–2258.

(94) Schimpf, A. M.; Gunthardt, C. E.; Rinehart, J. D.; Mayer, J. M.; Gamelin, D. R. *J. Am. Chem. Soc.* **2013**, *135*, 16569–16577.

(95) Kröger, J.; Jiménez-Solano, A.; Savasci, G.; Rovó, P.; Moudrakovski, I.; Küster, K.; Schlomberg, H.; Vignolo-González, H. A.; Duppel, V.; Grunenberg, L.; Dayan, C. B.; Sitti, M.; Podjaski, F.; Ochsenfeld, C.; Lotsch, B. V. *Adv. Energy Mater.* **2021**, *11*, 2003016.

(96) Xia, P.; Antonietti, M.; Zhu, B.; Heil, T.; Yu, J.; Cao, S. *Adv. Funct. Mater.* **2019**, *29*, 1900093.

(97) Sun, Y.; Zhang, W.; Xiong, T.; Zhao, Z.; Dong, F.; Wang, R.; Ho, W.-K. *J. Colloid Interface Sci.* **2014**, *418*, 317–323.

(98) Huang, L.; Xu, H.; Li, Y.; Li, H.; Cheng, X.; Xia, J.; Xu, Y.; Cai, G. *Dalton Trans.* **2013**, *42*, 8606.

(99) Hong, S.; Yu, Y.; Yi, Z.; Zhu, H.; Wu, W.; Ma, P. *Nano* **2016**, *11*, 1650121.

(100) Uspal, W. E. *J. Chem. Phys.* **2019**, *150*, 114903.

(101) Ajiboye, T. O.; Kuvarega, A. T.; Onwudiwe, D. C. *Nano-Struct. Nano-Objects* **2020**, *24*, 100577.

(102) Becquerel, A. E. *Rendu Rendus L'academie Sci. Paris* **1839**, *9*, 561.

(103) *Nature* **1873**, *7*, 303–303.

(104) *Proc. R. Soc. Lond.* **1877**, *25*, 113–117.

(105) Marques Lameirinhas, R. A.; Torres, J. P. N.; de Melo Cunha, J. P. *Energies* **2022**, *15*, 1823.

(106) Laboratory, N. R. E. Best Research-Cell Efficiency Chart `https://www.nrel.gov/pv/interactive-cell-efficiency.html` (accessed 04/06/2023).

(107) Einstein, A. *Annalen Der Phys.* **1905**, *322*, 891–921.

(108) Ohl, R. S. (corporation, A.). Light-sensitive electric device, US2402662A, 1941.

(109) Labs, N. B. Bell Labs' Greatest Innovations `https://www.bell-labs.com/about/history/` (accessed 04/06/2023).

(110) Chodos, A. *APS Advancing Physics* **2009**, *18*, 4.

(111) Baechle, S.; Dimroth, F. *Press. Release, Fraunhofer Ise* **May 30, 2022**, 1–3.

(112) Zakutayev, A. *Curr. Opin. Green Sustainable Chem.* **2017**, *4*, 8–15.

(113) Giannouli, M. *Int. J. Photoenergy* **2021**, *2021*, 1–19.

(114) O'Regan, B.; Grätzel, M. *Nature* **1991**, *353*, 737–740.

(115) Shalini, S.; Balasundaraprabhu, R.; Kumar, T. S.; Prabavathy, N.; Senthilarasu, S.; Prasanna, S. *Int. J. Energy Res.* **2016**, *40*, 1303–1320.

(116) Halme, J.; Vahermaa, P.; Miettunen, K.; Lund, P. *Adv. Mater.* **2010**, *22*, E210–E234.

(117) Listorti, A.; O'Regan, B.; Durrant, J. R. *Chem. Mater.* **2011**, *23*, 3381–3399.

(118) O'Regan, B. C.; Durrant, J. R. *Acc. Chem. Res.* **2009**, *42*, 1799–1808.

(119) Masud, N.; Kim, H. K. *ACS Omega* **2023**, 6139–6163.

(120) Zhou, H.; Wu, L.; Gao, Y.; Ma, T. *J. Photochem. Photobiol. A: Chem.* **2011**, *219*, 188–194.

(121) Alhamed, M.; Issa, A. S.; Doubal, A. W. In 2012.

(122) Chang, H.; Wu, H.; Chen, T.; Huang, K.; Jwo, C.; Lo, Y. *J. Alloy. Compd.* **2010**, *495*, 606–610.

(123) Han, L.; Islam, A.; Chen, H.; Malapaka, C.; Chiranjeevi, B.; Zhang, S.; Yang, X.; Yanagida, M. *Energy Environ. Sci.* **2012**, *5*, 6057.

(124) Mathew, S.; Yella, A.; Gao, P.; Humphry-Baker, R.; Curchod, B. F. E.; Ashari-Astani, N.; Tavernelli, I.; Rothlisberger, U.; Nazeeruddin, M. K.; Grätzel, M. *Nat. Chem.* **2014**, *6*, 242–247.

(125) Kang, S. H.; Jeong, M. J.; Eom, Y. K.; Choi, I. T.; Kwon, S. M.; Yoo, Y.; Kim, J.; Kwon, J.; Park, J. H.; Kim, H. K. *Adv. Energy Mater.* **2017**, *7*, 1602117.

(126) Kakiage, K.; Aoyama, Y.; Yano, T.; Oya, K.; Fujisawa, J.-i.; Hanaya, M. *Chem. Commun.* **2015**, *51*, 15894–15897.

(127) Eom, Y. K.; Kang, S. H.; Choi, I. T.; Yoo, Y.; Kim, J.; Kim, H. K. *J. Mater. Chem. A* **2017**, *5*, 2297–2308.

(128) Benesperi, I.; Michaels, H.; Freitag, M. *J. Mater. Chem. C* **2018**, *6*, 11903–11942.

(129) Zhang, W.; Wu, Y.; Bahng, H. W.; Cao, Y.; Yi, C.; Saygili, Y.; Luo, J.; Liu, Y.; Kavan, L.; Moser, J.-E.; Hagfeldt, A.; Tian, H.; Zakeeruddin, S. M.; Zhu, W.-H.; Grätzel, M. *Energy Environ. Sci.* **2018**, *11*, 1779–1787.

(130) Wang, M.; Grätzel, C.; Zakeeruddin, S. M.; Grätzel, M. *Energy Environ. Sci.* **2012**, *5*, 9394.

(131) Wang, Z.-S.; Sayama, K.; Sugihara, H. *J. Phys. Chem. B* **2005**, *109*, 22449–22455.

(132) Rodrigues, R. R.; Peddapuram, A.; Dorris, A. L.; Hammer, N. I.; Delcamp, J. H. *ACS Appl. Energy Mater.* **2019**, *2*, 5547–5556.

(133) Zhang, D.; Stojanovic, M.; Ren, Y.; Cao, Y.; Eickemeyer, F. T.; Socie, E.; Vlachopoulos, N.; Moser, J.-E.; Zakeeruddin, S. M.; Hagfeldt, A.; Grätzel, M. *Nat. Commun.* **2021**, *12*, 1777.

(134) Zhang, Z.; Chen, P.; Murakami, T.; Zakeeruddin, S.; Grätzel, M. *Adv. Funct. Mater.* **2008**, *18*, 341–346.

(135) Wang, M.; Chamberland, N.; Breau, L.; Moser, J.-E.; Humphry-Baker, R.; Marsan, B.; Zakeeruddin, S. M.; Grätzel, M. *Nat. Chem.* **2010**, *2*, 385–389.

(136) Cappel, U. B.; Smeigh, A. L.; Plogmaker, S.; Johansson, E. M. J.; Rensmo, H.; Hammarström, L.; Hagfeldt, A.; Boschloo, G. *J. Phys. Chem. C* **2011**, *115*, 4345–4358.

(137) Zhang, J.; Vlachopoulos, N.; Jouini, M.; Johansson, M. B.; Zhang, X.; Nazeeruddin, M. K.; Boschloo, G.; Johansson, E. M.; Hagfeldt, A. *Nano Energy* **2016**, *19*, 455–470.

(138) Yang, L.; Cappel, U. B.; Unger, E. L.; Karlsson, M.; Karlsson, K. M.; Gabrielsson, E.; Sun, L.; Boschloo, G.; Hagfeldt, A.; Johansson, E. M. J. *Phys. Chem. Chem. Phys.* **2012**, *14*, 779–789.

(139) Snaith, H.; Grätzel, M. *Adv. Mater.* **2007**, *19*, 3643–3647.

(140) Cao, Y.; Saygili, Y.; Ummadisingu, A.; Teuscher, J.; Luo, J.; Pellet, N.; Giordano, F.; Zakeeruddin, S. M.; Moser, J. .-.; Freitag, M.; Hagfeldt, A.; Grätzel, M. *Nat. Commun.* **2017**, *8*, 15390.

(141) Freitag, M.; Giordano, F.; Yang, W.; Pazoki, M.; Hao, Y.; Zietz, B.; Grätzel, M.; Hagfeldt, A.; Boschloo, G. *J. Phys. Chem. C* **2016**, *120*, 9595–9603.

(142) Green, M. A. In 1981.

(143) Peng, B.; Jungmann, G.; Jäger, C.; Haarer, D.; Schmidt, H.-W.; Thelakkat, M. *Coord. Chem. Rev.* **2004**, *248*, 1479–1489.

(144) Yang, X.; Zhao, L.; Wang, S.; Li, J.; Chi, B. *J. Materiomics* **2021**, *7*, 728–741.

(145) Yuan, Z.; Tang, R.; Zhang, Y.; Yin, L. *J. Alloy. Compd.* **2017**, *691*, 983–991.

(146) Qi, K.; Liu, S.-y.; Chen, Y.; Xia, B.; Li, G.-D. *Sol. Energy Mater. Sol. Cells* **2018**, *183*, 193–199.

(147) Wang, G.; Zhang, J.; Kuang, S.; Zhang, W. *Chem. Eur. J.* **2016**, *22*, 11763–11769.

(148) Afshari, M.; Dinari, M.; Momeni, M. M. *Ultrason. Sonochemistry* **2018**, *42*, 631–639.

(149) Queisser, H. J. *Mater. Sci. Eng. B* **2009**, *159-160*, 322–328.

(150) Sampaio, P. G. V.; González, M. O. A. *Int. J. Energy Res.* **2022**, *46*, 17813–17828.

(151) Anrango-Camacho, C.; Pavón-Ipiales, K.; Frontana-Uribe, B. A.; Palma-Cando, A. *Nanomaterials* **2022**, *12*, 443.

(152) He, Y.; Wang, B.; Lüer, L.; Feng, G.; Osvet, A.; Heumüller, T.; Liu, C.; Li, W.; Guldi, D. M.; Li, N.; Brabec, C. J. *Adv. Energy Mater.* **2022**, *12*, 2103406.

(153) Wilken, S.; Sandberg, O. J.; Scheunemann, D.; Österbacka, R. *Sol. Rrl* **2020**, *4*, 1900505.

(154) Clarke, T. M.; Durrant, J. R. *Chem. Rev.* **2010**, *110*, 6736–6767.

(155) Kurpiers, J.; Ferron, T.; Roland, S.; Jakoby, M.; Thiede, T.; Jaiser, F.; Albrecht, S.; Janietz, S.; Collins, B. A.; Howard, I. A.; Neher, D. *Nat. Commun.* **2018**, *9*, 2038.

(156) Seyler, H.; Wong, W. W. H.; Jones, D. J.; Holmes, A. B. *J. Org. Chem.* **2011**, *76*, 3551–3556.

(157) Yu, G.; Gao, J.; Hummelen, J. C.; Wudl, F.; Heeger, A. J. *Science* **1995**, *270*, 1789–1791.

(158) Liu, Y.; Zhao, J.; Li, Z.; Mu, C.; Ma, W.; Hu, H.; Jiang, K.; Lin, H.; Ade, H.; Yan, H. *Nat. Commun.* **2014**, *5*, 5293.

(159) Zhang, G.; Zhao, J.; Chow, P. C. Y.; Jiang, K.; Zhang, J.; Zhu, Z.; Zhang, J.; Huang, F.; Yan, H. *Chem. Rev.* **2018**, *118*, 3447–3507.

(160) Li, C. et al. *Nat. Energy* **2021**, *6*, 605–613.

(161) Song, J.; Zhu, L.; Li, C.; Xu, J.; Wu, H.; Zhang, X.; Zhang, Y.; Tang, Z.; Liu, F.; Sun, Y. *Matter* **2021**, *4*, 2542–2552.

(162) Yu, H. et al. *Adv. Funct. Mater.* **2021**, *31*, 2100791.

(163) Luo, Z. et al. *Adv. Mater.* **2020**, *32*, 2005942.

(164) Xu, X.; Zhang, G.; Li, Y.; Peng, Q. *Chin. Chem. Lett.* **2019**, *30*, 809–825.

(165) Zhao, G.; He, Y.; Li, Y. *Adv. Mater.* **2010**, *22*, 4355–4358.

(166) Chen, J.-D.; Cui, C.; Li, Y.-Q.; Zhou, L.; Ou, Q.-D.; Li, C.; Li, Y.; Tang, J.-X. *Adv. Mater.* **2015**, *27*, 1035–1041.

(167) Zhao, J.; Li, Y.; Yang, G.; Jiang, K.; Lin, H.; Ade, H.; Ma, W.; Yan, H. *Nat. Energy* **2016**, *1*, 15027.

(168) Li, Y.; Huang, W.; Zhao, D.; Wang, L.; Jiao, Z.; Huang, Q.; Wang, P.; Sun, M.; Yuan, G. *Molecules* **2022**, *27*, 1800.

(169) Jin, K.; Xiao, Z.; Ding, L. *J. Semicond.* **2021**, *42*, 010502.

(170) Cui, Y.; Yao, H.; Zhang, J.; Xian, K.; Zhang, T.; Hong, L.; Wang, Y.; Xu, Y.; Ma, K.; An, C.; He, C.; Wei, Z.; Gao, F.; Hou, J. *Adv. Mater.* **2020**, *32*, 1908205.

(171) Firdaus, Y. et al. *Nat. Commun.* **2020**, *11*, 5220.

(172) Proctor, C. M.; Kuik, M.; Nguyen, T.-Q. *Prog. Polym. Sci.* **2013**, *38*, 1941–1960.

(173) Li, Q.; Wang, L.-M.; Liu, S.; Guo, L.; Dong, S.; Ma, G.; Cao, Z.; Zhan, X.; Gu, X.; Zhu, T.; Cai, Y.-P.; Huang, F. *ACS Energy Lett.* **2020**, *5*, 3637–3646.

(174) Hong, L.; Yao, H.; Cui, Y.; Bi, P.; Zhang, T.; Cheng, Y.; Zu, Y.; Qin, J.; Yu, R.; Ge, Z.; Hou, J. *Adv. Mater.* **2021**, *33*, 2103091.

(175) Li, Y.; Lin, Y. *J. Mater. Chem. C* **2021**, *9*, 11715–11721.

(176) Tait, J. G.; Paetzold, U. W.; Cheyns, D.; Turbiez, M.; Heremans, P.; Rand, B. P. *ACS Appl. Mater. Interfaces* **2016**, *8*, 2211–2219.

(177) Mihailetchi, V. D.; Wildeman, J.; Blom, P. W. M. *Phys. Rev. Lett.* **2005**, *94*, 126602.

(178) Rühle, S. *Sol. Energy* **2016**, *130*, 139–147.

(179) Nayak, P. K.; Mahesh, S.; Snaith, H. J.; Cahen, D. *Nat. Rev. Mater.* **2019**, *4*, 269–285.

(180) Keyser, P. T. *J. Near East. Stud.* **1993**, *52*, 81–98.

(181) Whittingham, M. S. *Proc. Ieee* **2012**, *100*, 1518–1534.

(182) Whittingham, M.; Gamble, F. R. *Mater. Res. Bull.* **1975**, *10*, 363–371.

(183) Xie, J.; Lu, Y.-C. *Nat. Commun.* **2020**, *11*, 2499.

(184) Kim, B. K.; Sy, S.; Yu, A.; Zhang, J. *Handb. Clean Energy Syst.* **2015**, 1–25.

(185) Ho, J.; Jow, T.; Boggs, S. *Ieee Electr. Insul. Mag.* **2010**, *26*, 20–25.

(186) Noori, A.; El-Kady, M. F.; Rahmanifar, M. S.; Kaner, R. B.; Mousavi, M. F. *Chem. Soc. Rev.* **2019**, *48*, 1272–1341.

(187) Simon, P.; Gogotsi, Y. *Nat. Mater.* **2008**, *7*, 845–854.

(188) Trasatti, S.; Buzzanca, G. *J. Electroanal. Chem. Interfacial Electrochem.* **1971**, *29*, A1–A5.

(189) Chen, H.; Cong, T. N.; Yang, W.; Tan, C.; Li, Y.; Ding, Y. *Prog. Nat. Sci.* **2009**, *19*, 291–312.

(190) Simon, P.; Gogotsi, Y.; Dunn, B. *Science* **2014**, *343*, 1210–1211.

(191) Chen, G. Z. *Prog. Nat. Sci. Mater. Int.* **2013**, *23*, 245–255.

(192) Jiang, H.; Li, C.; Sun, T.; Ma, J. *Nanoscale* **2012**, *4*, 807–812.

(193) Shen, J.; Yang, C.; Li, X.; Wang, G. *ACS Appl. Mater. Interfaces* **2013**, *5*, 8467–8476.

(194) Fleischmann, S.; Mitchell, J. B.; Wang, R.; Zhan, C.; Jiang, D.-e.; Presser, V.; Augustyn, V. *Chem. Rev.* **2020**, *120*, 6738–6782.

(195) Augustyn, V.; Simon, P.; Dunn, B. *Energy Environ. Sci.* **2014**, *7*, 1597.

(196) Adekoya, G. J.; Sadiku, R. E.; Hamam, Y.; Ray, S. S.; Mwakikunga, B. W.; Folorunso, O.; Adekoya, O. C.; Lolu, O. J.; Biotidara, O. F. In *Fracture and Damage Mechanics: Theory, Simulation and Experiment*, Mallorca, Spain, AIP Publishing: 2020.

(197) Shao, Y.; El-Kady, M. F.; Sun, J.; Li, Y.; Zhang, Q.; Zhu, M.; Wang, H.; Dunn, B.; Kaner, R. B. *Chem. Rev.* **2018**, *118*, 9233–9280.

(198) Stoller, M. D.; Park, S.; Zhu, Y.; An, J.; Ruoff, R. S. *Nano Lett.* **2008**, *8*, 3498–3502.

(199) Velasco, A.; Ryu, Y. K.; Boscá, A.; Ladrón-de-Guevara, A.; Hunt, E.; Zuo, J.; Pedrós, J.; Calle, F.; Martinez, J. *Sustainable Energy Fuels* **2021**, *5*, 1235–1254.

(200) Ji, H.; Zhao, X.; Qiao, Z.; Jung, J.; Zhu, Y.; Lu, Y.; Zhang, L. L.; MacDonald, A. H.; Ruoff, R. S. *Nat. Commun.* **2014**, *5*, 3317.

(201) Largeot, C.; Portet, C.; Chmiola, J.; Taberna, P.-L.; Gogotsi, Y.; Simon, P. *J. Am. Chem. Soc.* **2008**, *130*, 2730–2731.

(202) Zhong, C.; Deng, Y.; Hu, W.; Qiao, J.; Zhang, L.; Zhang, J. *Chem. Soc. Rev.* **2015**, *44*, 7484–7539.

(203) Wang, F.; Xiao, S.; Hou, Y.; Hu, C.; Liu, L.; Wu, Y. *Rsc Adv.* **2013**, *3*, 13059.

(204) Long, J. W.; Bélanger, D.; Brousse, T.; Sugimoto, W.; Sassin, M. B.; Crosnier, O. *MRS Bull.* **2011**, *36*, 513–522.

(205) Yang, X.; Cheng, C.; Wang, Y.; Qiu, L.; Li, D. *Science* **2013**, *341*, 534–537.

(206) Gu, W.; Yushin, G. *Wiley Interdiscip. Rev. Energy Environ.* **2014**, *3*, 424–473.

(207) Sun, L.; Wang, X.; Wang, Y.; Zhang, Q. *Carbon* **2017**, *122*, 462–474.

(208) Choi, W. H.; Choi, M. J.; Bang, J. H. *ACS Appl. Mater. Interfaces* **2015**, *7*, 19370–19381.

(209) Lin, X.-Q.; Wang, W.-D.; Lü, Q.-F.; Jin, Y.-Q.; Lin, Q.; Liu, R. *J. Mater. Sci. Technol.* **2017**, *33*, 1339–1345.

(210) Zhu, Y.; Cheng, S.; Zhou, W.; Jia, J.; Yang, L.; Yao, M.; Wang, M.; Wu, P.; Luo, H.; Liu, M. *ACS Appl. Mater. Interfaces* **2017**, *9*, 13173–13180.

(211) Fleischmann, S.; Zhang, Y.; Wang, X.; Cummings, P. T.; Wu, J.; Simon, P.; Gogotsi, Y.; Presser, V.; Augustyn, V. *Nat. Energy* **2022**, *7*, 222–228.

(212) Choi, C.; Ashby, D. S.; Butts, D. M.; DeBlock, R. H.; Wei, Q.; Lau, J.; Dunn, B. *Nat. Rev. Mater.* **2019**, *5*, 5–19.

(213) Conway, B. E.; Angerstein-Kozlowska, H. *Acc. Chem. Res.* **1981**, *14*, 49–56.

(214) Hadzi-Jordanov, S.; Angerstein-Kozlowska, H.; Vukovič, M.; Conway, B. E. *J. Electrochem. Soc.* **1978**, *125*, 1471–1480.

(215) Galizzioli, D.; Tantardini, F.; Trasatti, S. *J. Appl. Electrochem.* **1974**, *4*, 57–67.

(216) Conway, B. *Electrochimica Acta* **1993**, *38*, 1249–1258.

(217) Brousse, T.; Bélanger, D.; Long, J. W. *J. Electrochem. Soc.* **2015**, *162*, A5185–A5189.

(218) Shin, J.-Y.; Samuelis, D.; Maier, J. *Adv. Funct. Mater.* **2011**, *21*, 3464–3472.

(219) Bryan, A. M.; Santino, L. M.; Lu, Y.; Acharya, S.; D'Arcy, J. M. *Chem. Mater.* **2016**, *28*, 5989–5998.

(220) Gholamian, M.; Sundaram, J.; Contractor, A. Q. *Langmuir* **1987**, *3*, 741–744.

(221) Snook, G. A.; Kao, P.; Best, A. S. *J. Power Sources* **2011**, *196*, 1–12.

(222) Costentin, C.; Savéant, J.-M. *Chem. Sci.* **2019**, *10*, 5656–5666.

(223) Bandaru, P.; Yamada, H.; Narayanan, R.; Hoefer, M. *Mater. Sci. Eng. R: Rep.* **2015**, *96*, 1–69.

(224) Ando, Y.; Okubo, M.; Yamada, A.; Otani, M. *Adv. Funct. Mater.* **2020**, *30*, 2000820.

(225) Hui, J.; Burgess, M.; Zhang, J.; Rodriguez-López, J. *ACS Nano* **2016**, *10*, 4248–4257.

(226) Yan, W.; Kim, J. Y.; Xing, W.; Donavan, K. C.; Ayvazian, T.; Penner, R. M. *Chem. Mater.* **2012**, *24*, 2382–2390.

(227) Li, X.; Wu, G.; Liu, X.; Li, W.; Li, M. *Nano Energy* **2017**, *31*, 1–8.

(228) Kim, H.-S.; Cook, J. B.; Lin, H.; Ko, J. S.; Tolbert, S. H.; Ozolins, V.; Dunn, B. *Nat. Mater.* **2017**, *16*, 454–460.

(229) Liu, C.; Neale, Z. G.; Cao, G. *Mater. Today* **2016**, *19*, 109–123.

(230) Asenbauer, J.; Eisenmann, T.; Kuenzel, M.; Kazzazi, A.; Chen, Z.; Bresser, D. *Sustainable Energy Fuels* **2020**, *4*, 5387–5416.

(231) Manthiram, A. *Nat. Commun.* **2020**, *11*, 1550.

(232) Mong, A. L.; Shi, Q. X.; Jeon, H.; Ye, Y. S.; Xie, X. L.; Kim, D. *Adv. Funct. Mater.* **2021**, *31*, 2008586.

(233) Yurkiv, V.; Sharifi-Asl, S.; Ramasubramanian, A.; Shahbazian-Yassar, R.; Mashayek, F. *Comput. Mater. Sci.* **2017**, *140*, 299–306.

(234) Tran, M.-K.; DaCosta, A.; Mevawalla, A.; Panchal, S.; Fowler, M. *Batteries* **2021**, *7*, 51.

(235) Wu, Z.; Sun, K.; Wang, Z. *Batteries* **2022**, *8*, 246.

(236) Nzereogu, P.; Omah, A.; Ezema, F.; Iwuoha, E.; Nwanya, A. *Appl. Surf. Sci. Adv.* **2022**, *9*, 100233.

(237) Zhang, H.; Yang, Y.; Xu, H.; Wang, L.; Lu, X.; He, X. *InfoMat* **2022**, *4*, e12228.

(238) Nitta, N.; Wu, F.; Lee, J. T.; Yushin, G. *Mater. Today* **2015**, *18*, 252–264.

(239) Schipper, F.; Erickson, E. M.; Erk, C.; Shin, J.-Y.; Chesneau, F. F.; Aurbach, D. *J. Electrochem. Soc.* **2017**, *164*, A6220–A6228.

(240) Wang, Y.; Wang, Y.; Liu, X.; Zhu, B.; Wang, F. *Rsc Adv.* **2017**, *7*, 14354–14359.

(241) Sánchez-Díez, E.; Ventosa, E.; Guarnieri, M.; Trovò, A.; Flox, C.; Marcilla, R.; Soavi, F.; Mazur, P.; Aranzabe, E.; Ferret, R. *J. Power Sources* **2021**, *481*, 228804.

(242) Suryatna, A.; Raya, I.; Thangavelu, L.; Alhachami, F. R.; Kadhim, M. M.; Altimari, U. S.; Mahmoud, Z. H.; Mustafa, Y. F.; Kianfar, E. *J. Chem.* **2022**, *2022*, 1–32.

(243) Zhang, Z.; Shao, Y.; Lotsch, B.; Hu, Y.-S.; Li, H.; Janek, J.; Nazar, L. F.; Nan, C.-W.; Maier, J.; Armand, M.; Chen, L. *Energy Environ. Sci.* **2018**, *11*, 1945–1976.

(244) Lotsch, B. V.; Maier, J. *J. Electroceramics* **2017**, *38*, 128–141.

(245) Chua, L. *Ieee Trans. On Circuit Theory* **1971**, *18*, 507–519.

(246) Strukov, D. B.; Snider, G. S.; Stewart, D. R.; Williams, R. S. *Nature* **2008**, *453*, 80–83.

(247) Van de Burgt, Y.; Melianas, A.; Keene, S. T.; Malliaras, G.; Salleo, A. *Nat. Electron.* **2018**, *1*, 386–397.

(248) Keene, S. T.; Lubrano, C.; Kazemzadeh, S.; Melianas, A.; Tuchman, Y.; Polino, G.; Scognamiglio, P.; Cinà, L.; Salleo, A.; van de Burgt, Y.; Santoro, F. *Nat. Mater.* **2020**, *19*, 969–973.

(249) Sun, K.; Chen, J.; Yan, X. *Adv. Funct. Mater.* **2021**, *31*, 2006773.

(250) Kim, J.; Pershin, Y. V.; Yin, M.; Datta, T.; Di Ventra, M. *Adv. Electron. Mater.* **2020**, *6*, 2000010.

(251) Pershin, Y. V.; Di Ventra, M. *J. Phys. D: Appl. Phys.* **2019**, *52*, 01LT01.

(252) Vongehr, S.; Meng, X. *Sci. Rep.* **2015**, *5*, 11657.

(253) Xiao, Y.; Jiang, B.; Chen, X.; Ke, S.; Jin, Y.; Wen, X.; Ye, C. *Sci. Technol. Adv. Mater.* **2023**, *24*, 2162323.

(254) Shi, T.; Wang, R.; Wu, Z.; Sun, Y.; An, J.; Liu, Q. *Small Struct.* **2021**, *2*, 2000109.

(255) Cho, B.; Song, S.; Ji, Y.; Kim, T.-W.; Lee, T. *Adv. Funct. Mater.* **2011**, *21*, 2806–2829.

(256) Rivnay, J.; Inal, S.; Salleo, A.; Owens, R. M.; Berggren, M.; Malliaras, G. G. *Nat. Rev. Mater.* **2018**, *3*, 17086.

(257) Novembre, C.; Guérin, D.; Lmimouni, K.; Gamrat, C.; Vuillaume, D. *Appl. Phys. Lett.* **2008**, *92*, 103314.

(258) Son, D. I.; You, C. H.; Kim, W. T.; Jung, J. H.; Kim, T. W. *Appl. Phys. Lett.* **2009**, *94*, 132103.

(259) Burr, G. W. et al. *Adv. Phys. X* **2017**, *2*, 89–124.

(260) Sharbati, M. T.; Du, Y.; Torres, J.; Ardolino, N. D.; Yun, M.; Xiong, F. *Adv. Mater.* **2018**, *30*, 1802353.

(261) Wu, X.; Ge, R.; Chen, P.-A.; Chou, H.; Zhang, Z.; Zhang, Y.; Banerjee, S.; Chiang, M.-H.; Lee, J. C.; Akinwande, D. *Adv. Mater.* **2019**, *31*, 1806790.

(262) Gonzalez-Rosillo, J. C.; Balaish, M.; Hood, Z. D.; Nadkarni, N.; Fraggedakis, D.; Kim, K. J.; Mullin, K. M.; Pfenninger, R.; Bazant, M. Z.; Rupp, J. L. M. *Adv. Mater.* **2020**, *32*, 1907465.

(263) Jang, J.; Pan, F.; Braam, K.; Subramanian, V. *Adv. Mater.* **2012**, *24*, 3573–3576.

(264) Wu, Y.; Lee, B.; Wong, H.-S. P. *Ieee Electron Device Lett.* **2010**, *31*, 1449–1451.

(265) Yao, J.; Sun, Z.; Zhong, L.; Natelson, D.; Tour, J. M. *Nano Lett.* **2010**, *10*, 4105–4110.

(266) Wu, S.; Tsuruoka, T.; Terabe, K.; Hasegawa, T.; Hill, J. P.; Ariga, K.; Aono, M. *Adv. Funct. Mater.* **2011**, *21*, 93–99.

(267) Van de Burgt, Y.; Lubberman, E.; Fuller, E. J.; Keene, S. T.; Faria, G. C.; Agarwal, S.; Marinella, M. J.; Alec Talin, A.; Salleo, A. *Nat. Mater.* **2017**, *16*, 414–418.

(268) Kong, L.-a.; Sun, J.; Qian, C.; Fu, Y.; Wang, J.; Yang, J.; Gao, Y. *Org. Electron.* **2017**, *47*, 126–132.

(269) Leydecker, T.; Herder, M.; Pavlica, E.; Bratina, G.; Hecht, S.; Orgiu, E.; Samorì, P. *Nat. Nanotechnol.* **2016**, *11*, 769–775.

(270) Tondelier, D.; Lmimouni, K.; Vuillaume, D.; Fery, C.; Haas, G. *Appl. Phys. Lett.* **2004**, *85*, 5763–5765.

(271) Gao, H. J.; Sohlberg, K.; Xue, Z. Q.; Chen, H. Y.; Hou, S. M.; Ma, L. P.; Fang, X. W.; Pang, S. J.; Pennycook, S. J. *Phys. Rev. Lett.* **2000**, *84*, 1780–1783.

(272) Naber, R. C. G.; Asadi, K.; Blom, P. W. M.; de Leeuw, D. M.; de Boer, B. *Adv. Mater.* **2010**, *22*, 933–945.

2

Fundamentals & Methods

The second chapter underlines fundamental methods to develop and investigate energy conversion and storage technologies by means of electrochemical studies.

Contents

2.1. Fundamentals of the Photovoltaic Effect 82
2.1.1. Carrier Dynamics in Semiconductors 82
2.1.2. P-N Junctions 84
2.2. Fundamentals of Electrochemistry 87
2.2.1. The Electrochemical Cell 88
2.2.2. Interfacial Electron Transfer 91
2.2.3. Mass Transport and Diffusion Layers 94
2.3. Electrochemical Characterization Techniques 96
2.3.1. Voltammetry 96
2.3.1.1. Voltammetry of Solar Cells. 99
2.3.1.2. Voltammetry of Energy Storage Devices. 100
2.3.1.3. Voltammetry of Information Storage Devices. 103
2.3.2. Chrono Methods 104
2.3.2.1. Galvanostatic Charging and Discharging (GCD) in Energy Storage Devices. 104
2.3.3. Electrochemical Response of Devices 107
2.4. References 109

2.1. Fundamentals of the Photovoltaic Effect

Solar irradiation occurs *via* electromagnetic waves, which are described by their wavelengths λ, frequency ν, and phase ϕ. While long wavelength electromagnetic radiation (*e.g.*, radio waves or microwaves) are typically termed waves, short wavelength electromagnetic radiation (*e.g.*, infrared or visible wavelength) are often described as photons. The latter behaves as a particle (or wavelet) with a certain discrete energy associated with its wavelength ($E = \frac{hc}{\lambda}$). Both definitions – waves and particles – are valid, thus underlining the wave-particle duality principle of electromagnetic radiation described by fundamental quantum mechanics.[1]

2.1.1. Carrier Dynamics in Semiconductors

To understand the interaction between photons and matter, we first describe the fundamental principle of light absorption in crystalline silicon (Si) as an exemplary semiconductor. Crystalline Si in its intrinsic, undoped form is composed of a diamond cubic crystal lattice structure. The electrons are located in continuous energy bands, which form from the discrete energy levels of the Si atoms. The levels are broadened by atomic interactions as shown in Figure 2.1 (a). The energetically highest occupied energy band is termed VB, the lowest unoccupied energy level is called CB. The energy difference between VB and CB is called bandgap E_b.[2] Intrinsic implies that the amount of free electrons and holes (*e.g.*, generated by external dopants, see below) is much smaller than the thermally generated electrons and holes.[3] The amount of free electrons n per volume in the conduction band can be calculated as follows:

$$n = \int_{E_1}^{E_2} N_c(E) \cdot f(E) dE \tag{2.1}$$

where $N_c(E)$ gives the density of state of electrons at a specific energy E, $f(E)$ gives the Fermi-Dirac distribution of occupation probability for respective states, and the conduction band stretches from an energy E_1 to E_2. In metals, the Fermi level describes the highest occupied energy level. It separates occupied from unoccupied levels. In a semiconductor, the Fermi level falls into the gap between CB and VB. It is a hypothetical energy level, which gives the highest energy of any electron when the semiconductor is in its ground state (Figure 2.1 (a), dashed line).[4] In an intrinsic semiconductor, it is located in the middle between VB and CB at any given

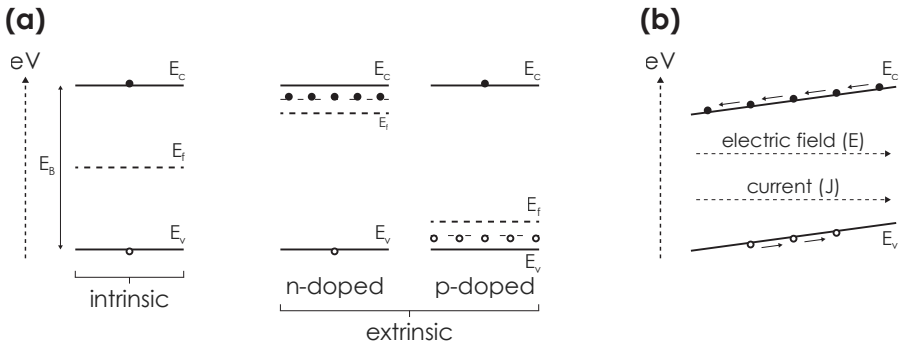

Figure 2.1. Fundamental semiconductor properties. (a) Band schemes of both intrinsic (*i.e.*, undoped) and extrinsic (either n-doped or p-doped) semiconductors, showing the energy of the VB E_v, CB E_c, Fermi level E_f, and bandgap E_b. Electrons are marked with black circles, holes with white circles. **(b)** Drift of electrons and holes alongside an electric field.

temperature. Thus, we can calculate the occupation density n also *via* the Fermi level energy:

$$n = N_c \cdot exp\left(\left(-\frac{E_c - E_f}{kT}\right)\right) \tag{2.2}$$

where E_c and E_f gives the respective energy level of CB and Fermi level, k is the Boltzmann constant, and T the temperature. Extrinsic semiconductors on the other hand imply that electrons and holes generated by impurities are not negligible and govern the charge dynamics. For Si this can either occur *via* doping with group III atoms such as boron (B), or group V elements such as phosphorous (P). The former has one electron less than Si (p-doping), the latter has an additional electron (n-doping). For P, the additional electron is bound very loosely with Si and ionizes at room temperature, effectively creating a delocalized electron close to the CB – P becomes an electron donor. Due to the larger n, electrons are the majority carrier and E_f increases accordingly. The donor concentration N_d can be linked directly to the increase in E_f:

$$E_c - E_f = kT \cdot ln\left(\frac{N_c}{N_d}\right) \tag{2.3}$$

Doping with B works analogous: The vacant electron produces a positively charge hole close to the VB which can easily ionize neighboring Si atoms and thus, is mobile.[3] B becomes an electron acceptor and holes are the majority carrier. Due to the reduced n, E_f decreases. The concentration of acceptor N_a is linked to E_f as

follows:

$$E_f - E_v = kT \cdot ln\left(\frac{N_v}{N_a}\right) \tag{2.4}$$

where E_v gives the energy of VB and N_v gives the density of states of holes. A scheme of the concept is shown in Figure 2.1.

CARRIER TRANSPORT. In any case, the only mobile species in the semiconductor are delocalized majority charge carriers: electrons for n-doped or holes for p-doped semiconductors. Main driving forces for their random movement are Brownian motion and thermal energy, the latter producing a thermal velocity of 2×10^5 m s^{-1} at room temperature.[2] The main inhibiting force of this movement is scattering of the charge carriers by the lattice atoms, causing parts of the motion energy to be transferred to the lattice atoms in form of phonons (*i.e.*, lattice vibrations). However, upon applying an external electric field E, the carrier motion becomes oriented along the field gradient (see Figure 2.1 (b)) and a drift current develops. Note that electrons and holes drift into opposite directions due to the respective coulombic forces.[3] The electron current density J_n is given by:

$$J_n = nq\mu_n E \tag{2.5}$$

where q is the elementary charge (1.6×10^{-19} C) and μ_n is the electron mobility. The hole current density J_p can be calculated analogously. Since the charge carriers experience repulsive coulombic forces between each other and an isotropic conduction is affected by diffusion according to Fick's law with a respective diffusion coefficient (D_n for electrons), the overall electron current density is defined as follows:

$$J_n = nq\mu_n E + qD_n\frac{dn}{dx} \tag{2.6}$$

where $\frac{dn}{dx}$ gives the spatial change of electron concentration. The overall current density is the sum of electron and hole current densities:

$$J = J_n + J_p \tag{2.7}$$

2.1.2. P-N Junctions

A p-n junction develops, when a n-doped and p-doped semiconductor are brought into contact. In case of crystalline Si, this would occur *e.g.*, *via* Si with P doping and Si with B doping as discussed above (see Figure 2.3 (b)). The Fermi levels align, as

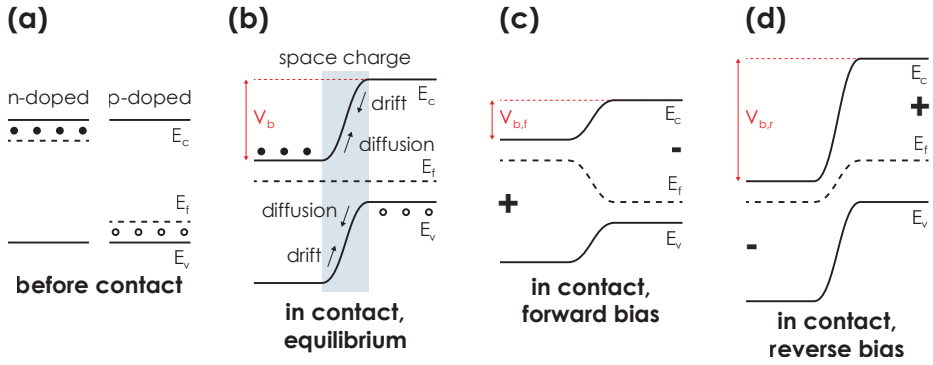

Figure 2.2. Developing p-n junction. (a) A p-n junction develops by contacting a n-doped (electron majority carriers, black circles) with a p-doped (hole majority carriers, white circles) semiconductor. The VB, CB, and Fermi level are termed E_v, E_c, and E_f, respectively. **(b)** Upon contacting, the Fermi levels align *via* charge carrier diffusion and drift – both are opposing forces and at equilibrium cancel each other out. The contact region becomes depleted of charge carriers and is called space charge region. A built-in potential V_b develops. **(c)** and **(d)** When a bias is applied, the junction voltage is modified. In case of connecting the positive and negative terminals to the n-doped and p-doped side, respectively, the mode is termed forward bias, and *vice versa*.

visualized in Figure 2.2 (a) and (b). Two forces are at play: (1) The charge carrier concentration gradients cause carrier diffusion – electrons diffuse from n-doped to the p-doped side, holes diffuse in the reverse direction. (2) As a consequence of this diffusion, a potential gradient develops between n and p side, with the n-side being positively charged (electron depletion) whilst the p-side is negatively charged (Figure 2.2 (b)). The potential gradient between VB and CB of n-doped and p-doped semiconductor produce carrier drifting. Both forces are described with Equation 2.6 and upon reaching equilibrium in the junction, they cancel each other out. A carrier depletion zone develops at the junction due to the carrier diffusion, which is positively charged at the n-doped side due to electron depletion, and negatively charged at the p-doped side due to hole depletion. This region is termed space charge region (Figure 2.2 (b), gray box). Note that compared to before contacting, VB and CB of n-doped and p-doped semiconductors change their relative band positions as a result of Fermi level aligning. A built-in potential V_b develops, which is a function of acceptor and donor doping concentration and the amount of intrinsic charge carriers n_i:

$$V_b = \frac{kT}{q} \cdot \ln\left(\frac{N_a N_d}{n_i^2}\right) \tag{2.8}$$

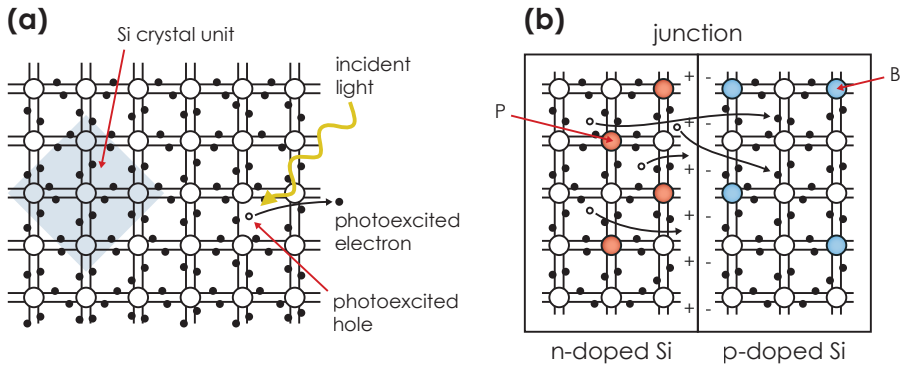

Figure 2.3. Illumination of a crystalline Si semiconductor. (a). A crystalline semiconductor is illuminated with light of a sufficiently small wavelength to excite an electron from VB into the CB, creating a photoexcited electron in the process. The remaining electron vacancy is termed photoexcited hole. Both electron and hole are delocalized. The Si crystal unit cell is indicated with the blue box. **(b)** Formation of a p-n-junction *via* contacting n-doped and p-doped Si. The former is doped with P (indicated with orange circles), the latter is doped with B (indicated with purple circles). Electrons diffuse to the p-doped side, thus charging the n-doped side slightly positive. When diffusion force equals drift force, the junction is at equilibrium. Both (a) and (b) are reprinted with permission from the National Renewable Energy Laboratory, https://www.nrel.gov/docs/legosti/old/16319.pdf, accessed April 17, 2023.[5]

Upon applying an external bias potential to the junction, V_b is modified as illustrated in Figure 2.2 (c) and (d): When the positive terminal is connected to the n-doped side and the negative terminal is connected to the p-doped side, the junction potential decreases and the depletion zone fills with charge carriers, and *vice versa*.

Photoexcitation of the semiconductor. Upon light irradiation with a sufficiently high photon energy, an electron can get excited from the VB to an excited state and thermalizes into the CB – a process termed photoexcitation. The process is illustrated in Figure 2.3 (a) for crystalline Si. Note that the electrons and holes experience attractive coulombic interactions between each other. Thus, they are not totally free, but tend to form electron-hole pairs (excitons). The amount of electron-hole pair formation is proportional to the incident light intensity. In the space charge region, electrons drift towards the n-doped side, holes drift towards the p-doped side. The potential V_b of the junction is sufficient to overcome attractive coulombic interaction in the electron-hole pair, which as a result splits apart. Photoexcited electron diffusion in a crystalline Si p-n junction is visualized in Figure 2.3 (b). The drift of photoexcited charge carriers produces the photocurrent. We discuss how to calculate and measure performance parameters next.

2.2. Fundamentals of Electrochemistry

We will continue by giving an introduction into the dynamic electrochemistry. Note that formulas and explanations in the following are extracted from textbooks by A. C. Fisher[6] as well as A. J. Bard and L. R. Faulkner,[7] except of when referenced otherwise. We can define several key factors governing the electrochemical response, *i.e.*, kinetics of the charge transfer process:[6]

- Electrode potential
- Mass transport between electrode and reactant (*e.g.*, solution)
- Reactivity of reactants
- Nature of the surface of the electrode
- Structure of the interfacial region between electrode and reactant

EQUILIBRIUM ELECTROCHEMISTRY. Let us consider an electrode with a respective electrode potential ϕ_m, which is in contact with an electrolyte containing a redox active species with a solution potential ϕ_s (for instance, $Fe^{2+}_{(aq)} \rightleftharpoons Fe^{3+}_{(aq)} + e^-$). The potential difference between ϕ_m and ϕ_s produces a potential difference $\phi_{m/s}$ at the electrode-solution interface (Figure 2.4):

$$\Delta\phi_{m/s} = \phi_m - \phi_s \tag{2.9}$$

As long as the potential difference is not equal to zero and sufficient to drive an electron transfer reaction, the system will strive to achieve equilibrium. Reaction rate depends on the ratio between thermodynamic reagent activity of oxidized and reduced species (α_{ox} and α_{red}), which is proportional to the ratio between concentrations $[ox]$ and $[red]$. Upon achieving chemical equilibrium, the reaction rate is termed equilibrium constant K:

$$K = \frac{\alpha_{ox}}{\alpha_{red}} = \frac{[ox]}{[red]} \tag{2.10}$$

To understand the impact of this concentration difference on $\Delta\phi_{m/s}$, we need to briefly mention the difference of *Gibbs* free energy ΔG in a reaction, which can be defined *via* the sum of stoichiometric coefficients ν and α of all products and reac-

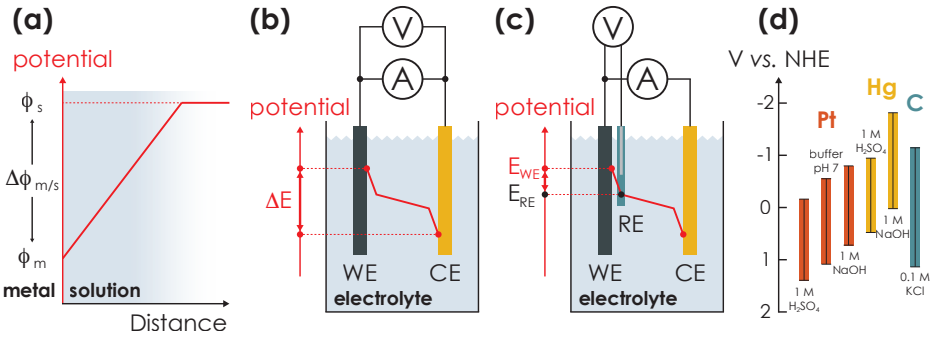

Figure 2.4. Fundamental concepts of electrochemistry. (a) Schematic diagram showing the potential drop at a metal-solution junction with O and R being an oxidized and reduced species, respectively. **(b-c)** Electrochemical measurement setups and the potential drop between respective electrodes (red line). Two-electrode setup (b) requires Working Electrode (WE) and Counter Electrode (CE), Three-electrode setup (c) requires in addition a Reference Electrode (RE). **(d)** ESW of aqueous electrolytes with different electrodes (platinum Pt, mercury Hg, carbon C) and at different pH values. Adapted with permission.[8] Copyright 2008, Wiley-VCH.

tants, or *via* cell potential change $\phi_{m/s}$ as a function of transferred electrons z:

$$\Delta G = \Delta G^0 + RT \cdot \ln(K) \tag{2.11}$$

$$\Delta G = -zF\Delta E \tag{2.12}$$

where ΔG^0 is the standard *Gibbs* energy, R gives the molar gas constant, T the absolute temperature, and F is the Faraday constant. Utilizing Equation 2.11 and Equation 2.12, we can define the *Nernst* equation:

$$\Delta\phi_{m/s} = \Delta\phi^0 + \frac{RT}{zF} \cdot \ln(K) \tag{2.13}$$

In simple words, this equation relates the concentration of oxidized and reduced species to the interfacial potential difference. While this potential difference is a well-defined metric, in real-world experiments it can be quite difficult to measure, leading electrochemists to develop an electrochemical cell.

2.2.1. The Electrochemical Cell

Measuring the potential difference $\phi_{m/s}$ is challenging, since it requires a complete conducting circuit and the potential drop needs to be referenced against a second electrode with a well-defined potential. The most straight-forward cell setup would

be to add a second electrode (*e.g.*, Au, Pt, carbon, or mercury electrodes) and measure potential as well as apply a current between both electrodes. Such a setup is termed *Two-electrode setup* and shown in Figure 2.4 (b). The electrode which contains the sample is termed WE and the electrode to which the potential is applied is called counter electrode (CE). The overall potential ΔE results from the potential decrease at junctions to WE and CE as well as within the electrolyte – the latter occurring as a result of the limited conductivity of electrolytes. It becomes evident however that it is challenging to separate individual contributions of the overall potential difference, especially $\Delta\phi_{m/s}$. Therefore, electrochemists developed a different measurement setup consisting of a third RE that we show in Figure 2.4 (c). Potential is measured between WE and RE, current is applied between WE and CE. Typically, a RE is chosen with a well-defined potential E_{RE}. This not only allows to measure only $\Delta\phi_{m/s}$, but also to reference this potential against the electrochemical scale or vacuum potential scale. The electrochemical scale utilizes the water reduction reaction under standard conditions (pressure H_2 = 1 bar, pH = 0, $\alpha(H^+)$ = 1) as reference point. The WE electrode potential is thus:

$$E_{WE} = \Delta\phi_{m/s} - E_{RE} \tag{2.14}$$

Several key reference electrodes are given in Table 2.1. With this, Equation 2.10, and Equation 2.13, we can give the *Nernst* equation in its more well-known form:

$$E_{WE} = E^{\theta} + \frac{RT}{zF} \cdot \ln\left(\frac{[ox]}{[red]}\right) \tag{2.15}$$

where E^{θ} gives the standard potential of the investigated redox couple, measured under standard conditions defined above.

Electrolyte electrochemical stability window. Let us conclude this section by briefly discussing ESW. In general, every electrolyte can be oxidized and reduced at a certain potential (in case of water, the difference between thermodynamic oxidation and reduction potential is $1.23\,V$[10]). From a thermodynamic point of view, investigations of electrodes can thus only be performed within this inert potential range to prevent decomposition of the electrode – a limit which in case of batteries, capacitors, or solar cells limits their cell voltage. In case of aqueous electrolytes, the pH must be considered, since both water reduction (HER: $2\,H^+ + 2\,e^- \longrightarrow H_2$) and oxidation (OER: $H_2O \longrightarrow \frac{1}{2}\,O_2 + 2\,H^+ + 2\,e^-$) reactions incorpo-

rate protons as a reactant. Using Equation 2.15, we can calculate the pH dependence of HER and OER potentials in an aqueous electrolyte (respective E_{HER} and E_{OER} potentials):[10]

$$E_{HER} = E^{\theta}_{HER} + 2.303 \cdot \frac{RT}{F}(14 - \text{pH}) \tag{2.16}$$

$$E_{OER} = E^{\theta}_{OER} - 2.303 \cdot \frac{RT}{F}(\text{pH}) \tag{2.17}$$

where E^{θ}_{HER} and E^{θ}_{OER} are respective standard potentials. Note that when adding ions to water, anions can play a vital role in producing a H-bond network *via* anion hydration shells, which can widen the ESW window.[10] Cations (*e.g.*, Li) can accept lone-pair electrons of the O atoms, which lowers the HOMO level of water and in return raises the oxidation potential.[11]

From a kinetic perspective, the oxidation and reduction process at the solid-liquid interface of the electrode govern respective reactions, which in return can widen the ESW window. For instance, the formation of an EDL (see Section 1.4.2) of water containing ions can influence the water content at the interface. Passivation layers can form from the produced gases (*e.g.*, for Li anodes in aqueous batteries, Solid Electrolyte Interface (SEI) formation can occur from dissolved O_2 and CO_2, producing Li_2CO_3 and Li_2O on the anode.[12]). Overpotentials for respective reduction and oxidation reactions can also widen the ESW. We show several ESWs for aqueous electrolytes for electrodes with a low overpotential for HER and OER (Pt) and large overpotential for HER (Hg) in Figure 2.4 (d).

Table 2.1. Standard potential for different reference electrodes. Potentials are measured at standard conditions (pressure H_2 = 1 bar, pH = 0, $\alpha(H^+)$ = 1).

Redox couple, electrolyte	Potential (V *vs.* NHE)	Reference
Hg/HgO, 1 M NaOH	0.140	[9]
Ag/AgCl, saturated KCl	0.197	[7]
Hg/Hg_2Cl_2, saturated NaCl	0.236	[7]
Ag/AgCl, 0.1 M KCl	0.288	[9]
Hg/Hg_2SO_4, saturated K_2SO_4	0.64	[7]
Ag/Ag_2SO_4, 0.1 M K_2SO_4	0.72	[7]

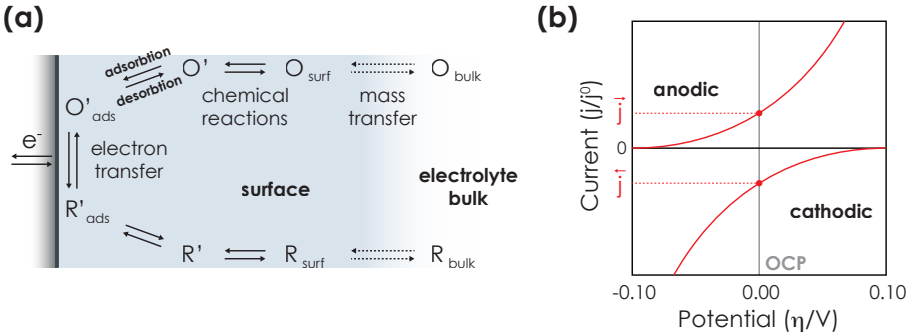

Figure 2.5. Interfacial reactions. (a) Schematic diagram showing the individual steps during an electrode reaction. Adapted with permission.[7] Copyright 2022, Wiley-VCH. **(b)** Scheme showing anodic and cathodic currents at the equilibrium potential η.

2.2.2. Interfacial Electron Transfer

There are several distinct steps involved to perform a reaction of a species in the electrolyte on the surface of an electrode, which can all govern the kinetics of the reaction that in return results in the size of the current response. We show the different steps in Figure 2.5 (a). A reactant (*e.g.*, in case of a reduction reaction an oxidizable species O_{bulk}) diffuses from the bulk electrolyte solution to the surface (O_{surf}) – a process governed by mass transport. Subsequent chemical reactions can precede the adsorption, *e.g.*, homogeneous processes (protonation or dimerization) or heterogeneous processes (catalytic decomposition) (O'). The reactant then adsorbs (O'_{ads}) and the redox reaction can occur, accompanied by an electron transfer ($O'_{ads} \rightleftharpoons R'_{ads} + e^-$, with O'_{ads} and R'_{ads} being the oxidized and reduced adsorbed species). Analogous to the reactant, the product desorbs (R'), can undergo chemical reactions at the surface (R_{surf}) and diffuses into the bulk electrolyte (R_{bulk}). The electrochemical response is dominated by the *rate determining step* (*i.e.*, the slowest step). In case where the transport of molecules to and from the surface is limiting, the reaction is called *mass transport limited*. When mass transport is fast, but electron transfer is rate determining, one talks about *electron transfer limited* reactions.

The measured current i reflects the reaction rate and can be expressed as a product of number of transferred electrons z and reaction rate $k[C_{surf}]$, with k being the rate constant and $[C_{surf}]$ giving the concentration of reactants at the surface:

$$i = k[C_{surf}] \cdot zF \tag{2.18}$$

We can define a current for the oxidizing $\overrightarrow{i}$ and the reducing $\overleftarrow{i}$ reaction. At equilibrium potential η, the currents of the oxidizing and reducing reactions are equal and termed *exchange current density* i^0. Note that this potential develops when electrodes are immersed into an electrochemical cell and without applying any potential. Hence, it is also termed OCP. We show this concept in a scheme in Figure 2.5 (b). With this, we can define current densities of both reactions:

$$\overrightarrow{i} = zF\overrightarrow{k} \cdot [C_{ox}] \tag{2.19}$$

$$\overleftarrow{i} = zF\overleftarrow{k} \cdot [C_{red}] \tag{2.20}$$

TRANSITION STATE THEORY. The rate constants from both forward and backward reactions result from the activation energy *via* the *Arrhenius* equation:

$$\overrightarrow{k} = A \cdot \exp\left(-\frac{\overrightarrow{E_a}}{RT}\right) \tag{2.21}$$

$$\overleftarrow{k} = A \cdot \exp\left(-\frac{\overleftarrow{E_a}}{RT}\right) \tag{2.22}$$

where A is the pre-exponential factor, and $\overrightarrow{E_a}$ and $\overleftarrow{E_a}$ give the activation energy for oxidation and reduction reactions, respectively. We show this concept in Figure 2.6 (a). Reactants and products are separated by a transition state of higher free energy that first must be overcome. Note that the activation energy can also be described with the *enthalpy of activation* $\Delta H^{\ddagger}$ and since *entropy of activation* is a dimensionless constant, upon modifying the pre-exponential factor ($A = A' \cdot \exp\left(\frac{\Delta S^{\ddagger}}{RT}\right)$) we can express Equation 2.21 or Equation 2.22 with the *Gibbs free energy* (keeping in mind that enthalpy and Gibbs free energy are related *via* $\Delta G = \Delta H - T \cdot \Delta S$) as follows: $k = A' \cdot \exp\left(-\frac{\Delta G^{\ddagger}}{RT}\right)$.

Let us now consider what effect an applied potential has on the transition state. We will consider the simplest redox reaction of an oxidized (O) and reduced (R) species ($O + e^- \rightleftharpoons R^-$) and show the respective free energy profile in Figure 2.6 (b). The black curves show the initial state at E^0, that is, no potential is applied. The required free energy for reduction $\Delta G_r^{\ddagger 0}$ and oxidation $\Delta G_o^{\ddagger 0}$ (defined as the difference of free energy of a reactant and related product species after undergoing the respective reaction) are governed by the transition state energy (Figure 2.6 (a)). When applying a potential E that facilitates oxidation (Figure 2.6 (b), red line), the

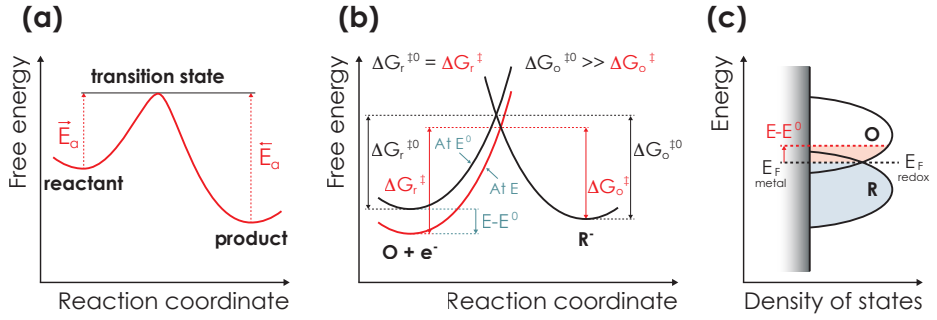

Figure 2.6. Effect of applied potential. (a) Change of free energy during the reaction. Reactant and product are separated by a transition state with largest free energy. Activation energies E_a given with dashed lines. **(b)** Effect of an applied potential E on free energy profiles (red). While the required free energies for reduction ($\Delta G_r^{\ddagger}$ and $\Delta G_r^{\ddagger 0}$ for applied and no applied potential, respectively) remain constant, the required free energy for oxidation $\Delta G_o^{\ddagger}$ gets smaller in comparison to when no potential is applied ($\Delta G_r^{\ddagger 0}$). Both (a) and (b) are adapted with permission.[7] Copyright 2022, Wiley-VCH. **(c)** Effect of an applied potential, when looking at the Density Of States (DOS) instead of free energy profiles.

free energy profile of the oxidized state gets shifted to lower free energy values, thus causing an intersection with the reductive state profile at lower free energies (*i.e.*, transition state is at lower energies). Hence, the required free energy of oxidation (or barrier of oxidation) $\Delta G_o^{\ddagger}$ is reduced.

We will conclude by applying this effect to the influence on the Fermi level of a redox couple, in analogy to the carrier dynamics that we have discussed for semiconductors in Section 2.1.1. A redox couple in solution shows two distinct density of state areas – one for the reduction and one for the oxidation – which results from the distribution of energies of the redox couple species in a solution (Figure 2.6 (c)). The redox potential $E_{F,\,redox}$ results from the middle of the density of state distributions and reactions between the oxidized and reduced species occur in the area of overlap. If an electrode comes into contact with the solution and no external current is applied, both $E_{F,\,redox}$ and the Fermi level of the electrode (in case of a metal electrode: $E_{F,\,metal}$) align at the OCP. If a potential is applied that modifies $E_{F,\,metal}$ to larger energies (Figure 2.6 (c), red), the area of the DOS in the oxidation region increases. This increases the reduction rate, decreases oxidation rate, and produces a negative current, and *vice versa*.

2.2.3. Mass Transport and Diffusion Layers

Let us continue with an introduction into mass transport and its effect on a diffusion layer that occurs in any electrochemical device which requires mobile species. Three principal mechanisms occur:

- **Diffusion** describes the movement of molecules along a concentration gradient from a higher to a lower concentration area. We will discuss it in more detail in the following.
- **Migration** occurs, when a charged species B is transported along an external electric field. The migration flux j_m along the electric field $\frac{\mathrm{d}\phi}{\mathrm{d}x}$ is proportional to the electric field and ionic mobility μ, which is a function of the concentration of the species $\mu[B]$:[6]
$$j_m \propto -\mu[B]\frac{\partial\phi}{\partial x} \tag{2.23}$$
Experimental means to reduce the effects of migration (that are difficult to control) are typically to add an ionic *background electrolyte* in high concentrations of typically >0.1 M, which is inert to the reaction and can screen the developing electric field to maintain electroneutrality.
- **Convection** is the transport of species *via* hydrodynamic transport. One generally differentiates between two types of convection: Natural convection occurs due to thermal gradients or density gradients and is present in any solution. It is undesirable since it is difficult to predict. Forced convection results from the experimental setup, *i.e.*, stirring, gas bubbling, pumping, etc. Forced convection can have a controllable quantitative hydrodynamic behavior, which can sometimes be used to reduce the effects of natural convection (*e.g.*, stirring in an electrocatalysis reaction).

As a rule of thumb, in a normal electrochemical experiment one tries to minimize effects of migration and convection, since they are more difficult to control. Diffusion occurs according to *Fick's* diffusion laws. *Fick's* first law of diffusion quantifies the movement of a species in a concentration gradient under diffusion control. The flux of the species j can be described as follows:

$$j = \frac{i}{zFa} = -D_B\frac{\partial[B]}{\partial x} \tag{2.24}$$

where $i/_{zFa}$ gives the Faradaic flux that relates current i to the flux (z, F, and a

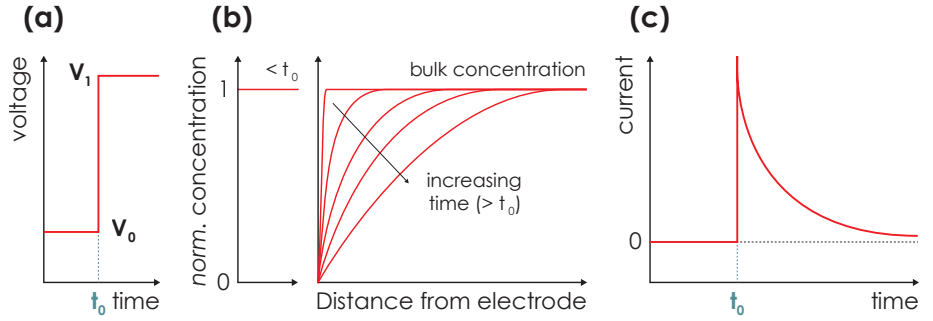

Figure 2.7. Impact of diffusion on an electrochemical reaction. (a) Let us consider a voltage step (from V_0 to V_1) initiating a reaction of a species B in an electrolyte at time t_0. **(b)** Prior to t_0 (left), the normalized concentration of B on top the electrode surface is 1. Post t_0 (right), the concentration decreases rapidly at the electrode surface and slower in the bulk. **(c)** The current response shows a spike at t_0, which subsequently decays according to Equation 2.26.

give the amount of transferred electrons, Faraday constant, and surface area of the flux, respectively), D_B is the diffusion coefficient, and $[B]$ is the concentration of the species under diffusion control. Using the mass continuity equation, *Fick's* second law can be calculated from Equation 2.24, which relates change of surface concentration $[B]$ as a function of time:

$$\frac{\partial[B]}{\partial t} = D_B \left(\frac{\partial^2[B]}{\partial x^2} \right) \tag{2.25}$$

Using Equation 2.18 and Equation 2.25 we can calculate the *Cottrell* equation, which relates the current i of a reaction to D_B at a certain time t:[13]

$$i = \frac{zFa[B]\sqrt{D_B}}{\sqrt{\pi}\sqrt{t}} \tag{2.26}$$

Let us now look at the impact of these effects on the concentration gradient above a planar electrode surface and the respective impact on current. Let us consider a planar electrode immersed in an electrolyte with a respective redox active species B. An oxidation or reduction reaction is initiated by applying a potential at a time t_0 (Figure 2.7 (a): increase potential from V_0 to V_1). Prior to starting the reaction, the concentration of B is constant (Figure 2.7 (b), left). When the reaction is started, the concentration on top of the electrode rapidly decays to zero, whereas the concentration in the bulk close to the electrode surface is still very high (Figure 2.7 (b), right, short times). With continuing reaction time, the concentration at larger distances

to the electrode is getting smaller (Figure 2.7 (b), right, long times). Concentration decay over time is described by Equation 2.24. The thickness l of the diffusion layer results from the diffusion coefficient ($l = \sqrt{\pi D_B t}$)

The current response is shown in Figure 2.7 (c). Upon applying V_1 at t_0, a current spike occurs, which subsequently rapidly decays. This decay occurs, since the concentration of B at the electrode surface rapidly decays as discussed in the previous paragraph. Note that the decaying current is proportional to the inverse square root of time ($i \propto {}^1/\sqrt{t}$) and can be calculated *via* Equation 2.26. In fact, this measurement can be used to calculate the diffusion coefficient of B in the electrolyte by linearizing Equation 2.26 in a ${}^1/i^2$ *vs.* t plot:

$$\frac{1}{i^2} = \frac{\pi}{z^2 F^2 a^2 [B]^2 \cdot D_B} \cdot t \tag{2.27}$$

2.3. Electrochemical Characterization Techniques

In the following, we will give an introduction into electrochemical measurement methods. We will start with a general introduction and then continue to describe specific characterization techniques for different devices. Note that we will only focus on DC techniques, since the majority of Part IV relies heavily on these techniques. In general, one differentiates between *potentiometric* and *galvanostatic* techniques. The former uses an applied potential to control the measurement and observes current, the latter applies a current and observes the resulting potential.

2.3.1. Voltammetry

Scanning voltammetry works by scanning a potential between two vertex potentials E_1 and E_2. Since potential is controlled, this technique is potentiometric. Two main modes are typically performed: LSV scans the potential into one direction (Figure 2.8 (a): from A to C). CV cycles the potential both forwards and subsequently backwards (Figure 2.8 (a): from A to C to E).[14] This results in a graph, where current response is measured at different potentials. Let us consider a CV measurement of a reversible reaction and a sufficiently high rate constant k so that the measured behavior is dominated by planar diffusion. The resulting CV graph is shown in Figure 2.8 (b). In case of a positive or negative current, an oxidation or reduction reaction occurs. We show the diffusion layer *via* concentration as a function of distance to the electrode surface in Figure 2.8 (c). When sweeping from E_1 to E_2 (oxidizing

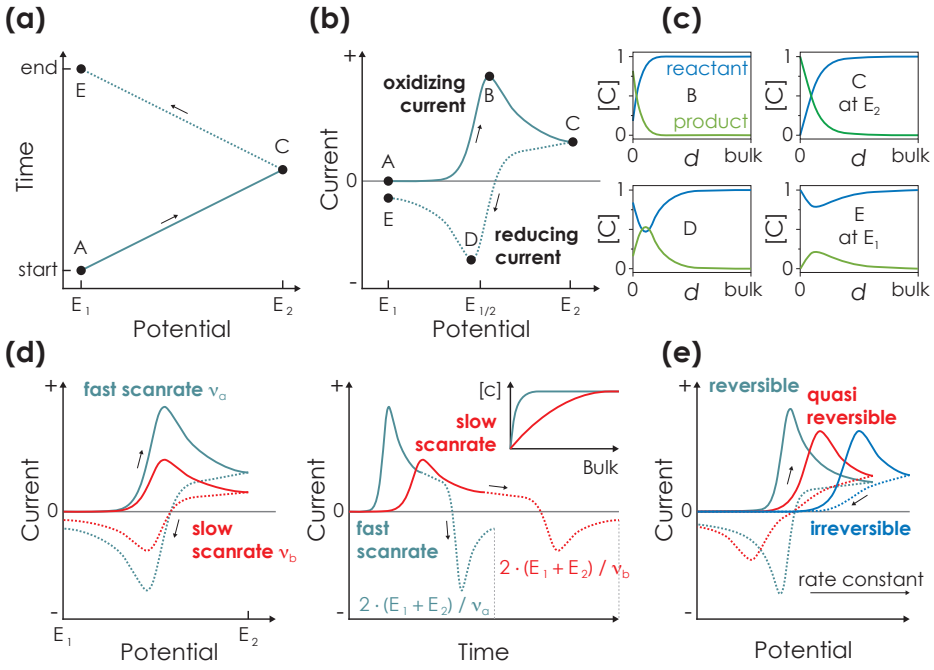

Figure 2.8. Concept of scanning voltammetry measurements. (a) In a scanning voltammetry measurement, current is cycled between two potentials E_1 and E_2 – in case of a Linear Scanning Voltammetry (LSV) measurement only into one direction (solid line), in case of a Cyclic Voltammetry (CV) measurement in both directions (solid and dashed line). **(b)** The resulting CV measurement shows both oxidizing and reducing currents. **(c)** Resulting diffusion layers (blue line for reactant, green line for product) at different points during the measurement shown in (a) and (b). Adapted according to the open access ACS Authors Choice license.[14] Copyright 2018, American Chemical Society. **(d)** Influence of different scan rates on the CV measurement. Smaller scan rates cause a longer measurement time, which in return reduces current response due to the thicker diffusion layer. Adapted with permission.[15] Copyright 2021, American Chemical Society **(e)** Scheme showing different types of reversible CV measurements, which is governed by the rate constant. Adapted from J. Lee.[16]

current direction), the current increases and reaches a maximum (Figure 2.8 (b) and (c): B). At this point, the concentration of reactant at the surface has reached zero and subsequent current is mass transport limited, as explained in the previous section. The current decrease saturates, and the diffusion layer develops (Figure 2.8 (b) and (c): C). When reversing the scan direction, similarly the reduction current maximizes – the point where the concentration of original reactant species at the surface has reached 100 % again (Figure 2.8 (b) and (c): D). The current subsequently decreases, while the remainder of the product species reacts back to the

original reactant (Figure 2.8 (b) and (c): E). Note that the redox potential $E_{1/2}$ can be calculated from the middle of both peak potentials (Figure 2.8 (b): B and D).

Note that kinetics significantly govern the current response of the measurement (Figure 2.8 (d)), controllable *via* the scan rate ν (measured in $^{\mathrm{mV}}/_{\mathrm{s}}$). If for instance an electrode is cycled very fast (*i.e.*, with a large scan rate), the diffusion layer will be much thinner as the measurement time will be shorter (see Figure 2.7 (b)). At the same time, unreacted reactant at the surface will experience a larger potential and hence, more driving force for the reaction. This results in a larger peak current response. The peak current i_p for a species B in dependence of ν and concentration $[B]$ can be calculated *via* the *Randles-Sevčik* equation:[17]

$$i_p = (2.69 \times 10^5) z^{\frac{3}{2}} a \sqrt{D_B \nu} \cdot [B] \tag{2.28}$$

where ν is the scan rate and all other variables are defined as in Section 2.2.3. Note that this formula is empirical and only really works for simple redox events. In case of quasi-reversible or irreversible reactions (*i.e.*, oxidation and reduction reaction have different electron transfer rate constants k; see Figure 2.8 (e)), this equation does not describe peak currents accurately. The current dependence on scan rate can be expressed with:[18]

$$i = n \cdot \nu^m \tag{2.29}$$

where i gives the current and both n and m are adjustable parameters. We will

Table 2.2. Calculating metrics from CV measurements. Summary of formulas to extract key performance metrics from CV measurements.

Description	Unit	Formula	Label
Capacity of charging	A h	$Q_{ch} = \int I_{ch} dt$	(2.30)
Capacity of discharging	A h	$Q_{dch} = \int I_{dch}\, \mathrm{d}t$	(2.31)
Energy density of discharging	W h	$E_{dch} = \int I_{dch} \cdot t_{dch}\, \mathrm{d}U_{dch}$	(2.32)
Power density at a potential E	W	$P = I \cdot E$	(2.33)
Coulombic efficiency	%	$CE = \frac{Q_{dch}}{Q_{ch}} \cdot 100$	(2.34)

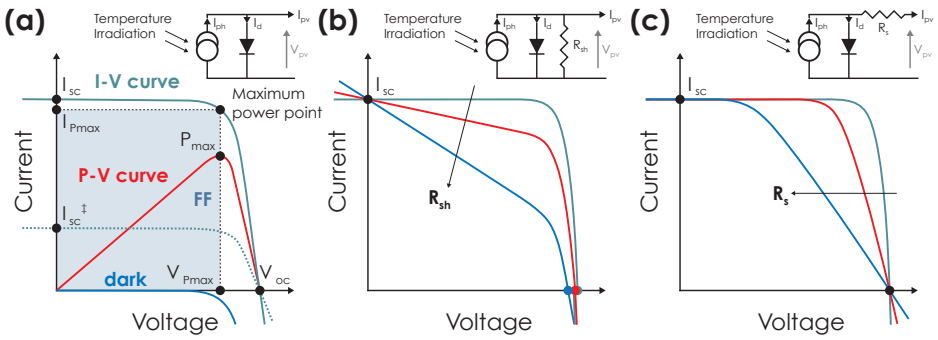

Figure 2.9. LSV measurements (IV curves) in solar cells. (a) Schematic IV (green) and PV (red) curves from a solar cell, with respective voltage and current parameters. The diode curve in the dark is shown in blue. The electric circuit of the respective devices in (a-c) is shown at the top, with respective currents (current generated from light absorption I_{ph}, diode current I_d, resulting photocurrent I_{pv}), resistances (shunt resistance R_{sh} and series resistance R_s), and resulting device voltage V_{pv}. Adapted according to the open access CC BY license.[19] Copyright 2021, MDPI. **(b-c)** Schemes of shunt (b) and series resistance (c) affecting the IV curves. Respective electric circuits are shown on top. Adapted from.[20]

discuss them more in Section 2.3.2. Several different metrics can be extracted from the measurement. The charge and discharge capacity Q_{ch} and Q_{dch} results from integrating the current response. The Coulombic efficiency CE is the ratio between Q_{dch} and Q_{ch}. The energy results from integrating the charge response (current over time) over voltage. Power output depends on the current at the respective voltage. Note that energy and power can only be calculated in two-electrode setups and not in three-electrode setups (Section 2.2.1), since the latter calculates potential against a RE with a modifiable potential and not against a specific CE. Key formulas are summarized in Table 2.2.

2.3.1.1. Voltammetry of Solar Cells. A typical metric to characterize solar cells are current-voltage curves under illumination (IV-curves), which are measured by performing a LSV measurement in Two-electrode configuration of the device under illumination. The LSV is typically started at $0\,\mathrm{V}$ and scanned to larger voltages until the current reaches zero. We show such a measurement in Figure 2.9 (a) (green solid line). One can extract several key performance metrics: Short circuit current I_{sc} is the maximum achievable photocurrent, which occurs at a photovoltage of $0\,\mathrm{V}$. The maximum photovoltage on the other hand is termed OCP V_{oc} and occurs at a photocurrent of $0\,\mathrm{A}$, *i.e.*, no photocurrent is extracted from the solar cell. Power results from both maximum photocurrent and photovoltage ($P = U \cdot I$).

This occurs at a specific *maximum power point*, which results from the peak of the power *vs.* voltage curve P_{max} (Figure 2.9 (a), red line). In a theoretically ideal solar cell, this occurs at J_{sc} and V_{oc} – however, in reality several losses cause a deviation from the ideal behavior and maximum power occurs at slightly lower I_{Pmax} and V_{Pmax}. A metric to compare ideality of a solar cell is the *FF*, which results from:

$$FF = \frac{V_{Pmax} \cdot I_{Pmax}}{V_{oc} \cdot I_{sc}} \tag{2.35}$$

If $FF = 1$, the device operates as an ideal solar cell. Si-solar cells reach *FF* values of around 0.8, organic solar cells achieve about 0.6 to 0.8.[21,22] With smaller light intensities, the photocurrent decreases (Figure 2.9 (a) (green dashed line)). If operated in the dark, one can observe the diode curve (Figure 2.9 (a), blue line), which results from the p-n-junction becoming conductive at a certain bias voltage (Section 2.1.2).[19] The electric circuit of the solar cell is shown in Figure 2.9 (a), top.

Resistive losses can occur either in parallel (shunt resistance R_{sh}, Figure 2.9 (b)) or in series to the solar cell (series resistance R_s, Figure 2.9 (c)). Both alter the shape of the IV-curve significantly and reduce *FF* and photocurrent of the device I_{pv} according to the following implicit function:[20]

$$I_{pv} = I_{ph} - I_0 \cdot \exp\left(\frac{q(V_{pv} + I_{pv}R_s)}{nkT}\right) - \frac{V_{pv}}{R_{sh}} \tag{2.36}$$

where I_{pv} is the photocurrent, I_{ph} is the light generated current (*i.e.*, I_{pv} without losses), V_{pv} is the photovoltage, q is the elemental charge, n is the ideality factor, k is the Boltzmann constant, and T is the temperature at which the device is being operated at.

2.3.1.2. VOLTAMMETRY OF ENERGY STORAGE DEVICES. Voltammetry is a key technique to analyze energy storage devices – typically CV measurements are performed to measure both charging and discharging. Similar to solar cells, the shape of the voltammetry measurement can tell a lot about the type of energy storage as well as its performance. We show scan rate dependent CVs of a capacitor, pseudocapacitor, and battery in Figure 2.10 (a-c).

Let us start by discussing the shape of the capacitor (Figure 2.10 (a)). Capacitors store energy *via* capacitance F (Section 1.4.2), that is, increase of charge with voltage (C V^{-1}). When cycling with a specific scan rate ν (mV s^{-1}), the resulting current response is linearly dependent on ν ($i = \nu \cdot F$), but independent of voltage. We can

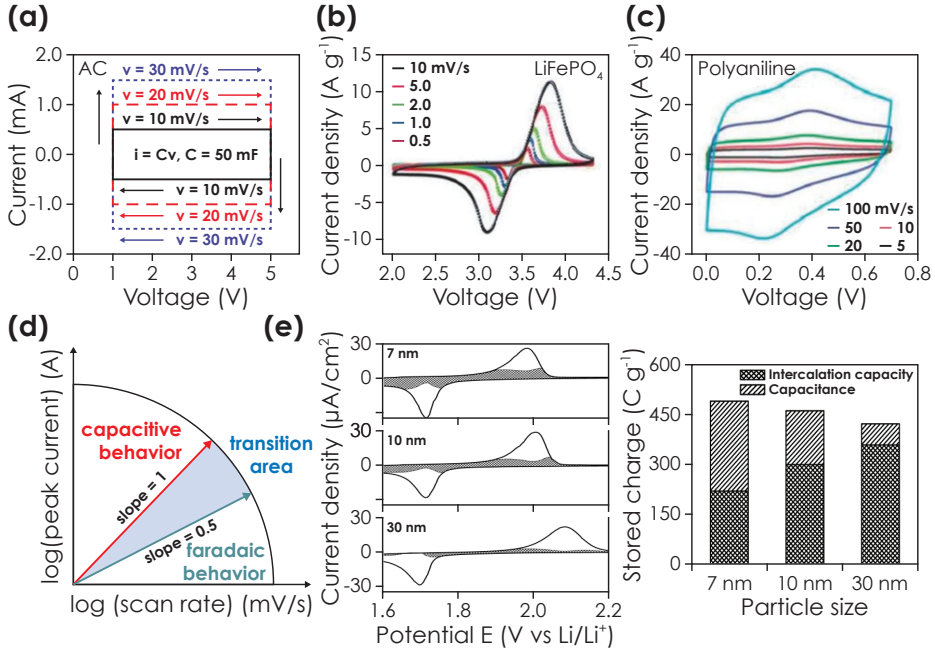

Figure 2.10. CV measurements in energy storage devices. (a) Exemplary CV shape of a capacitor from a carbon-based supercapacitor, measured with different scan rates. Reproduced with permission[24] Copyright 2013, Elsevier Ltd. **(b)** Exemplary CV shape of a battery at different scan rates, based on a Li-ion battery which uses a LFP cathode. Reproduced with permission.[25] Copyright 2015, Royal Society of Chemistry. **(c)** Exemplary CV shape of the pseudocapacitive material PANI, measured with different scan rates. Reproduced with permission.[26] Copyright 2013, Royal Society of Chemistry. **(d)** Interpretation of the exponential factor m of Equation 2.29. Reproduced according to the open access CC BY 4.0 license.[18] Copyright 2018, Wiley-VCH. **(e)** Calculation of capacitive and faradaic contributions of a CV measurement of anatase TiO_2 at different particle sizes. Reproduced with permission.[27] Copyright 2007, American Chemical Society.

write Equation 2.29 in its linear form:[23]

$$i = k_{cap} \cdot \nu^1 \tag{2.37}$$

where k_{cap} describes the kinetics of the capacitor. If a constant ν occurs throughout the entire measurement, the resulting shape of the CV measurement is rectangular and scales with ν.

Batteries on the other hand possess a faradaic energy storage mechanism, which occurs at a material-specific redox potential (Section 1.4.4). Hence, charging and discharging is not potential independent. The resulting CV shape (Figure 2.10 (b)) shows distinct oxidation and reduction peaks. Since the charge storage process is

faradaic and accompanied by ion (de)intercalation, it is diffusion limited. As evident from Equation 2.28, the current at the peaks scales with the root of the scan rate:[23]

$$i = k_{farad} \cdot \nu^{0.5} \tag{2.38}$$

The most ambiguous case is pseudocapacitance. Here, faradaic charge storage occurs in a non or minimal-diffusion limited mechanism and thus is very fast (Section 1.4.3). This results in a system, which has an electrochemical signature like a capacitor, but stores charges like a battery. The resulting CV shape looks rectangular, but also shows redox peaks (Figure 2.10 (c)). There are several different approaches to model the current-scan rate dependence. One can for instance utilize the exponent of Equation 2.37 and Equation 2.38 as a variable and a measure of "how" diffusion limited the mechanism is:[18]

$$i = k_{total} \cdot \nu^{m} \tag{2.39}$$

Plotting this equation in its linearized form ($\log(i) = \log(k_{total}) + \log(\nu) \cdot m$) allows to extract m, as shown in Figure 2.10 (d). A slope below ≤ 0.5 indicates diffusion-controlled behavior, a slope ~ 1 suggests a capacitive behavior, and everything in-between may be explained with a mixed diffusion-controlled/capacitive response, *e.g.*, due to pseudocapacitance.[18] A more advanced approach proposes to fit both capacitive and faradaic contributions at the same time *via* a linear combination of Equation 2.37 and Equation 2.38:[28,29]

$$i = k_1 \cdot \nu^1 + k_2 \cdot \nu^{0.5} \tag{2.40}$$

A quantitative relationship can be extracted *via* the multiplication factors k_1 and k_2. In fact, this analysis can be performed not only at the peak potential, but at every single potential step throughout the CV measurement. This allows to observe respective capacitive and faradaic contributions of the current. An example of such an analysis was performed by B. Dunn *et. al.* for energy storage in anatase TiO_2 for different particle sizes.[27] The resulting analysis is shown in Figure 2.10 (e). The authors could elucidate the capacitive effect on the nanoscale, which became increasingly important for smaller particle sizes. This not only led to larger capacities for smaller particles, but also faster charging/discharging due to the faster kinetics of capacitive processes compared to faradaic processes.

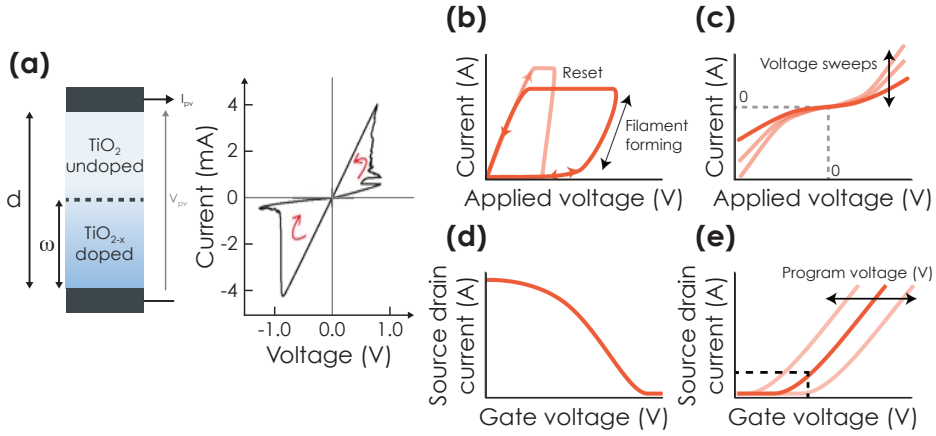

Figure 2.11. CV measurements in memristors and resistance switching devices. (a) Electric circuit of the first prototypical memristor (left; reproduced from Figure 1.17 (a)) and CV measurement of the first memristor, unveiling the typical pinched hysteresis loop (right). Adapted with permission.[30] Copyright 2008, Springer Nature. **(b-e)** CV curves of respective resistance switching devices that are shown in Figure 1.17 (b-e). Adapted with permission.[31] Copyright 2018, Springer Nature.

2.3.1.3. Voltammetry of Information Storage Devices. While research of energy storage devices presents a main application field for CV measurements, it is by far not the only one. We will briefly discuss investigations of novel memristive and resistance switching devices in the following. The typical CV memristor curve is shown in Figure 2.11 (a). Let us discuss the shape in the following. Forward and backward sweeps have distinctly different slopes, which results from the different resistances depending on the voltage/current history (see Section 1.5 for an explanation of the working principle of the memristor). Note that the slope of the forward and backward sweep reflects the resistance (as such, if the device would be a resistor, forward and backward slopes would be the same). The relationship between time-dependent current $i(t)$ and voltage $V(t)$ can be expressed as follows:[32]

$$i(t) = \begin{cases} a_1 x(t) \sinh(bV(t)), & \text{if } V(t) > 0 \\ a_2 x(t) \sinh(bV(t)), & \text{if } V(t) < 0 \end{cases} \tag{2.41}$$

where $x(t)$ is the state variable that accounts for the sizes of more conductive doped and less conductive undoped layers. The non-linear phenomenon is modeled with the variables a_1 and a_2 (magnitude parameters, which model the size of polarization input voltage), and b (control parameter, which reflects the dopant density that

is responsible for the increase in the conductivity of the doped layer). The mathematical function sinh models the pinched hysteresis loop.

Different resistive switching devices can have multiple different CV shapes (Figure 2.11 (b)).[31] Voltage-dependent interface modification (Figure 1.17 (b)) requires larger potentials at which the filament is forming (Figure 2.11 (b), dark red), and upon contact a larger current resets the filament (Figure 2.11 (b), bright red). Redox-based switching (Figure 1.17 (c)) modifies conductance of a polymer due to redox reactions, thus changing the conductivity of the polymer film (Figure 2.11 (c), dark red *vs.* bright red). This reflects in an approximately linear resistance curve with larger slope – as discussed above for memristors. Organic electrochemical redox-based switching (Figure 1.17 (d)) applies a voltage at the gate, which drives ions from the electrolyte into a polymer film (Figure 2.11 (d), dark red), thus changing its conductivity. Charge-trapping based switching in a conductive polymer containing nanoparticles acting as nanoscale capacitors consists of two steps. A certain potential at the gate (Figure 2.11 (e), dark red) is required to produce a current between source and drain. In the first step (programming), applying a potential at the gate drives mobile charge carriers (*e.g.*, holes) of the polymer onto nanoparticles immersed within the polymer (Figure 1.17 (e)), thus charging the nanoscale capacitors. This modifies the conductivity of the film, which can be subsequently read out in the second step by measuring the modified gate voltage that is required to generate the current response between source and drain (Figure 2.11 (e), bright red).

2.3.2. Chrono Methods

Chrono methods involve applying either a potential (*chrono-potentiometry*) or current (*chrono-amperometry*) over a set time and observing respective current or potential response. Note that for energy storage devices the latter is often referred to by GCD.

In case of a chrono potentiometry, the current response can be calculated *via* Equation 2.26. In case of chrono amperometry, the response significantly depends on the sample that is being investigated. We will discuss the response for energy storage devices in the next section. Key performance metrics are given in Table 2.3.

2.3.2.1. GCD IN ENERGY STORAGE DEVICES. The GCD response depends on which type of charge storage device is being used, *i.e.*, capacitor, battery, or pseudocapac-

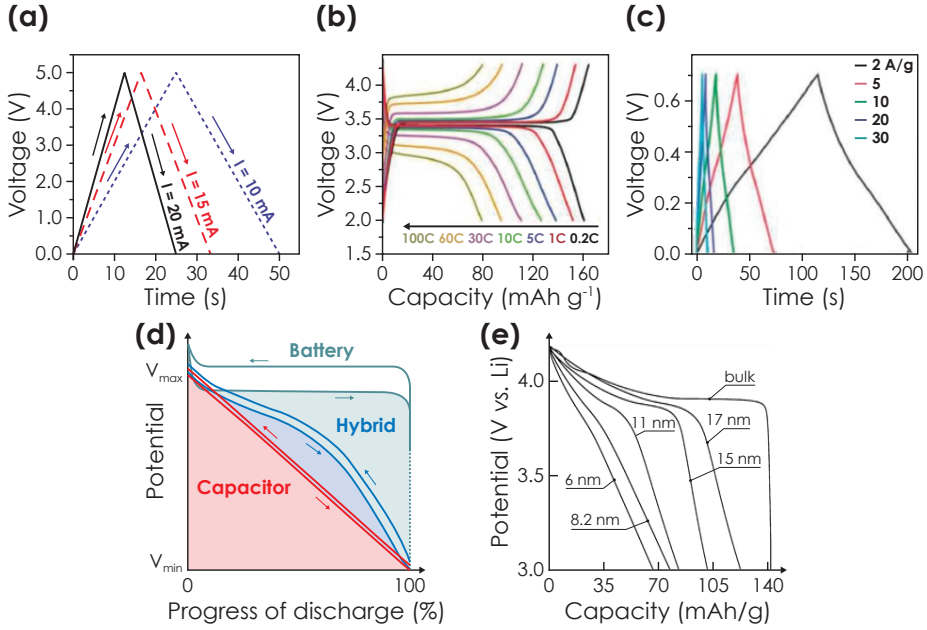

Figure 2.12. GCD measurements in energy storage devices. (a) Exemplary GCD shape of a capacitor from a carbon-based supercapacitor at different currents (same device as Figure 2.10 (a)). Reproduced with permission.[24] Copyright 2013, Elsevier Ltd. **(b)** Exemplary GCD shape of a Li-ion battery with LFP cathode at different currents (same device as Figure 2.10 (b)). Reproduced with permission.[25] Copyright 2015, Royal Society of Chemistry. **(c)** Exemplary GCD shape of pseudocapacitive PANI at different currents (same device as Figure 2.10 (c)). Reproduced with permission.[26] Copyright 2013, Royal Society of Chemistry. **(d)** Summary of shapes of GCD measurements. Adapted with permission.[23] Copyright 2019, Royal Society of Chemistry. **(e)** GCD discharging response of a LCO cathode with different particle sizes. Large particles show a battery response, very small particles show a capacitive response. Reproduced with permission.[33] Copyright 2007, American Chemical Society

itor. As discussed in Section 2.3.1.2, the electrochemical response of a capacitor is governed by its capacitance F ($\mathrm{C\,V^{-1}}$). Hence, upon applying a constant current over time, the resulting charge Q increases linearly, which causes a linear increase in voltage. An exemplary GCD plot for (dis)charging of a carbon-based supercapacitor is shown in Figure 2.12 (a), unveiling the typical triangular shape. The resulting slope is governed by the size of current i and capacitance F. The voltage V_{cap} can be expressed with:

$$V_{cap}(i) = \frac{i}{F} \cdot t = \frac{Q}{F} \tag{2.48}$$

Energy output can be calculated as described in Table 2.3. However, since the slope is linear, integration is facile and yields a linear relationship between energy and

charge ($E_{cap} = \frac{1}{2}QV$).
Batteries on the other hand operate distinctly different. Since charge storage occurs at defined redox potentials (Section 1.4.4), the potential response during charging and discharging remains approximately constant until the battery is charged or discharged, respectively. The potential subsequently sharply increases or decreases. We show GCD charging and discharging profiles of an exemplary device for different currents in Figure 2.12 (b). The voltage is hence equal to the redox potential of the electrode. For an ideal battery, as a consequence of the rectangular shape energy output can be expressed with $E_{farad} = QV$.

Pseudocapacitors show a mixed behavior between the triangular capacitive shape and the square battery shape. We show an exemplary GCD measurement in Figure 2.12 (c) and summarize the different GCD shapes in Figure 2.12 (d). Energy can be expressed with $E_{pseud} = n \cdot QV$, where $0 < n < 1$. Note that the amount of pseudocapacitive response can depend on the particle morphology, which may inhibit or facilitate fast surface diffusion effects (as explained in Section 1.4.3). I. Honma *et. al.* underlined this effect by studying particle size dependent electrochemical response of nanosized LCO cathodes in Li-ion batteries.[33] The GCD discharging curves in dependence of particle size are shown in Figure 2.12 (e). It becomes evident that with smaller particles sizes <15 nm, the response deviates from a faradaic battery-

Table 2.3. Calculating metrics from chrono-amperometry measurements. Summary of formulas to extract key performance metrics from chrono-amperometry measurements.

Description	Unit	Formula	Label
Capacity of charging	A h	$Q_{ch} = \Delta q_{ch} = \int I_{ch} dt$	(2.42)
Capacity of discharging	A h	$Q_{dch} = \Delta q_{dch} = \int I_{dch}\, \mathrm{d}t$	(2.43)
Energy density of discharging	W h	$E_{dch} = \int V_{dch}\, \mathrm{d}q_{dch}$	(2.44)
Average power density of discharging	W	$P_{dch} = \frac{E_{dch}}{t_{dch}}$	(2.45)
Coulombic efficiency	%	$CE = \frac{Q_{dch}}{Q_{ch}} \cdot 100$	(2.46)
Round-trip efficiency	%	$RT = \frac{E_{dch}}{E_{ch}} \cdot 100$	(2.47)

type behavior to a more pseudocapacitive behavior (for very small particles of ca. <8.2 nm the GCD looks capacitive). The authors concluded that very small particle sizes increase the charging/discharging kinetics, albeit at a significantly reduced capacity (approx. 120 mA h g^{-1} for 30 nm *vs.* 30 mA h g^{-1} for 5 nm).

2.3.3. Electrochemical Response of Devices

Let us conclude our introduction into electrochemistry by discussing how the electrochemical signature of full-cell energy storage devices relates to the signature of half-cells. We term an experiment as "half-cell", when only anode or cathode are measured individually against a reference electrode in a three-electrode setup. The respective measurements are discussed in Section 2.3.1.2 and Section 2.3.2.1 and shown in Figure 2.13 (a-c) for batteries, capacitors, and hybrid devices. Hybrid devices use both faradaic (*i.e.*, battery-type) and capacitive (*i.e.*, capacitor-type) electrodes in one device to combine advantages of both device types.

The voltage operation range of the battery device results from the redox potentials of the respective half-cells. Charging or discharging occurs, when the voltage difference (V_{ch} or V_{dch}, respectively) is greater than the half-cell peak onset potential (Figure 2.13 (a)). The operation range is in general governed by the width of redox peaks, and too large voltages beyond the peaks (V_{max}) result in a sharp increase of measured voltage (see Figure 2.12 (b)). Discharging is completed, when the voltage is smaller than peak potential onsets of half-cells (V_{min}), resulting in a sharp voltage drop. For capacitors, since charge storage occurs voltage-independent there is not a defined charging or discharging voltage.

We define full-cell measurements as when anode is measured against cathode in a two-electrode configuration. The electrochemical response thus results from overlaying responses of anode and cathode. For batteries and capacitors, the shape can be linked intuitively to half-cell measurements, *i.e.*, batteries show a large charging and discharging peak separated from 0 V by respective V_{ch} and V_{dch} (Figure 2.13 (d)) and capacitors produce a rectangular shape with a voltage width resulting from adding both half-cell potentials (Figure 2.13 (e)). Hybrid devices show a more complex shape, since the response is mixed faradaic (from the battery-type electrode) and capacitive (from the capacitor-type electrode) (Figure 2.13 (f)). While the shape of the measurement looks pseudocapacitive, one should not confuse it with three-electrode pseudocapacitor measurements (as discussed in Section 1.4.3), since the charge storage mechanism of individual electrodes is not that of a pseudocapac-

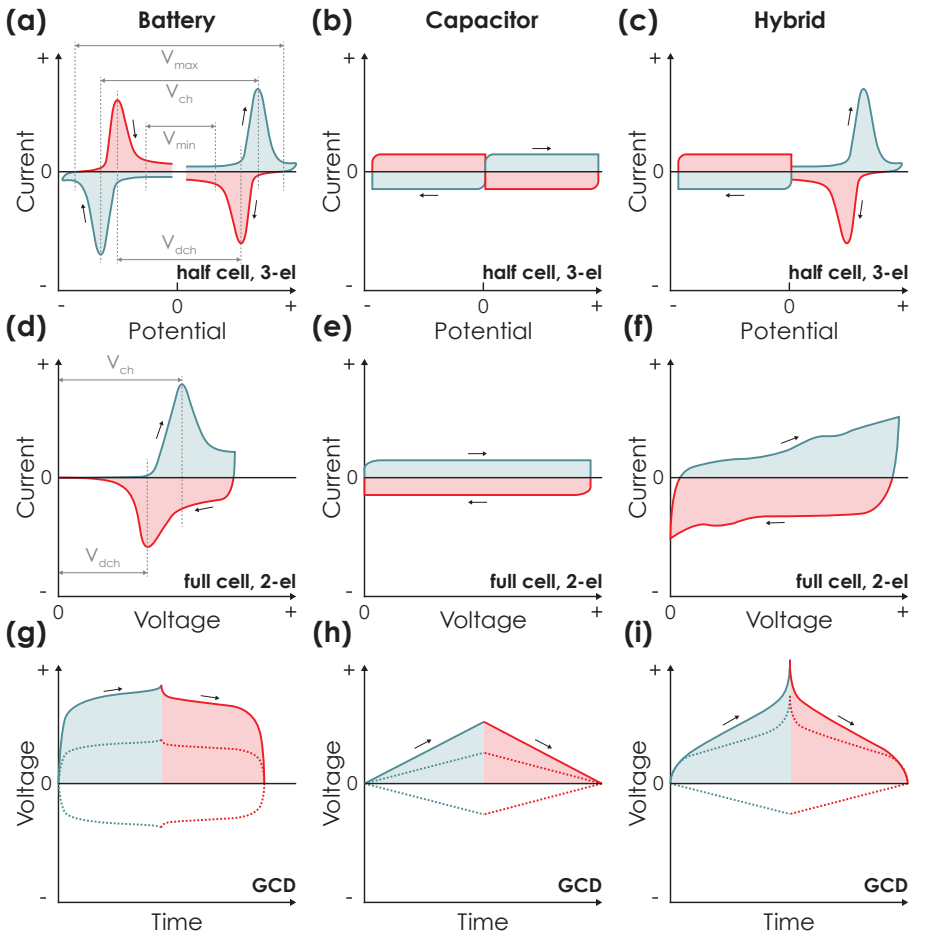

Figure 2.13. From half-cell to full-cell. The response of a full-cell results from the two half-cells. **(a-c)** CV measurements of half-cells in a three-electrode setup for (a) battery, (b) capacitor, or (c) hybrid battery/capacitor devices. For the battery device (a), we show charging (V_{ch}) and discharging voltage (V_{dch}), as well as theoretical maximum (V_{max}) and minimum (V_{min}) voltages. **(d-f)** CV measurements of resulting full-cells in two-electrode setup. We show the response for batteries (d), capacitors (e), and hybrid devices (f). **(g-i)** GCD measurements of full-cells (d-f) in two-electrode configuration. The dashed lines show GCD measurements of respective half-cells in three-electrode setup. All schemes adapted with permission.[23] Copyright 2019, Royal Society of Chemistry.

itor, but rather only the overlaying response of battery and capacitor electrodes may resemble pseudocapacitive behavior.

GCD full-cell measurements are – analogous to CV measurements – an overlay of half-cell measurements (Figure 2.13 (g-i), dashed lines). We discuss respective half-cell measurements in Section 2.3.2.1. While the shape of the full-cell measure-

ment does not deviate a lot from half-cell measurements in case of batteries and capacitors (respective Figure 2.13 (g-h), solid lines), the hybrid device full-cell measurement has a significant slope during both charging and discharging – analogous to a pseudocapacitor but only as a result of overlaying battery-type and capacitor-type responses of respective charge storage electrodes, as discussed above for CV measurements.

To conclude, understanding half-cells allows to predict full-cells. Noteworthy, hybrid systems – analogous to pseudocapacitors (see discussion in Section 1.4) – strive to combine advantages of both capacitive and battery energy storage systems, that is, high power and energy densities.[23,29]

Note that when calculating performance metrics such as capacity, energy density, or power density from CV or GCD measurements, a reasonable value can only be obtained in full-cell measurements and not in half-cell measurements. This is because the potential against which the WE is referenced needs to result from a charge storing CE and not a RE, which can be chosen at will. Hence, Equation 2.32, 2.33, and 2.34 for CV measurements and Equation 2.44, 2.45, 2.46, and 2.47 for GCD measurements should be only used for full-cell measurements.

2.4. References

(1) Feynman, R. P.; Leighton, R. B.; Sands, M.; Hafner, E. M. *Am. J. Phys.* **1965**, *33*, 750–752.

(2) Bredas, J.-L. *Mater. Horiz.* **2014**, *1*, 17–19.

(3) Soga, T. In Elsevier: 2006, pp 3–43.

(4) Kahn, A. *Mater. Horiz.* **2016**, *3*, 7–10.

(5) Cook, G.; Billman, L.; Adcock, R. Photovoltaic Fundamentals; 1000 Independence Avenue, SW Washington, DC20585, 1995.

(6) Fisher, A. C., *Electrode dynamics*; Oxford University Press: 1996.

(7) Bard, A. J.; Faulkner, L. R.; White, H. S., *Electrochemical methods - fundamentals and applications*, 3rd Edition; Wiley: 2022.

(8) Bard, A. J.; Faulkner, L. R., *Electrochemical methods - fundamentals and applications*, 2nd Edition; Wiley: 2008.

(9) Meites, L. **1963**.

(10) Lv, T.; Suo, L. *Curr. Opin. Electrochem.* **2021**, *29*, 100818.

(11) Yamada, Y.; Usui, K.; Sodeyama, K.; Ko, S.; Tateyama, Y.; Yamada, A. *Nat. Energy* **2016**, *1*, 16129.

(12) Suo, L. et al. *J. Am. Chem. Soc.* **2017**, *139*, 18670–18680.

(13) Cottrell, F. G. *Z. Für Phys. Chem.* **1903**, *42U*, 385–431.

(14) Elgrishi, N.; Rountree, K. J.; McCarthy, B. D.; Rountree, E. S.; Eisenhart, T. T.; Dempsey, J. L. *J. Chem. Educ.* **2018**, *95*, 197–206.

(15) Khalafi, L.; Cunningham, A. M.; Hoober-Burkhardt, L. E.; Rafiee, M. *J. Chem. Educ.* **2021**, *98*, 3957–3961.

(16) Lee, J. Electrochemical sensing of oxygen gas in ionic liquids on screen printed electrodes, Ph.D. Thesis, Curtin University, 2014.

(17) Randles, J. E. B. *Discuss. Faraday Soc.* **1947**, *1*, 11.

(18) Liu, J.; Wang, J.; Xu, C.; Jiang, H.; Li, C.; Zhang, L.; Lin, J.; Shen, Z. X. *Adv. Sci.* **2018**, *5*, 1700322.

(19) Morales-Aragonés, J. I.; Dávila-Sacoto, M.; González, L. G.; Alonso-Gómez, V.; Gallardo-Saavedra, S.; Hernández-Callejo, L. *Electronics* **2021**, *10*, 1283.

(20) Honsberg, C. B.; Bowden, S. G. PVEducation `https://www.pveducation.org/` (accessed 03/15/2023).

(21) Qi, B.; Wang, J. *Phys. Chem. Chem. Phys.* **2013**, *15*, 8972.

(22) Jao, M.-H.; Liao, H.-C.; Su, W.-F. *J. Mater. Chem. A* **2016**, *4*, 5784–5801.

(23) Noori, A.; El-Kady, M. F.; Rahmanifar, M. S.; Kaner, R. B.; Mousavi, M. F. *Chem. Soc. Rev.* **2019**, *48*, 1272–1341.

(24) Chen, G. Z. *Prog. Nat. Sci. Mater. Int.* **2013**, *23*, 245–255.

(25) Wang, H.; Liu, L.; Wang, R.; Zhang, D.; Zhu, L.; Qiu, S.; Wei, Y.; Jin, X.; Zhang, Z. *J. Mater. Chem. A* **2015**, *3*, 8062–8069.

(26) Chen, W.; Rakhi, R. B.; Alshareef, H. N. *J. Mater. Chem. A* **2013**, *1*, 3315.

(27) Wang, J.; Polleux, J.; Lim, J.; Dunn, B. *J. Phys. Chem. C* **2007**, *111*, 14925–14931.

(28) Liu, T.-C.; Pell, W. G.; Conway, B. E.; Roberson, S. L. *J. Electrochem. Soc.* **1998**, *145*, 1882–1888.

(29) Fleischmann, S.; Mitchell, J. B.; Wang, R.; Zhan, C.; Jiang, D.-e.; Presser, V.; Augustyn, V. *Chem. Rev.* **2020**, *120*, 6738–6782.

(30) Strukov, D. B.; Snider, G. S.; Stewart, D. R.; Williams, R. S. *Nature* **2008**, *453*, 80–83.

(31) Van de Burgt, Y.; Melianas, A.; Keene, S. T.; Malliaras, G.; Salleo, A. *Nat. Electron.* **2018**, *1*, 386–397.

(32) Ouaja Rziga, F.; Mbarek, K.; Ghedira, S.; Besbes, K. *Appl. Phys. A* **2017**, *123*, 288.

(33) Okubo, M.; Hosono, E.; Kim, J.; Enomoto, M.; Kojima, N.; Kudo, T.; Zhou, H.; Honma, I. *J. Am. Chem. Soc.* **2007**, *129*, 7444–7452.

3

Research Objective

Solar batteries aspire to achieve the next level of energy conversion and energy storage integration *via* multifunctional devices capable of performing both operations in the same device. The research field is young and as such rich and diverse in concepts (Chapter 5), but also with a distinct lack in design guidelines.[1–3] Its multidisciplinary nature requires optimizing battery metrics such as capacitor, power, and energy density, but also solar cell metrics such as photocurrent and photovoltage. An example which elucidates how challenging it is to join these very contrary design vectors is the issue of normalizing performance metrics: Batteries require gravimetric or volumetric normalization, solar cells on the other hand typically use areal normalization. In addition, it remains a challenge to transfer the photogenerated charge carrier that is not stored on the photoelectrode to the counter electrode. Furthermore, charge storage may go beyond a "traditional" battery towards memristive switches and sensors, technologies which especially when coupled to light absorption functionalities are still very much in their infancy. For instance, photo-induced charge storage to sense an analyte may pave the way for memristive information storage sensors with many addressable states that can store the analyte concentration, but such a functionality has prior to this thesis not been shown. Hence, the motivation of this thesis is to elucidate devices and design guidelines of such novel devices, both from a theoretical perspective *via* simulations and by designing proof-of-concept devices that show the desired functionality. With this, we aim to aid not only understanding of the underlying mechanisms, but also to guide future research towards more multifunctional devices.

The exciting optoelectronic and optoionic effects of 2D polymeric carbon nitrides – namely K-PHI (Section 1.2) – have been investigated in great detail,[4–7] and a solar battery concept was proposed by our group in 2018, which involves K-PHI as a *bifunctional* photoanode, capable of absorbing light and storing photoexcited electrons.[8] We use this early knowledge as a starting point to investigate a full solar

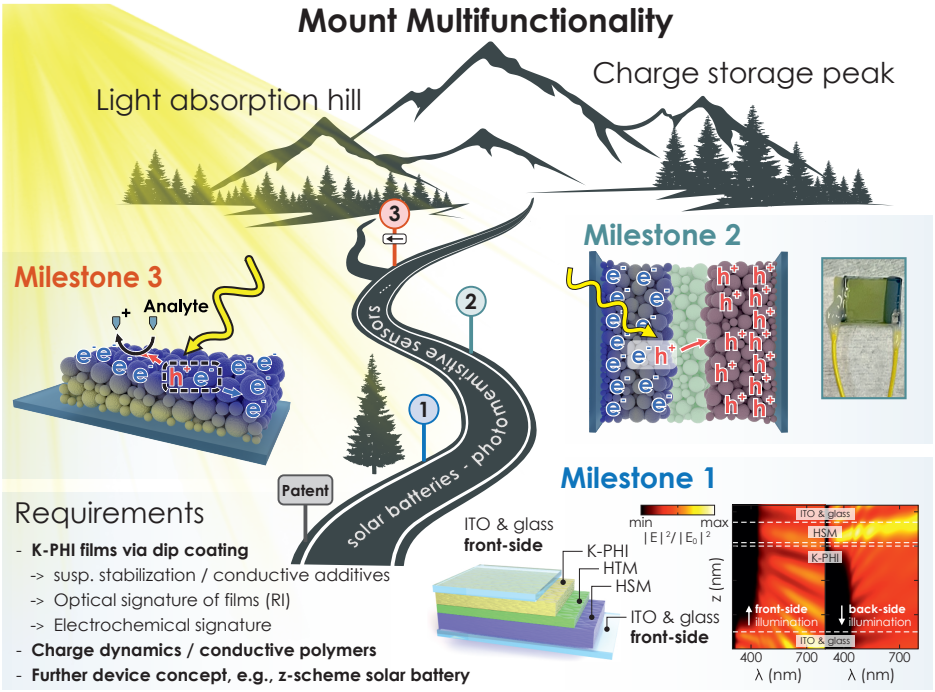

Figure 3.1. Summary of the progress of this thesis. The three main Milestones are underlined, which lead to a higher level of integration in multifunctional devices. Adapted from Chapter 6, Chapter 7, and Chapter 8.

battery (that is, a complete device with anode, cathode, and electrolyte) *via* internal rectified charge transfer with a solid-state hole transporting layer, which transfers photogenerated holes from the photoanode K-PHI to the hole storage layer. Contrary to most current solar battery designs, no external circuit is required during photocharging in such a device. However, to design a proof-of-concept device, we not only need to understand light transmission and absorption features of the individual materials, but also must optimize film preparation techniques. This includes knowing suitable film thicknesses and understanding a technique that – contrary to active layers in solar cells – can also prepare very thick layers in the range of µm. This motivated us to designed a theoretical model of the device, where – inspired from thick bulk heterojunction solar cells[9] – light absorption occurs in a *collection layer* at the K-PHI hole transporter junction. With this, we have performed extensive optical simulations and half-cell electrochemical characterizations to elaborate on design guidelines, as well as to develop an understanding of the electrochemical signature of these new devices.

Milestone 1: Chapter 6

Modeling solar cells allowed us to extract vital device parameters, such as film thickness, illumination pathway, material choices, and – very importantly – the electrochemical signature of the device. For instance, scaling of energy and power density deviates significantly in a solar battery as compared to more traditional batteries, leading to an extended *Ragone* plot with a device specific area that shows performance as a function of illumination time. We have also learned valuable lessons in how to engineer the conceptual problem of active layer thickness: thick layers support a large capacity; thin layers enable a large photocurrent. This leads us to propose several design guidelines towards a more concise research effort, based on a proposed model of a thin charge collection layer at the junction to the hole transport layer.

The knowledge from this predominantly theoretical analysis and an extensive study of K-PHI exfoliation in different solvents as well as film fabrication *via* dip coating with and without additives motivated us to proceeded and develop a proof-of-concept full solar battery device. Key of this new solar battery concept is the ladder-type hole transport mechanism, which requires precise redox-level alignment between K-PHI VB, hole transporter, and hole storage electrode. We took inspiration from solid-state dye sensitized solar cells to incorporate several different hole transporters *via* a complex multilayer fabrication.[10] The electrochemical signature of this device is unique – it can operate as a planar heterojunction solar cell, as a classical battery, or as a light-assisted battery.

Milestone 2: Chapter 7

Equipped with knowledge of Milestone 1, we have developed a proof-of-concept solar battery, consisting of K-PHI as photoanode and an all-organic internal hole transfer and storage process *via* different conductive polymers. Photogenerated hole transfer occurs internally through redox ladder-type alignment between the layers. Light and light-assisted charging showed a significantly enhanced energy output compared to dark operation.

As we have detailed in Section 1.5, energy storage due to (light-assisted) ion motion can enable novel functionalities beyond simply "storing energy". In the solar battery device of Milestone 2, we shuttle photoexcited holes to the cathode. Noteworthy, these holes possess a significant oxidation force as a result of the large bandgap of K-PHI (2.7 eV, resulting in a VB of around 2.1 V *vs.* NHE[8]), which in return can drive manifold reactions, such as sacrificial electron donor oxidation in photocatalytic water splitting.[11,12] However, the question arises, whether it would be possible to link stoichiometric oxidation of an electron donor to charging of K-PHI and the respective accompanied change in photophysical properties, such as the distinct color change from yellow to blue.[13] This question motivated us to propose a novel photomemristive sensing concept (Milestone 3).

Milestone 3: Chapter 8

We design a photomemristive sensor, which senses *via* charge storage. In comparison to Milestone 2, we extract photogenerated holes through sacrificial oxidation of an organic analyte, *e.g.*, glucose. The change in photophysical properties can be extracted through several electrochemical (potentiometric, impedimetric, coulometric) and optical (fluorometric, colorimetric) techniques.

As the first step, we introduce a more traditional amperometric sensing approach with glucose as an example analyte. This mode relates best to solar cell operation in Milestone 2, since a continuous photocurrent is extracted from the device, the magnitude of which relates to the analyte concentration. We then show how the analyte can charge the sensor. Since the amount of charging is proportional to not only analyte concentration but also how long and with which light intensity the sensor was illuminated during charging, the sensitivity (that is, the lowest measurable concentration) can be modified by changing the illumination conditions. Note that this concept could be seen as an extension to the concept of "dark photocatalysis", where the excited state is not used to quantify the analyte, but rather to drive a catalytic reaction in the dark when adding a respective cocatalyst (Pt for water reduction).[13]

3.1. References

(1) Lv, J.; Xie, J.; Mohamed, A. G. A.; Zhang, X.; Wang, Y. *Chem. Soc. Rev.* **2022**, *51*, 1511–1528.

(2) Salunke, A. D.; Chamola, S.; Mathieson, A.; Boruah, B. D.; de Volder, M.; Ahmad, S. *ACS Appl. Energy Mater.* **2022**, *5*, 7891–7912.

(3) Gurung, A.; Qiao, Q. *Joule* **2018**, *2*, 1217–1230.

(4) Wang, X.; Maeda, K.; Thomas, A.; Takanabe, K.; Xin, G.; Carlsson, J. M.; Domen, K.; Antonietti, M. *Nat. Mater.* **2009**, *8*, 76–80.

(5) Schlomberg, H.; Kröger, J.; Savasci, G.; Terban, M. W.; Bette, S.; Moudrakovski, I.; Duppel, V.; Podjaski, F.; Siegel, R.; Senker, J.; Dinnebier, R. E.; Ochsenfeld, C.; Lotsch, B. V. *Chem. Mater.* **2019**, *31*, 7478–7486.

(6) Sridhar, V.; Podjaski, F.; Alapan, Y.; Kröger, J.; Grunenberg, L.; Kishore, V.; Lotsch, B. V.; Sitti, M. *Sci. Robot.* **2022**, *7*, 62.

(7) Sridhar, V.; Podjaski, F.; Kröger, J.; Jiménez-Solano, A.; Park, B.-W.; Lotsch, B. V.; Sitti, M. *Proc. National Acad. Sci.* **2020**, *117*, 24748–24756.

(8) Podjaski, F.; Kröger, J.; Lotsch, B. V. *Adv. Mater.* **2018**, *30*, 1705477.

(9) Tait, J. G.; Paetzold, U. W.; Cheyns, D.; Turbiez, M.; Heremans, P.; Rand, B. P. *ACS Appl. Mater. Interfaces* **2016**, *8*, 2211–2219.

(10) Benesperi, I.; Michaels, H.; Freitag, M. *J. Mater. Chem. C* **2018**, *6*, 11903–11942.

(11) Kröger, J.; Jiménez-Solano, A.; Savasci, G.; Rovó, P.; Moudrakovski, I.; Küster, K.; Schlomberg, H.; Vignolo-González, H. A.; Duppel, V.; Grunenberg, L.; Dayan, C. B.; Sitti, M.; Podjaski, F.; Ochsenfeld, C.; Lotsch, B. V. *Adv. Energy Mater.* **2021**, *11*, 2003016.

(12) Kröger, J.; Jiménez-Solano, A.; Savasci, G.; Lau, V. W. h.; Duppel, V.; Moudrakovski, I.; Küster, K.; Scholz, T.; Gouder, A.; Schreiber, M.-L.; Podjaski, F.; Ochsenfeld, C.; Lotsch, B. V. *Adv. Funct. Mater.* **2021**, *31*, 2102468.

(13) Lau, V. W.-h.; Klose, D.; Kasap, H.; Podjaski, F.; Pignié, M.-C.; Reisner, E.; Jeschke, G.; Lotsch, B. V. *Angew. Chem. Int. Ed.* **2017**, *56*, 510–514.

Part II

Perspectives Towards Novel Photo Devices and Concepts

4

Optoionics 2.0: A toolkit to design novel applications for the post-Silicon age

Andreas Gouder and Bettina V. Lotsch

We present an excerpt of an invited perspective for:

Journal of Materials Chemistry A.

Keywords: optoionics, photoionics, layered compounds, carbon nitrides

Author contributions

Andreas Gouder and Bettina V. Lotsch conceived the project and wrote the manuscript.

Contents

4.1. A brief historical context of optoionics and photoionics 122
4.2. The optoionic mechanism 126
4.2.1. Extending the concept of intrinsic/extrinsic and 1-/2-phase optoionic systems 128
4.2.2. Experimental impact of the different field effects 130
4.3. References 131

4.1. A brief historical context of optoionics and photoionics

The field of optoionics has seen a huge boost in research activity, fueled through a recent report by Maier and coworkers on the light-induced increase in ionic conductivity of MAPI by several orders of magnitude.[1] Given the popularity of this emerging research field, it is timely to recapitulate the historical context of light-ion interactions, for which the earliest reports date back to the beginning of the 20st century. These early works use the term photoionics rather than optoionics (see literature review in Figure 4.1), which motivates a closer look at the semantics of and relationships between these two terms.

Notably, with more than 600 mentions in publications, the term photoionics has far outpaced the term optoionics. We will start by giving an overview of historical occurrences of both terms, irrespective of their definitions and in the broadest possible sense. We will then (Section 4.2) proceed by giving a more focused definition of the term optoionics as used in current literature. Karrer was the first to coin the term photoionics in 1924, defining it as the influence of light on the equilibrium constant of an ionization reaction.[2] It took until the 1970s and 80s for a more focused research effort centered around photoionics, with reports of direct copper

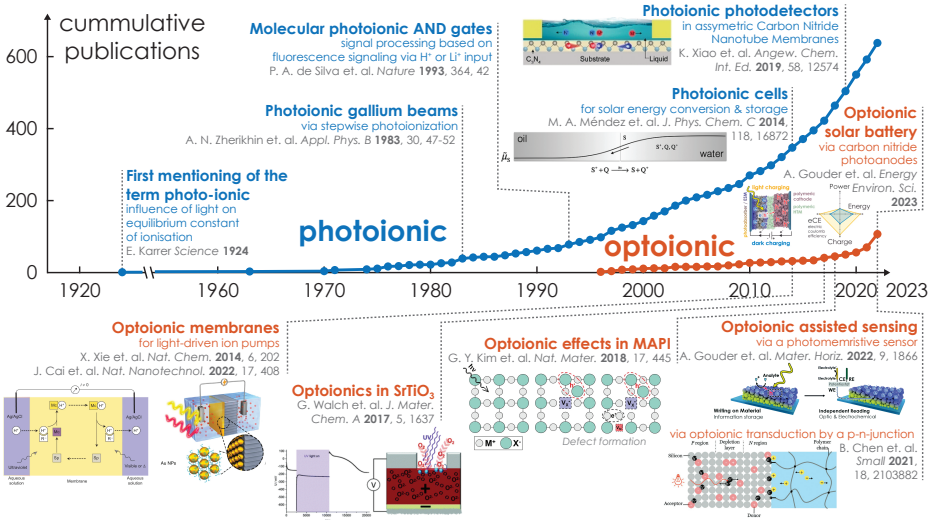

Figure 4.1. Literature overview of reported light-ion interactions. Literature overview of reports in the last century that use the term photoionic (blue) or optoionic (red). A significant increase can be observed in recent years, underlining the huge research interest that this field currently experiences. The literature review was performed using the database *Google Scholar*. Key reports are mentioned, including first mentioning of the term photoionic in literature albeit with a different definition of our current understanding of optoionic mechanisms,[2] photoionic gallium beams,[3] molecular photoionic AND gates,[4] photoionic cells (reproduced with permission. Copyright 2014, American Chemical Society),[5] optoionic membranes (reproduced with permission. Copyright 2014, Springer Nature; Copyright 2022, Springer Nature),[6,7] optoionic effects in $SrTiO_3$ (reproduced under the terms of open access CC BY 3.0 license. Copyright 2017, Royal Society of Chemistry)[8] and in MAPI (reproduced with permission. Copyright 2020, Wiley-VCH),[1,9] carbon nitride based photoionic detectors (reproduced under the terms of open access CC BY 4.0 license. Copyright 2019, Wiley-VCH),[10] optoionic sensing *via* a p-n-junction polarizing a membrane (reproduced with permission. Copyright 2022, Wiley-VCH)[11] and photomemristive sensing in carbon nitrides (reproduced under the terms of open access CC BY 3.0 license. Copyright 2022, Royal Society of Chemistry),[12] and solar battery (reproduced under the terms of open access CC BY 3.0 license. Copyright 2023, Royal Society of Chemistry)[13] concepts.

photoionization under UV – a distinct concept, which is not closely related to our current understanding of (photo)optoionic effects. Photoionization for instance, reported by Fedoseyev and coworkers to produce photoionic gallium (Ga) beams,[3] occurs by directly ionizing atoms *via* laser irradiation (in case of Ga: 200 to 400 nm irradiation). Molecular photoionics on the other hand was discussed by McCoy and coworkers for various organic receptor molecules, which included anthracene derivatives with crown ether groups that showed Photoinduced Electron Transfer (PET) functionalities.[4] In PET, photoexcited charge carrier separation occurs by injecting the electron from a (here molecular) donor into an acceptor species, which

in return causes a fluorescence signal. Injecting of ions into the material such as protons or Li^+ can suppress the charge transfer energetics (by coordination of the ion with the crown ether), resulting in fluorescence emission. This process is well known by now and extensively employed for designing logical operation switches (AND, OR gates[4]), but also highly selective ion sensors.[14] While strictly speaking, the complexation of organic ligands, which in turn affects photogenerated electron transfer, appears unrelated to (photo)optoionic phenomena described in the literature, we note that the interaction between photogenerated electronic and ionic charge carriers is also the key ingredient of such photoionic effects. The influence of ion intercalation on optical properties such as the refractive index has also been extensively investigated. Rubin and coworkers described the influence and quantity of oxygen vacancies on the optical properties SnO_x ($1<x<2$) thin films, which allowed to control weak electrochromic effects when intercalating Li ions.[15] Bhattacharya and coworkers investigated the impact of oxygen vacancy concentration on optical properties of nanocrystalline CeO_2/PrO_x 'optoionic films'.[16] Both Rubin and Bhattacharya proposed smart electrochromic windows as a possible pathway to application. Note, however, that in both cases the term "opto" refers to the nexus between optical and ionic properties, rather than the control of ionic properties by light. In other words, the term optoionics as used in these examples does not involve light-induced changes in ionic properties, but a correlated change in optical and ionic properties induced by a "dark" stimulus.

Simple ionic crystals like alkali metal and silver halides are arguably the prototypes of light-responsive materials in which light has a direct effect on the ionic sublattice. Silver halides, for example, are known for their photolytic decomposition under visible light irradiation, a process that enabled late 19th century photography. More recently, this process has been revisited by Ohta and coworkers in the context of photoswitching.[17] The authors measured a significant increase in bulk conductivity (3 orders of magnitude) when irradiating silver iodide (AgI). Note that no conceiving evidence for higher ionic conductivity during the decomposition process was presented so far. In 2014, Bakker and coworkers reported the idea of a light-driven proton pump *via* a membrane consisting of photochromic spiropyran derivatives, which are photoacids/-bases.[6] The affinity of the spiropyran to H^+ becomes significantly enhanced at the UV-illuminated terminus compared to the visible light side and hence, protons are transported through the membrane (producing a pH gradient of 3.6). Note the conceptual relation to the initial definition of photoionics by Karrer mentioned at the beginning. Kuang and coworkers recently investigated

optoionic phenomena in ion transporting nanoscale membranes of plasmonic Au nanoparticles decorated with chiral phenylalanine (Phe).[7] Au nanoparticles absorb polarized light and produce 'hot' electrons, which subsequently get trapped by the surrounding Phe. To induce charge compensation, Phe transports ions to and from the nanoparticle interface, hence making the membrane more or less ion permeable depending on illumination – a process that the authors described as optoionic effect.

Photoionic cells were first reported by Girault and coworkers in 2014 as a further light-ion interaction-based concept to store energy in a redox couple in solution.[5] Here, two electrolytes with different polarizability (producing an electrochemical potential difference at the junction due to the difference of solvation energy of different species) are in contact through a liquid-liquid junction (a hydrophilic and a hydrophobic phase). A dye (*e.g.*, leucothionine) is present in one phase, together with a redox couple (*e.g.*, $Th^{+}-[Co(II)EDTA]^{2-}$). Light absorption excites the dye, which is subsequently quenched by the redox couple, forming two charged ionic species with different surface charges. The potential difference at the liquid-liquid junction of both electrolytes drives the two species into the different electrolyte solutions (depending on solvation energies), where they can be separated and subsequently discharged in an electrochemical cell. In essence, photogenerated charges are trapped in different ionic species, hence the term 'photoionic' cell. As such, there is a notable analogy between these systems and current light-ion interaction concepts.

The prototypical optoionic effect that serves as eponym of the field was published by Maier and coworkers in 2018 and describes a substantial increase in ionic conductivity through the creation of iodide vacancies in MAPI under illumination.[1] We explain the mechanism in detail in the next Section and only emphasize here that light absorption indirectly produces an increase in ionic charge carriers, mediated by the light-induced generation of electronic charge carriers, which can be considered a hallmark of optoionics as it will be used in the following. This study has triggered intense the interest in optoionic effects, such as enhanced conductivity at grain boundaries in Gd-doped ceria thin films under illumination,[18] the trapping of photogenerated electrons in ionic carbon nitrides employed for solar batteries by our group,[19,20] and carbon nitride asymmetric nanotube membranes used as a photodetector by Antonietti and coworkers.[10] The latter invokes the build-up of a gradient in surface charges in carbon nitride nanotubes under asymmetric illumination, which causes a n-type conductivity-induced band bending, that in return

leads to movement of external electrolyte ions along the field gradient within the pore channel, thus resulting in the accumulation of differently charged ions at the different termini of the tubes. Two further concepts capitalizing on optoionic effects in the 2D polymeric carbon nitride potassium poly(heptazine imide), abbreviated as K-PHI, were recently published by our group, namely photomemristive sensors[12] and bifunctional solar batteries.[13] In both devices, the interaction between photoinduced electronic and ionic charge carriers enables the trapping of photogenerated electrons on K-PHI – in the case of the photomemristive sensor to store the analyte concentration information on the material, in case of the solar battery to store charges and release them on demand, akin to a battery. We discuss the optoionic mechanism in the next Section in detail.

4.2. The optoionic mechanism

From the previous section it becomes clear that the manifold reports on photo- or optoionic effects are extremely heterogeneous, and so are the – either proposed or proven – mechanisms that explain these effects. This raises the question as to whether it is possible to come up with a concise definition that covers most or all hitherto observed (photo)optoionic phenomena. Maier and coworkers proposed a general definition of optoionic effects, that is, the modification of ionic conductivity ($\sigma = nq \cdot \mu$, where σ is the ionic conductivity, nq is the concentration of ionic charge carriers carrying charge q, and μ is the mobility) through irradiation, either by enhancing the ionic mobility μ, or by increasing the amount of ionic charge carriers n.[9,23] Henceforth, we will use the term optoionics to discuss any devices linked to this mechanism – by analogy to the term optoelectronics. In this context and taking the example of the hybrid perovskite MAPI mentioned above, an excitonic mechanism may be formulated as follows: Above-bandgap irradiation results in light absorption by the material, which causes reduction of the backbone (Pb^{2+} to Pb^0) *via* photogenerated electrons and oxidation of iodide (I^- to I^0) *via* the photogenerated holes (Figure 4.2 (a), top). As a result of the narrow VB of MAPI, the hole localizes on a consequentially neutral iodine,[9] which then stabilizes by displacement into an interstitial site, forming either dimers (I_2^-) or – in case of bromide perovskites – trimers (Br_3^{2-}). The displacement of the halogens into interstitial sites gives rise to the formation of halide vacancies, that in return give rise to independent halogen movement as a result of increasing the amount of mobile ionic charge carriers (*i.e.*, vacancies) and, hence, the ionic conductivity. A somewhat similar mech-

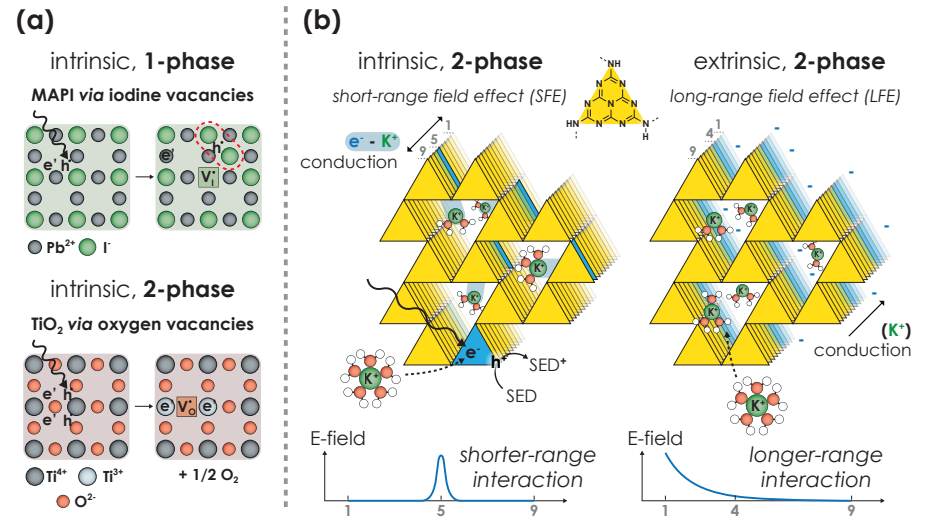

Figure 4.2. Extending optoionic concepts to 2-phase K-PHI systems. (a) Recently reported optoionic effects in MAPI (top) and TiO_2 (bottom). In case of MAPI, light absorption results in the formation of iodine interstitials and hence iodide vacancies *via* photogenerated holes and electron trapping on the backbone. In case of TiO_2, photogenerated holes form oxygen vacancies, electrons are trapped on the backbone, and oxygen is removed *via* O_2 gas. A solid phase and a gas phase participate; hence we term it a 2-phase intrinsic mechanism. Adapted under the terms of open access CC BY 4.0 license.[21] Copyright 2021, Wiley-VCH. **(b)** In case of K-PHI, K^+ ions are not extracted from the lattice forming a vacancy but are present as (partially) hydrated ions in an aqueous liquid phase. Hence, we term this case 2-phase (solid, liquid). Upon light absorption and when removing the photogenerated hole, *e.g.*, by oxidizing a SED, the backbone is reduced and exhibits a field effect that locally attracts a K^+ (left). Intercalation accompanied by partial dehydration and possibly orbital coupling between K^+ and the backbone[22] occurs, hence we call the effect intrinsic. Due to its shorter range, we term it Short-range Field Effect (SFE). However, when charge accumulation occurs due to, *e.g.*, anisotropic illumination, the electrons can cause a longer-range field effect (right) – henceforth termed Long-range Field Effect (LFE). Here, there is no direct coupling between K^+ and electrons and the attraction is solely electrostatic, hence we term the effect extrinsic.

anism occurs in transition metal oxides such as TiO_2 or $SrTiO_3$:[9,24] In the context of (photo)optoionics, UV light absorption causes localization of the photogenerated hole on the oxygen sublattice, which in turn displaces the oxygen from its lattice site, forming a vacancy (Figure 4.2 (a), bottom). Photogenerated electrons may either be trapped by oxygen vacancies or by reducing Ti^{4+} to Ti^{3+}. Both electron trapping mechanisms cause a color change of the material.[25] In case of TiO_2, for instance, a distinct color change to blue can be observed upon trapping of photogenerated electrons as a result of forming Ti^{3+} at the surface.[26] Notably, these effects rely on intrinsic, coupled optoelectronic and ionic effects within the photoabsorbing mate-

rial (*i.e.*, light interaction with the host lattice produces (mobile) vacancies within the material) – we therefore denote them as intrinsic optoionic effects. We note that the term intrinsic refers to the fact that the optoionic process occurs within a single material, although the surrounding environment – the liquid or gas phase – may act as ion-reservoir or sink, thus altering the overall stoichiometry of the material. To name specific examples: Ion excorporation (in the form of I_2) is a known decomposition pathway in MAPI,[27,28] and incorporation was also observed under sufficient iodine vapor pressure.[29] In case of $SrTiO_3$, UV light-driven oxygen uptake from the surrounding environment was reported by Fleig and coworkers. Here, an electrochemical cell was developed based on $SrTiO_3$ contacted with an oxygen reservoir on one side through an O_2 permeable current collector, resulting in a 'light-charged oxygen battery'.[8]

Since the terminology intrinsic/extrinsic is not free from ambiguities (and also may cause confusion due to its similarity with semiconductor doping), we propose an additional classification in terms of the number of phases/interfaces involved. A 1-phase system (here: solid phase) would be MAPI if no excorporation of iodine into the gas phase (and hence, decomposition) occurs, and a 2-phase system would be $SrTiO_3$, where the solid and gas phase are involved through oxygen in- or excorporation.

4.2.1. Extending the concept of intrinsic/extrinsic and 1-/2-phase optoionic systems

As pointed out above and in our earlier perspective,[21] the above (intrinsic, 1-phase) mechanism can be generalized and extended to 2-phase systems in which the environment plays a vital role as reservoir for the (de)intercalation species. In addition to the (solid-gas) systems discussed above (MAPI, $SrTiO_3$, TiO_2), interfacial systems based on a solid-liquid interface where ions are ex- or incorporated can likewise serve as prototypical intrinsic 2-phase optoionic systems based on an effect that is known as photointercalation.[21] This process was first proposed by Tributsch in 1980, who envisaged light-induced charge storage in semiconductors *via* ion intercalation mediated by photogenerated charge carriers.[30] Here, the (quasi-)Fermi level is increased upon band gap illumination, acting as a driving force to incorporate (and, hence, store) cations from the electrolyte into the bulk of the semiconductor. Consequently, the photogenerated electrons are stored in an intra-band gap intercalation state (forming a band), while the majority charge carriers (holes) are

extracted *via* an applied potential. Tributsch and Betz proposed different n- and p-type layered semiconducting compounds (*e.g.*, $ZrSe_2$ for Li, InSe for Cu, or V_2O_5 and WO_3 for H intercalation) as possible photoactive host materials,[31] and more recently Amal and coworkers demonstrated photointercalation of Na^+ in MoO_3 as a photoanode for solar batteries.[32]

The processes occurring upon photointercalation are mirrored by K-PHI: Upon irradiation with light <450 nm (2.7 eV bandgap), electron-hole pairs are produced, which are separated by rapid quenching of the photoexcited hole with a SED.[12] The photoinduced electron is then trapped (and hence, stabilized) on the heptazine units by a combination of electronic (*i.e.*, energetically low lying LUMO/CB) and ionic effects, the latter likely driven by attractive interactions between the electrons and hydrated mobile K^+ ions residing in the structural pores of K-PHI.[20,33] In addition, further charge compensating ions from the electrolyte enter the pore channels to screen the accumulating charge on the carbon nitride backbone, thus reducing the system's overall energy and assisting in electron trapping.

As mentioned above, local field effects significantly govern the intercalation process: Local photoexcitation at the solid/liquid interface, followed by quenching of the hole *via* a SED, produces an electron localized on one heptazine unit that exhibits an electric field attracting ions (Figure 4.2 (b), left. Electric field along the stacking direction through a heptazine unit is schematically shown at the bottom). As a first approximation, the attractive force F between the two charge carriers (electron e^- and ion species K^+) may be expressed based on Coulomb's law as follows:[34]

$$F = \frac{1}{4\pi\varepsilon} \times \frac{n_{e^-} q_{e^-} \times n_{K^+} q_{K^+}}{\left(x_{e^-} - x_{K^+}\right)^2} \times \hat{r} \tag{4.1}$$

where q_{e^-} and q_{K^+} are the respective point charges, n_{e^-} and n_{K^+} the amount of charges (here n_{e^-} and n_{K^+} are both 1, since one electron interacts with one K^+ ion, *i.e.*, a 'stoichiometric' electron-ion interaction), x_{e^-} and x_{K^+} the respective distances of charges along the unit vector $\hat{r}$, and ε the electric permittivity of the medium, which is more commonly referred to as dielectric constant.[35] We can deduce several key messages from this equation that may impact optoionic effects in K-PHI: (1): F is inversely proportional to the squared distance between e^- and K^+ – hence, our rationale behind terming this effect short-range field effect (SFE). (2) F is inversely proportional to ε. As a consequence of the relatively small ε value of K-PHI (reports range from 3 to 8[36,37]), F should be large. However, on the other hand as a result of the large dielectric constant of water of 78,[38] the hydration shell

will be very polarized and reduce the electric field intensity produced by the ion, which in return should significantly reduce F and thus, may increase the distance between e^- and K^+. (3) F is proportional to $n_{e^-}q_{e^-}$ and $n_{K^+}q_{K^+}$. This allows us to hypothesize that a second, more long-range optoionic field effect in K-PHI is at play (consequently termed by us long-range field-effect (LFE)): To understand why, let us consider an experiment where light-induced charge carrier generation and stabilization occurs in only one part of the material. From an experimental perspective this is easily conceivable, *e.g.*, due to the Lambert-Beer like decay of light intensity within a material or asymmetric illumination across a particle or film.[39] Such uneven illumination leads to asymmetric charge carrier generation across the material and, hence, to asymmetric charging.[40,41] Alternatively, one could also imagine an experiment where K-PHI is only partially in contact with a hole extraction medium such as hole transporting polymers[13] or at a solid-liquid junction with the liquid phase containing SEDs.[12,42] The low intrinsic electronic conductivity of K-PHI largely inhibits diffusion and drifting of electronic charge carriers to other parts of the sample.[20] Consequently, electrons accumulate and form an electron ensemble, which results in a significant increase of n_{e^-} and thus F. Due to the larger electric field intensity, this field effect should be more long-range, as shown in Figure 4.2 (b), right.

We term this effect a 2-phase effect, since the ions – here K^+ – do not result from the backbone of K-PHI (that is, PHI), but rather a second (in a hydrated environment aqueous) phase, *e.g.*, externally when suspended in water or internally *via* hydrated ions within the pores of the material. If upon intercalation the hydration shell stays intact, the interaction could be termed extrinsic, since the ion remains in the liquid phase and interacts locally only capacitively. If the hydration shell partially decomposes and a closer interaction between ion and electron occurs (*i.e.*, orbital coupling *via* hybridization),[22] one could view this process as (more) intrinsic. We propose, that this depends on the degree of hydration of ions in the confined pores.

4.2.2. Experimental impact of the different field effects

While theoretically we can disentangle SFE and LFE processes, in reality likely a mixing of both effects will affect electron trapping (*i.e.*, charging) of the material at different stages of the charging process. This complicates the kinetics of the charging process, since the charge accumulation-induced LFE field-effect could only occur through uneven illumination or due to the device geometry (*e.g.*, asymmetric

junctions) and may be relevant mainly at the later stages of the charging process when a significant amount of electrons has accumulated asymmetrically across a particle or film. Note also that LFE will only lead to an anisotropic enhancement of ionic mobility, that is, towards the electric field. This may be beneficial for certain applications such as ion channels for photodetectors,[10] photoelectric energy conversion,[41] or more generally optogenetics,[43] but also for polarized membranes,[11] membranes for possible reverse osmosis devices,[6,7] or enhanced ionic conductivity at grain boundaries due to a modified space charge region.[18]

On the other hand, the local SFE should govern more the early charging process and occur in systems, where a more homogeneous charging may occur. Indeed, it is not always clear whether SFE leads to an enhanced ionic conductivity (as underlined in *e.g.*, MAPI[1] or $SrTiO_3$[8]) or only assists charge trapping (as in K-PHI[21]).

We conclude that in order to understand the different types of field effect, a better understanding of the junction dynamics between the photoabsorbing material and the ion containing phase is vital.

4.3. References

(1) Kim, G. Y.; Senocrate, A.; Yang, T.-Y.; Gregori, G.; Grätzel, M.; Maier, J. *Nat. Mater.* **2018**, *17*, 445–449.

(2) Karrer, E. *Science* **1924**, *60*, 30–33.

(3) Zherikhin, A. N.; Letokhov, V. S.; Mishin, V. I.; Muchnik, M. E.; Fedoseyev, V. N. *Appl. Phys. B Photophysics Canarias Chem.* **1983**, *30*, 47–52.

(4) De Silva, P. A.; Gunaratne, N. H. Q.; McCoy, C. P. *Nature* **1993**, *364*, 42–44.

(5) Méndez, M. A.; Peljo, P.; Scanlon, M. D.; Vrubel, H.; Girault, H. H. *J. Phys. Chem. C* **2014**, *118*, 16872–16883.

(6) Xie, X.; Crespo, G. A.; Mistlberger, G.; Bakker, E. *Nat. Chem.* **2014**, *6*, 202–207.

(7) Cai, J. et al. *Nat. Nanotechnol.* **2022**, *17*, 408–416.

(8) Walch, G.; Rotter, B.; Brunauer, G. C.; Esmaeili, E.; Opitz, A. K.; Kubicek, M.; Summhammer, J.; Ponweiser, K.; Fleig, J. *J. Mater. Chem. A* **2017**, *5*, 1637–1649.

(9) Senocrate, A.; Kotomin, E.; Maier, J. *Helvetica Chim. Acta* **2020**, *103*, e2000073.

(10) Xiao, K.; Tu, B.; Chen, L.; Heil, T.; Wen, L.; Jiang, L.; Antonietti, M. *Angew. Chem. Int. Ed.* **2019**, *58*, 12574–12579.

(11) Chen, B.; Suo, Z. *Small* **2022**, *18*, 2103882.

(12) Gouder, A.; Jiménez-Solano, A.; Vargas-Barbosa, N. M.; Podjaski, F.; Lotsch, B. V. *Mater. Horiz.* **2022**, *9*, 1866–1877.

(13) Gouder, A.; Podjaski, F.; Jiménez-Solano, A.; Kröger, J.; Wang, Y.; Lotsch, B. V. *Energy Environ. Sci.* **2023**, DOI: 10.1039/d2ee03409c.

(14) Roy, N.; Dutta, A.; Mondal, P.; Paul, P. C.; Sanjoy Singh, T. *J. Fluoresc.* **2017**, *27*, 1307–1321.

(15) Isidorsson, J.; Granqvist, C. G.; von Rottkay, K.; Rubin, M. *Appl. Opt.* **1998**, *37*, 7334.

(16) Hartridge, A.; Ghanashyam Krishna, M.; Bhattacharya, A. *Materials Science and Engineering: B* **1999**, *57*, 173–178.

(17) Sabeth, F.; Iimori, T.; Ohta, N. *J. Phys. Chem. C* **2012**, *116*, 9209–9213.

(18) Defferriere, T.; Klotz, D.; Gonzalez-Rosillo, J. C.; Rupp, J. L. M.; Tuller, H. L. *Nat. Mater.* **2022**, *21*, 438–444.

(19) Podjaski, F.; Kröger, J.; Lotsch, B. V. *Adv. Mater.* **2018**, *30*, 1705477.

(20) Kröger, J.; Podjaski, F.; Savasci, G.; Moudrakovski, I.; Jiménez-Solano, A.; Terban, M. W.; Bette, S.; Duppel, V.; Joos, M.; Senocrate, A.; Dinnebier, R.; Ochsenfeld, C.; Lotsch, B. V. *Adv. Mater.* **2022**, *34*, 2107061.

(21) Podjaski, F.; Lotsch, B. V. *Adv. Energy Mater.* **2021**, *11*, 2003049.

(22) Ando, Y.; Okubo, M.; Yamada, A.; Otani, M. *Adv. Funct. Mater.* **2020**, *30*, 2000820.

(23) Senocrate, A.; Maier, J. *J. Am. Chem. Soc.* **2019**, *141*, 8382–8396.

(24) Merkle, R.; De Souza, R. A.; Maier, J. *Angew. Chem. Int. Ed.* **2001**, *40*, 2126–2129.

(25) Popov, A.; Kotomin, E.; Maier, J. *Nucl. Instrum. Methods Phys. Res. Sect. B: Beam Interact. With Mater. At.* **2010**, *268*, 3084–3089.

(26) *J. Am. Chem. Soc.* **2017**, *139*, 2868–2871.

(27) Wei, D. et al. *Adv. Mater.* **2018**, *30*, 1707583.

(28) Yang, T.-Y.; Jeon, N. J.; Shin, H.-W.; Shin, S. S.; Kim, Y. Y.; Seo, J. *Adv. Sci.* **2019**, *6*, 1900528.

(29) Senocrate, A.; Moudrakovski, I.; Kim, G. Y.; Yang, T.-Y.; Gregori, G.; Grätzel, M.; Maier, J. *Angew. Chem. Int. Ed.* **2017**, *56*, 7755–7759.

(30) Tributsch, H. *Appl. Phys.* **1980**, *23*, 61–71.

(31) Betz, G.; Tributsch, H. *Prog. Solid State Chem.* **1985**, *16*, 195–290.

(32) Lou, S. N.; Sharma, N.; Goonetilleke, D.; Saputera, W. H.; Leoni, T. M.; Brockbank, P.; Lim, S.; Wang, D.-W.; Scott, J.; Amal, R.; Ng, Y. H. *Adv. Energy Mater.* **2017**, *7*, 1700545.

(33) Schlomberg, H.; Kröger, J.; Savasci, G.; Terban, M. W.; Bette, S.; Moudrakovski, I.; Duppel, V.; Podjaski, F.; Siegel, R.; Senker, J.; Dinnebier, R. E.; Ochsenfeld, C.; Lotsch, B. V. *Chem. Mater.* **2019**, *31*, 7478–7486.

(34) Purcell, E. M., *Electricity and Magnetism*, 3rd edition; Cambridge University Press: 2013.

(35) Braslavsky, S. E. *Pure Appl. Chem.* **2007**, *79*, 293–465.

(36) Patra, P. C.; Mohapatra, Y. N. *Appl. Phys. Lett.* **2021**, *118*, 103501.

(37) Li, Y.; Jin, S.; Xu, X.; Wang, H.; Zhang, X. *J. Appl. Phys.* **2020**, *127*, 170903.

(38) Vidulich, G. A.; Kay, R. L. *J. Phys. Chem.* **1962**, *66*, 383–383.

(39) Gouder, A.; Yao, L.; Wang, Y.; Podjaski, F.; Rabinovich, K. S.; Jimenez-Solano, A.; Lotsch, B. V. *ACS Energy Lett.* **2023**.

(40) Sridhar, V.; Podjaski, F.; Alapan, Y.; Kröger, J.; Grunenberg, L.; Kishore, V.; Lotsch, B. V.; Sitti, M. *Sci. Robot.* **2022**, *7*, 62.

(41) Xiao, K.; Chen, L.; Chen, R.; Heil, T.; Lemus, S. D. C.; Fan, F.; Wen, L.; Jiang, L.; Antonietti, M. *Nat. Commun.* **2019**, *10*, 74.

(42) Kröger, J.; Jiménez-Solano, A.; Savasci, G.; Lau, V. W. h.; Duppel, V.; Moudrakovski, I.; Küster, K.; Scholz, T.; Gouder, A.; Schreiber, M.-L.; Podjaski, F.; Ochsenfeld, C.; Lotsch, B. V. *Adv. Funct. Mater.* **2021**, *31*, 2102468.

(43) Beck, S.; Yu-Strzelczyk, J.; Pauls, D.; Constantin, O. M.; Gee, C. E.; Ehmann, N.; Kittel, R. J.; Nagel, G.; Gao, S. *Front. Neurosci.* **2018**, *12*, 643.

5

Integrated Solar Batteries: Design and Device Concepts

Andreas Gouder and Bettina V. Lotsch

This perspective was published in:

ACS Energy Letters **2023**.
doi: 10.1021/acsenergylett.3c00671

Keywords: solar cell, battery, solar battery, photo battery, solar energy storage, optoionics

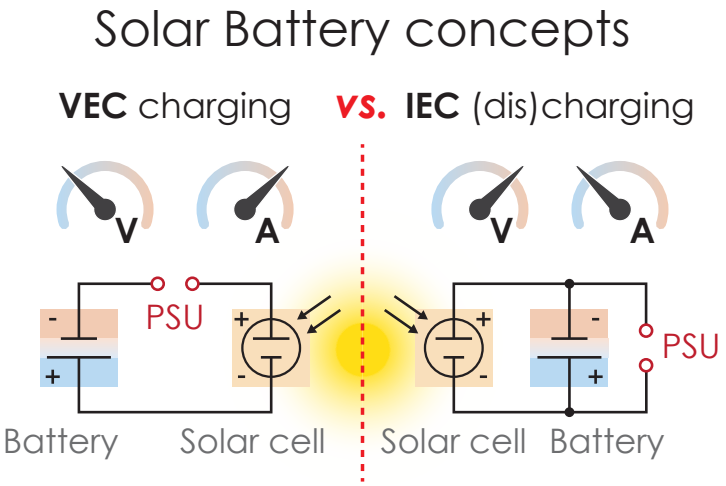

Author contributions

Andreas Gouder and Bettina V. Lotsch conceived the project and wrote the manuscript.

Contents

5.1. The Solar Battery Experiment 139
5.2. A brief overview of current solar battery concepts 142
5.2.1. Three-electrode designs 142
5.2.2. Bifunctional electrodes *via* heterojunctions 144
5.2.3. Bifunctional electrodes *via* bifunctional materials 148
5.3. Design philosophy of solar batteries: Improving power or energy balance 151
5.4. References 158

5

Abstract

Solar batteries present an emerging class of devices, which enable simultaneous energy conversion and energy storage in one single device. This high level of integration enables new energy storage concepts ranging from short-term solar energy buffers to light-enhanced batteries, thus opening up exciting vistas for decentralized energy storage. The dynamics of this emerging field have evolved a number of different solar battery designs, which not only significantly differ in the charge storage mechanism, but also in terms of device design. Herein, we first discuss the fundamental electrochemical signature of these devise, revisit all reported solar battery concepts and categorize them in a set of five designs by carving out key similarities in how both electric and light charging fluxes interact, classifying them either as charge efficient or power efficient charging devices. We then re-discuss solar batteries in the context of our classification scheme and propose design guidelines for solar batteries.

Short Author Biographies

Andreas Gouder. Andreas Gouder received his BSc and MSc in chemistry from the Ludwig-Maximilians-University Munich in 2017 and 2019. Since 2019, he is

enrolled as PhD student in the group of Bettina V. Lotsch (Max-Planck-Institute for Solid State Research), developing applications from bifunctional organic materials using the toolkit of optoelectronic and optoionic features.

Bettina V. Lotsch. Bettina V. Lotsch is Director of the Nanochemistry Department at the Max Planck Institute for Solid State Research, Stuttgart. Her group combines the toolbox of solid-state chemistry, nanochemistry, and molecular chemistry for applications in energy conversion and storage. Recent research interests focus on developing novel optoionic materials, concepts and devices.

Main text

Solar energy conversion is paramount to provide sustainable energy solutions, owing to the huge photon energy influx provided by solar irradiation. However, while this form of renewable energy can power our world's economies, it experiences fluctuations on timescales of minutes (weather conditions), hours (day-night rhythm), and years (seasons), which must be balanced to prevent overload or depletion of the energy grid.[1] Solar cell PV technology has advanced significantly over recent years, showing record breaking power conversion efficiencies of up to $47.1\,\%$ for a six junction solar cell under 143 Sun concentration[2] and, closer to consumer implementation, $26.7\,\%$ for single junction crystalline silicon solar cells.[3]

Balancing solar irradiation fluctuations requires energy storage solutions. Metal-ion batteries provide energy storage on required timescales[4] as well as flexibility and scalability and thus have experienced a huge growth as an off-site energy storage solution for renewable energy sources in recent years.[5,6] The efficiency of solar energy storage is thus governed by the individual efficiencies of the solar cell and battery, but also by required transmission lines, inverters, and rectifiers (efficiencies of ca. 93 to $97\,\%$ for inverters and $97\,\%$ for rectifiers) to transform the solar cell DC into Alternating Current (AC) of the grid and subsequently back into DC battery charging current – a process controlled by a charge controller:[7]

$$\eta_{\textit{solar to grid to battery}} = \eta_{PV} \cdot \eta_{\textit{inverter, rectifier}} \cdot \eta_{\textit{transmission}} \cdot \eta_{\textit{charge controller}} \cdot \eta_{\textit{DC charging}} \tag{5.1}$$

On-site storage has seen a significant boost in research interest, since fewer steps are required to transfer energy to the storage device. Various levels of integration

exist such as on-site battery storage, in which the solar cell DC current can charge batteries directly (DC battery charging efficiency of ca. $100\,\%$).[7] For an efficient operation, both battery cell voltage and maximum power point of the solar cell as well as charging currents need to match.[8] Dai and coworkers used a stack of four perovskite solar cells ($CH_3NH_3PbI_3$ as active material), which generate a charging voltage of approximately $3\,V$ – sufficient to charge a LFP ($LiFePO_4$ cathode) LiB battery with an overall efficiency of $7.80\,\%$.[9] Qiao and coworkers achieved an overall efficiency of $9.36\,\%$ with a perovskite solar cell (with $\eta_{PV} \approx 14\,\%$) charging a LCO ($LiCoO_2$ as cathode) LiB battery *via* a DC-DC converter (efficiency of approximately $88\,\%$).[10] For on-site energy storage in a two-component device, the overall efficiency can be expressed as:

$$\eta_{solar\ to\ battery} = \eta_{PV} \cdot \eta_{charge\ controller} \cdot \eta_{DC\ charging} \tag{5.2}$$

Solar batteries which integrate a solar cell and battery on a much smaller single device level present the next step of integration. No centralized charging controller is required, and charging occurs within the device between different distinct electrodes, tasked with solar energy conversion (PV), energy storage (battery anode or cathode) or bifunctional electrodes (also referred to as coupled light absorption and storage electrodes) capable of both energy conversion and charge storage at the same time. Since charging occurs directly and within the device, efficiency depends solely on the PV electrode and battery charging:

$$\eta_{direct\ solar\ battery} = \eta_{PV} \cdot \eta_{DC\ charging} \tag{5.3}$$

The first pathfinding solar battery concept of combined solar energy harvesting and storage was investigated already in 1976 by Hodes, Manassen, and Cahen, consisting of a Cd-Se polycrystalline chalcogenide photoanode, capable of light absorption and photogenerated electron transfer to the S_2^-/S redox couple in the electrolyte.[11] The redox couple subsequently re-oxidized at the silver (Ag) cathode, forming Ag_2S and effectively storing the photogenerated electrons. More recently, direct solar batteries have seen a huge boost in research activity, with manifold device designs being proposed with various levels of integration.[12–16]

As this emerging research field is burgeoning with different design approaches, the community lacks understanding of the processes involved during photocharging, as well as design guidelines to move the field forward in a concerted effort.[12]

Herein, we address this issue by organizing all currently reported designs into an ensemble of six distinct solar battery types with different levels of integration. We discuss the electrochemical signature of the devices, provide design principles, and give our perspective of how different designs lead to different solar battery features for specialized applications. Note that we will touch upon solar redox flow batteries (or Solar Flow Batterys (SFBs)) only peripherally for cases where the active photoelectrode is not a redox flow electrolyte. For a more comprehensive treatment of this topic, we refer the reader to more extensive papers and reviews on this topic.[17–21]

5.1. The Solar Battery Experiment

Let us start by discussing the operation principle and electrochemical signature of solar battery devices. Upon illumination, absorbed photons in the light absorbing layer are tasked with (1) providing a charging photocurrent I_{ph} or (2) reducing the required charging voltage V_c by decreasing the required charging voltage (resulting from the voltage gap between battery cathode and anode) *via* the photovoltage V_{ph} of the light absorber. We classify the former as IEC and the latter as VEC mode. One can understand these modes from the respective electric circuits with solar cell, battery, and power supply being connected in parallel or in series, respectively (Figure 5.1 (a)). Both designs reduce the overall energy required to charge the device but provide different charging characteristics that we will discuss in the following.

Different light operation modes are available (Figure 5.1 (b)). We describe them with the following terminology: Charging and discharging operations are abbreviated with 'c' and 'd', applied electric current and photocurrent flux is abbreviated with 'E' and 'L', respectively. The device can be operated in the dark (cEdE), reminiscent of a classical battery. Light can charge the device solely (cLdE), assist charging (cLEdE), or assist both charging and discharging (cLEdLE).

The electrochemical signature of the device depends on the mode of operation. GCD applies a charging and subsequent discharging current (Figure 5.1 (c): I_c and I_d). For IEC, since the overall current results from cumulative I_c and photocurrent I_{ph}, during illuminated charging (charging Light Electric (cLE)) the required charge from I_c to fully charge the device ($C_{el,c}$) decreases compared to the dark operation (charging Electric (cE)). During illuminated discharging (discharging Light Electric (dLE)), the extracted charge ($C_{el,d}$) increases. VEC operates differently: Since V_{ph} decreases V_c during illuminated charging (cLE), the required power $P_{el,c}$ from V_c

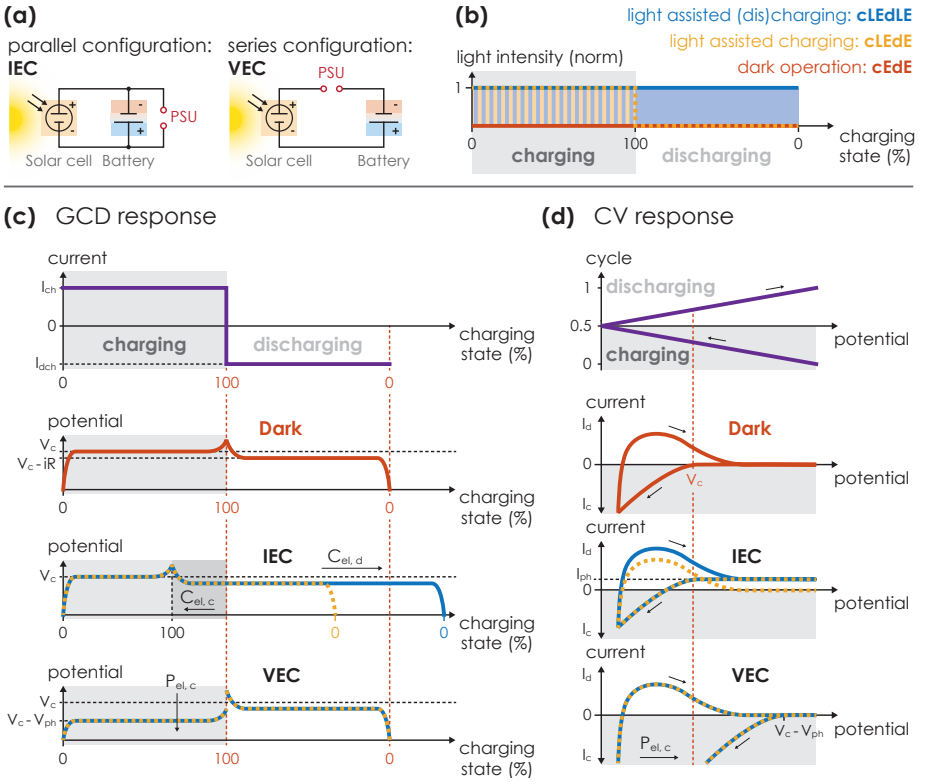

Figure 5.1. Operation mechanism of a solar battery. **(a)** In a solar battery the solar cell functionality can either operate in parallel (IEC) or in series (VEC) to the battery and power supply/consumer (Power Supply (PSU)). **(b)** Illumination intensity depending on the charging state (Charging State (ch)) for three distinct light operation modes: Electric charging and discharging *via* an applied current in the dark (charging Electric, discharging Electric (cEdE)), light assisting only charging (charging Light Electric, discharging Electric (cLEdE); in case of light only charging: charging Light, discharging Electric (cLdE)), or light assisting both charging and discharging (charging Light Electric, discharging Light Electric (cLEdLE)). **(c)** GCD response of a solar battery. Applied current (top) and respective potential response for classical batteries in the dark, IEC, and VEC devices for different operation modes (b). **(d)** CV response of a solar battery. Applied potential (top) and respective CV measurements for classical batteries in the dark, IEC, and VEC devices for different operation modes (b).

also decreases ($P_{el,c} = (V_c - V_{ph}) \times I_c$). On the contrary, illumination during discharging (dLE) does not significantly affect the extracted charge or discharging power. Numerous examples of GCD signatures for IEC[10,22,23] and VEC[24–27] can be found in the literature and will be discussed more in more detail in the last section. CV on the other hand applies an increasing and subsequent decreasing potential ramp, which can be understood as charging and subsequent discharging operation

(Figure 5.1 (d)). Both IEC and VEC devices produce the same CV shape in dark (cEdE) operation: A sharp increase in I_c when V_c is reached and upon reversing the potential ramp an increase in I_d is observed. When illuminating during charging (cLE), IEC devices produce the photocurrent I_{ph}, which causes I_c and associated $_{Cel,c}$ to decrease (note that integrating the CV charging sweep results in $C_{el,c}$). VEC devices on the other hand decrease the V_c onset and associated $P_{el,c}$. Similar to GCD measurements, light-assisted discharging (dLE) only affects IEC devices by producing an offset of I_d *via* I_{ph}. The much larger integrated area of the CV discharging sweep in case of cLEdLE underlines that illuminating during discharging can significantly increase extracted charge.

Light-only charging (cLdE) is a facile operation in the IEC design, but not possible for the VEC design, since a conduction band (CB) at lower absolute energy (or from an electrochemical perspective more negative potential) than the Fermi level of the (charged) battery anode is required. This is challenging if for example Li-metal anodes with very negative reduction potentials (-3.04 V *vs.* NHE) are employed.

Light is utilized by solar batteries to improve overall energy efficiency by reducing either the required charging current (current efficient charging: IEC) or charging voltage (voltage efficient charging: VEC).

Let us conclude with some general design considerations: In case of IEC and all operation modes involving light, the battery output voltage is restricted by the bandgap of the light absorber. VEC designs do not have this limitation but are not capable of light-only (charging Light (cL)) charging. Photogenerated charge carriers can possess a significant oxidative/reductive power, which is beneficial to transfer one carrier during cL or cLE (*e.g.*, for metal-air batteries the Oxygen Evolution Reaction (OER) during photocharging is facilitated through this oxidative power).[28] However, the large oxidative power comes with the risk of easier degradation of the electrolyte. For readers interested in electrolyte decomposition in solar battery concepts, we recommend reviews discussing this effect in more detail.[12,14] In addition, the illumination pathway of very thick battery electrodes with intrinsic short carrier diffusion lengths presents conceptional difficulties: a thick layer is beneficial for capacity, but detrimental for light absorption at the junction where the photocurrent is produced.[29]

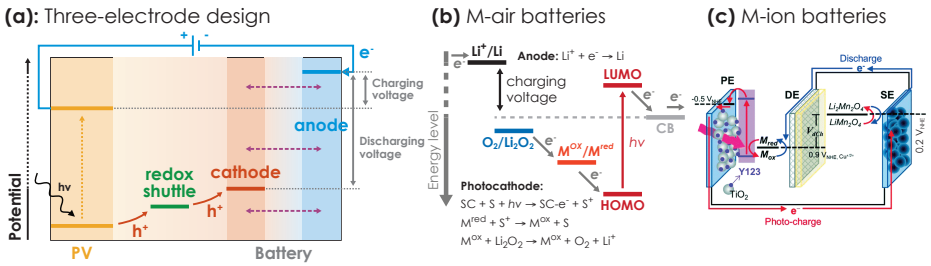

Figure 5.2. Three-electrode solar battery designs during photocharging. (a) Light energy conversion and energy storage can be implemented in the same device *via* three distinct electrodes (photoactive electrode, battery cathode, and anode). Multiple charge transfer mechanisms are required within the cell (*e.g.*, redox shuttles) and externally *via* a wire to transfer the photogenerated charges. Many implementations of this design have been reported, *e.g.*, **(b)** as metal-air (Li^+/Li as anode, SC as photoactive semiconductor cathode, carbon paper @ stainless steel gauze as O_2/Li_2O_2 cathode, a DSSC as photoelectrode, and I^-/I_3^- as redox shuttle (abbreviated with M^{ox}/M^{red})) Adapted with permission from Ref.,[26] Springer Nature 2014. **(c)** Further reports include a metal-ion battery (overlithiated $LiMn_2O_4$ @ Gn as anode, Pt @ PEDOT as cathode, Y123 dye as DSSC photoelectrode, and $Cu^{+/2+}(dmp)_2$ as redox shuttle). Reproduced with permission from Ref.,[30] Royal Society of Chemistry 2020.

5.2. A brief overview of current solar battery concepts

As introduced above, the field of solar batteries is in its infancy and as such rich yet heterogenous in terms of concepts and approaches. Solar battery designs can be organized according to the type of charge storage mechanism:[12] Photogenerated charge carriers assist in ion (de)insertion or oxidize/reduce a redox mediator. While this classification of reports captures fundamental mechanistic similarities, it falls short of comparing characteristics on the device level. To set the stage to discuss similarities between different device designs, we first mention designs relying on three electrodes with distinct tasks (light absorption, battery cathode, and anode) and then proceed to devices using bifunctional (or coupled light absorption and storage) electrodes that can perform two tasks at the same time.

5.2.1. Three-electrode designs

The concept of three-electrode designs is summarized in Figure 5.2 (a). Upon illumination, photoexcited electrons and holes are generated in the photoactive electrode. Photogenerated electrons and holes are transferred to the battery electrodes *via* the external circuit and a redox shuttle, respectively. In the following, we will

discuss different implementations of this design, exemplified by key publications.

Metal air (M-O_2) batteries present an attractive battery type due to their potentially large cell voltage and high theoretical specific energy density (for lithium-air (Li-air): ~ 2.96 V and ~ 5928 W h kg^{-1}).[12] Traditional Li-O_2 batteries consist of a lithium metal anode and a porous cathode, which is saturated with oxygen. Upon discharging, the oxygen is reduced at the cathode and reacts with Li^+ ions to form Li_2O_2. However, recharging the battery is challenging, since a large overpotential is required for re-oxidation of the oxidized Li-species (here Li_2O_2) to oxygen (OER reaction) and Li_2O_2 is both insoluble and insulating.[31] Solar batteries present an exciting solution to overcome this challenge, since photoexcited holes may produce a significant oxidative force for the OER reaction – a feature of many light absorbing materials, which is widely taken advantage of in photo(electro)catalysis. As such, already in 2014 Wu and coworkers investigated a Li-O_2 battery that included a dye-sensitized photoelectrode (Figure 5.2 (b)).[26] Since the electrons possess a significant energy due to photoexcitation when injected into the CB of dye-sensitized TiO_2, the required charging voltage significantly decreased from ca. 4 to 2.7 V *vs.* Li/Li^+. Thus, light energy is used here both to reduce the applied charging voltage *via* photoexcited electrons and to increase energy density as well as round-trip efficiency. In addition, the OER reaction at the cathode is facilitated (carbon paper on top of stainless-steel gauze) *via* photoexcited holes (Figure 5.2 (b)).[28] Further variations on this theme have been reported, including Li-O_2 batteries with carbon nitrides as photoelectrode.[32] Zinc-air (Zn-O_2) batteries have also been reported with carbon nitrides[33] or poly(1,4-di(2-thienyl))benzene (PDTB) photocathode in conjunction with TiO_2 as photoelectrode.[34] Note that for all these reported battery designs no pure photocharging is possible, since photoexcited electrons do not have a larger potential than the very negative electrode potential of M_x^+/M. We recommend the following reviews for the interested reader to dive further into this exciting research field.[28,35–37]

While three-electrode solar batteries have clear advantages for metal-air type batteries in terms of both a reduced applied charging voltage and significantly more driving force for the photoexcited hole extraction, metal-ion batteries have also been reported. These three-electrode designs benefit from a reduced charging voltage, whereas high energy photogenerated holes are rather problematic since they can potentially degrade (that is, oxidize) the electrolyte.[12] For instance, Zhou and coworkers reported a Li-ion battery with LFP as cathode material and a TiO_2 photoelectrode, resulting in a 20 % larger round-trip efficiency and a reduction in charging

cell voltage from 3.45 to 2.78 V.[38] A sodium-ion (Na-ion) battery with a similar device structure has also been reported by Zhou and coworkers reducing the charging voltage from 0.86 to 0.08 V under illumination.[39] Harvesting diffuse indoor light is an area of possible energy recovery with huge potential that has so far not seen widespread application. Recently the first 1-device 3-electrode solar battery was reported by Song and coworkers (Figure 5.2 (c)), that is tailored towards indoor light absorption with light intensities <0.5 % of 1 Sun illumination.[30] The device consists of dye-sensitized TiO_2 nanoparticles (Y123 and DN-F10 dyes), which transfer photoexcited electrons to the cathode ($LiMn_2O_4$, LMO) while photoexcited holes are stored in the liquid redox mediators I^-/I_3^- or $Cu^{+/2+}(dmp)_2$. During discharging, LMO is oxidized and the mediator is reduced *via* an auxiliary platinum (Pt) electrode functionalized with PEDOT (cathode). An overall efficiency of 11.5 % was achieved. Note, however, that strictly speaking this concept does not fall into the category of devices discussed herein, since holes are not stored in a dedicated cathode but rather in the electrolyte – this concept can thus rather be classified as a half-solid-half-redox flow photo battery. A similar device has recently also been published for Li-S batteries.[40]

To conclude, the family of devices consisting of three electrodes in one enclosure present a further step towards integration and mark a significant milestone in the solar battery field. While the concept requires only one single device, integration is challenging on the device level as three electrodes are required and charge transfer between the electrodes has to be more carefully tuned, for example by using redox mediators and external wires. For instance, it is essential to form an effective redox cycle which requires potential energies of the individual electrodes to align. Furthermore, in its configuration incorporating a metal electrode with a very negative standard potential such as Li^+/Li (as shown in Figure 5.2 (a)) it is challenging to charge the battery solely by light (a photoabsorber with a more negative CB potential is required), somewhat limiting the implementation of such devices.[12] Thus, the benefit of illumination is mainly to assist in reducing the charging voltage, *i.e.*, charging power.

5.2.2. Bifunctional electrodes *via* heterojunctions

Bifunctional electrodes consist of one or multiple materials, which possess the dual functionality of light absorption and charge storage on a single electrode. In principle, two different design routes exist: (1) A heterojunction of two materials – ei-

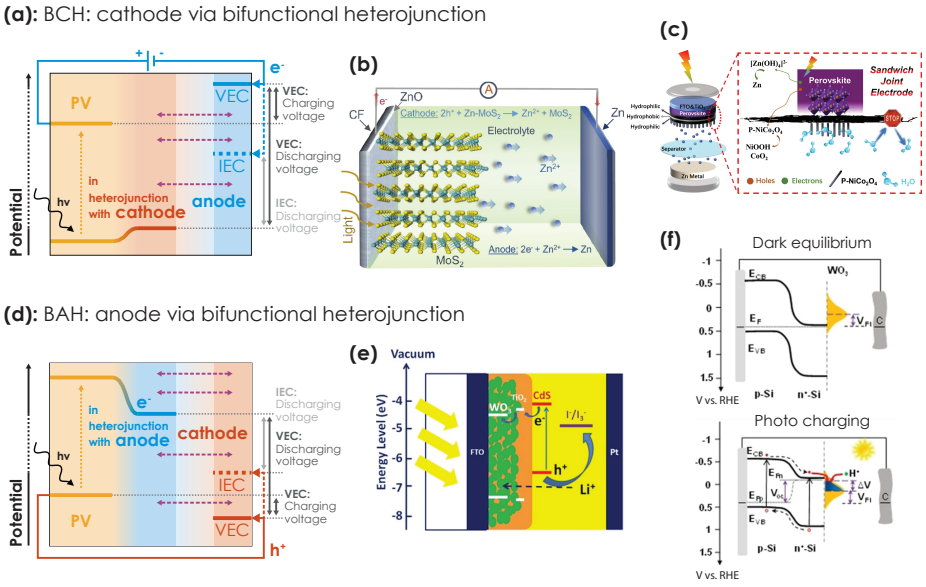

Figure 5.3. Two-electrode solar battery designs during photocharging, which employ bifunctional heterojunction electrodes. Bifunctional electrodes can be developed either as composites or planar heterojunctions. **(a)** Working scheme of a Bifunctional Cathode Heterojunction (BCH) electrode in a solar battery. Electrode colors are defined analogous to Figure 5.2 (a): Yellow for photoactive layer, blue and red for anode and cathode, respectively, blue arrows outside the device indicate necessary external wires for flow of electrons, and purple dashed arrows indicate ion movement within the battery. Schematic anode band positions are shown for both VEC (solid) and IEC (dashed) devices. Photoactive cathodes can be developed as composites **(b)** as shown for MoS_2 @ ZnO in a Zn-ion battery during photocharging. Reproduced from Ref.[22] under the terms of open access CC BY 4.0 license (http://creativecommons.org/licenses/by/4.0/), American Chemical Society 2021. Photoactive can also occur as planar heterojunctions **(c)** as shown for a Zn-ion battery consisting of perovskites as photoabsorber and Co_2P-CoP-$NiCoO_2$ as charge storage layer. Reproduced from Ref.[41] under the terms of open access CC BY 4.0 license (http://creativecommons.org/licenses/by/4.0/), Springer Nature 2022. Both schemes show photocharging of the device. **(d)** Working scheme of a Bifunctional Anode Heterojunction (BAH) electrode in a solar battery. Color scheme is analogous to (a); red arrows outside the device indicate necessary external wires for hole transfer during photocharging. Cathode band positions are shown for VEC (solid) and IEC (dashed) devices. **(e)** The anode can be developed as composite, as shown for photocharging for a CdS-sensitized WO_3 anode which uses I^-/I_3^- as cathode. Reproduced from Ref.,[42] John Wiley & Sons 2019. **(f)** Capacitor-type charge storage in a Faradaic junction between Si and WO_3 was shown as a BAH, in which Si injects photoelectrons into WO_3 where they are stored. Reproduced from Ref.,[43] John Wiley & Sons 2021.

ther as a composite (bulk heterojunction) or a layered planar structure (Figure 5.3), which perform and are optimized for the two tasks, *i.e.*, light absorption and charge storage. Alternatively, (2) inherently bifunctional materials can be utilized, which

are capable of absorbing light and storing the photogenerated charges (Figure 5.4). In this section we will elucidate *bifunctional electrode* approaches *via* heterojunctions, while in the forthcoming sections we will focus on electrodes based on *bifunctional materials*.

Bifunctional cathode heterojunctions (BCHs) absorb photons and store photoexcited holes, *e.g.*, by assisting Li deintercalation during photocharging. Photogenerated electrons are transported *via* an external circuit to the anode. A scheme of the working mechanism is shown in Figure 5.3 (a). Numerous BCHs have been investigated for metal-air batteries, due to their attractive features in facilitating OER *via* photoexcited holes, *i.e.*, photo-electrocatalysis.[28] The photocathode has to possess good light absorption properties and at the same time good electrocatalytic OER performance. In fact, the overpotential for photo-electrocatalytic OER is likely the main challenge.[31] Yu and coworkers reported a TiO_2 @ Fe_2O_3 composite BCH for a Li-O_2 battery, in which nanostructuring of the cathode allowed a more uniform evolution of the Li_2O_2 film upon discharging. This significantly increased the kinetics of the OER reaction due to a very low overpotential of only 0.19 V.[44] Reports of BCHs for Li-O_2 batteries are vast and we will name several different examples utilizing nanomaterials in the following: CdSe/ZnS quantum dots @ CNT nanocomposite,[45] Fe_2O_3 @ NiOOH,[46] Au nanoparticles @ TiO_2 (the Au nanoparticles show significant visible light absorption due to a localized surface plasmon resonance effect),[47] or Au nanoparticles @ NV - C_3N_4.[48]

Metal-ion batteries on the other hand have also been reported with composite BCHs *via* organic based BCHs such as perovskite quantum dots @ Metal Organic Framework (MOF),[49] or inorganic based BCHs such as molybdenum disulfide (MoS_2) @ zinc oxide (ZnO) (Figure 5.3 (b))[22] for Zinc-ion (Zn-ion) batteries, and SnO_2 @ TiO_2,[50] or perovskites and carbon for Li-sulfur batteries.[51]

An example for a BCH *via* a planar junction between photoabsorber and charge storage material was recently published by Gao and coworkers for a Zn-ion battery using a perovskite (photoabsorber) and Co_2P-CoP-$NiCoO_2$ nanometric arrays, which showed a solar-to-output efficiency of around 6 %.[41] A scheme of the battery is shown in Figure 5.3 (c).

Bifunctional anode heterojunctions (BAH) based solar batteries (Figure 5.3 (d)) rely on a different light charging mechanism: Upon light absorption, the photoexcited electrons are stored on the bifunctional anode. The hole is then trans-

ferred to the cathode *via* the external circuit. Far fewer solar batteries of this type have been reported, likely due to the different types of anodes used: no metal anodes or metal ion intercalation anodes with highly negative oxidation potentials (electrochemical scale) enables high cell voltages can be used. At the same time, designing a suitable storage cathode is more challenging as compared to the choice of anode in BCH designs due to the stringent requirements for hole storage: Hole storage should occur at potentials as positive as possible to enable a reasonably large cell voltage, but at the same time not too positive to enable sufficient driving force for the transfer of the photogenerated holes on the anode side and to prevent electrolyte degradation. Recently, Demopoulos and coworkers reported a CdS-sensitized WO_3 composite BAH, which utilizes I^-/I_3^- in the electrolyte as a liquid storage cathode (Figure 5.3 (e)).[42] Note that this design does not require an external wire and can be classified as a half-redox flow battery (or solar redox flow battery), since the cathode is part of the electrolyte solution and a Pt electrode is used as current collector. A voltage of ca. $0.2\,\mathrm{V}$ was achieved under discharging, underlining the challenges of reaching a large cell voltage in this design. Other reported BAH designs are TiO_2 as light absorber and V_2O_5 as electron storage material.[52] The system reached a good overall efficiency of $7.61\,\%$. A similar design but with a dye-sensitized solar cell was reported by Wang, reaching an overall efficiency of $0.82\,\%$.[53] However, while research output on BCHs by far surpasses BAHs for battery-type devices, there are more examples of photocapacitors based on photoanodes. Devices include heterojunctions between nanostructured Indium Tin Oxide (ITO) and P3HT as photoabsorber where during photocharging photo-induced electrons cause capacitive charging.[54] A Faradaic junction based on Si/WO_3 has been reported by Z. Zou and coworkers, which can capture and store photo-induced electrons *via* a capacitor-type storage mechanism (Figure 5.3 (f)).[43] Here, Si and WO_3 form a Faradaic junction. Before charging, the Si Fermi levels align with WO_3 (Figure 5.3 (f), top). Upon illumination, a photovoltage of $0.5\,\mathrm{V}$ is produced, that is sufficient to inject photogenerated electrons into WO_3 (Figure 5.3 (f), bottom). We emphasize that the charge storage mechanism here is more a surface than a bulk process and as such capacitance shows a linear dependence on cell voltage.

In summary, bifunctional electrodes present the next step of integrated solar battery designs. Only two electrodes are required, since one of the electrodes is capable of effectively performing two functions: light absorption and charge storage. Heterojunctions have been demonstrated for anodes (BAHs) and cathodes (BCHs) as either composites or bilayers in a planar junction. Charge transfer occurs *via* an

external wire, or in case of solar redox flow batteries *via* a redox shuttle. Illumination allows to reduce the required applied electric charging voltage or provides a photocurrent in parallel to the applied electric charging current (see Figure 5.1 (a) or (b)). However, there are also challenges associated with BCH and BAH designs: The photogenerated holes possess a significant oxidation force, which can possibly oxidize and thus degrade the electrolyte.[12] Formation of a heterojunction is a very complex process, which is inherently difficult to control and thus challenging to optimize.[55]

5.2.3. Bifunctional electrodes *via* bifunctional materials

Bifunctional electrodes discussed above require two distinct materials, tasked with light absorption and charge storage. However, recently the field of solar batteries moves towards a single material performing both light absorption and charge storage. While this design presents the highest level of integration, it is simultaneously most difficult and comes with both conceptual and practical challenges.[12,14,28,35,57–59] This is because a material must function both as a light absorber and as a mixed electronic-ionic conductor (Mixed Electronic-Ionic Conductor (MIEC)) to harvest light, shuttle electronic, and store ionic charges – complex photophysical effects which must occur simultaneously. Bifunctional materials exist both for cathodes and anodes, albeit by far more cathodes than anodes. In the following, we will present key reports.

Bifunctional cathode materials (BCMs) work similar to the BCHs discussed above but require only one bifunctional material (Figure 5.4 (a)): The BCM simultaneously absorbs light and stores holes, while photogenerated electrons are transferred *via* an external circuit to a suitable storage anode. Recently, there has been a stark increase in reports on BCMs for different battery types, both organic and inorganic. Wang and coworkers reported a COF as BCM for a Zn-ion battery (Figure 5.4 (b)).[25] The device showed a good overall efficiency of 1.1 % at 1 Sun illumination. Here, a donor-acceptor COF @ carbon nanotube core-shell photocathode acts as an electron relay that shuttles electrons to the Zn anode while storing OTf^- anions on the oxidized donor units and Zn^{2+} cations on the reduced acceptor units of the COF during the respective charging and discharging operation. More recently, the same group published another bifunctional donor-acceptor COF cathode for Zn-ion batteries, that consists of a COF with different donor and acceptor linkers.[60]

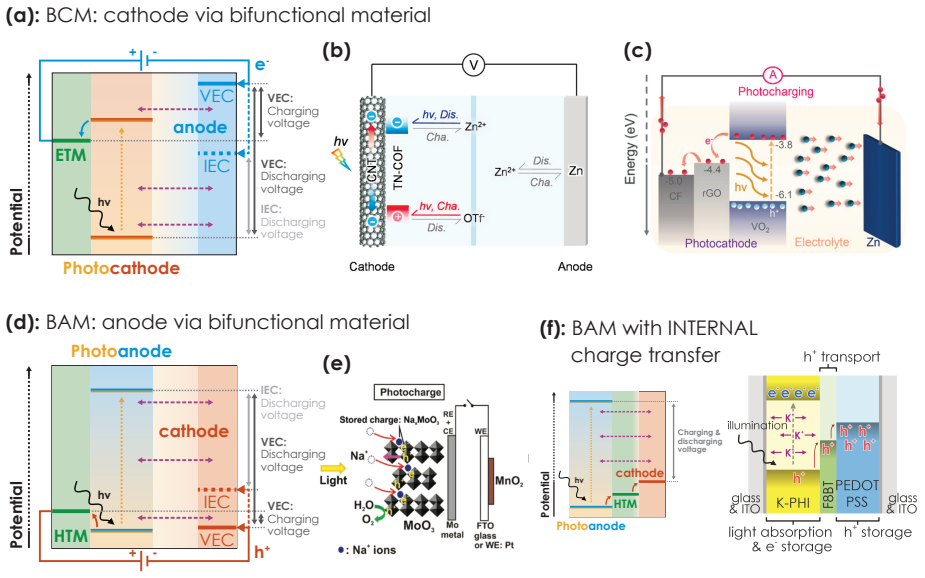

Figure 5.4. Two-electrode solar battery designs during photocharging, which employ bifunctional materials. **(a)** Working scheme of a Bifunctional Cathode Material (BCM) electrode in a solar battery. Electrode colors are defined analogous to Figure 5.2 (a), except gradients: Yellow-red gradient signifies the BCM, blue the respective anode, green the ETM; blue arrows indicate flow of electrons, and purple dashed arrows indicate ion movement within the battery. Note that blue arrows outside the device indicate necessary external wires for photocharging. Anode band positions are shown for VEC (solid) and IEC (dashed) devices. Examples include **(b)** a Covalent Organic Framework (COF) acting as organic BCM. Reproduced from Ref.,[25] John Wiley & Sons 2022. **(c)** Another example is VO_2 acting as inorganic BCM – both for Zn-ion batteries and both schemes showing photocharging. Reproduced from Ref.[24] under the terms of open access CC BY 4.0 license (http://creativecommons.org/licenses/by/4.0/), John Wiley & Sons 2021. **(d)** Working scheme of a Bifunctional Anode Material (BAM) electrode in a solar battery. The color scheme is defined analogous to (a) with the exception that yellow-blue gradients show the BAM, red and green the respective cathode, and HTM. The red arrows indicate flow of holes, with red arrows outside the device showing the necessary external wires. Cathode band positions are shown for VEC (solid) and IEC (dashed) devices. **(e)** Example of MoO_3 acting as BAM for a Na-ion battery during photocharging. Reproduced from Ref.,[56] John Wiley & Sons 2017. **(f)** BAM with internal charge transfer. Color scheme is defined similar to (d). No external wires are required, since photogenerated holes are transferred internally *via* the separator. An example of such a solar battery is shown on the right, with the carbon nitride K-PHI acting as BAM. Reproduced from Ref.,[23] Royal Society of Chemistry 2023.

This architecture, similarly engineered to optimize charge separation, achieved an extra round-trip efficiency of 35 %. In both publications, the authors showed that such donor-acceptor structures can form nanoscale heterojunctions analogous to BCHs but on one bifunctional material, in which different parts (here linkers) per-

form the respective tasks. Organic BCMs for Li-ion batteries have been reported for Covalent Organic Polymers (COPs),[61] tetrakislawone molecules,[62] C_{60} @ porous organic cages with an overall efficiency of $1\,\%$,[63] and perovskites with an overall efficiency of $0.5\,\%$[64] and $0.43\,\%$.[65] Organic BCMs for Li-O_2 batteries have been reported for large sized siloxane nanosheets.[66] An inorganic BCM has recently been reported for vanadium dioxide (VO_2) as Zn-ion battery by De Volder and coworkers (Figure 5.4 (c)), reaching an overall efficiency of $0.18\,\%$.[24] The same group also reported vanadium pentoxide (V_2O_5), performing the same task with a slightly larger overall efficiency of $0.22\,\%$ for 1 Sun and $2.6\,\%$ for 455 nm illumination.[67] BCMs for Li-O_2 batteries have been reported for WO_3 nanowires[68] and metal-organic polymer nanosheets composed of cobalt tetramino-benzoquinone.[69] Zn-O_2 batteries with BCMs have also been reported with $BiVO_4$ and α-Fe_2O_3 BCMs.[70]

Bifunctional anode materials (BAMs) analogous to BCMs, are the bifunctional material variant of BAHs. A BAM material absorbs light and stores photoexcited electrons (Figure 5.4 (d)). The photoexcited holes are shuttled *via* an external wire to the respective cathode. Similar to BAHs and as discussed above, there are only few recent reports of BAMs. Ng and coworkers reported MoO_3 as BAM for Na-ion batteries, which under illumination stores photogenerated electrons that assist in intercalation of Na ions (Figure 5.4 (e)).[56] A discharging voltage of about $0.2\,V$ was achieved, significantly lower than the voltages achieved for BCMs.

Note that apart from the solar redox flow BAM all proposed designs so far require external charge transfer during photocharging to transport one of the photogenerated charge carriers to the other electrode. This is due to the challenging design of simultaneous electron storage and directional hole transfer *via* the electrolyte. For instance, if a redox shuttle is utilized, preventing recombination of photogenerated hole and electron on this redox shuttle before hole transfer to the cathode occurs is both a conceptual and practical challenge. Note that this is also a challenge for BCH, BAH, and BCM designs, if using internal charge transfer *via* a redox shuttle. Very recently, our group proposed an alternative internal charge transport mechanism using the BAM carbon nitride modification K-PHI (Figure 5.4 (f)).[23,71,72] Upon photoexcitation, photogenerated electrons are stored on K-PHI and photogenerated holes are injected into a HTM. This HTM then transfers the holes to the cathode, thus acting as both battery separator, electrolyte and rectified internal hole transporter. The efficiency of this process is reasonable, likely because hole transfer *via* the HTM occurs faster than recombination with the photogenerated electrons. Since no ex-

ternal wires are required for photocharging and a BAM is employed, this solar battery design represents a very high level of integration.

By performing both light absorption and charge storage, bifunctional materials enable the most recent and highest level of material integration in solar batteries.

To conclude, bifunctional materials are the most recent development in solar battery research. The solar battery charging and discharging mechanism is comparable to BCH and BAH solar batteries discussed above; however, the charge storage mechanism deviates significantly: No charge transfer between photoabsorber and charge storage electrode is necessary. Illumination can reduce the applied electric charging voltage or required electric charging current. While this design is likely the most integrated, it is also the most challenging: Electron extraction (for BCM) or hole extraction (for BAM) is likely more challenging compared to BAH and BCH systems due to easier recombination of photogenerated charges as a result of the high charge concentration on the same material. Additionally, the photocurrent may be reduced as a result of enhanced photogenerated exciton recombination on the BCM or BAM when charged – due to the high concentration of stored electrons or holes modifying the electric field in the BCM or BAM layer and inducing recombination.[73,74] Illumination pathway is difficult, since thick active layers providing a significant capacity may also produce significant parasitic absorption and thus reduce the light intensity at the where excitons are separated – which is likely only a small area due to the short exciton's or carrier's diffusion length.[12] The bifunctional material needs to fulfill key requirements such as a reasonably large bandgap to enable a large cell voltage albeit not too large to reduce visible light absorption too much. Lastly, the complex interplay of photophysical properties greatly complicates investigation of the light absorption and charge storage mechanism, which results in the absence of general design principles in the solar battery community.[12]

5.3. Design philosophy of solar batteries: Improving power or energy balance

As outlined above, different device designs lead to light-assisted battery operation with different charging modes. To classify the devices, we propose different charg-

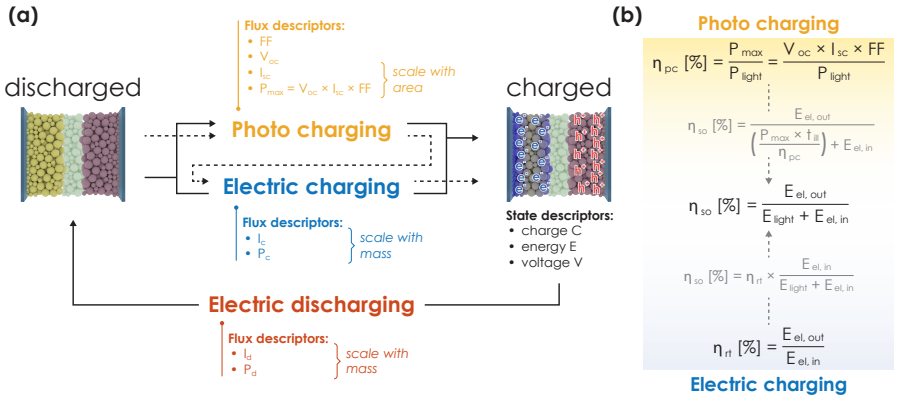

Figure 5.5. Charging and discharging during solar battery operation. (a) Energy flux and charging state descriptors. Charging occurs *via* photocharging (defined by the open circuit voltage V_{oc}, short circuit current I_{sc}, fill factor FF, and maximum power point P_{max}) or electric charging (defined by the charging current I_c and power P_c) and discharging occurs *via* electric discharging (defined by the discharging current I_d and power P_d). Photocharging and electric charging can occur in parallel (solid lines), or in series (dashed lines). The charging state of the solar battery is defined by charge C, energy E, and voltage U. **(b)** Efficiency of photocharging η_{pc}, electric charging (round-trip efficiency) η_{rt}, and overall efficiency of photo- and electric charging (solar-to-output efficiency) η_{so}. Additional (or extra) round-trip efficiency is also often calculated, which results from subtracting η_{rt} of the solar battery operated under illumination from η_{rt} in the dark. Conversion of efficiencies is given in grey color.

ing and discharging energy fluxes between the light absorber and charge storage materials (Figure 5.5 (a)).

The charging state of the solar battery can be described by the amount of charges $C\ [\mathrm{C\,g^{-1}}]$ stored on the device, the energy $E\ [\mathrm{W\,s\,g^{-1}}]$ of the accumulated charges, and a cell voltage U [V] that develops from the energy difference between the potential of the anode and cathode. Performance is typically normalized against the mass (or volume) of the electrode to give the specific energy or power densities, respectively.[75] During operation of the solar battery, the charging state descriptors C, E, and U are modified by different inbound or outbound energy fluxes (Figure 5.5 (a), middle): (1) Photocharging occurs upon light absorption and separation of the electron hole pair. Both charge carriers then are available for charging the battery. The short circuit current $J_{sc}\ [\mathrm{mA\,cm^{-2}}]$ and the open circuit voltage V_{oc} [V] describe the maximum possible photocurrent and photovoltage, respectively. Maximum power $P_{max}\ [\mathrm{W\,cm^{-2}}]$ depends on the fill factor FF, which acts as an ideality criterion of photocurrent in solar cells (how much the solar cell deviates from J_{sc} and V_{oc}, when operated at P_{max}) and solar batteries.[76] All these parameters serve as photocharg-

ing descriptors and scale with illumination area. (2) Electric charging on the other hand occurs when a charging current is applied – analogous to GCD of a battery. The applied current J_c governs the charging rate and power P_c. Note that normalization occurs typically against mass (or volume) of the battery electrode, analogous to the charging state descriptors.[75] (3) Electric discharging occurs if a discharging current J_d is applied, which governs the discharging power P_d. Analogous to electric charging, normalization is performed with device mass (or volume).

Photocharging and electric charging can occur in parallel as delineated in Figure 5.1 (a), if the photoactive material provides a photocurrent additionally to the applied electric current (Figure 5.5 (a), solid lines). While the overall charging current increases, the applied voltage is the same than if the device is operated in the dark. As mentioned above, we term this IEC, since energy efficiency is improved by increasing overall charging current *via* the photocurrent (Figure 5.6 (a)). Note that in theory the required charging voltage remains the same, *i.e.*, is equal to the battery voltage. As discussed above, the following charging modes are available: cEdE, cLdE, cLEdE, cLEdLE.

On the other hand, photocharging and electric charging can also occur in series as outlined in Figure 5.1 (a) (Figure 5.5 (a), dashed lines). In this case, the overall charging current remains the same, but the required applied voltage decreases significantly through the additional photopotential – hence, we termed it VEC. Note that while cLE is enabled, charging only *via* the photocurrent (cL) is not possible, since the CB of the light absorber is located at smaller energies than the battery anode – a potential difference that needs to be overcome *via* the applied charging voltage. Note that if the light absorber CB has a larger energy than the anode, cL becomes possible but the design can be understood as an IEC device. To name an example: Li-ion batteries have a strongly negative anode standard potential (Li/Li^+ = $-3.04\,V$ *vs.* NHE) and are thus employed for VEC devices that can only perform cLE. Zn-ion batteries on the other hand have a far less negative anode standard potential (Zn/Zn^{2+} = $-0.76\,V$ *vs.* NHE) and are thus typically employed in IEC devices capable of both cL and cLE.[22,77]

Charging efficiencies of electric and photocharging are given in Figure 5.5 (b). The overall charging efficiency (often termed solar-to-output efficiency or solar-to-output electricity efficiency (SOEE)) η_{so} is defined by dividing the extracted energy E_{el}, out with the incoming energy $E_{light} + E_{el,in}$. If the device is charged only *via* an applied electric current in the dark (cEdE; $E_{el,out}$ divided by $E_{el,in}$), the efficiency is known as round-trip efficiency η_{rt}. The increase of efficiency during light-assisted

operation in comparison to the round-trip efficiency in the dark is often termed additional (or extra) round-trip efficiency. When a liquid charge carrier extraction mechanism is used (*e.g.*, a redox couple or in case of a SFB a catholyte/anolyte) the ratio between η_{so} and η_{pc} may hold information on the voltage matching of photoelectrode and the charge-extracting material and was recently termed solar power conversion utilization ratio (SPUR).[78] Note that when calculating with charge instead of energy, the round-trip efficiency becomes the coulomb efficiency CE. To account for photocharging, CE is sometimes specified as electric coulomb efficiency eCE, where the calculation remains the same than for CE, but incoming charges result from both applied current and photocurrent.[23]

The photocharging efficiency η_{pc} (for solar cells also known as power conversion efficiency) on the other hand is defined as the power that the solar cell provides *via* its photocurrent (Figure 5.5 (a)). To convert it into the overall charging efficiency η_{so} of a solar battery during light or light-assisted charging (Figure 5.5 (b)), the illumination time t_{ill} is required, which defines the time at which the solar battery operates at P_{max}.

The different energy fluxes (Figure 5.5 (a)) can also be utilized to derive improvement strategies of solar batteries towards a larger overall efficiency η_{so} (Figure 5.5 (b)). An increase in performance of the solar cell (*e.g.*, layer geometry (bulk or planar heterojunction, film thickness), charge transfer, separation and extraction efficiencies)[76,79] or battery functionality (*e.g.*, electrode mass, large cell voltage, good electronic and ionic conductivity)[75] both govern η_{so} and should be chosen according to the desired application. However, choosing improvement strategies may also produce conflicts. An example is illumination area vs. mass: Solar cell performance scales with area and generally requires thin films, while battery capacity scales with mass (Figure 5.5 (a)). We have recently introduced a form factor ($\left[\mathrm{g\,cm^{-1}}\right]$) to account for the device's geometry, which could be a viable strategy to compare different solar battery designs while also allowing to normalize for both area and mass.[29]

Examples of both IEC and VEC designs are shown in Figure 5.6. A straightforward example for IEC designs are three-electrode two-device designs that we mention in the introduction: A solar cell is connected in parallel to the battery and thus, provides a constant photocurrent charging the battery. The resulting GCD measurement of a design reported by Qiao and coworkers that we discuss in the introduction is shown in Figure 5.6 (a) for 10 cycles of charging *via* the solar cell and 10 cycles of charging *via* an applied electric current (DC supply charged).[10] The system consists of a Li-ion battery connected to a perovskite solar cell. Note that the shape

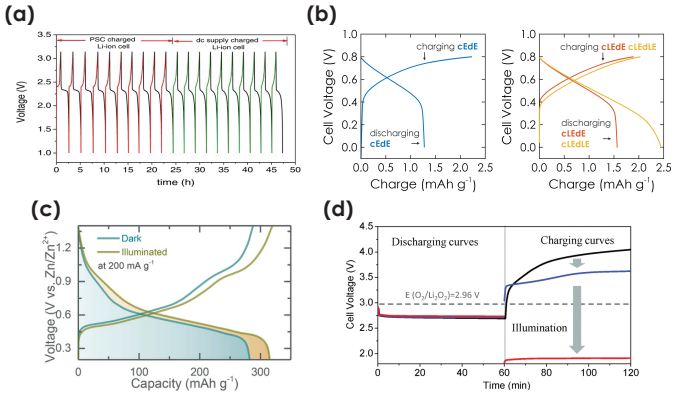

Figure 5.6. GCD measurements of IEC and VEC devices. IEC requires around the same applied voltage during charging, irrespective of whether the device is operated in the dark or under illumination. The charge C is proportional to photocurrent J_{sc} that is generated under illumination for the charging duration t_{ill}. Simultaneously, discharging under illumination lasts longer and produces a larger apparent capacity due to the photocurrent. **(a)** IEC based Li-ion battery charged with perovskite solar cells with an overall reported efficiency of $9.36\,\%$, that we discuss in the introduction. Reproduced from Ref.,[10] John Wiley & Sons 2017. **(b)** IEC based solar battery with the carbon nitride K-PHI as BAM with internal charge transfer reported recently by us shows light operation modes with larger apparent capacity. Reproduced from Ref.,[23] Royal Society of Chemistry 2023. **(c)** IEC based solar battery with VO_2 as BCM shows improved apparent capacity when operated under illumination. Reproduced from Ref.[24] under the terms of open access CC BY 4.0 license (http://creativecommons.org/licenses/by/4.0/), John Wiley & Sons 2021. **(d)** VEC reduces the required charging voltage (*i.e.*, power) when charged under illumination, and increases the discharging voltage (*i.e.*, power) when discharged under illumination. The required electric charging power is inversely proportional to the power provided by illumination. Typical examples are three electrode (Figure 5.2 (a)) Li-air batteries, where Zhou and coworkers reported a design with C_3N_4 photoabsorbers decreasing the required charging voltage from around 4.0 to $1.9\,$V. Reproduced from Ref.,[27] Royal Society of Chemistry 2015.

of the GCD cycles does not change, underlining the similar charging behavior *via* photocurrent or applied DC current.

An example of a BAM solar battery operating *via* IEC was recently reported by us (Figure 5.4 (f)).[23] In this design, K-PHI acts as both anode and light absorber (*i.e.*, as photoanode). A GCD cycle is shown in Figure 5.6 (b) for dark (cEdE) and light (cLEdE or cLEdLE) operation. Note that while the charging cycles look similar independent of illumination mode, discharging unveils a larger capacity at approximately similar power output.

De Volder and coworkers reported a VO_2-based BCM solar battery in IEC design that we discuss in Figure 5.4 (c), where photogenerated electrons are injected into the Zn anode.[24] When discharging, the apparent capacity is larger when operated

under illumination (Figure 5.6 (c)). This requires that the CB of the photoabsorber VO_2 is at a larger energy than the Zn-anode. The authors report an increase of apparent capacity from $282\,\mathrm{mA\,h\,g^{-1}}$ in the dark to $315\,\mathrm{mA\,h\,g^{-1}}$ under illumination.

In both IEC examples one can observe slight deviations in the charging and discharging plateau voltages. Moreover, in several literature reports of IEC-type designs, voltage variations become visible.[12,24] We hypothesize that the reason for this is either an anisotropic photocharging caused by uneven illumination, or the influence of enhanced conductivity under illumination. The latter produces a reduced iR drop within the active layer, which in turn reduces the required charging voltage, while during discharging under illumination the photovoltage could increase the discharging voltage. As expected, this effect is more pronounced when larger currents are used.[24]

VEC designs can be implemented as Li-air batteries discussed in the previous section. As an example, we show the GCD cycles of a Li-air solar battery presented by Zhou and coworkers in Figure 5.6 (d), which uses C_3N_4 as photoabsorber.[27] While discharging occurs at similar voltage, the charging voltage deviates significantly depending on the illumination conditions: While a voltage of around $4.0\,\mathrm{V}$ is required in the dark, under illumination this voltage is reduced to $1.9\,\mathrm{V}$. Since in a GCD experiment the applied current is constant, the required voltage is proportional to the required charging power.

Not only the electrochemical signature but also the operation modes of a solar battery depend on whether it is derived from IEC or VEC architectures. While light-assisted charging is possible for both IEC and VEC, light-only charging is only possible in IEC designs.

Let us conclude as follows: In this Perspective we lay out and classify different design philosophies of solar batteries. We have first discussed the electrochemical signature of two distinct operation principles: Current efficient (IEC) and voltage efficient (VEC) charging. We have then organized the literature of this burgeoning field into six distinct device categories: Three-electrode approaches use three electrodes with a distinct task in one device. Two-electrode approaches make use of bifunctional electrodes (either cathode or anode), which are realized by either producing a heterojunction between a light absorber material and a charge storage material (as bulk heterojunction composite or with layered planar geometry; termed

BCH and BAH) or by incorporating inherently bifunctional materials which provide the double functionality of light absorption and charge storage (termed BCM and BAM). We then outline different state descriptors which describe the charging state of the battery, as well as flux descriptors of energy flux during operation of the solar battery. This allows us to then understand the electrochemical signature of devices that we theoretically discuss at the beginning.

Thus, IEC systems have a constant charging voltage but reduce charging current, while VEC systems reduce the charging voltage albeit with no charging current reduction. Consequently, different applications arise: IEC systems may be more useful for microdevices or decentralized small-scale solar power plants where voltage fluctuations require additional more complex transformers. Implementation into existing systems might therefore be easier. VEC systems on the other hand are more beneficial for buffering DC devices with a variable voltage output, such as wind turbines. In any case, the new class of single-component devices circumvents the required electronics to connect a solar cell to a battery (such as DC-DC converter that make up a significant part of the costs of a solar power plant), albeit still requiring electronics to feed the energy into the grid.

The ideas presented in this Perspective are universal and can be applied to all solar battery designs proposed so far. They also help us classify and unify the literature in this rapidly evolving field, and to understand the key characteristics, main differences and pertinent performance criteria guiding the development of solar batteries. The concepts presented herein provide design principles to develop solar batteries with specific performance characteristics and thus target applications, especially as 'buffer' system for intermittent renewable energy supply as well as decentralized and cost-effective energy storage.

Acknowledgements

Financial support was granted by the Max Planck Society, the University of Munich (LMU), the Center for Nanoscience and the Cluster of Excellence e-conversion.

Conflict of interest

The authors declare no conflict of interest.

5.4. References

(1) Brunner, C.; Deac, G.; Braun, S.; Zöphel, C. *Renew. Energy* **2020**, *149*, 1314–1324.

(2) Geisz, J. F.; France, R. M.; Schulte, K. L.; Steiner, M. A.; Norman, A. G.; Guthrey, H. L.; Young, M. R.; Song, T.; Moriarty, T. *Nat. Energy* **2020**, *5*, 326–335.

(3) Yamamoto, K.; Yoshikawa, K.; Uzu, H.; Adachi, D. *Jpn. J. Appl. Phys.* **2018**, *57*, 08RB20.

(4) Tomaszewska, A. et al. *eTransportation* **2019**, *1*, 100011.

(5) IEA **2022**.

(6) Astakhov, O.; Merdzhanova, T.; Kin, L.-C.; Rau, U. *Sol. Energy* **2020**, *206*, 732–740.

(7) Gibson, T. L.; Kelly, N. A. *J. Power Sources* **2010**, *195*, 3928–3932.

(8) Sheryazov, S. K.; Nikishin, Y. A.; Schelybaev, M. V.; Chigak, A. S.; Doskenov, A. K. *IOP Conf. Ser.: Earth Environ. Sci.* **2022**, *949*, 012088.

(9) Xu, J.; Chen, Y.; Dai, L. *Nat. Commun.* **2015**, *6*, 8103.

(10) Gurung, A.; Chen, K.; Khan, R.; Abdulkarim, S. S.; Varnekar, G.; Pathak, R.; Naderi, R.; Qiao, Q. *Adv. Energy Mater.* **2017**, *7*, 1602105.

(11) HODES, G.; MANASSEN, J.; CAHEN, D. *Nature* **1976**, *261*, 403–404.

(12) Lv, J.; Xie, J.; Mohamed, A. G. A.; Zhang, X.; Wang, Y. *Chem. Soc. Rev.* **2022**, *51*, 1511–1528.

(13) Kandpal, S.; Ghosh, T.; Rani, C.; Chaudhary, A.; Park, J.; Lee, P. S.; Kumar, R. *ACS Energy Lett.* **2023**, 1870–1886.

(14) Salunke, A. D.; Chamola, S.; Mathieson, A.; Boruah, B. D.; de Volder, M.; Ahmad, S. *ACS Appl. Energy Mater.* **2022**, *5*, 7891–7912.

(15) Feng, H.; Liu, D.; Zhang, Y.; Shi, X.; Esan, O. C.; Li, Q.; Chen, R.; An, L. *Adv. Energy Mater.* **2022**, *12*, 2200469.

(16) Liu, R.; Wang, Z. L.; Fukuda, K.; Someya, T. *Nat. Rev. Mater.* **2022**, *7*, 870–886.

(17) Li, W.; Jin, S. *Acc. Chem. Res.* **2020**, *53*, 2611–2621.

(18) Ma, W.; Xie, C.; Wang, X.; Wang, H.; Jiang, X.; Zhang, H.; Guo, X.; Zong, X.; Li, X.; Li, C. *ACS Energy Lett.* **2020**, *5*, 597–603.

(19) McCulloch, W. D.; Yu, M.; Wu, Y. *ACS Energy Lett.* **2016**, *1*, 578–582.

(20) Sánchez-Díez, E.; Ventosa, E.; Guarnieri, M.; Trovò, A.; Flox, C.; Marcilla, R.; Soavi, F.; Mazur, P.; Aranzabe, E.; Ferret, R. *J. Power Sources* **2021**, *481*, 228804.

(21) Wedege, K.; Bae, D.; Smith, W. A.; Mendes, A.; Bentien, A. *J. Phys. Chem. C* **2018**, *122*, 25729–25740.

(22) Boruah, B. D.; Wen, B.; De Volder, M. *ACS Nano* **2021**, *15*, 16616–16624.

(23) Gouder, A.; Podjaski, F.; Jiménez-Solano, A.; Kröger, J.; Wang, Y.; Lotsch, B. V. *Energy Environ. Sci.* **2023**, DOI: 10.1039/d2ee03409c.

(24) Deka Boruah, B.; Mathieson, A.; Park, S. K.; Zhang, X.; Wen, B.; Tan, L.; Boies, A.; De Volder, M. *Adv. Energy Mater.* **2021**, *11*, 2100115.

(25) Wang, W.; Zhang, X.; Lin, J.; Zhu, L.; Zhou, E.; Feng, Y.; Yuan, D.; Wang, Y. *Angew. Chem. Int. Ed.* **2022**, *61*, e202214816.

(26) Yu, M.; Ren, X.; Ma, L.; Wu, Y. *Nat. Commun.* **2014**, *5*, 5111.

(27) Liu, Y.; Li, N.; Wu, S.; Liao, K.; Zhu, K.; Yi, J.; Zhou, H. *Energy Environ. Sci.* **2015**, *8*, 2664–2667.

(28) Du, D.; Zhu, Z.; Chan, K.-Y.; Li, F.; Chen, J. *Chem. Soc. Rev.* **2022**, *51*, 1846–1860.

(29) Gouder, A.; Yao, L.; Wang, Y.; Podjaski, F.; Rabinovich, K. S.; Jimenez-Solano, A.; Lotsch, B. V. *ACS Energy Lett.* **2023**.

(30) Kim, B.-M.; Lee, M.-H.; Dilimon, V. S.; Kim, J. S.; Nam, J. S.; Cho, Y.-G.; Noh, H. K.; Roh, D.-H.; Kwon, T.-H.; Song, H.-K. *Energy Environ. Sci.* **2020**, *13*, 1473–1480.

(31) McCloskey, B. D.; Scheffler, R.; Speidel, A.; Bethune, D. S.; Shelby, R. M.; Luntz, A. C. *J. Am. Chem. Soc.* **2011**, *133*, 18038–18041.

(32) Zhu, Z.; Shi, X.; Fan, G.; Li, F.; Chen, J. *Angew. Chem. Int. Ed.* **2019**, *58*, 19021–19026.

(33) Fang, Z.; Li, Y.; Li, J.; Shu, C.; Zhong, L.; Lu, S.; Mo, C.; Yang, M.; Yu, D. *Angew. Chem. Int. Ed.* **2021**, *60*, 17615–17621.

(34) Du, D.; Zhao, S.; Zhu, Z.; Li, F.; Chen, J. *Angew. Chem. Int. Ed.* **2020**, *59*, 18140–18144.

(35) Yu, X.; Liu, G.; Wang, T.; Gong, H.; Qu, H.; Meng, X.; He, J.; Ye, J. *Chem. – A Eur. J.* **2022**, *28*, e202202104.

(36) Ola, O.; Wang, N.; Walker, G.; Zhu, Y.; Grant, D. *Curr. Opin. Electrochem.* **2022**, *35*, 101040.

(37) Yuan, Z.; Mao, H.; Yu, D.; Chen, X. *Chem. Eur. J.* **2023**.

(38) Li, Q.; Li, N.; Ishida, M.; Zhou, H. *J. Mater. Chem. A* **2015**, *3*, 20903–20907.

(39) Li, Q.; Li, N.; Liu, Y.; Wang, Y.; Zhou, H. *Adv. Energy Mater.* **2016**, *6*, 1600632.

(40) Qu, Y.; He, X.; Hu, J.; Duan, L.; Wang, J.; Liao, S.; Lu, F. *J. Power Sources* **2023**, *555*, 232374.

(41) Chen, P.; Li, T.-T.; Yang, Y.-B.; Li, G.-R.; Gao, X.-P. *Nat. Commun.* **2022**, *13*, 64.

(42) Wang, Z.; Chiu, H.-C.; Paolella, A.; Zaghib, K.; Demopoulos, G. P. *ChemSusChem* **2019**, *12*, 2220–2230.

(43) Wang, P.; Chen, X.; Sun, G.; Wang, C.; Luo, J.; Yang, L.; Lv, J.; Yao, Y.; Luo, W.; Zou, Z. *Angew. Chem. Int. Ed.* **2020**, *60*, 1390–1395.

(44) Li, M.; Wang, X.; Li, F.; Zheng, L.; Xu, J.; Yu, J. *Adv. Mater.* **2020**, *32*, 1907098.

(45) Veeramani, V.; Chen, Y.-H.; Wang, H.-C.; Hung, T.-F.; Chang, W.-S.; Wei, D.-H.; Hu, S.-F.; Liu, R.-S. *Chem. Eng. J.* **2018**, *349*, 235–240.

(46) Gong, H.; Xue, H.; Gao, B.; Li, Y.; Yu, X.; Fan, X.; Zhang, S.; Wang, T.; He, J. *Chem. Commun.* **2020**, *56*, 13642–13645.

(47) Tong, S.; Luo, C.; Li, J.; Mei, Z.; Wu, M.; O'Mullane, A. P.; Zhu, H. *Angew. Chem. Int. Ed.* **2020**, *59*, 20909–20913.

(48) Zhu, Z.; Ni, Y.; Lv, Q.; Geng, J.; Xie, W.; Li, F.; Chen, J. *Proc. National Acad. Sci.* **2021**, *118*, e2024619118.

(49) Qiao, G.-Y.; Guan, D.; Yuan, S.; Rao, H.; Chen, X.; Wang, J.-A.; Qin, J.-S.; Xu, J.-J.; Yu, J. *J. Am. Chem. Soc.* **2021**, *143*, 14253–14260.

(50) Hu, C.; Chen, L.; Hu, Y.; Chen, A.; Chen, L.; Jiang, H.; Li, C. *Adv. Mater.* **2021**, *33*, 2103558.

(51) Chen, P.; Li, G.-R.; Li, T.-T.; Gao, X.-P. *Adv. Sci.* **2019**, *6*, 1900620.

(52) Wang, C.-T.; Huang, H.-H. *J. Non _crystalline Solids* **2008**, *354*, 3336–3342.

(53) Guo, W.; Xue, X.; Wang, S.; Lin, C.; Wang, Z. L. *Nano Lett.* **2012**, *12*, 2520–2523.

(54) Dong, W. J.; Cho, W. S.; Lee, J.-L. *ACS Appl. Mater. Interfaces* **2021**, *13*, 22676–22683.

(55) Hong, L.; Yao, H.; Cui, Y.; Bi, P.; Zhang, T.; Cheng, Y.; Zu, Y.; Qin, J.; Yu, R.; Ge, Z.; Hou, J. *Adv. Mater.* **2021**, *33*, 2103091.

(56) Lou, S. N.; Sharma, N.; Goonetilleke, D.; Saputera, W. H.; Leoni, T. M.; Brockbank, P.; Lim, S.; Wang, D.-W.; Scott, J.; Amal, R.; Ng, Y. H. *Adv. Energy Mater.* **2017**, *7*, 1700545.

(57) Xue, H.; Gong, H.; Yamauchi, Y.; Sasaki, T.; Ma, R. *Nano Res. Energy* **2022**, *1*, e9120007.

(58) Wang, R.; Liu, H.; Zhang, Y.; Sun, K.; Bao, W. *Small* **2022**, *18*, 2203014.

(59) Tewari, N.; Lam, D.; Li, C. H. A.; Halpert, J. E. *APL Mater.* **2022**, *10*, 040905.

(60) Zhou, E.; Zhang, X.; Zhu, L.; Yuan, D.; Wang, Y. *Adv. Funct. Mater.* **2023**, 2213667.

(61) Cao, X.; Shi, Q.; Feng, Y.; Zhang, X.; Zhou, E.; Zhu, L.; Wang, Y. *Mater. Today Chem.* **2022**, *26*, 101082.

(62) Kato, K.; Puthirath, A. B.; Mojibpour, A.; Miroshnikov, M.; Satapathy, S.; Thangavel, N. K.; Mahankali, K.; Dong, L.; Arava, L. M. R.; John, G.; Bharadwaj, P.; Babu, G.; Ajayan, P. M. *Nano Lett.* **2021**, *21*, 907–913.

(63) Zhang, X.; Su, K.; Mohamed, A. G. A.; Liu, C.; Sun, Q.; Yuan, D.; Wang, Y.; Xue, W.; Wang, Y. *Energy Environ. Sci.* **2022**, *15*, 780–785.

(64) Chen, Y.; Chen, Z.; Zhang, X.; Chen, J.; Wang, Y. *Nanoscale* **2022**, *14*, 10903–10909.

(65) Tewari, N.; Shivarudraiah, S. B.; Halpert, J. E. *Nano Lett.* **2021**, *21*, 5578–5585.

(66) Jia, C.; Zhang, F.; She, L.; Li, Q.; He, X.; Sun, J.; Lei, Z.; Liu, Z.-H. *Angew. Chem. Int. Ed.* **2021**, *60*, 11257–11261.

(67) Boruah, B. D.; Wen, B.; De Volder, M. *Nano Lett.* **2021**, *21*, 3527–3532.

(68) Feng, Y.; Xue, H.; Wang, T.; Gong, H.; Gao, B.; Xia, W.; Jiang, C.; Li, J.; Huang, X.; He, J. *ACS Sustainable Chem. Eng.* **2019**, *7*, 5931–5939.

(69) Lv, Q.; Zhu, Z.; Zhao, S.; Wang, L.; Zhao, Q.; Li, F.; Archer, L. A.; Chen, J. *J. Am. Chem. Soc.* **2021**, *143*, 1941–1947.

(70) Liu, X.; Yuan, Y.; Liu, J.; Liu, B.; Chen, X.; Ding, J.; Han, X.; Deng, Y.; Zhong, C.; Hu, W. *Nat. Commun.* **2019**, *10*, 4767.

(71) Podjaski, F.; Kröger, J.; Lotsch, B. V. *Adv. Mater.* **2018**, *30*, 1705477.

(72) Gouder, A.; Jiménez-Solano, A.; Vargas-Barbosa, N. M.; Podjaski, F.; Lotsch, B. V. *Mater. Horiz.* **2022**, *9*, 1866–1877.

(73) Savateev, O. *Adv. Energy Mater.* **2022**, *12*, 2200352.

(74) Yang, W.; Godin, R.; Kasap, H.; Moss, B.; Dong, Y.; Hillman, S. A. J.; Steier, L.; Reisner, E.; Durrant, J. R. *J. Am. Chem. Soc.* **2019**, *141*, 11219–11229.

(75) Noori, A.; El-Kady, M. F.; Rahmanifar, M. S.; Kaner, R. B.; Mousavi, M. F. *Chem. Soc. Rev.* **2019**, *48*, 1272–1341.

(76) Nayak, P. K.; Mahesh, S.; Snaith, H. J.; Cahen, D. *Nat. Rev. Mater.* **2019**, *4*, 269–285.

(77) Boruah, B. D.; Mathieson, A.; Wen, B.; Feldmann, S.; Dose, W. M.; De Volder, M. *Energy Environ. Sci.* **2020**, *13*, 2414–2421.

(78) Li, W.; Zheng, J.; Hu, B.; Fu, H.-C.; Hu, M.; Veyssal, A.; Zhao, Y.; He, J.-H.; Liu, T. L.; Ho-Baillie, A.; Jin, S. *Nat. Mater.* **2020**, *19*, 1326–1331.

(79) He, Y.; Wang, B.; Lüer, L.; Feng, G.; Osvet, A.; Heumüller, T.; Liu, C.; Li, W.; Guldi, D. M.; Li, N.; Brabec, C. J. *Adv. Energy Mater.* **2022**, *12*, 2103406.

Part III

Research Publications

6

Bridging the Gap between Solar Cells and Batteries: Optical Design of Bifunctional Solar Batteries based on 2D Carbon Nitrides

Andreas Gouder, Liang Yao, Yang Wang, Filip Podjaski, Ksenia S. Rabinovich Alberto Jiménez-Solano, and Bettina V. Lotsch

This article was published on May 26th 2023 in:

Advanced Energy Materials **2023**, 2300245.
doi: 10.1002/aenm.202300245

Keywords: carbon nitrides, photobatteries, poly(heptazine imide), solar batteries, solar cells, solar energy storage

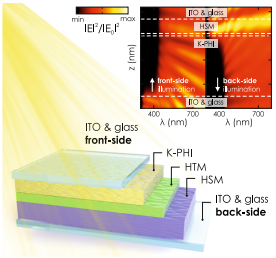

We design a solar battery based on K-PHI as bifunctional photoanode by means of optical simulations and electrochemical measurements. Performance improvement is modelled *via* Ragone plots and general design guidelines for solar batteries are put forward, including new approaches to circumvent the conceptual problem of active layer thickness.

Author contributions

Andreas Gouder performed the electrochemical measurements and Ragone Plot calculations. Andreas Gouder and Alberto Jiménez-Solano, with assistance of Liang Yao, analyzed the data. Andreas Gouder and Alberto Jiménez-Solano wrote the manuscript with assistance of all authors.

Contents

6.1. Introduction **167**
6.2. Results and discussion **169**
6.2.1. Optical design 170
6.2.2. The device thickness paradigm 172
6.2.3. Efficiency limitations beyond optical engineering 178
6.2.4. Evaluating performance of solar batteries *via* Ragone plots 179
6.3. Conclusion **182**
6.4. References **184**

Abstract

While solar cell technology is booming, intermittent availability of sunlight motivates new vistas for multifunctional devices capable of energy capture and storage on the same material, *i.e.*, direct or two-electrode bifunctional solar batteries. Herein, simulations and experiments are utilized to take a closer look at efficiency limitations and design considerations, and guidelines are proposed to operate a solar battery comprised of the 2D carbon nitride potassium poly(heptazine imide), K-PHI, as a bifunctional solar battery photoanode in conjunction with the separator PVK and cathode PEDOT:PSS. An optical design of this device is developed by proposing light absorption in a charge collection layer within the photoanode and calculating photocharging current and charging time as figures of merit. The much larger efficiency of operation via rear illumination for K-PHI layer thicknesses >200 nm is highlighted and enhancement strategies without modifying the photoactive layer are proposed. Finally, adapted Ragone plots are introduced and it is shown how the solar batteries are capable of improving energy and charge output

solely via illumination (for the design under 1 sun, the energy and charge output increase by 60 % and 63 %, respectively) without modifying the device.

6.1. Introduction

New devices to harvest energy from renewable sources such as abundant sunlight and store this energy are essential to transition our energy infrastructure into a sustainable and economically viable future. Solar cells present an easy way to extract electric energy and are widely employed,[1] but suffer from short-, medium-, and long-term fluctuations in supply due to weather, day-night, and seasonal cycles.[2,3] Electric energy storage technologies such as batteries have the ability to buffer fluctuations and minimize residual load, but require a dedicated infrastructure. Solar batteries present a novel decentralized and integrated approach, combining both solar cells and batteries in the same device, thus minimizing losses caused by charge extraction from the solar cell, wiring, and voltage or current mismatch.[4–6] Different design approaches are being evaluated for capacitive and faradaic energy storage, either with a discrete photoactive electrode (*i.e.*, three electrode systems),[7] or, more recently, an "integrated" solar battery electrode capable of both charge storage and light absorption (*i.e.*, two electrode systems). The latter can be realized in layered configurations,[8,9] by utilizing composites of charge storage and photoactive materials,[10] or by utilizing materials which provide an intrinsic bifunctionality of simultaneous light absorption and charge storage.[4–6,11–15] We recently proposed an integrated bifunctional solar battery design, which consists of only one material performing both light absorption and charge storage at the same time.[16] An internal hole transfer cascade shuttles the hole to the cathode, enabling photocharging solely *via* illumination, without external wiring and under open circuit conditions. This is enabled by the fully earth-abundant 2D carbon nitride potassium poly(heptazine imide), K-PHI,[16–18] as the active material. Its versatile toolkit of optoelectronic and optoionic properties,[19,20] including a visible light bandgap of $\sim$2.7 eV (459 nm), enables a bifunctionality of light absorption and charge storage at the same time, leading to applications in (dark) photocatalysis,[21–25] photomemristive sensing,[26] as well as light driven micromachines.[27,28] To transform this solar battery concept into a working device, it is essential to develop a better understanding of its architectural design, *i.e.*, which materials to choose, which geometric properties are suitable (*e.g.*, layer thickness) and how the materials interact with each other (*e.g.*, parasitic light absorption, interfacial charge separation and storage). Simulations

as presented herein give pathfinding vistas to extract such parameters.

On a general note, while the emerging field of photoactive batteries possesses huge potential in theory, there are still key challenges to overcome, such as loss channels from photogenerated charge carriers, a precise understanding of the photocharging process, and design principles both regarding materials choice as well as device setup.[4–6] More importantly, the nature of these devices presents the conceptual problem of active layer thickness (termed in this work "active layer thickness dilemma"), which on the one hand should be maximized to achieve a reasonable capacity (*i.e.*, battery part), but on the other hand thick active layers suffer from worse photocharging kinetics as charge transport and parasitic light absorption become limiting (*i.e.*, solar cell part). Solar cells based on bulk heterojunctions experience operational losses in efficiency (governing photocurrent, photopotential, fill factor, as well as power and energy output) due to the Shockley-Queisser limit, defects in layers, junction resistances, as well as limits in conductivity, the latter reducing charge diffusion distances in the active layer and with it, increasing recombination losses.[1,4–6,29,30] In addition, a Lambert-Beer like decay of light intensity when penetrating the active layer causes uneven illumination. All these effects worsen solar cell performance with thicker active layers, which underlines the conceptual challenge solar batteries are facing, and further accentuates the need for simulations of how to design and operate such a device. Herein, we present numerical optical simulations as well as electrochemical experiments for a solar battery based on K-PHI and an internal hole transfer cascade (Figure 6.1 (a)) to understand the active layer thickness dilemma, derive design principles and propose approaches to work around this conceptional difficulty. We first develop an optical model, which introduces the idea of optimizing light absorption not within the entire active layer but rather in parts where the IQE is highest and which we henceforth term collection layer. Subsequently, we utilize thickness and illumination modes as variables to tune photocurrent output and charging time as a proposed figure of merit. We then adapt the Ragone plot for solar batteries, which is commonly employed to compare energy storage devices,[31] and propose strategies toward addressing the abovementioned bottlenecks in the field of solar batteries.

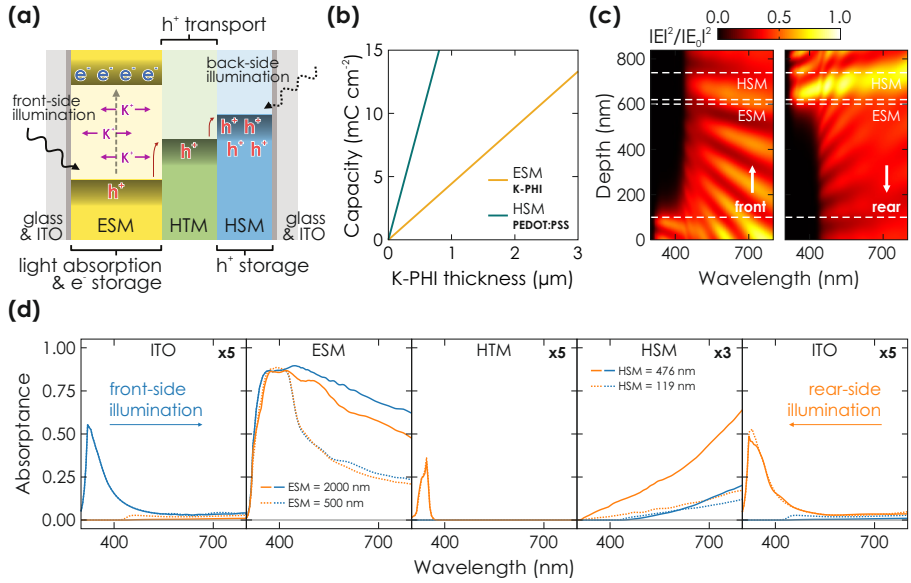

Figure 6.1. Description and optical challenges that a solid-state solar battery based on K-PHI and PEDOT:PSS provides. (a) Scheme of the solar battery, comprising the active material K-PHI, which acts both as light absorber and Electron Storage Material (ESM), the HTM PVK and the Hole Storage Material (HSM) PEDOT:PSS, sandwiched between two ITO substrates. Upon illumination, charge carriers generated in the active area of the ESM charge K-PHI and holes are shuttled to PEDOT:PSS. **(b)** Scaling of theoretical capacity with thickness of the charge storage layers K-PHI and PEDOT:PSS. **(c)** Calculated spatial and spectral distribution of the normalized electric field intensity across the section of the solar battery structure, assuming a plane wave propagating along the direction perpendicular to the layered surface in front-side (left) and rear-side illumination (right). **(d)** Calculated absorptance of each constituent layer for two different devices ($d_{\mathrm{ESM}} = 2000$ nm and $d_{\mathrm{HSM}} = 476$ nm (solid lines); $d_{\mathrm{ESM}} = 500$ nm and $d_{\mathrm{HSM}} = 119$ nm (dashed lines)), when illuminated from the front (blue) or the rear (orange).

6.2. Results and discussion

The generic design of the integrated solid-state solar battery was recently realized by us and is depicted in Figure 6.1 (a).[32] In its simplest form, the device comprises three distinct layers.[4–6,16] (1): The electron storing and light absorbing anode, which we denote as ESM layer (Figure 6.1 (a), yellow) and which is formed by the carbon nitride K-PHI. (2): The hole transport layer (HTM; Figure 6.1 (a), green) is situated between anode and cathode. Its main task is to prevent a short circuit by acting as a rectifying separator between anode and cathode. Photogenerated holes are transported *via* a hole transfer cascade toward the cathode, which works in only one direction and herewith effectively prevents a self-discharge of the device. Its

valence band edge should be located between the VB of ESM and cathode, and the conduction band edge should be energetically higher than the CB of the ESM. Here, we utilize PVK, a HTM which is widely employed for optoelectronic devices.[33] It has a suitable VB location of -5.5 eV, which allows a theoretical hole injection from the K-PHI VB (at -5.9 eV).[34] The materials' bandgap of 3.5 eV prevents electron injection from K-PHI (CB of PVK at -2.4 eV; CB of K-PHI at -3.1 eV) and ensures optical transparency at wavelengths where we expect absorption of K-PHI (<450 nm; see Tauc plots in Figure A.1). (3): The hole storage cathode, which we term HSM layer (Figure 6.1 (a), blue). We chose the conductive polymer PEDOT:PSS due to its organic and environmentally friendly nature, its well-known pseudocapacitive charge storage properties and no significant light absorption <450 nm nm (see Figure A.1).[35,36] We give more details on the device and its experimental realization in our recent proof-of-concept report.[32] For the sake of simplicity and to focus our discussion of the device on the optical boundary conditions, we approximate the thickness capacity dependence of the charge storage layers as linear (Figure 6.1 (b)) and utilize respective capacity values of 6.3 mA h g^{-1} (see Section A.4 for details) for K-PHI and 51.3 mA h g^{-1}[37] for PEDOT:PSS.

6.2.1. Optical design

With knowledge of the materials' properties, we can design an optical model for the device. While we obtain refractive index values for the substrate comprising of glass coated with the transparent substrate ITO, PVK, and PEDOT:PSS from literature (see Figure A.2),[38–41] we have extracted the refractive index of K-PHI via ellipsometry from a pellet pressed from K-PHI powder (see Figure A.2 for details). Next, we have to define the thickness of the individual layers. The thickness of the K-PHI layer defines the main independent variable of device composition and major tuning route that we investigate in this work, *vide infra*. The thickness of PEDOT:PSS is governed by matching its charge storage capacity with that of K-PHI (see Figure 6.1 (b): $d_{\text{PEDOT:PSS}}[\text{nm}] = d_{\text{K-PHI}}[\text{nm}] \times 0.238$). We fix the PVK thickness to a common value of 10 nm to provide optimum hole transfer properties.[42] ITO as well as glass thickness is dictated by commercial availability (*Ossila Ltd.*; 100 nm ITO and 1 mm soda lime glass).

With an exemplary layer thickness of $d_{\text{K-PHI}} = 500$ nm and corresponding $d_{\text{PEDOT:PSS}} = 119$ nm, we can now calculate the spatial distribution of the normalized electric field intensity (abbreviated henceforth with E_n) (Figure 6.1 (c)) to evaluate how

light travels through the device (see Section A.2 for details of calculations). Illumination occurs with wavelengths between 300 and 800 nm and with a spectral distribution and photon flux according to AM1.5 global. We propose two operation modes: illumination from the front (*i.e.*, the active layer K-PHI is illuminated first) or the rear. When looking at illumination from the front (Figure 6.1 (c), left), the light intensity entering K-PHI (at a depth of 100 nm) is governed by absorption of the soda lime glass (compare E_n at a depth of 0 nm) and ITO. The former produces significant absorption at $\lambda < 320$ nm and the latter shows no significant absorption across the analyzed wavelength range. When entering the K-PHI layer, the expected significant absorption occurs $\lambda < 450$ nm (see Figure A.1), reducing E_n close to 0 within a depth of 50 to 100 nm. This underlines the strong light absorption ability of K-PHI. Illumination from the rear (Figure 6.1 (c), right) shows no significant absorption of both PEDOT:PSS and PVK in the chosen layer thicknesses (at a depth of 851 to 600 nm) and an absorption behavior of K-PHI analogous to front illumination. The rationale behind choosing the two illumination directions becomes evident: K-PHI shows significant light absorption only within the first 50 to 100 nm and this area can be situated either at the ITO and ESM or HTM and ESM junction with illumination from the front or rear, respectively.

To underline the magnitude of absorptance within the device, we show consecutive light absorptance of the individual layers in Figure 6.1 (d) for both illumination directions and two different thicknesses ($d_{\text{K-PHI}} = 500$ and 2000 nm and $d_{\text{PEDOT:PSS}} = 119$ and 476 nm, respectively), calculated *via* numerical simulations (see Section A.2). As expected, K-PHI absorbs nearly all photons (>0.80) at $\lambda < 450$ nm independent of layer thickness, and at larger wavelengths thicker layers cause more absorption. When illuminating from the front, light absorption is larger in K-PHI and smaller in PEDOT:PSS, *vice versa*. Note that absorption of ITO, PEDOT:PSS, and PVK is miniscule in the wavelength region of 300 to 450 nm, underlining why from an optical perspective they are suitable candidates as substrate, HSM, and HTM, respectively. The nearly same absorptance profile of K-PHI under front-side and rear-side illumination further underlines this. With these observations, we set the stage to investigate the solar battery active layer thickness relationship in light of solar cells and batteries.

6.2.2. The device thickness paradigm

As mentioned above, modifying active layer morphology in bulk heterojunction OSC devices is a key tuning parameter.[29,30,43] A first approach would thus suggest to increase light absorption *via* layer thickness. Utilizing the computed electric field intensity (Figure 6.1 (c)) calculated *via* numerical simulations, we can extract the spatially resolved absorptance in a solar battery device with a K-PHI thickness of $d_{\text{K-PHI}} = 500\,\text{nm}$, shown in Figure 6.2 (a). The majority of light absorption occurs in the part of the active layer where light enters first. Note that the amount of absorption in the active layer is independent of illumination direction (front or rear), since the other layers show miniscule absorptance, as mentioned above.

Typically, solar cell charge generation is regulated by SCLC and will be discussed in the context of solar batteries in the following.[43,44] Note that while it is not entirely clear how well this model applies to K-PHI since many material properties are unknown or difficult to access,[21–25] we assume a behavior similar to SCLC. In an OSC comprised of a thin active layer, electron and hole depletion zones develop at the respective cathode and anode, producing band bending and assisting to extract the charge carriers.[44] The electric field between cathode and anode is assumed to be sufficiently strong to extract all photogenerated carriers in the bulk of K-PHI. However, for thick active layers (as utilized for the solar battery herein) the electric field intensity shrinks, reducing the charge collection efficiency in the bulk.[44] Second, the ability to accumulate charges in the active layer, which is essential for solar batteries, increases the amount of electrons within the layer as a consequence of photocharging and the low electronic conductivity of K-PHI[19,20] in parts of the active layer, spatially close to the collection layer. Both effects could produce an additional electron-accumulation-induced or mobility-induced space charge region, further reducing charge collection efficiency in the bulk.[44,45] Since we operate in a bilayer structure (planar heterojunction) and not a bulk heterojunction, exciton and/or charge separation most likely only occurs at the junctions within the space charge region. Note that albeit bulk heterojunctions were designed for certain solar battery geometries,[11–15] they are impractical for the geometry discussed here since the very thick active layers inhibit light absorption in the bulk anyways. All these effects lead us to conclude that when charging the solar battery *via* illumination, electron and hole collection occurs predominantly at the interfacial depletion region of the junction K-PHI/PVK. The K-PHI/ITO junction is not significant when charging the solar battery with illumination, since photogenerated charge carriers are trans-

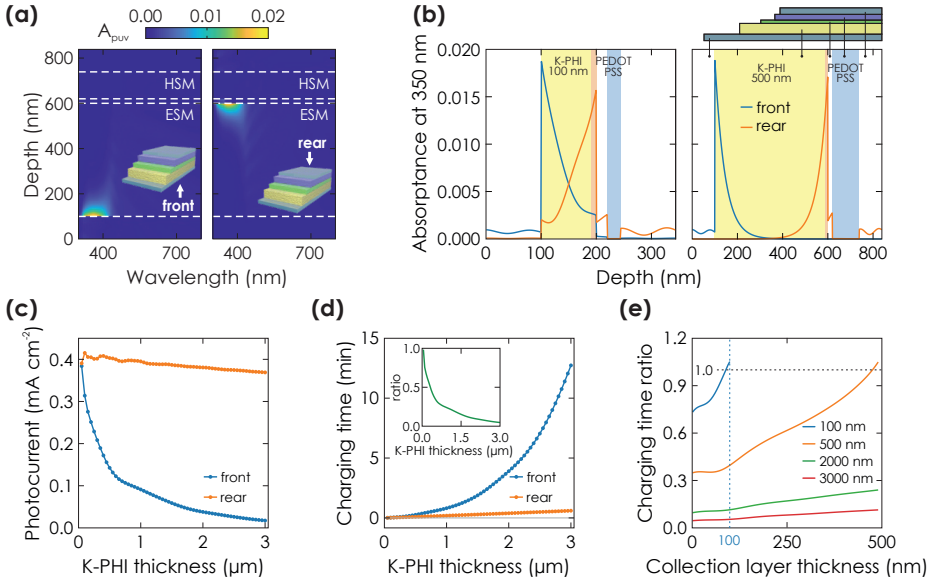

Figure 6.2. Optical design of the solar battery based on the ESM K-PHI and HSM PEDOT:PSS. (a) Calculation of the absorption per unit volume across the section of the solar battery structure. **(b)** Absorptance profiles of the solar battery device at a wavelength of 350 nm, when illuminating from the front (blue) or the rear (orange). Two different configurations are shown, with K-PHI ESM thicknesses of $d_{\text{K-PHI}} = 100$ nm (left) and 500 nm (right), and corresponding PEDOT:PSS HSM thicknesses of $d_{\text{PEDOT:PSS}} = 23.8$ and 119 nm, respectively. The collection layer, where light absorption has the highest probability to lead to charging (IQE $\sim$100 %), is marked with the red area. **(c)** The internal photocurrent that a solar battery with different K-PHI active layer thicknesses provides under 1 Sun illumination, depending on whether the device is illuminated from the front (blue) or the rear (orange). The latter leads to a much larger internal photocurrent for thicker devices. Internal photocurrents for different illumination intensities are given in Table A.6. **(d)** The time required to charge the entire solar battery *via* illumination for different K-PHI active layer thicknesses, depending on whether the device is illuminated from the front (blue) or the rear (orange). The ratio between charging times from rear and front configurations (rear:front) is shown in the inset. While for thinner K-PHI layer devices the illumination direction matters less, for thicker devices only rear illumination makes sense. **(e)** Influence of collection layer thickness on the charging time ratio between illumination from the rear and front (compare to inset in (d)), calculated for devices with four K-PHI active layer thicknesses (100 (blue), 500 (orange), 2000 (green), and 3000 nm (red)). Simulation steps of all results shown in this figure are summarized in Table A.4.

ferred to the cathode internally *via* the HTM and thus, the device operates under open circuit-like conditions, *i.e.*, no significant electron or hole extraction occurs *via* the substrate. Note that this effect should be independent of illumination direction (front or rear; comparable to inverse or regular solar cell architectures) and explain

our rationale behind defining a collection layer where light absorption leads to photocharging. Thus, we define an area in the active layer next to the junction with the HTM, where light absorption produces such an internal photocurrent with a very high collection efficiency, *i.e.*, the local IQE of K-PHI is assumed to be $100\,\%$ (see red area in Figure 6.2 (b)) and term it collection layer. In the remaining part of the active layer (which is the majority of K-PHI: for a $500\,\text{nm}$ device: $92\,\%$), the IQE is assumed to be $0\,\%$. Note that the assumption for a very small collection layer with very high IQE and bulk with IQE of $0\,\%$ is not uncommon for thick active layer[44] and low carrier mobility semiconductor OSCs.[46] As an approximation for further calculations, we have elaborated a rectangular collection layer function (step function), as proposed for the absorption edge by the Shockley-Queisser model,[1] with a width of $10\,\text{nm}$ (we further discuss our rationale behind the rectangular shape in Section A.3). It is essential to maximize light absorption not in the entire active layer, but rather within the collection layer of the photoabsorber material.

We show the absorptance profile of two solar batteries with thicknesses of $d_{\text{K-PHI}} = 100$ and $500\,\text{nm}$ and $d_{\text{PEDOT:PSS}} = 23.8$ and $119\,\text{nm}$ in Figure 6.2 (b). Major absorption occurs only in K-PHI and shows an initial Lambert-Beer like decay when entering the active layer. Due to parasitic absorption of PVK and PEDOT:PSS, when illuminating from the front the initial absorption in K-PHI is slightly higher as compared to rear illumination. However, it becomes evident that illumination from the rear produces much more absorption in the collection layer (red area in Figure 6.2 (b)). The device with the thinner active layers shows an increase in absorptance in the collection layer in conflict with the Lambert-Beer decay when illuminating from the front, indicating photonic resonance effects as a result of the active layer thickness being in the range of the incident light.[47] Note that we cannot utilize this effect, since thin layers do not yield a reasonable electric capacity.

To evaluate photo-electrochemical properties of the solar battery, we calculate the theoretically achievable internal photocurrent as a function of the active layer thickness (Figure 6.2 (c)) using

$$I_{pc}[\text{A cm}^{-2}] = q_e \int_{\lambda_1}^{\lambda_2} \int_{x_1}^{x_2} A_{\text{K-PHI}}\,(x,\lambda) \cdot \Phi\,(\lambda) \cdot \text{IQE}\,(x,\lambda) \cdot \text{d}\lambda\,\text{d}x \tag{6.1}$$

here $A_{\text{K-PHI}}$ is the absorptance profile of K-PHI, x is the collection layer thickness, Φ is the incident photon flux according to AM1.5G, IQE is the step-function of the collection layer ($100\,\%$ inside the collection layer, $0\,\%$ outside), and q_e is the elementary charge. When illuminating from the front, the simulated device shows an

initial internal photocurrent of 0.384 mA cm^{-2} at an active layer thickness of 50 nm, which quickly decays (half of its initial value at a thickness of 350 nm) and reaches merely 0.0589 mA cm^{-2} at 3 µm. Conversely, internal photocurrent generated *via* rear illumination remains far more constant with thickness, with 0.391 mA cm^{-2} at 50 nm and 0.369 mA cm^{-2} at 3 µm, underlining the significant advantage of the rear illumination mode for devices with thicker layers. Note that the calculated internal photocurrent has to be understood as a maximum possible internal photocurrent if nonidealities are absent, such as significant scattering of the film surface, conductivity limitations, exciton or charge recombination in the collection layer, or limited donor oxidation efficiency. To evaluate the dependence of both solar cell and battery performance metrics on thickness, we propose charging time t_{ch} as a figure of merit, *i.e.*, the time that is required to charge the solar battery solely *via* illumination to its calculated capacity for a given thickness. Shorter charging times are more desirable for a given layer thickness, since the internal photocurrent is more effective in charging the battery. We can calculate the charging time with

$$t_{ch}[\mathrm{s}] = \frac{C_{\text{K-PHI}}}{I_{pc}} \tag{6.2}$$

where $C_{\text{K-PHI}}$ is the capacity (charges per mass) of the solar battery. Note that the decay of internal photocurrent with charging state, which we discuss in Section 6.2.3, is not taken into account here, *i.e.*, we assume a constant initial internal photocurrent throughout the entire charging process. Scaling of charging time with thickness for both front and rear illumination is shown in Figure 6.2 (d). As expected, thicker layers require a longer charging time. Furthermore, rear illumination produces a far less significant increase of charging time compared to front illumination (at a thickness of 3 µm corresponding to a capacity of 13.3 mC cm^{-2}, illumination requires 0.60 min from the rear and 12.7 min from the front). Thus, a larger internal photocurrent leads to shorter charging times and at the same time, thicker layers with a larger capacity require a longer charging time. This becomes more evident when looking at the ratio between charging times from the rear and the front (inset in Figure 6.2 (d)) At a thickness of 312 nm, front illumination is only half as efficient as rear illumination. It is also worth looking at the impact of the collection layer thickness on charging time, since it allows us to extrapolate our results to materials with different optoelectronic properties influencing the shape of this layer, as well as to evaluate the accuracy of our estimate of the collection layer thickness of 10 nm.

In Figure 6.2 (e), we show the calculated ratio between charging times from the

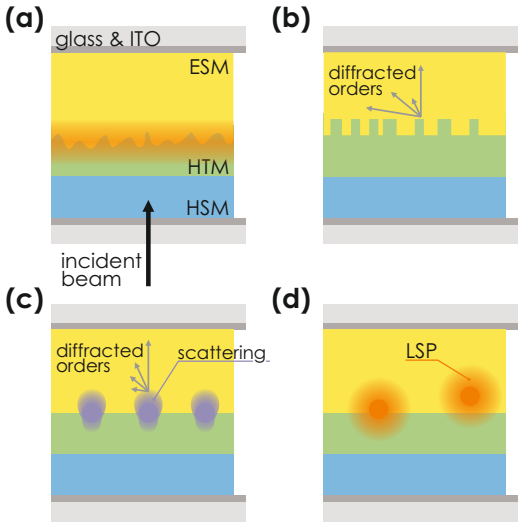

Figure 6.3. Proposed strategies for light harvesting efficiency increase in the collection layer without tuning the active layer thickness. (a) *Via* scattering from a random textured surface between HTM and ESM. Incident beam shows illumination *via* the rear. **(b)** *Via* the enhanced diffraction intensity of high orders supported by quasi-random binary gratings. **(c)** *Via* the diffraction supported by arrays of dielectric Nanoparticles (NPs) embedded in the device. Additionally, these NPs also show scattering. **(d)** *Via* the excitation of localized surface plasmons in metal NPs embedded in the device next to the HTM-ESM interface.

6

rear and front for solar batteries with four different active layer thicknesses (100, 500, 2000 and 3000 nm). In all cases, the ratio stays approximately constant for collection layer thicknesses <10 nm and subsequently increases. With thinner active layers, the ratio becomes larger independent of the collection layer thickness, suggesting a more efficient operation *via* front illumination. We explain this increase in the ratio with a decreasing impact of "parasitic" absorption from parts of K-PHI outside of the collection layer, which only contribute to electron storage of charges generated within the collection layer. This part of the active layer becomes thinner with decreasing layer thickness, thus reducing the negative impact on the front illumination mode (see also decay in absorptance shown in Figure 6.2 (b)). Note though that apart from when nearly the entire active layer is the collection layer, the ratio never rises above 1, which emphasizes the better operation *via* rear illumination for essentially all layer thicknesses. Front illumination is only advantageous when active layer absorptance outside of the collection layer is not significant, since parasitic light absorption from HTM and HSM then start to play a more dominant

role. For 500 nm, the ratio increase above 1 is insignificant (1.05, when the entire active layer is the collection layer), which in turn underlines the insignificant absorption of PEDOT:PSS and PVK, in line with our discussion of absorption of the independent layers above.

To conclude, irrespective of illumination direction, changing the active layer thickness does not provide an effective pathway to enhance absorption in the collection layer due to its adverse impact on battery capacity. For instance, decreasing the active layer thickness to improve front illumination would also decrease the capacity of the device. This motivates us to propose alternative means of enhancing light absorption in the collection layer, which we disclose in Figure 6.3. A rough surface produces more scattering, which in return causes a longer effective pathway of photons through the collection layer, when scattered at a significant angle (Figure 6.3 (a)). Note that in any case the film deposition of K-PHI produces films with significant surface roughness and scattering.[16,26] This optimization strategy is very facile and straightforward, however comes at the expense of increasing light absorption along the entire spectrum, which will conversely affect transparency of the device – potentially problematic for applications where transparency is key (*e.g.*, solar batteries prepared on windows). Alternatively, a more controlled periodic surface structuring (*e.g.*, *via* lithography techniques) could produce a grating in which diffraction orders maximize light absorption in the collection layer (Figure 6.3 (b)), an approach that is already employed for photovoltaic devices.[48] This design follows a wavelength selective enhancement approach, at the price of a more complex preparation routine. Selective enhancement implies that by controlling the diffraction order *via* the type of diffraction grating, scattering increases only at selective wavelengths at energies larger than the bandgap.[48,49] Transparency is thus not negatively affected. In addition, no additional particles are required for these approaches, hence not reducing the amount of active material. Controlled diffraction can also be generated using dielectric nanoparticles (*e.g.*, SiO_2 nanoparticles) deposited in-between K-PHI and HTM (Figure 6.3 (c)). While generating controlled diffraction, the nanoparticles also produce dielectric inclusions which increase the electric field intensity due to photonic resonance effects, an approach which was recently postulated to increase efficiency in perovskite solar cells.[50] This effect produces a broader increase in absorption edge, making it very versatile for different active materials. Last, we also propose the inclusion of metal nanoparticles, capable of producing localized surface plasmon resonance effects which can maximize local electric field intensity and as a consequence increase absorption (Figure 6.3 (d)).[51]

This effect produces a very sharp absorption onset, which in comparison to the previously mentioned enhancement strategies might produce the most significant absorption improvement. Furthermore, the metal nanoparticle fabrication routine is very much optimized in respect to morphology.[52] In fact, Au and Ag plasmonic nanoparticles have already been employed for example to enhance the efficiency of carbon nitride based photocatalysts.[53,54]

6.2.3. Efficiency limitations beyond optical engineering

Thus far, we have discussed the nature of the solar battery from a purely optical perspective in regard to absorption. We acknowledge that energy losses in real world solar cells depend on more, namely, resistive losses at junctions, electronic and ionic conductivity reducing charge transport in the active layer (particularly for very thick active layers) and recombination losses (radiative and/or nonradiative) – all of which govern the overall cell efficiency.[1,29,30] Likewise, battery efficiency is significantly governed by the electric potential gradient and electronic/ionic conductivity of electrodes and electrolyte, limiting its energy and power density.[55] Similarly, solar batteries possess further effects limiting their photocharging efficiency, also commonly referred to as solar-to-output efficiency[4–6] or photoconversion efficiency,[11–15] and defined as the ratio between electric discharging energy and incident light energy ($\eta_c = \frac{E_{output}}{E_{light}}$). We study in Section A.5 two potential efficiency loss channels, which are unique to integrated solar batteries that rely on a bifunctionality of the active material. With more charges present on the material, the internal photocurrent charging the device actually decreases, which is expected since electron-hole pair recombination increases as more electrons are stored on the material.[56,57] This effect of decreasing internal photocurrent can probably be reduced when a more efficient SED is used. We show in a photoelectrochemical experiment in Section A.5.1 (we charge a K-PHI film with 1 Sun illumination and perform hole extraction *via* an SED), that when K-PHI is 50 % charged, 26 and 3 % of the initial internal photocurrent remains when using the more and less efficient SED 4-MBA and MeOH, respectively. The internal photocurrent charging the device thus is a function of the accumulated charge. It can be expressed as follows

$$I_{avg}\,(t)\,[\mathrm{mA}] = \frac{\mathrm{d}C\,(t)}{\mathrm{d}t} \tag{6.3}$$

We discuss implementation of this equation into simulating the charging state of the solar battery in Section A.5.1 and utilize it to calculate performance parameters in Section 6.2.4.

Second, many charge storage materials show (photo) electro chromic behavior upon charging, which has stimulated the development of manifold devices such as dimmable windows of filters.[58] Moreover, both K-PHI and PEDOT:PSS employed herein are prone to color changes when charging (see Section A.5.2). It is important to evaluate such effects when choosing materials, since in the worst-case transmission through an HSM or HTM decreases when charging the device, leading to a smaller internal photocurrent. In case of K-PHI and PEDOT:PSS, however, upon charging the transmission at wavelengths <450 nm is not affected for K-PHI and increases for PEDOT:PSS, underlining their good match for a solar battery device. In perspective, color/transmission changes accompanying charging/discharging of the device could even be used as a visual read-out for the charging state of such devices.

6.2.4. Evaluating performance of solar batteries *via* Ragone plots

We conclude our study by comparing the solar battery performance (gains) to other energy storage devices. A common way of comparing the performance of energy storage systems are Ragone plots, in which power output is plotted against energy output for different discharging currents.[31,59] Capacitors are typically located at low energy and high power outputs, batteries at high energy and low power outputs. Ideally, a device shows both high energy and high power. To understand how solar batteries fit into the Ragone plot, we first must understand how photocharging affects the plot. Based on the model we introduced above, we calculate iterative discharging of a solar battery device with properties as follows: $d_{\text{K-PHI}} = 500$ nm, $d_{\text{PEDOT:PSS}} = 119$ nm, mass = 100 µg, illumination area = 1 cm^2. We give a thorough discussion of the calculations in Section A.6, performance data normalization in Section A.6.2, and assumptions as well as further conditions in Section A.6.3. In brief, we calculate the initial internal photocurrent according to Equation 6.1, the change with charging state according to experimental approximation of the decay of internal photocurrent of K-PHI upon charging (Section 6.2.3), and the photocharging efficiency using a constant solar-to-output efficiency of $\eta_c = 0.1$ % – an average value for reported solar batteries.[4–6] We denote the resulting current as “photocharging

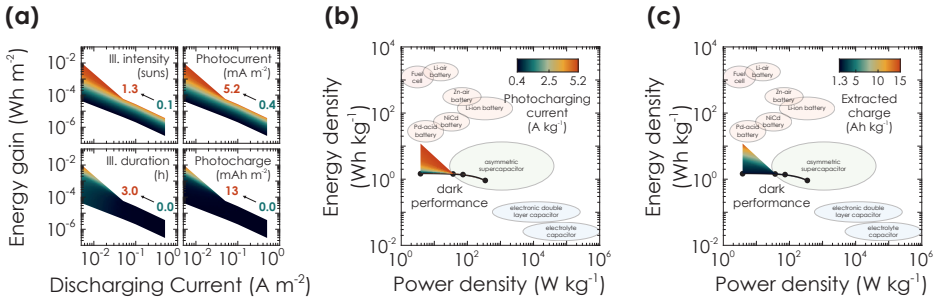

Figure 6.4. Performance enhancement of a solar battery *via* illumination compared to other energy conversion and storage devices. (a) Scaling of energy gains *via* illumination with electric discharging current of the solar battery. Illumination at different light intensities generates different photocharging currents (top left and top right, for definition of photocharging current see text). Energy gains are most significant for small discharging currents, since with longer illumination times, the photogenerated charge increases (bottom left and bottom right). **(b-c)** Modified Ragone plot, which shows the solar battery performance when discharged with distinct currents (5.01, 50.1, 100 and $501\,\mathrm{A\,kg^{-1}}$) in the dark (black dots; see Section A.4 for experimental details). The area above the black line shows the potential improvement *via* illumination during electric discharge. The generated photocharging current assists charge (re)generation and thereby increases the apparent extracted charge (*i.e.*, capacity) and energy density. We show scaling with photocharging current in (b) and extracted charge from both electric and light charging in (c). Ragone plot energy conversion and storage device data. Adapted with permission.[31] Copyright 2018, American Chemical Society. Scaling of area with mass was normalized with a form factor of fofa $= 1 \times 10^{-4}\,\mathrm{g\,cm^{-2}}$ (see Section A.6.2). Simulation steps to obtain results shown in this figure are summarized in Table A.4.

6

current". This current is the current which actually charges the device, *i.e.*, theoretically the difference between discharging currents in the dark and under illumination. Note that with the charging state dependent internal photocurrent, the charging time shown in Figure 6.2 (d) gets longer, as shown in Figure A.9 (a). Front or rear illumination is affected similarly and the ration between front and rear charging times remains similar (Figure A.9 (b)).

In Figure 6.4 (a) we show how energy increases due to photocharging during the discharging process as a function of electric discharging current. The area relates to energy gains *via* photocharging during battery operation (charging and discharging), which are larger with smaller electric discharging currents, causing a longer duration of the discharging process and thus longer illumination. Photocharging conditions govern the magnitude of energy gain. Larger illumination intensities cause a more significant photocharging current, which in return produces a larger energy gain (compare Figure 6.4 (a) top left and top right). This effect is more pronounced at smaller electric discharging currents, which drop to the size of the pho-

tocharging current (see Equation A.11). Note that for illuminations >1.3 Sun, the photocharging current becomes larger than the electric discharging current, causing the energy gain to rise into infinity since discharging is never complete. This demonstrates the unique potential of solar batteries with this design in terms of capacity gain over conventional batteries. In fact, small currents and large illumination intensities cause a significant increase in discharge duration (Figure 6.4 (a) bottom left) and a much larger extracted capacity (Figure 6.4 (a) bottom right). As photocharging current depends on light absorption in the collection layer and not on active layer thickness, we refrain from normalizing (Figure 6.4 (a)) against mass as commonly done for Ragone plots and instead normalize against the device's geometric area.

To combine both discharge performance of the solar battery in the dark and the enhancement *via* illumination during discharge, we measure the electric dark energy and power performance of a "separated" solar battery utilizing a K-PHI film and a PEDOT:PSS film in analogous film thicknesses and use them as an input for subsequent simulations on illumination performance gains (see Section A.4 for details). Briefly, the sample was charged as well as discharged at four different rates ($5.01, 50.1, 100$ and 501 A kg^{-1}) in the dark. Results are shown *via* the black dots and line (fit) in Figure 6.4 (b-c) with 5.01 A kg^{-1} giving the largest energy and smallest power, etc. The areas above the black line represents the area of theoretical enhancement *via* illumination, increasing energy output of the device as expected. Energy output can be calculated with

$$E_{total}\left[\mathrm{W\,h\,kg^{-1}}\right] = E_{dark} + V_p \cdot \eta_c \cdot \int I_{avg,normP}\left(ch\left(t_d\right), I_{pc}\right)\,\mathrm{d}t_d \cdot \mathrm{fofa} \quad (6.4)$$

where E_{dark} gives the energy density of electric discharge in the dark, V_p is the photopotential, $I_{avg,normP}$ describes the decay of photocharging current with charging state according to Equation A.8, $ch(t)$ gives the charging state according to Equation A.5, I_{pc} is the initial photocharging current when fully discharged, t_d gives the discharge time in the dark, and fofa is the form factor, which relates photocharging current scaling with area to mass of the battery. Power output remains approximately constant since it is governed by the electric discharging current, albeit the photovoltage decays slightly over the duration of the discharge (see Figure A.5). The energy enhancement gets more significant for smaller discharging currents (as discussed in Figure 6.4 (a): at 5.01 A kg^{-1}, when illuminating with 1 or 1.3 Sun, the extracted electrical energy density increases from 1.5 W h kg^{-1} (in the dark case) to

$2.4\,\mathrm{W\,h\,kg^{-1}}$ ($60\,\%$ enhancement) and $12\,\mathrm{W\,h\,kg^{-1}}$ ($700\,\%$ enhancement), respectively. Simultaneously, the extracted charge increases from 1.9 to $3.1\,\mathrm{A\,h\,kg^{-1}}$ ($63\,\%$ enhancement) and $15\,\mathrm{A\,h\,kg^{-1}}$ ($689\,\%$ enhancement) for 1 and 1.3 Sun, respectively. Note the huge difference between 1 and 1.3 Sun illumination, which results from the electric discharging current of $5.01\,\mathrm{A\,kg^{-1}}$ being larger than the photocharging current. At this point, the solar battery never fully discharges, and the charging state of the device stabilizes at a finite value where the charging state-dependent photocharging current equals the electric discharging current (we thus have to abort the simulation at 3 h, see Section A.6.3). When utilizing a larger discharging current of $50.1\,\mathrm{A\,kg^{-1}}$, the charge increases by only 3.1 and $4.1\,\%$ for 1 and 1.3 Sun illumination, respectively, underlining how important suitable operation conditions for solar batteries are. While energy and power are lower compared to conventional batteries, the gains *via* illumination parallel to discharge shown herein open new vistas for engineering performance without modifying the device itself.

6.3. Conclusion

In conclusion, utilizing optic simulations as well as (photo)electrochemical experiments we provide a more holistic view on performance of the novel class of integrated solar battery devices, which employ the active material K-PHI as a model system which is bifunctional in terms of light absorption and charge storage. We first suggest a model based on solar cell designs, in which light absorption with an IQE of $100\,\%$ only occurs in a collection layer with a width of 10 nm at the junction between K-PHI and PVK HTM. By calculating the absorptance within the solar battery comprising different K-PHI active layer thicknesses and the corresponding PEDOT:PSS HSM layer thicknesses, we can extract certain design specifications and performances (as summarized in Table A.4). (1): Thinner active layers lead to larger photocharging currents (better solar cell functionality), albeit with the payoff of a smaller electric capacity (worse battery functionality). This issue has been pinpointed as a key conceptual challenge of solar batteries.[4–6] (2): Illumination through the rear of the device is superior irrespective of active layer thickness, assuming that the collection layer is thinner than the active layer. This mode helps to minimize the impact of active layer thickness on photocharging current, *i.e.*, a pathway to improve apparent capacity (battery functionality) without limiting the photocharging current significantly (solar cell functionality), if HTM and HSM materials with no relevant absorption are used. (3): We propose different qualita-

tive approaches to increase absorption within the collection layer beyond tuning active layer thickness: *via* scattering of a rough surface which is a common strategy to improve light absorption for solar cells.[60,61] We further propose enhancement strategies incorporating a grating, which causes higher diffraction orders, dielectric nanoparticles supporting both diffraction as well as scattering, and plasmonic nanoparticles maximizing electric field intensity in their close vicinity. (4): We look at solar battery specific efficiency limitations beyond solar cells and batteries. The internal photocharging current is decreasing with increasing charging state, *i.e.*, the more the battery is charged, the smaller the photocharging current becomes. (5): Electrochromic effects upon charging are important to consider, but their influence on the K-PHI/PEDOT:PSS is negligible since they do not decrease transmission of blue light to the collection layer of K-PHI.

We believe that these observations as well as proposed design pathways will prove to be valuable to understand the behavior of this novel class of devices and optimize their efficiency. To visualize the potential of solar batteries, we adapt Ragone plots to show not only a line corresponding to the power and energy density for different discharging currents, but also an area proportional to a potential enhancement *via* photocharging current generated under illumination. We show how energy output increases most significantly for small electric discharging currents which are in the range of the photocharging current generated *via* illumination. This leads us to conclude that only minor light intensity increases can lead to major performance boosts. Implementation of a low-intensity solar concentrator could yield a significant increase in energy efficiency.[62] While the solar battery based on a bifunctional photoanode and a hole transfer cascade *via* an HTM possesses the ability to be operated as a solar cell and facilitates simultaneous light charging and electric discharging, design and operation considerations as well as performance metrics presented herein are transferable to other solar battery concepts, such as photocapacitors or solar redox flow batteries – both with bifunctional electrodes (photoanode or photocathode) or with separated light absorption and charge storage material heterojunctions.

Acknowledgements

The authors thank T. Gouder for fruitful discussions and J. Kröger as well as A. V. Boris (MPI-FKF) for assistance regarding the K-PHI ellipsometry sample preparation, characterization, and discussion. Financial support was granted by the Max

Planck Society, the University of Munich (LMU), the Deutsche Forschungsgemeinschaft (DFG) *via* the Cluster of Excellence "e-conversion" (Project No. EXC2089/1-390776260), and by the Center for NanoScience (CENS). A.J.-S. gratefully acknowledges Spanish Ministry of Universities for funding through a Beatriz Galindo Research Fellowship BG20/00015. F.P. gratefully acknowledges UKRI funding under the grant reference EP/X027449/1.
Open access funding enabled and organized by Projekt DEAL.

Declaration of interests

The authors declare no conflict of interest.

6.4. References

(1) Nayak, P. K.; Mahesh, S.; Snaith, H. J.; Cahen, D. *Nat. Rev. Mater.* **2019**, *4*, 269–285.

(2) Brunner, C.; Deac, G.; Braun, S.; Zöphel, C. *Renew. Energy* **2020**, *149*, 1314–1324.

(3) Astakhov, O.; Merdzhanova, T.; Kin, L.-C.; Rau, U. *Sol. Energy* **2020**, *206*, 732–740.

(4) Gurung, A.; Qiao, Q. *Joule* **2018**, *2*, 1217–1230.

(5) Lv, J.; Xie, J.; Mohamed, A. G. A.; Zhang, X.; Wang, Y. *Chem. Soc. Rev.* **2022**, *51*, 1511–1528.

(6) Lv, J.; Xie, J.; Mohamed, A. G. A.; Zhang, X.; Feng, Y.; Jiao, L.; Zhou, E.; Yuan, D.; Wang, Y. *Nat. Rev. Chem.* **2023**, *7*, 91–105.

(7) Zeng, Q.; Lai, Y.; Jiang, L.; Liu, F.; Hao, X.; Wang, L.; Green, M. A. *Adv. Energy Mater.* **2020**, *10*, 1903930.

(8) Chen, P.; Li, T.-T.; Yang, Y.-B.; Li, G.-R.; Gao, X.-P. *Nat. Commun.* **2022**, *13*, 64.

(9) Um, H.-D.; Choi, K.-H.; Hwang, I.; Kim, S.-H.; Seo, K.; Lee, S.-Y. *Energy Environ. Sci.* **2017**, *10*, 931–940.

(10) Paolella, A. et al. *Nat. Commun.* **2017**, *8*, 14643.

(11) Zhang, X.; Su, K.; Mohamed, A. G. A.; Liu, C.; Sun, Q.; Yuan, D.; Wang, Y.; Xue, W.; Wang, Y. *Energy Environ. Sci.* **2022**, *15*, 780–785.

(12) Tewari, N.; Shivarudraiah, S. B.; Halpert, J. E. *Nano Lett.* **2021**, *21*, 5578–5585.

(13) Lou, S. N.; Sharma, N.; Goonetilleke, D.; Saputera, W. H.; Leoni, T. M.; Brockbank, P.; Lim, S.; Wang, D.-W.; Scott, J.; Amal, R.; Ng, Y. H. *Adv. Energy Mater.* **2017**, *7*, 1700545.

(14) Wang, W.; Zhang, X.; Lin, J.; Zhu, L.; Zhou, E.; Feng, Y.; Yuan, D.; Wang, Y. *Angew. Chem. Int. Ed.* **2022**, *61*, e202214816.

(15) Boruah, B. D.; Wen, B.; De Volder, M. *ACS Nano* **2021**, *15*, 16616–16624.

(16) Podjaski, F.; Kröger, J.; Lotsch, B. V. *Adv. Mater.* **2018**, *30*, 1705477.

(17) Schlomberg, H.; Kröger, J.; Savasci, G.; Terban, M. W.; Bette, S.; Moudrakovski, I.; Duppel, V.; Podjaski, F.; Siegel, R.; Senker, J.; Dinnebier, R. E.; Ochsenfeld, C.; Lotsch, B. V. *Chem. Mater.* **2019**, *31*, 7478–7486.

(18) Lau, V. W.-h.; Moudrakovski, I.; Botari, T.; Weinberger, S.; Mesch, M. B.; Duppel, V.; Senker, J.; Blum, V.; Lotsch, B. V. *Nat. Commun.* **2016**, *7*, 12165.

(19) Kröger, J.; Podjaski, F.; Savasci, G.; Moudrakovski, I.; Jiménez-Solano, A.; Terban, M. W.; Bette, S.; Duppel, V.; Joos, M.; Senocrate, A.; Dinnebier, R.; Ochsenfeld, C.; Lotsch, B. V. *Adv. Mater.* **2022**, *34*, 2107061.

(20) Podjaski, F.; Lotsch, B. V. *Adv. Energy Mater.* **2021**, *11*, 2003049.

(21) Lau, V. W.-h.; Klose, D.; Kasap, H.; Podjaski, F.; Pignié, M.-C.; Reisner, E.; Jeschke, G.; Lotsch, B. V. *Angew. Chem. Int. Ed.* **2017**, *56*, 510–514.

(22) Banerjee, T.; Podjaski, F.; Kröger, J.; Biswal, B. P.; Lotsch, B. V. *Nat. Rev. Mater.* **2020**, *6*, 168–190.

(23) Kröger, J.; Jiménez-Solano, A.; Savasci, G.; Lau, V. W. h.; Duppel, V.; Moudrakovski, I.; Küster, K.; Scholz, T.; Gouder, A.; Schreiber, M.-L.; Podjaski, F.; Ochsenfeld, C.; Lotsch, B. V. *Adv. Funct. Mater.* **2021**, *31*, 2102468.

(24) Wang, X.; Maeda, K.; Thomas, A.; Takanabe, K.; Xin, G.; Carlsson, J. M.; Domen, K.; Antonietti, M. *Nat. Mater.* **2009**, *8*, 76–80.

(25) Mazzanti, S.; Savateev, A. *ChemPlusChem* **2020**, *85*, 2499–2517.

(26) Gouder, A.; Jiménez-Solano, A.; Vargas-Barbosa, N. M.; Podjaski, F.; Lotsch, B. V. *Mater. Horiz.* **2022**, *9*, 1866–1877.

(27) Sridhar, V.; Podjaski, F.; Kröger, J.; Jiménez-Solano, A.; Park, B.-W.; Lotsch, B. V.; Sitti, M. *Proc. National Acad. Sci.* **2020**, *117*, 24748–24756.

(28) Sridhar, V.; Podjaski, F.; Alapan, Y.; Kröger, J.; Grunenberg, L.; Kishore, V.; Lotsch, B. V.; Sitti, M. *Sci. Robot.* **2022**, *7*, 62.

(29) Sharma, N.; Gupta, S. K.; Singh Negi, C. M. *Superlattices Microstruct.* **2019**, *135*, 106278.

(30) Duijnstee, E. A.; Ball, J. M.; Le Corre, V. M.; Koster, L. J. A.; Snaith, H. J.; Lim, J. *ACS Energy Lett.* **2020**, *5*, 376–384.

(31) Shao, Y.; El-Kady, M. F.; Sun, J.; Li, Y.; Zhang, Q.; Zhu, M.; Wang, H.; Dunn, B.; Kaner, R. B. *Chem. Rev.* **2018**, *118*, 9233–9280.

(32) Gouder, A.; Podjaski, F.; Jiménez-Solano, A.; Kröger, J.; Wang, Y.; Lotsch, B. V. *Energy Environ. Sci.* **2023**, DOI: 10.1039/d2ee03409c.

(33) He, L.; Wang, D.; Zhao, Y.; Zhang, Y.; Wei, W.; Shen, L. *J. Mater. Chem. C* **2021**, *9*, 11722–11728.

(34) Kröger, J.; Jiménez-Solano, A.; Savasci, G.; Rovó, P.; Moudrakovski, I.; Küster, K.; Schlomberg, H.; Vignolo-González, H. A.; Duppel, V.; Grunenberg, L.; Dayan, C. B.; Sitti, M.; Podjaski, F.; Ochsenfeld, C.; Lotsch, B. V. *Adv. Energy Mater.* **2021**, *11*, 2003016.

(35) Sun, K.; Zhang, S.; Li, P.; Xia, Y.; Zhang, X.; Du, D.; Isikgor, F. H.; Ouyang, J. *J. Mater. Sci. Mater. Electron.* **2015**, *26*, 4438–4462.

(36) Volkov, A. V.; Wijeratne, K.; Mitraka, E.; Ail, U.; Zhao, D.; Tybrandt, K.; Andreasen, J. W.; Berggren, M.; Crispin, X.; Zozoulenko, I. V. *Adv. Funct. Mater.* **2017**, *27*, 1700329.

(37) Gao, X.; Zu, L.; Cai, X.; Li, C.; Lian, H.; Liu, Y.; Wang, X.; Cui, X. *Nanomaterials* **2018**, *8*, 335.

(38) Chang, J.-F.; Huang, Y.-S.; Chen, P.-T.; Kao, R.-L.; Lai, X.-Y.; Chen, C.-C.; Lee, C.-C. *Opt. Express* **2015**, *23*, 14695.

(39) Chen, C.-W.; Hsiao, S.-Y.; Chen, C.-Y.; Kang, H.-W.; Huang, Z.-Y.; Lin, H.-W. *J. Mater. Chem. A* **2015**, *3*, 9152–9159.

(40) König, T. A. F.; Ledin, P. A.; Kerszulis, J.; Mahmoud, M. A.; El-Sayed, M. A.; Reynolds, J. R.; Tsukruk, V. V. *ACS Nano* **2014**, *8*, 6182–6192.

(41) Rubin, M. *Sol. Energy Mater.* **1985**, *12*, 275–288.

(42) Anrango-Camacho, C.; Pavón-Ipiales, K.; Frontana-Uribe, B. A.; Palma-Cando, A. *Nanomaterials* **2022**, *12*, 443.

(43) Kirchartz, T.; Agostinelli, T.; Campoy-Quiles, M.; Gong, W.; Nelson, J. *J. Phys. Chem. Lett.* **2012**, *3*, 3470–3475.

(44) Tait, J. G.; Paetzold, U. W.; Cheyns, D.; Turbiez, M.; Heremans, P.; Rand, B. P. *ACS Appl. Mater. Interfaces* **2016**, *8*, 2211–2219.

(45) Wilken, S.; Sandberg, O. J.; Scheunemann, D.; Österbacka, R. *Sol. Rrl* **2020**, *4*, 1900505.

(46) Listorti, A.; O'Regan, B.; Durrant, J. R. *Chem. Mater.* **2011**, *23*, 3381–3399.

(47) Brandsrud, M. A.; Blümel, R.; Lukacs, R.; Seim, E.; Marstein, E. S.; Olsen, E.; Kohler, A. *J. Photonics For Energy* **2021**, *11*, 024501.

(48) Martins, E. R.; Li, J.; Liu, Y.; Zhou, J.; Krauss, T. F. *Phys. Rev. B* **2012**, *86*, 041404(R).

(49) Martins, E. R.; Li, J.; Liu, Y.; Depauw, V.; Chen, Z.; Zhou, J.; Krauss, T. F. *Nat. Commun.* **2013**, *4*, 2665.

(50) Jiménez-Solano, A.; Carretero-Palacios, S.; Míguez, H. *Opt. Express* **2018**, *26*, A865.

(51) Carretero-Palacios, S.; Jiménez-Solano, A.; Míguez, H. *ACS Energy Lett.* **2016**, *1*, 323–331.

(52) Grzelczak, M.; Pérez-Juste, J.; Mulvaney, P.; Liz-Marzán, L. M. *Chem. Soc. Rev.* **2008**, *37*, 1783.

(53) Jiménez-Salcedo, M.; Monge, M.; Tena, M. T. *Materials* **2021**, *14*, 3912.

(54) Qin, J.; Zeng, H. *Appl. Catal. B: Environ.* **2017**, *209*, 161–173.

(55) Tomaszewska, A. et al. *eTransportation* **2019**, *1*, 100011.

(56) Yang, W.; Godin, R.; Kasap, H.; Moss, B.; Dong, Y.; Hillman, S. A. J.; Steier, L.; Reisner, E.; Durrant, J. R. *J. Am. Chem. Soc.* **2019**, *141*, 11219–11229.

(57) Savateev, O. *Adv. Energy Mater.* **2022**, *12*, 2200352.

(58) K, N.; Rout, C. S. *Rsc Adv.* **2021**, *11*, 5659–5697.

(59) Noori, A.; El-Kady, M. F.; Rahmanifar, M. S.; Kaner, R. B.; Mousavi, M. F. *Chem. Soc. Rev.* **2019**, *48*, 1272–1341.

(60) Scholtz, L.; Ladanyi, L.; Mullerova, J. *Adv. Electr. Electron. Eng.* **2015**, *12*, 631–638.

(61) Kim, M. S.; Lee, J. H.; Kwak, M. K. *Int. J. Precis. Eng. Manuf.* **2020**, *21*, 1389–1398.

(62) Jiménez-Solano, A.; Delgado-Sánchez, J.-M.; Calvo, M. E.; Miranda-Muñoz, J. M.; Lozano, G.; Sancho, D.; Sánchez-Cortezón, E.; Míguez, H. *Prog. Photovolt. Res. Appl.* **2015**, *23*, 1785–1792.

7

An Integrated Solar Battery based on a Charge Storing 2D Carbon Nitride

Andreas Gouder, Filip Podjaski, Alberto Jiménez-Solano, Julia Kröger, Yang Wang, and Bettina V. Lotsch

This article was published on February 15th 2023 in:

Energy & Environmental Science **2023**, 16, 1520-1530.
doi: 10.1039/D2EE03409C

Keywords: carbon nitride, PHI, solar battery, photobattery, energy storage

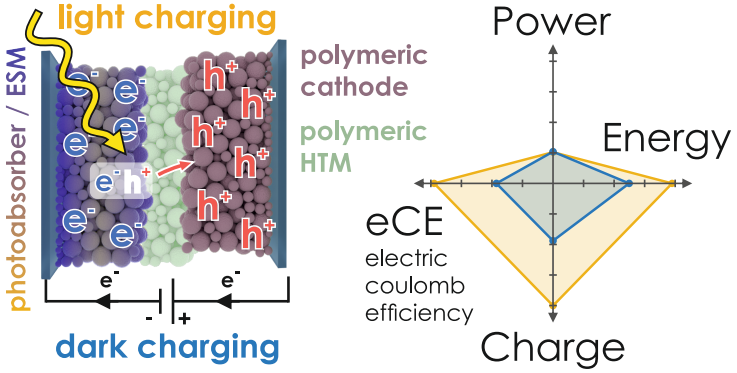

We present an integrated solar battery with a bifunctional carbon nitride (K-PHI) photoanode, combined with polymeric hole transport and cathode materials. Light charging enables energy storage and increases battery round-trip efficiency by 94 %.

Back cover art of *Energy & Environmental Science* **2023**, *16*, 1800.

Designed by Vera Hiendl.

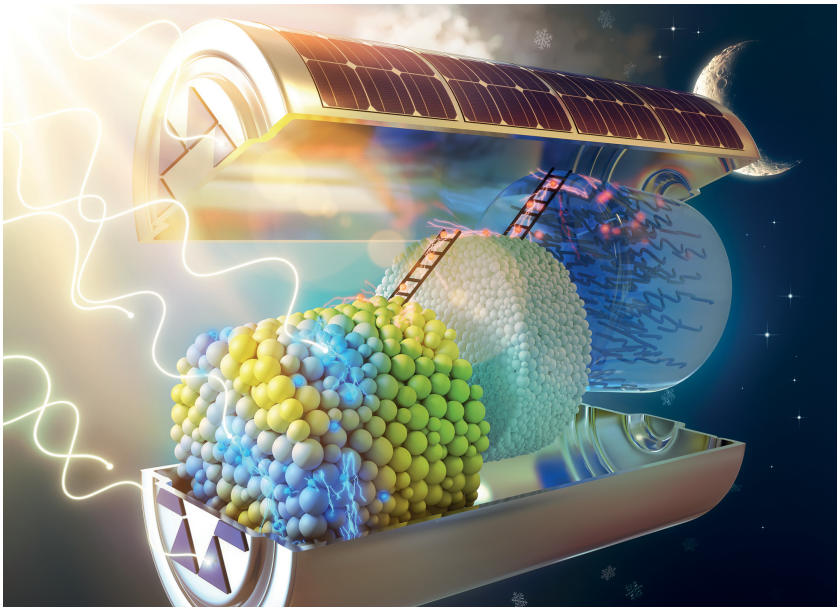

Showcasing research from Professor Bettina V. Lotsch's department, Max Planck Institute for Solid State Research, Stuttgart, Germany.

An integrated solar battery based on a charge storing 2D carbon nitride

We present an integrated solar battery based on an optoionic, bifunctional carbon nitride (K-PHI) photoanode, a polymeric hole transporter and a hole-storage organic cathode material for discharge on demand. The ladder-type internal charge transfer enables wireless light-only or light-assisted charging, while the device can also be operated as a normal battery. Simultaneous solar energy conversion and storage in a single device increases battery round-trip efficiency by 94%. We acknowledge V. Hiendl @ e-conversion for the cover art.

As featured in:

See F. Podjaski, B. V. Lotsch *et al.*, *Energy Environ. Sci.*, 2023, **16**, 1520.

ROYAL SOCIETY OF CHEMISTRY

rsc.li/ees

Registered charity number: 207890

Author contributions

Andreas Gouder, Filip Podjaski, Alberto Jiménez-Solano, Julia Kröger, and Bettina V. Lotsch conceived the project. Andreas Gouder performed the measurements. Andreas Gouder and Filip Podjaski, with assistance of Yang Wang, analyzed the data. Andreas Gouder and Filip Podjaski wrote the manuscript with assistance of all authors.

Contents

7.1. Introduction **193**
7.2. Results and discussion **195**
7.2.1. Device design 195
7.2.2. Operation modes of the device 198
7.2.2.1. Solar cell operation. 198
7.2.2.2. Solar battery operation *via* light charging. 200
7.2.2.3. Solar battery operation *via* electric and light – assisted electric charging. 202
7.3. Conclusion **207**
7.4. Experimental **210**
7.5. References **212**

7

Abstract

Solar batteries capable of harvesting sunlight and storing solar energy present an attractive vista to transition our energy infrastructure into a sustainable future. Here we present an integrated, fully earth-abundant solar battery based on a bifunctional (light absorbing and charge storing) carbon nitride (K-PHI) photoanode, combined with organic hole transfer and storage materials. An internal ladder-type hole transfer cascade *via* a transport layer is used to selectively shuttle the photogenerated holes to the PEDOT:PSS cathode. This concept differs from previous designs such as light-assisted battery schemes or photocapacitors and allows charging with light during both electrical charge and discharge, thus substantially increasing the energy output of the cell. Compared to battery operation in the dark, light-

assisted (dis)charging increases charge output by 243 %, thereby increasing the electric coulombic efficiency from 68.3 % in the dark to 231 %, leading to energy improvements of 94.1 % under illumination. This concept opens new vistas towards compact, highly integrated devices based on multifunctional, carbon-based electrodes and separators, and paves the way to a new generation of earth-abundant solar batteries.

Broader context

Harvesting abundant solar radiation presents a very promising avenue to produce renewable energy, yet provides its own set of challenges: Stochastic fluctuations of the solar flux generate intermittency on timescales of months (winter-summer), days (day-night) or minutes to hours (*e.g.*, weather), which requires energy storage functionalities to balance. The emerging concept of solar batteries incorporates light absorption functionality into batteries. Bifunctional photoanodes or -cathodes push this idea further by utilizing materials capable of both charge storage and light absorption, at the expense of a complex charge transfer mechanism. In this work, we present the earth-abundant carbon nitride K-PHI as bifunctional photoanode to simultaneously absorb light and store electrons, and design a new internal charge transfer mechanism *via* an organic polymer hole transporter as battery separator to enable both ion conduction and rectified photogenerated hole transfer to the cathode. Our internal mechanism resembling a planar heterojunction solar cell facilitates operation of the device and only requires low-cost earth abundant materials, both key for applications, which requires high levels of integration.

7.1. Introduction

While the world transitions from fossil to sustainable energy sources, integrating fluctuating renewable energy into the power grid provides its very own set of challenges. Volatile wind and solar energy suffer from intermittent availability; this requires enhanced flexibility of the power grid as well as new energy storage technologies. In particular, photovoltaics (PV) produces significant stochastic intraday fluctuations (*e.g.*, due to cloud overcast), which requires short-term energy storage solutions in the time range of minutes to hours.[1,2] Energy storage technologies can help to balance this residual load.

Solar batteries and solar capacitors are a relatively new class of devices, which

aim to integrate energy harvesting functionalities into energy storage devices.[3,4] While discrete charging technologies are widely employed nowadays (*i.e.*, battery and PV are independent units that are connected as stacks or *via* DC-DC converters[5]),[6] integrating PV and batteries into a single device is attracting increased interest due to its more facile implementation, flexibility, and volume minimization.[7] Such devices can be categorized as three-electrode configurations (PV electrode, anode, and cathode) and two-electrode configurations (either bifunctional anode and cathode, or bifunctional cathode and anode). Three-electrode configurations were demonstrated using photoelectrodes inside of batteries[8–10] or *via* different solar redox flow battery designs.[11–13] Two-electrode configurations have been enabled *via* heterojunctions by depositing photoactive layers onto the anode of a battery or capacitor,[14] or *via* composites of charge storage materials and photoactive materials.[15,16]

However, a third vista is gaining momentum: utilizing bifunctional photoelectrochemical energy storage materials, which are capable of performing both light absorption and charge storage in a single material.[17] There are several reports of bifunctional materials, both inorganic (*e.g.*, V_2O_5,[18,19] MoO_3,[20] TiO_2,[21] or 2D perovskites[22]) and organic (*e.g.*, covalent organic frameworks,[23] quinone derivatives,[24] or porous organic cages[25]). Notably, all existing device designs rely on transfer of the photogenerated charge carriers to the anode or cathode *via* an electrolyte or additional external circuit during charging, with the separator between the electrodes acting solely to conduct ions and prevent a short circuit, inspired by traditional battery designs, and thus resemble integrated PV-batteries. Note that three-electrode designs such as photo(super) capacitors also require an external charge transfer of photogenerated charge carriers and additional redox shuttles to close the internal circuit.[4,26,27] Simultaneous photocharging and discharging *via* a load is complicated, since the external wiring is engaged in the charging process, and external electronics are necessary to change from charging to discharging mode. These drawbacks motivate us to investigate pathways of internal photogenerated hole transfer with a separator that simultaneously acts as hole shuttle.

We recently reported a bifunctional solar battery electrode material based on the fully earth-abundant 2D carbon nitride potassium poly(heptazine imide) (K-PHI).[17] Upon light excitation (bandgap of $\sim$2.7 eV), electron-hole pair separation, and extraction of the hole, K-PHI can "trap" photoexcited electrons up to several hours[28,29] to days[30,31] and release them on demand, accompanied by a color change from yellow to blue. This combination of optoelectronic and optoionic properties, which are

linked to photointercalation of K^+ ions[32] and electron trapping in an intercalation band within the bandgap produces (pseudo)capacitive electron storage[17,29] and has led to applications in "dark" photocatalysis,[33–37] photomemristive sensing,[29] and multifunctional light-driven microswimmers.[38,39]

Herein, we design a proof-of-concept "direct solar battery" using K-PHI as active layer, which is tasked with absorbing light and storing photoexcited electrons as well as balancing charges with intrinsic K^+ ion movement. Contrary to currently published designs discussed above, we do not use an external circuit to transfer holes to the hole storage material (HSM) counter (electrode), but rather rely on an internal ladder-type hole transfer cascade performed by a multifunctional hole transport material (HTM) – a design more reminiscent of planar heterojunction-type solar cells than of batteries (Figure 7.1 (a)). Photocharging occurs internally under open circuit potential (OCP) conditions. We first identify suitable materials, poly(9,9 - dioctylfluorene - alt - benzothiadiazole) (F8BT) as HTM and poly(3,4 - ethylendioxythiophene) polystyrene sulfonate (PEDOT:PSS) as HSM, and then investigate kinetics and performance of different operation modes: (1) charging *via* illumination only and under open circuit potential (OCP) conditions, (2) solely electric in the dark with an external current, and finally (3) in a light-assisted electric mode.

7.2. Results and discussion

7.2.1. Device design

The concept of the solar battery is visualized in Figure 7.1 (a): K-PHI absorbs light and generates electron-hole pairs. Charge separation likely occurs close to the junction to the hole acceptor,[34,40] which can either be a redox shuttle or hole transport material (HTM). A solid HTM presents fewer self-discharge pathways *via* an electrolyte (*e.g.*, water oxidation or reduction) and is less prone to recombination since charges are immediately shuttled to the hole storage material (HSM) – a problem which has been identified as major challenge for solar batteries.[3] In the integrated direct solar battery we propose herein, we use a solid HTM, which acts as a battery separator and redox shuttle to transport photogenerated holes from K-PHI to the HSM, while mobile ions (K^+, H^+) provide internal electrostatic charge compensation (Figure 7.1 (a), green for HTM (F8BT) and blue for HSM (PEDOT:PSS)).[17,41–43] Simultaneously, the HTM acts as a rectifier and prevents self-discharge *via* an inter-

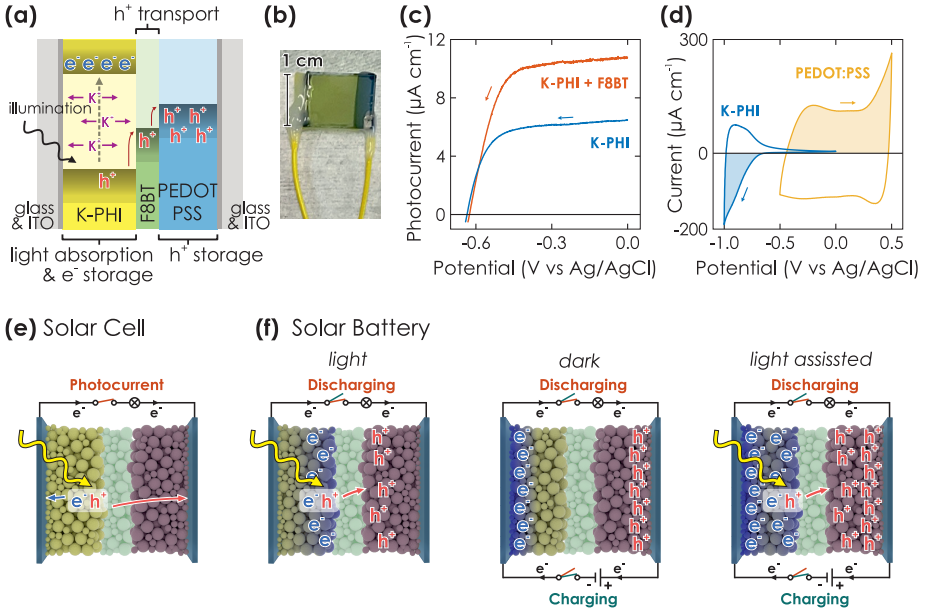

Figure 7.1. Concept and requirements of a solar battery device. **(a)** Scheme of a direct solar battery device, comprising K-PHI as photoactive and electron storage material, the HTM F8BT and the HSM PEDOT:PSS, sandwiched between two ITO sheets. The hole transport process is indicated with red arrows. **(b)** Picture of a direct solar battery device. The left and right wires are soldered to the substrate which is in contact with K-PHI and PEDOT:PSS, respectively. **(c)** Linear scanning voltammetry (LSV) curves of K-PHI (blue) and K-PHI decorated with the HTM F8BT (red), measured in an aqueous electrolyte containing the sacrificial electron donor methanol (100 mM) in 3-electrode configuration. K-PHI + F8BT shows a significantly larger photocurrent at potentials more positive than -0.4 V *vs.* Ag/AgCl, evidencing enhanced photogenerated hole extraction rates with the HTM. **(d)** Cyclic voltammetry (CV) measurements of ITO electrodes containing K-PHI (blue) and PEDOT:PSS (yellow), measured in 3-electrode configuration. **(e)** and **(f)** Schemes of different operation modes of the device, either as solar cell (e) or solar battery with various operation modes (f). Yellow and blue balls represent K-PHI in its respective discharged and photoreduced charged state, green balls refer to the HTM, and red balls represent the HSM. The blue rectangular cuboids represent the ITO substrate. Black lines show external wire connection and current flux direction during different operations. We show the charging mechanism of the solar battery *via* only light (left), only electric (middle) or simultaneously using light and electric (right) power simultaneously. Color code of the switches defines the circuit switches in respective operations (red when extracting charges from the device (either as photocurrent or *via* discharging), green when charging the battery). Note that both circuits utilize the same connection on the device, but are plotted on top and bottom of the device to visualize different operations.

nal short-circuit between K-PHI and HSM (*i.e.*, if holes are not only shuttled from K-PHI to the HSM, but also back from the HSM to K-PHI to quench the electrons trapped on K-PHI). The solar battery can be discharged on demand *via* an external

electric circuit. Note that this approach with a multifunctional HTM separator is thus far unique since it does not require an external wire to shuttle charge carriers from one electrode to another during charging, further facilitating implementation by allowing simultaneous light charging and electric discharging, as well as operation as a solar cell.

We now discuss the fabrication of the device and the rationale behind the materials selection (Figure 7.1 (b)): Films of K-PHI on indium tin oxide substrates (ITO) were prepared according to a procedure recently described by us.[17,29] In brief, K-PHI was synthesized in a salt melt containing KSCN and the 1D heptazine based polymer melon.[35,44,45] Subsequently, the product was washed, exfoliated *via* sonication in isopropanol, and homogeneous films of 0.5 to 2 µm thickness were obtained *via* dip coating (see Section 7.4 and Section B.1 for more details). In order to optimize charge separation at the K-PHI/HTM interface, we first performed screening experiments of both conductive polymer and small molecule HTMs (deposited *via* spin coating onto K-PHI) utilizing the sacrificial electron donor methanol as a replacement for the HSM (see Section B.2 for a more detailed discussion).[17] By evaluating photocurrent as a figure of merit, we identified F8BT as the most suitable candidate. The linear sweep voltammogram of K-PHI and F8BT, measured against a reference electrode in three-electrode configuration, is shown in Figure 7.1 (c) under 1 Sun illumination and compared to bare K-PHI. At a potential of 0 V *vs.* Ag/AgCl where photogenerated electrons are discharged, an oxidative photocurrent of 10.7 and 6.47 µA is reached for K-PHI with and without F8BT, respectively, highlighting the beneficial role of F8BT to extract holes from K-PHI. With more negative potentials, the photocurrent decreases nearly linearly due to a decreasing driving force for electron extraction, until at -0.4 V *vs.* Ag/AgCl it collapses to 0 µA. For all samples, we observed an open circuit potential (OCP) of about -0.6 V *vs.* Ag/AgCl (Figure 7.1 (c)). We explain the increase in photocurrent upon addition of the HTM by an improvement of the photogenerated hole extraction efficiency – a step which is known to be limiting for carbon nitride photo(electro)catalysts[29] – which in return decreases recombination of photogenerated charge carriers and increases the photocurrent response, leading to better photocharging of K-PHI. As HSM, we chose the widely studied conductive polymer PEDOT:PSS, deposited analogous to F8BT *via* spin coating. PEDOT:PSS was shown to operate as a p-type substrate capable of reductively quenching holes on n-type K-PHI upon photoexcitation. This process is akin to photocharging and underlines the suitability of PEDOT:PSS as HSM.[40] Charge storage is enabled at potentials more positive than the valence band of K-PHI

and F8BT *via* a well investigated pseudocapacitive mechanism, making it a suitable cathode material.[46] The ladder-type redox band position (band alignment) of the HTM and HSM (Figure 7.1 (a)) is thus suitable for extracting photogenerated holes in a cascade process. Three-electrode cyclic voltammetry (CV) measurements of K-PHI and PEDOT:PSS samples in the dark show the charge storage potential and capacity of both materials (see overlay in Figure 7.1 (d)). While K-PHI shows its well-reported typical CV shape with a charging onset at $-0.65\,\mathrm{V}$ *vs.* Ag/AgCl,[17] PEDOT:PSS produces a nearly rectangular CV – typical for its pseudocapacitive charge storage mechanism.[47] Note that the capacity of PEDOT:PSS is chosen larger than of K-PHI to prevent a performance bottleneck on the cathode side. Utilizing all these components allows us to realize the integrated solar battery (Figure 7.1 (b)).

7.2.2. Operation modes of the device

A solar battery can be operated in different modes.[3,7] Upon illumination, the resulting photocurrent can be accessed by connecting the anode and cathode to the potentiostat and applying a suitable bias voltage. The device then operates analogous to a solar cell (Figure 7.1 (e)). However, when operating under OCP conditions (*i.e.*, no current is extracted *via* the current collectors), the photogenerated electrons and holes accumulate in the anode and cathode and thus, charge the device (Figure 7.1 (f), left). Subsequently, the stored charges can be accessed in the dark by applying a suitable discharge current until the cell voltage reaches $0\,\mathrm{V}$ (voltage at which the device is fully discharged).

Conversely, we can also perform electric charging and discharging in the dark *via* an external current (*i.e.*, a current applied *via* the potentiostat) – analogous to a GCD experiment in a normal battery (Figure 7.1 (f), middle). The capacity depends on the charging and discharging current rates and voltage window. The latter should be estimated from the photovoltage measured during light charging. Notably, when illuminating the device during a GCD experiment, the current flux is created by both light generated charges and the electric charging *via* the potentiostat, thus maximizing performance (Figure 7.1 (f), right). The overall effective charging current is the sum of both applied "external" current and "internal" photocurrent from light absorption. We will discuss these different operation modes in the following.

7.2.2.1. Solar cell operation. We first evaluate performance of the solar battery when operated as a solar cell. A device is immersed into oxygen-free $0.1\,\mathrm{M}$

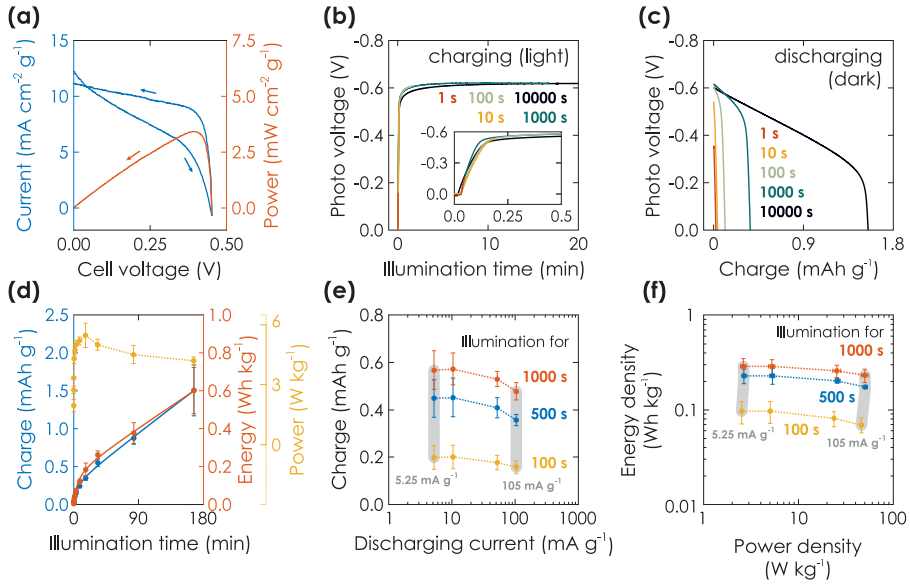

Figure 7.2. Solar battery characterization of light charging process. (a) Current-voltage (blue) and power (red) curves ($10\,\mathrm{mV\,s^{-1}}$) of a solar battery sample in solar cell mode, illuminated with 1 Sun. **(b)** Charging of the solar battery with different illumination times at 1 Sun and under OCP conditions (inset shows a zoom of short illumination times). **(c)** Subsequent electric discharging in the dark with a fixed current of $10.5\,\mathrm{mA\,g^{-1}}$ (normalized against mass of K-PHI, HTM, and HSM). **(d)** Gravimetric capacity, energy, and power density extracted from the charging *via* illumination (b). **(e)** Kinetic study of the discharging process. Charging is performed *via* illumination for 100 s (yellow), 500 s (blue), and 1000 s (red). Subsequent immediate discharging is carried out with different discharging currents (5.25, 10.5, 52.5 and $105\,\mathrm{mA\,g^{-1}}$; smallest and largest current shown with vertical grey bar). **(f)** Ragone plot displaying the energy and power output with increasing illumination times and same discharging currents given in (d). Vertical grey bars links dots measured at the same smallest and largest discharge current.

KCl electrolyte and an initial activation measurement is performed. Activation measurements are necessary to remove all unwanted charges from both anode and cathode, which might reside on the sample from synthesis (see Section B.3 for details) and affect device characterization. Subsequently, we illuminated the sample with a LED (365 nm, $100\,\mathrm{mW\,cm^{-2}}$) and performed a CV measurement between OCP and 0 V cell voltage with a slow scan rate of $10\,\mathrm{mV\,s^{-1}}$ to simulate quasi-static conditions. The voltage sweeps are shown in Figure 7.2 (a). At 0 V, we measured a short circuit current (I_{sc}) of $1.07\,\mu\mathrm{A\,cm^{-2}\,g^{-1}}$ on the backwards voltage sweep (from OCP to 0 V). Note that the mass of the device is calculated from the measured mass of K-PHI, HTM, and HSM. With increasing potential, the photocurrent decreases and at a potential of approximately 0.40 V it collapses to 0 V. The OCP is 0.45 V and max-

imum power of 0.326 µW cm^{-2} is reached at a current of 0.828 µA cm^{-2} and a voltage of 0.39 V, resulting in a *FF* of 0.73 (all values calculated from backwards sweep). This behavior is in principle also observed when illuminating with a 365 nm LED (100 mW cm^{-1}) increasing the photon flux that can be absorbed, albeit at higher absolute currents (FF of 0.70, see Section B.9). While this FF is considered to be high for organic solar cell devices and is larger than common solar cells incorporating carbon nitrides as dyes,[48,49] the losses result from the small but significant slope of the current between 0 and 0.3 V. This slope is probably caused by high series and low shunt resistance (*e.g.*, due to pinholes, or traps[50]) as well as a decreasing driving force for charge separation. In case of a solar battery, current increase or loss due to a partial charging of K-PHI and PEDOT:PSS seems also possible (*vide infra*). The hysteresis between positive and negative voltage sweeps further indicates such a behavior: the larger current on the backward voltage sweep (*i.e.*, from OCP to 0 V) might be a convolution of photocurrent and discharging current of K-PHI. Such a behavior is desirable for the solar battery light charging modes discussed next.

7.2.2.2. Solar battery operation *via* light charging. We can also employ the internal photocurrent to charge the device in lieu of extracting it immediately as discussed in the previous section. This enables the most characteristic function of a solar battery: its ability to charge solely *via* illumination. We demonstrate in an experiment charging under illumination and electric discharging in the dark in Figure 7.2 (b) and (c): After immersing a solar battery sample into a degassed 0.1 M aqueous KCl electrolyte and performing the activation measurement (see Section B.3), we illuminated the device from the backside for a given time at 1 Sun under OCP conditions. Note that the task of the 0.1 M KCl electrolyte in the reactor is only to provide an oxygen-free environment, ensure stable temperature during illumination, provide sufficient humidity and to facilitate reset measurements (see Section B.3). A photovoltage of 0.6 V developed during the first 50 s and remained constant during the ensuing illumination. Subsequently, the light was turned off and the device was discharged at a current of 10.5 mA g^{-1} until the cell voltage dropped back to 0 V. Electric discharging in the dark for increasing illumination charging times (1 to $10\,000$ s) is shown in Figure 7.2 (c). The shape looks similar to a typical GCD battery measurement and indicates a faradaic charge storage mechanism: A plateau-like potential decrease to ca. 0.5 V for short and 0.3 V for long illumination times, followed by a sharp voltage drop to 0 V. Note that the plateau has a certain slope <0, indicating pseudocapacitive contributions of the charge storage mecha-

nism, and possibly also caused by increasing K-PHI or cell resistance upon discharging.[17,29,47] We discuss the charge storage mechanism more thoroughly *via* a kinetic analysis with CV measurements in Section B.4.

The respective capacity, energy, and power output is plotted against the illumination time in Figure 7.2 (d). Energy output can be calculated with $E = \int I_{ph} \cdot V(t)\, dt$, with I being discharge current and $V(t)$ being the cell voltage during discharging. Average power is calculated with $P = E \cdot t^{-1}$, with t being the discharging time. When illuminating the sample for $10\,000$ s, we can extract a charge of 1.5 mA h g^{-1} and an energy of 0.60 W h kg^{-1}. A saturation behavior of the capacity becomes evident for illumination times above ca. 2000 s (Figure 7.2 (d), blue: initial slope is decreasing), but is not reached after $10\,000$ s, suggesting that the charging process is likely slowed down by the concomitant charge accumulation[29,51,52] limiting photocharging efficiency and that the true capacity of K-PHI is hence larger. It is noteworthy that the shape of the extracted charge and energy curves are similar; this is because energy output depends on the photovoltage $V(t)$, which is almost constant at illumination times where the plateau is reached (>100 s; see Figure 7.2 (d), yellow). Utilizing the energy data, a maximum solar-to-output efficiency of 0.012 % can be calculated when taking only light energy larger than the bandgap of K-PHI into account (see Figure B.6). If energy of the whole solar spectrum is considered, the solar-to-output efficiency is reduced to 0.002 %. Power output for these illumination times is approximately constant since it is governed by the photovoltage as well. We discuss self-discharge in Section B.8 and show a charge retention of 72 % after 1000 s, when the device is illuminated for 1000 s.

Next, in order to analyze discharging kinetics, a solar battery sample was illuminated with 1 Sun for three representative durations (100, 500 and 1000 s) under OCP conditions and subsequently discharged in the dark with different current densities (5.25, 10.5, 52.5 and 105 mA g^{-1}). The extracted charge is shown in Figure 7.2 (e). A smaller discharging current results in a larger capacity as common for batteries due to less diffusion limitations and less resistive losses resulting from the intrinsically low conductivity of K-PHI.[17,43] While we observe this larger capacity with lower currents for all illumination times, it is more pronounced for longer durations (when comparing currents of 5.25 mA g^{-1} and 105 mA g^{-1}: 26 % and 19 % larger capacity for the smaller discharge current at illumination times of 100 and 1000 s, respectively). Scaling of energy and power density with current is presented *via* a Ragone plot in Figure 7.2 (f): energy density behaves analogous to the capacity (Figure B.8), *i.e.*, a minor increase is observed for smaller currents (5.25 to 10.5 mA g^{-1}). With

illumination duration the energy density increases for all currents (Figure 7.2 (f): yellow to red) – analogous to the behavior of energy and charge scaling with illumination time discussed above. Power density increases with current, since the cell voltage for different discharge currents is approximately constant (see GCD profiles in Figure B.7 and respective power output in Figure B.8), in line with the discussion of power output dependence on illumination time above. Thus, the kinetic behavior results in a Ragone plot with rather horizontal lines, which scale upwards (*i.e.*, increase in energy density) with illumination time, highlighting the device's energy-stable operation at larger discharge currents, *i.e.*, increased power density (up to approx. $10\,\mathrm{W\,cm^{-2}\,kg^{-1}}$). We will discuss comparison to energy storage and solar battery devices in more detail in Section 7.2.2.3 in the context of light-assisted electric charging and discharging.

7.2.2.3. Solar battery operation *via* electric and light – assisted electric charging. So far, we have discussed the ability of the solar battery to charge *via* illumination. However, as a second pathway to modify the charging state, analogous to a normal battery we can apply an external electric charging current, which can be combined with the internal photocurrent to store both solar and electric energy simultaneously in one device. To differentiate between different illumination modes during GCD, we use the terminology "cEdE" to describe electric charging and discharging in the dark, "cLEdE" when illuminating during electric charging, and "cLEdLE" when illuminating during both charging and discharging. Cell efficiency metrics defined by parameters such as capacity, energy and power density, or electric Coulombic Efficiency (eCE) can significantly improve by these combined methods. The eCE gives the ratio between charges being electrically discharged and electrically charged and thus, presents a metric to evaluate charge gains *via* illumination (for cEdE: eCE is analogous to the coulombic efficiency). In the following, we will discuss solar battery operation modes which include electric charging *via* an applied current to modify the charging state.

We first perform GCD with a current of $10.5\,\mathrm{mA\,g^{-1}}$ from 0 to $0.8\,\mathrm{V}$ in similar conditions as for the light charging measurements discussed above (see Section B.7 for the rationale behind the chosen voltage window), but in the dark (cEdE mode). We show a cycle in Figure 7.3 (a). For charging, we observe an initial fast voltage increase to about $0.5\,\mathrm{V}$, followed by an area with significantly slower voltage increase (*i.e.*, "plateau" region). When discharging, we observe a similar trend: slow voltage decrease from 0.8 to $0.5\,\mathrm{V}$ and a subsequent collapse to $0\,\mathrm{V}$. Charging and discharg-

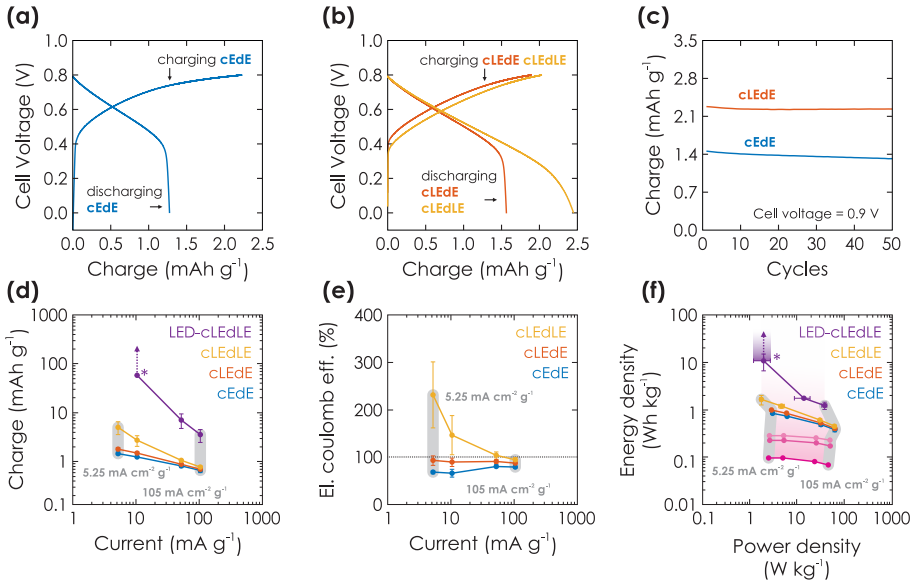

Figure 7.3. Solar battery characterization of electric and light-assisted electric charging process. **(a)** and **(b)** A cycle showing GCD in the dark (a) (cEdE) and under 1 Sun illumination (b) during charging (cLEdE) or during charging and discharging (cLEdLE) with a current of $10.5\,\mathrm{mA\,g^{-1}}$. **(c)** Extracted charge in cEdE and cLEdE mode and a cell voltage window of $0.9\,\mathrm{V}$, plotted against the cycle number. **(d)** Extracted charge as a function of electric charging and discharging current, when operating the solar battery in a voltage window of $0.8\,\mathrm{V}$ and cEdE, cLEdE or cLEdLE modes. Note that LED-cLEdLE is analogous to cLEdLE, but with a $365\,\mathrm{nm}$ LED (power analogous to 1 Sun: $100\,\mathrm{mW\,cm^{-2}}$) providing the illumination. The "*" marks a data point, where discharging could not be completed and the measurement was aborted (due to the photocurrent being larger than the discharging current). The vertical arrows show how charge would have increased with a later aborted measurement. The two exemplary vertical gray bars show measurements at the same charging and discharging current. **(e)** Electric coulombic efficiency for the measurement shown in (d), highlighting the performance gains from illumination. **(f)** Ragone plot, showing energy and power output at the currents given in (d) and (e), underlining how illumination can push the device performance to larger energy and power values. Charging solely *via* illumination is extracted from Figure 7.2 (e) and shown in purple, with illumination times increasing from 100 to $1000\,\mathrm{s}$ from dark to bright purple. Arrow and "*" mark again the aborted measurement (as discussed in (d)).

ing requires on average 580.2 and $417.9\,\mathrm{s}$, respectively. Note that the shape of the discharge curve looks similar to when the sample is only charged *via* illumination for short illumination times (Figure 7.2 (c); albeit at ca. $0.2\,\mathrm{V}$ smaller voltage), hinting onto a similar discharging mechanism.

Light-assisted GCD can be performed in cLEdE (Figure 7.3 (b), red) and cLEdLE (Figure 7.3 (b), yellow) operation modes. Compared to the dark measurement (Fig-

ure 7.3 (a)), for charging we observe again an initial region of fast voltage increase to about 0.5 V and a subsequent "plateau" region with a slope comparable to the dark measurement. However, for discharging the "plateau" lasts longer to about 0.4 V for cLEdE and 0.2 V for cLEdLE, analogous to charging with long illumination times (Figure 7.2 (c)). Charging and discharge requires on average 523.3 and 520.0 s for cLEdE as well as 608.8 and 1395 s for cLEdLE, respectively. This results in more extracted charge, which we show in Figure 7.3 (c) for a cell voltage of 0.9 V: Capacities of both dark and light GCD measurements are compared for 50 cycles, yielding an initial capacity of 1.4 and 2.3 mA h g^{-1} (92 and 98 % retained after 50 cycles), respectively. To explain mechanistic differences in electric charging *via* GCD (discussed here) and purely light charging (discussed in Section 7.2.2.2), we assume that GCD charges K-PHI and PEDOT:PSS close to the current collector (ITO substrate) first. In contrast, photocharging requires interfacial charge separation and therefore occurs rather at the junction to the HTM, or at least more in the bulk of the active layer of the battery (visualized in Figure 7.1 (f): compare position of electrons in left *vs.* middle panel). Since photogenerated electrons close to the HTM junction have to travel through the bulk of the K-PHI layer to discharge *via* the substrate, charge transport limitations due to the internal resistance of K-PHI (*i.e.*, larger iR drop) will have a larger effect as compared to electrons injected close to the substrate. Thus, self-discharge for light charging must be larger than for electric charging, which we show and discuss in Section B.8. Besides affecting discharging kinetics, the larger iR drop for photocharged electrons reduces the final cell voltage (compare cell voltage at the end of the discharging plateau in cEdE (0.5 V, Figure 7.3 (a)), cLEdE and cLEdLE (0.4 and 0.2 V, Figure 7.3 (b))). Thus, simultaneous charging *via* light and the substrate allows to access more of the solar battery volume on short time scales, which benefits the overall capacity and thus energy density. In addition, illumination increases the material's conductivity,[17] thereby facilitating also the electric charging process.

To deepen our understanding of the influence of light on parallel electric charging, we perform a kinetic study by changing charging and discharging currents. In Figure 7.3 (d), we show the respective charge output for cEdE, cLEdE, and cLEdLE modes (LED-cLEdLE is analogous to cLEdLE, but uses a 365 nm LED (100 mW cm^{-2}) as light source). Note that measurements were performed in a smaller voltage window of 0.8 V compared to 0.9 V used for the cycling stability discussed above (Figure 7.3 (c)) due to the more stable operation in this voltage window at small currents and under illumination, allowing for a more reliable comparison of differ-

ent operation modes. When operating in cEdE mode, with smaller currents (5.25 to 10.5 mA g^{-1}) the capacity increases as the system is kinetically less limited. At the same time, this increase starts to saturate for very small currents due to the longer discharging time invoking self-discharge (a discussion on self-discharge after electrical charging is given in Section B.8). When operating in cLEdE mode (Figure 7.3 (d), red), the change of capacity behaves analogous to the dark case, but with an offset to larger capacities (compared to the dark case: at a current of 5.25 mA g^{-1} we observe an increase of extracted charge of 22.0 % to 1.79 mA h g^{-1}). The offset results from the internal photocurrent assisting charging the device as discussed above. This effect is more pronounced for smaller currents (at a current of 105 mA g^{-1} we could only observe an increase of 5.54 %), which we explain with the longer charging time resulting from small currents leading to an elongated illumination time. When operating in cLEdLE mode (Figure 7.3 (d), yellow), the overall illumination time becomes much longer since the internal photocurrent is also continuously generated during discharge, which in return significantly increases the extracted charge output (compared to the dark case: at a current of 5.25 mA cm^{-2} g^{-1} we have observed an increase of extracted charge of 243 % to 5.02 mA h g^{-1}). Note that when the internal photocurrent is in the range of or larger than the external discharging current, the extracted charge increases very significantly (see cLEdLE in Figure 7.3 (d) for small currents) or even rises into infinity. We demonstrate the latter by providing illumination *via* a LED at similar illumination power compared to solar simulators with 1 Sun (100 mW cm^{-2}), but which only illuminates at wavelengths of ca. 360 to 375 nm where K-PHI can absorb (Figure 7.3 (d), LED-cLEdLE). IV curves of illumination *via* 1 Sun (Figure 7.2 (a)) and 365 nm LED are compared in Section B.9. At a discharge current as low as 10.5 mA g^{-1}, we could never complete discharging due to strong continuous internal photocurrent generation and had to abort the measurement after extracting a charge of 20 mC (58.4 mA h g^{-1}). Hence, the observed increase in extracted charge (243 %, see Figure 7.3 (d)) is larger than for reported devices with a similar bifunctional electrode, but different device designs (57 and 95 % increase in capacity for V2O5 photocathodes for lithium- and zinc-ion batteries[18,19]). This increase in charge should not be confused with an increase of capacity of the battery, but rather demonstrate a beneficial operation mode of a solar battery due to continuous charge generation under illumination. The capacity of K-PHI was reported to be 25.6 mA h g^{-1}, the equivalent of 1 electron per every 4th heptazine unit.[31] Nevertheless, the theoretical capacity of K-PHI is likely larger, especially when charged electrically to higher potentials than possi-

ble by bandgap excitation.

Next, we compare the eCE for the different solar battery operation modes (Figure 7.3 (e)), a metric which we define as the ratio between electric charging and electric discharging. Note that in comparison to the coulombic efficiency, eCE can exceed $100\,\%$ since charge generation stemming from the internal photocurrent is not taken into account in the electric external charging current.[23,24] In cEdE mode, we reach the maximum eCE (here the same as coulombic efficiency) of $80.7\,\%$ at a current of $52.5\,\mathrm{mA\,g^{-1}}$. Larger as well as smaller currents produce a decreased eCE due to kinetic limitations and self-discharge, respectively.[17] The eCE value is in fact larger than for K-PHI in a half-cell configuration reported by us earlier (approx. $72\,\%$[17]), which we explain with less self-discharge *via* the inevitable aqueous electrolyte of half-cell measurements (enabling water reduction *via* uncovered parts of the substrate). When operating in cLEdE, we can alleviate the eCE for small currents since additional charging occurs *via* the photocurrent. Thus, this mode allows a more efficient operation of the solar battery in a region where the capacity is larger (*i.e.*, smaller currents), with a maximum eCE of $92.9\,\%$ (for cEdE: $68.3\,\%$) at a current of $5.25\,\mathrm{mA\,g^{-1}}$. When operating in cLEdLE, we see a significant increase in eCE for small currents, with a maximum of $231\,\%$ at a current of $5.25\,\mathrm{mA\,g^{-1}}$. Analogous to our rationale behind the increase of extracted charge discussed above, we explain this behavior with a significantly longer illumination time compared to cLEdE, resulting in much more photocharging. Thus, the eCE reported here for cLEdLE is much larger than for literature reports of $112\,\%$.[24] Note that eCE is not a cell efficiency, since it only takes into account electron flux (*i.e.*, current) into and out of the cell and does not include the incoming photon flux, which is responsible for the photocurrents and hence, additional charges measured.

Finally, we compare power and energy density for different currents *via* a Ragone plot (Figure 7.3 (f)). The cEdE measurement resembles the behavior of a normal battery:[47] Maximum energy density ($0.846\,\mathrm{W\,h\,kg^{-1}}$) for small power at small currents and maximum power density ($62.3\,\mathrm{W\,kg^{-1}}$) for small energies at large currents. This behavior is caused by kinetic limitations of the discharging process, as discussed above. When operating in cLEdE or cLEdLE mode, we observe a similar curve shape as the dark case, but with an offset to larger energy densities (compared to cEdE at maximum energy: 16.0 and $94.1\,\%$ increase to 0.982 and $1.64\,\mathrm{W\,h\,kg^{-1}}$, respectively). This effect is more pronounced for smaller currents and can be explained analogous to our abovementioned rationale for larger capacities and improved eCE with internal photocurrent assisting in charging of the bulk. Power den-

sity slightly decreases concurrently due to the altered GCD discharging profile (compare Figure 7.3 (a) and (b)). Increasing illumination intensity *via* a LED (ca. 360 to 375 nm, 100 mW cm^{-1}) significantly amplifies the energy enhancement: Simultaneous to our discussion on extracted charge, we had to abort the measurement after extracting 10.8 W h kg^{-1} since the discharging process could not be completed, but upon longer operation the energy output should approach infinity, as indicated by the purple arrow in Figure 7.3 (f).

To understand the origin of performance improvements in the Ragone plot for cLEdE, cLEdLE, and LED-cLEdLE mode, we show the performance of charging solely *via* illumination as discussed in Section 7.2.2.2 in the same plot (Figure 7.3 (f), purple): Longer illumination times lead to more photocharging, *i.e.*, vertical scaling in the Ragone plot. Illumination assisted GCD measurements discussed here are affected in an analogous manner, *i.e.*, energy increases with illumination time. Power density on the other hand scales with current and is more or less independent of illumination duration, when not taking the effect of altered GCD shapes (Figure 7.3 (b)) into account. Thus, its scaling in the Ragone plot looks similar for all operation modes including charging solely *via* illumination (compare Figure 7.3 (f) data points at different currents, marked with gray bars). A direct comparison of energy and power scaling with discharge current for all operation modes shows the similar scaling best and is given in Figure B.8.

7.3. Conclusion

In this work, we have presented a proof-of-concept integrated solar battery device based on the earth-abundant carbon nitride K-PHI, which serves as both light absorber and charge storage (photo)anode. Photogenerated holes in K-PHI are shuttled *via* a HTM (F8BT) to the HSM (PEDOT-PSS) *via* an interfacial hole transfer cascade. This device can work as a solar cell; however, its capabilities exceed those of a solar cell: When kept under OCP (*i.e.*, no current is applied) the generated internal photocurrent charges the photoactive material and the HSM. No external wiring is required for this charging process. Subsequently, the charge can be accessed by applying a suitable discharge current. We also demonstrate purely electric charging *via* a charging current as a second path of accumulating charge on the device and also combine both modes, resulting in light-assisted electric (dis)charging that boosts the device performance further. *via* kinetic studies, the performance limitations and metrics of the device are discussed while showing how Ragone plots can

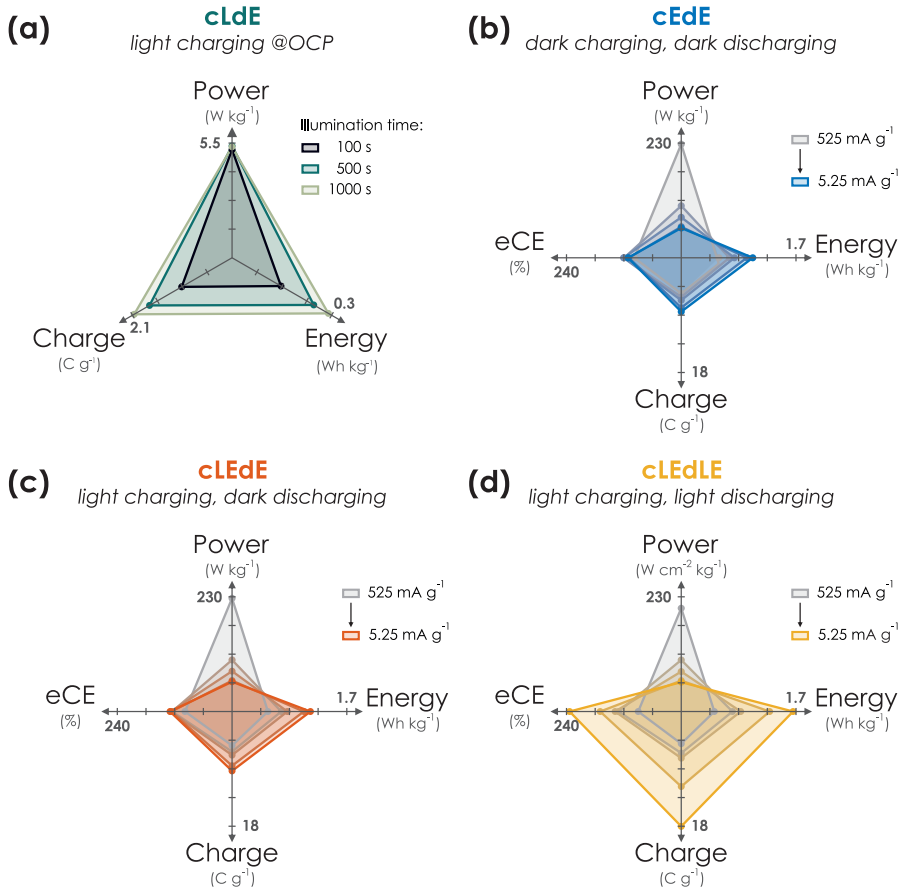

Figure 7.4. Performance summary of operation modes of the solar battery. (a) Pure photocharging at OCP and discharging in the dark (cLdE) at a constant current of $10.5\,\mathrm{mA\,g^{-1}}$. While power output remains approximately constant, charge and energy scales with illumination time. **(b)** GCD in the dark (cEdE) with different current densities (current decreases from grey to blue). With decreasing currents, power decreases and energy, charge as well as eCE slightly increases. **(c)** Same plot as in (b) for electric charging with different currents, but under illumination (1 Sun) during charging for additional photocharging (cLEdE). Discharging is performed with the same current in the dark. Power, energy, charge, and eCE scale with current akin to (b), but with slightly enhanced performance. **(d)** Same plot as in (b) and (c), but under illumination during both charging and discharging (cLEdLE). While power scales analogous to (b) and (c) with current, energy, charge and eCE is significantly enhanced thanks to the solar cell output during both charging and discharging, increasing the device performance significantly compared to when operated in the dark.

be used and behave for such devices. We summarize performance parameters for different modes and kinetics in Figure 7.4. A comparison to literature solar battery

devices is given in Table B.2, which suggests that our solar battery device favorably compares with other solar batteries utilizing bifunctional photoanodes.

An important message of this work is to provide a fundamental understanding of the solar battery operations as a convolution of different ingoing or outgoing energy fluxes, which impact the charging state. The charging contributions are as follows: (1) energy input *via* illumination depends on the generated internal photocurrent, which itself relies on the material's absorption profile, incident photon flux and illumination time (Figure 7.4 (a)). (2) Energy input *via* electric charging in the dark (Figure 7.4 (b)) emulates a classic battery (cEdE), *i.e.*, the capacity increases with lower charging and discharging currents due to smaller kinetic limitations. We show that a combination of light and electric charging during either charging (cLEdE) or both charging and discharging (cLEdLE) yields a performance enhancement in terms of apparent discharge energy, apparent capacity, and eCE. Thus, we provide an energy storage device, the apparent performance output of which can be tuned *via* illumination (see Ragone plot in Figure 7.3 (f)) and relies on a double functionality of light absorption and electron storage in a single material. The device design based on a ladder-type internal hole transfer cascade, which so far is the first of its kind for solar batteries, renders it a closer relative to solar cells than to classic batteries. It thus establishes a new generation of direct solar batteries derived from solar cells with bifunctional (both light absorbing and charge storing) components. Designing multifunctional polymeric separators in opens new avenues to solar battery devices that utilize both photogenerated electrons to improve the overall charging efficiency and photogenerated holes to efficiently shuttle them to the HSM. Our approach presents a cost and material efficient alternative route to circumvent oxidative reactions with the electrolyte, which has been identified as a key challenge for solar batteries.[3] In addition, the presented design based entirely on earth-abundant electrode materials makes production and application facile (*i.e.*, no external circuit is required for the charging process, simultaneous light charging and electric discharging is possible) and underscores the application potential of this new concept of truly integrated solar batteries based on bifunctional materials, especially where low cost and high levels of integration are key (for example in autonomous microsystems, self-powered sensors, or solar battery parks).

7.4. Experimental

Synthesis of K-PHI & anode preparation. K-PHI was synthesized as described in literature *via* a salt-melt of potassium thiocyanate (KSCN) and melon.[33,44,45] Precursors KSCN and melamine were acquired from Sigma Aldrich in reagent grade purity. Exfoliation was performed *via* sonication in an ice bath for 2 h in a 2-propanol (IPA) suspension (Sigma Aldrich) with a concentration of 3 mg mL^{-1}. Nanosheets were separated *via* two consecutive centrifugation steps (353 RCF for 20 min, then 795 RCF for 40 min; 3-30k, Sigma), akin to reported procedures.[17,29] Density was evaluated by drying 1 mL of suspension and subsequently weighing the residue. Particle concentration was increased to 0.3 mg mL^{-1} by evaporating the respective amount of IPA *via* a rotary evaporator. Films were deposited onto the transparent conductive substrate indium tin oxide (ITO; Ossila Ltd.) *via* dip coating (ca. 400 dips, 100 mm/min extraction speed, 2 min drying between dips; Rotary dip coater, Nadetech), yielding films of approx. 500 to 1000 nm.

Subsequently, for depositing the HTM a solution of F8BT (Ossila Ltd.) in chloroform with a concentration of 10 mg mL^{-1} was spin coated (2000 rpm for 30 s; WS-650MZ-23NPP, Laurell) onto the K-PHI film and annealed for 10 min on a hot plate at 80 °C. This process was repeated to increase the HTM film thickness. The sample was contacted by scratching off a small part of both films at a corner of the sample to uncover the substrate and by gluing a wire to it with conductive silver paste (Silver Conductive RS 186-3600, RS-Pro). The contact was then sealed with epoxy glue (DP410, 3M Scotch-Weld) to provide both a rigid connection and prevent the silver paste as well as ITO to participate in the measurements.

Cathode preparation. For the cathode, an aqueous suspension of PEDOT:PSS with a concentration of 3 to 4 wt% (Sigma Aldrich) was spin coated (2000 rpm, 30 s; WS-650MZ-23NPP, Laurell) onto an ITO substrate (Ossila Ltd) with dimensions of 10 × 12 mm, which underwent plasma cleaning with oxygen plasma (Femto, Diener) for 10 min prior to deposition to both clean the surface and make it more hydrophilic. Subsequently, the sample was annealed for 20 min at 145 °C in a nitrogen atmosphere. This process was repeated to increase PEDOT:PSS film thickness to approx. 600 nm. The samples was then contacted analogous to the anode as described in the previous section.

Fabrication of the solar battery full-cell. First, adsorbed oxygen was removed from both anode and cathode half-cell samples by applying vacuum and subsequent argon for 6 cycles using Schlenk techniques. Both samples were then sandwiched onto each other (with a contact area of $1\ \mathrm{cm}^2$), a weight of approx. 15 g was put on top to provide enough pressure, and epoxy (DP410, 3M Scotch-Weld) was applied on the two opposite edges to generate a sturdy connection, while leaving the two other faces open to enable contact with the surrounding electrolyte. Subsequently, after drying of the epoxy the sample was immersed into a degassed aqueous 0.1 M KCl solution. The mass of the device was calculated by weighting the K-PHI/HTM sample after film deposition on the substrate and calculating the mass of the PEDOT:PSS sample from measured film thickness and density of dried films reported by the manufacturer.

(Photo) electrochemical measurements. All electrochemical measurements were performed in a photo(electrochemical) reactor equipped with a quartz glass for illumination of the respective sample, and with a multichannel potentiostat (Autolab M204, Metrohm). An aqueous solution containing 0.1 M potassium chloride (KCl; Sigma Aldrich) was used as background electrolyte (for experiments requiring a sacrificial electron donor, the respective donor was added as well), which was degassed with argon ($>99\,\%$) prior to every measurement to ensure oxygen free conditions. For three-electrode-measurements, we have utilized an Ag/AgCl reference electrode with a saturated KCl electrolyte (RE-1CP, ALS Japan) and a gold foil (Sigma Aldrich) counter electrode. For two-electrode-measurements, the sample was directly connected to the potentiostat. Illumination was provided either with a calibrated solar simulator (LightLine A4, Sciencetech), providing artificial sunlight according to AM 1.5G with class AAA quality, or with a LED at 365 nm equipped with a collimator (M365LP1-C4, ThorLabs) and set to a power output of $100\ \mathrm{mW\ cm}^{-2}$.

Acknowledgements

The authors acknowledge N. Vargas-Barbosa and L. Yao for fruitful discussions. Financial support is gratefully acknowledged by the Max Planck Society, the European Research Council (ERC) under the European Union's Horizon 2020 Research and Innovation Program (grant agreement no. 639233, COFLeaf), the Deutsche Forschungsgemeinschaft (DFG) *via* the Cluster of Excellence "e-conversion" (project number EXC 2089/1-390776260) and by the Center for NanoScience (CENS). A. J.

S. gratefully acknowledges a postdoctoral scholarship from the Max Planck Society and the Spanish Ministry of Universities for funding through a Beatriz Galindo Research fellowship (BG20/00015). Open Access funding provided by the Max Planck Society.

Conflict of interests

The authors declare no conflict of interest.

7.5. References

(1) Brunner, C.; Deac, G.; Braun, S.; Zöphel, C. *Renew. Energy* **2020**, *149*, 1314–1324.

(2) Astakhov, O.; Merdzhanova, T.; Kin, L.-C.; Rau, U. *Sol. Energy* **2020**, *206*, 732–740.

(3) Lv, J.; Xie, J.; Mohamed, A. G. A.; Zhang, X.; Wang, Y. *Chem. Soc. Rev.* **2022**, *51*, 1511–1528.

(4) Zeng, Q.; Lai, Y.; Jiang, L.; Liu, F.; Hao, X.; Wang, L.; Green, M. A. *Adv. Energy Mater.* **2020**, *10*, 1903930.

(5) Gurung, A.; Chen, K.; Khan, R.; Abdulkarim, S. S.; Varnekar, G.; Pathak, R.; Naderi, R.; Qiao, Q. *Adv. Energy Mater.* **2017**, *7*, 1602105.

(6) Xu, J.; Chen, Y.; Dai, L. *Nat. Commun.* **2015**, *6*, 8103.

(7) Gurung, A.; Qiao, Q. *Joule* **2018**, *2*, 1217–1230.

(8) Yu, M.; Ren, X.; Ma, L.; Wu, Y. *Nat. Commun.* **2014**, *5*, 5111.

(9) HODES, G.; MANASSEN, J.; CAHEN, D. *Nature* **1976**, *261*, 403–404.

(10) Li, Q.; Li, N.; Ishida, M.; Zhou, H. *J. Mater. Chem. A* **2015**, *3*, 20903–20907.

(11) Li, W.; Jin, S. *Acc. Chem. Res.* **2020**, *53*, 2611–2621.

(12) Li, W.; Zheng, J.; Hu, B.; Fu, H.-C.; Hu, M.; Veyssal, A.; Zhao, Y.; He, J.-H.; Liu, T. L.; Ho-Baillie, A.; Jin, S. *Nat. Mater.* **2020**, *19*, 1326–1331.

(13) Li, W.; Fu, H.-C.; Zhao, Y.; He, J.-H.; Jin, S. *Chem* **2018**, *4*, 2644–2657.

(14) Um, H.-D.; Choi, K.-H.; Hwang, I.; Kim, S.-H.; Seo, K.; Lee, S.-Y. *Energy Environ. Sci.* **2017**, *10*, 931–940.

(15) Paolella, A. et al. *Nat. Commun.* **2017**, *8*, 14643.

(16) Tewari, N.; Shivarudraiah, S. B.; Halpert, J. E. *Nano Lett.* **2021**, *21*, 5578–5585.

(17) Podjaski, F.; Kröger, J.; Lotsch, B. V. *Adv. Mater.* **2018**, *30*, 1705477.

(18) Boruah, B. D.; Wen, B.; De Volder, M. *Nano Lett.* **2021**, *21*, 3527–3532.

(19) Boruah, B. D.; Mathieson, A.; Wen, B.; Feldmann, S.; Dose, W. M.; De Volder, M. *Energy Environ. Sci.* **2020**, *13*, 2414–2421.

(20) Lou, S. N.; Sharma, N.; Goonetilleke, D.; Saputera, W. H.; Leoni, T. M.; Brockbank, P.; Lim, S.; Wang, D.-W.; Scott, J.; Amal, R.; Ng, Y. H. *Adv. Energy Mater.* **2017**, *7*, 1700545.

(21) Andriamiadamanana, C.; Sagaidak, I.; Bouteau, G.; Davoisne, C.; Laberty-Robert, C.; Sauvage, F. *Adv. Sustainable Syst.* **2018**, *2*, 1700166.

(22) Ahmad, S.; George, C.; Beesley, D. J.; Baumberg, J. J.; De Volder, M. *Nano Lett.* **2018**, *18*, 1856–1862.

(23) Lv, J.; Tan, Y.-X.; Xie, J.; Yang, R.; Yu, M.; Sun, S.; Li, M.-D.; Yuan, D.; Wang, Y. *Angew. Chem. Int. Ed.* **2018**, *57*, 12716–12720.

(24) Kato, K.; Puthirath, A. B.; Mojibpour, A.; Miroshnikov, M.; Satapathy, S.; Thangavel, N. K.; Mahankali, K.; Dong, L.; Arava, L. M. R.; John, G.; Bharadwaj, P.; Babu, G.; Ajayan, P. M. *Nano Lett.* **2021**, *21*, 907–913.

(25) Zhang, X.; Su, K.; Mohamed, A. G. A.; Liu, C.; Sun, Q.; Yuan, D.; Wang, Y.; Xue, W.; Wang, Y. *Energy Environ. Sci.* **2022**, *15*, 780–785.

(26) Zhang, X.; Huang, X.; Li, C.; Jiang, H. *Adv. Mater.* **2013**, *25*, 4093–4096.

(27) Xu, J.; Ku, Z.; Zhang, Y.; Chao, D.; Fan, H. J. *Adv. Mater. Technol.* **2016**, *1*, 1600074.

(28) Kasap, H.; Caputo, C. A.; Martindale, B. C. M.; Godin, R.; Lau, V. W.-h.; Lotsch, B. V.; Durrant, J. R.; Reisner, E. *J. Am. Chem. Soc.* **2016**, *138*, 9183–9192.

(29) Gouder, A.; Jiménez-Solano, A.; Vargas-Barbosa, N. M.; Podjaski, F.; Lotsch, B. V. *Mater. Horiz.* **2022**, *9*, 1866–1877.

(30) Kröger, J.; Jiménez-Solano, A.; Savasci, G.; Rovó, P.; Moudrakovski, I.; Küster, K.; Schlomberg, H.; Vignolo-González, H. A.; Duppel, V.; Grunenberg, L.; Dayan, C. B.; Sitti, M.; Podjaski, F.; Ochsenfeld, C.; Lotsch, B. V. *Adv. Energy Mater.* **2021**, *11*, 2003016.

(31) Markushyna, Y.; Lamagni, P.; Teutloff, C.; Catalano, J.; Lock, N.; Zhang, G.; Antonietti, M.; Savateev, A. *J. Mater. Chem. A* **2019**, *7*, 24771–24775.

(32) Podjaski, F.; Lotsch, B. V. *Adv. Energy Mater.* **2021**, *11*, 2003049.

(33) Lau, V. W.-h.; Klose, D.; Kasap, H.; Podjaski, F.; Pignié, M.-C.; Reisner, E.; Jeschke, G.; Lotsch, B. V. *Angew. Chem. Int. Ed.* **2017**, *56*, 510–514.

(34) Banerjee, T.; Podjaski, F.; Kröger, J.; Biswal, B. P.; Lotsch, B. V. *Nat. Rev. Mater.* **2020**, *6*, 168–190.

(35) Kröger, J.; Jiménez-Solano, A.; Savasci, G.; Lau, V. W. h.; Duppel, V.; Moudrakovski, I.; Küster, K.; Scholz, T.; Gouder, A.; Schreiber, M.-L.; Podjaski, F.; Ochsenfeld, C.; Lotsch, B. V. *Adv. Funct. Mater.* **2021**, *31*, 2102468.

(36) Wang, X.; Maeda, K.; Thomas, A.; Takanabe, K.; Xin, G.; Carlsson, J. M.; Domen, K.; Antonietti, M. *Nat. Mater.* **2009**, *8*, 76–80.

(37) Mazzanti, S.; Savateev, A. *ChemPlusChem* **2020**, *85*, 2499–2517.

(38) Sridhar, V.; Podjaski, F.; Kröger, J.; Jiménez-Solano, A.; Park, B.-W.; Lotsch, B. V.; Sitti, M. *Proc. National Acad. Sci.* **2020**, *117*, 24748–24756.

(39) Sridhar, V.; Podjaski, F.; Alapan, Y.; Kröger, J.; Grunenberg, L.; Kishore, V.; Lotsch, B. V.; Sitti, M. *Sci. Robot.* **2022**, *7*, 62.

(40) Savateev, A.; Markushyna, Y.; Schüßlbauer, C. M.; Ullrich, T.; Guldi, D. M.; Antonietti, M. *Angew. Chem. Int. Ed.* **2021**, *60*, 7436–7443.

(41) Adekoya, G. J.; Sadiku, R. E.; Hamam, Y.; Ray, S. S.; Mwakikunga, B. W.; Folorunso, O.; Adekoya, O. C.; Lolu, O. J.; Biotidara, O. F. In *Fracture and Damage Mechanics: Theory, Simulation and Experiment*, Mallorca, Spain, AIP Publishing: 2020.

(42) Shahrim, N. A.; Ahmad, Z.; Wong Azman, A.; Fachmi Buys, Y.; Sarifuddin, N. *Mater. Adv.* **2021**, *2*, 7118–7138.

(43) Kröger, J.; Podjaski, F.; Savasci, G.; Moudrakovski, I.; Jiménez-Solano, A.; Terban, M. W.; Bette, S.; Duppel, V.; Joos, M.; Senocrate, A.; Dinnebier, R.; Ochsenfeld, C.; Lotsch, B. V. *Adv. Mater.* **2022**, *34*, 2107061.

(44) Lau, V. W.-h.; Moudrakovski, I.; Botari, T.; Weinberger, S.; Mesch, M. B.; Duppel, V.; Senker, J.; Blum, V.; Lotsch, B. V. *Nat. Commun.* **2016**, *7*, 12165.

(45) Schlomberg, H.; Kröger, J.; Savasci, G.; Terban, M. W.; Bette, S.; Moudrakovski, I.; Duppel, V.; Podjaski, F.; Siegel, R.; Senker, J.; Dinnebier, R. E.; Ochsenfeld, C.; Lotsch, B. V. *Chem. Mater.* **2019**, *31*, 7478–7486.

(46) Sellam, N.; Hashmi, S. A. *ACS Appl. Mater. Interfaces* **2013**, *5*, 3875–3883.

(47) Fleischmann, S.; Mitchell, J. B.; Wang, R.; Zhan, C.; Jiang, D.-e.; Presser, V.; Augustyn, V. *Chem. Rev.* **2020**, *120*, 6738–6782.

(48) Jao, M.-H.; Liao, H.-C.; Su, W.-F. *J. Mater. Chem. A* **2016**, *4*, 5784–5801.

(49) Yang, X.; Zhao, L.; Wang, S.; Li, J.; Chi, B. *J. Materiomics* **2021**, *7*, 728–741.

(50) Tumbleston, J. R.; Ko, D.-H.; Samulski, E. T.; Lopez, R. *J. Appl. Phys.* **2010**, *108*, 084514.

(51) Yang, W.; Godin, R.; Kasap, H.; Moss, B.; Dong, Y.; Hillman, S. A. J.; Steier, L.; Reisner, E.; Durrant, J. R. *J. Am. Chem. Soc.* **2019**, *141*, 11219–11229.

(52) Savateev, O. *Adv. Energy Mater.* **2022**, *12*, 2200352.

8

PHOTOMEMRISTIVE SENSING *VIA* CHARGE STORAGE IN 2D CARBON NITRIDES

Andreas Gouder, Alberto Jiménez-Solano, Nella M. Vargas-Barbosa, Filip Podjaski, and Bettina V. Lotsch

This article was published on April 26th 2022 in:

Materials Horizons **2022**, 9, 1866-1877.
doi: 10.1039/D2MH00069E

Keywords: carbon nitride, poly(heptazine imide), sensor, memristor, solar battery

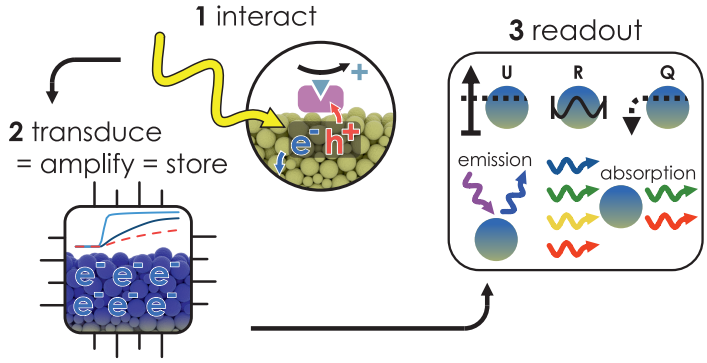

We present a photomemristive sensing concept based on light-induced charge storage in the 2D carbon nitride K-PHI. Our design enables memory sensing with tunable dynamic concentration ranges, combined with diverse operation and readout modes.

Front cover art of *Materials Horizons* **2022**, *9*, 1786.

Designed by Vera Hiendl.

Volume 9
Number 7
July 2022
Pages 1777–2010

Materials Horizons

rsc.li/materials-horizons

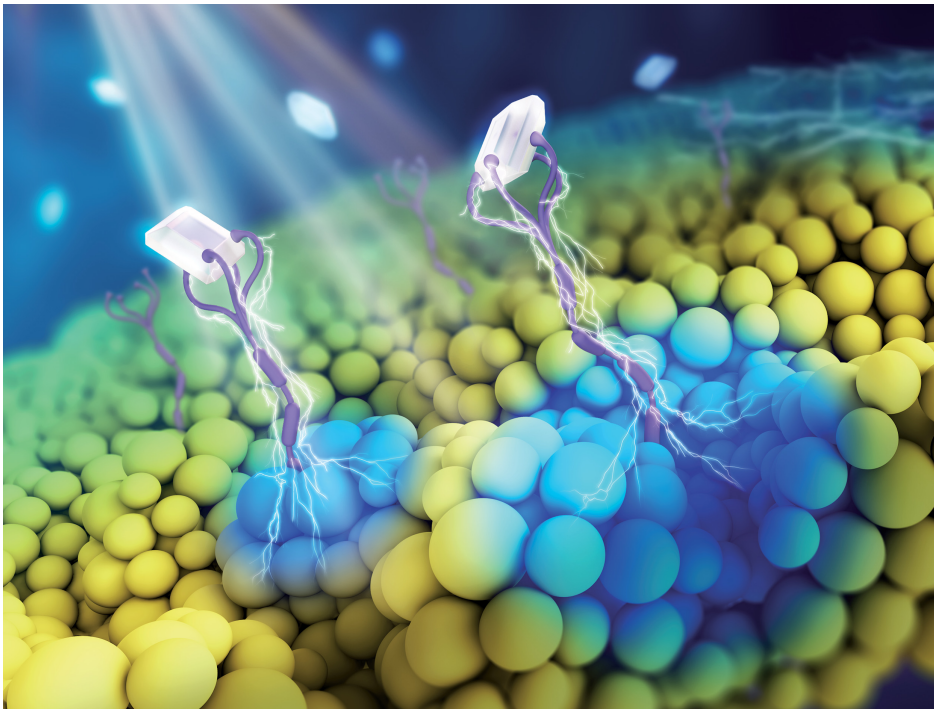

ISSN 2051-6347

ROYAL SOCIETY OF CHEMISTRY

COMMUNICATION
Filip Podjaski, Bettina V. Lotsch *et al.*
Photomemristive sensing *via* charge storage in 2D carbon nitrides

Author contributions

Andreas Gouder, Alberto Jiménez-Solano, Filip Podjaski and Bettina V. Lotsch conceived the project. Andreas Gouder performed the electrochemical measurements. Andreas Gouder and Alberto Jiménez-Solano performed the optical measurements. Andreas Gouder and Alberto Jiménez-Solano, with assistance of Filip Podjaski, analysed the data. Andreas Gouder, Alberto Jiménez-Solano and Filip Podjaski wrote the manuscript with assistance of all authors.

Contents

8.1. Introduction **222**
8.2. Results and discussion **224**
8.2.1. PEC sensing interaction on K-PHI 224
8.2.2. Photomemristive sensing with K-PHI films 225
8.2.2.1. Potentiometric readout. 227
8.2.2.2. Impedimetric readout. 229
8.2.2.3. Coulometric readout. 231
8.2.3. Photomemristive sensing with K-PHI wireless particles 232
8.2.3.1. Colorimetric readout. 233
8.2.3.2. Fluorometric readout. 234
8.3. Conclusion **236**
8.4. Experimental **237**
8.5. References **240**

Abstract

Photomemristive sensors have the potential to innovate current photo electrochemical sensors by incorporating new sensing capabilities including non-invasive, wireless and time-delayed (memory) readout. Here we report the charge storing 2D carbon nitride potassium poly(heptazine imide), K-PHI, as a direct photomemristive sensing platform by capitalizing on K-PHI's visible light bandgap, large oxidation potential, and intrinsic optoionic charge storage properties. Utilizing the

light-induced charge storage function of K-PHI nanosheets, we demonstrate memory sensing *via* charge accumulation and present potentiometric, impedimetric and coulometric readouts to write/erase this information from the material, with no additional reagents required. Additionally, wireless colorimetric and fluorometric detection of the charging state of K-PHI nanoparticles is demonstrated, enabling the material's use as particle-based autonomous sensing probe *in situ*. The various readout options of K-PHI's response enable us to adapt the sensitivities and dynamic ranges without modifying the sensing platform, which is demonstrated using glucose as a model analyte over a wide range of concentrations (50 µM to 50 mM). Since K-PHI is earth abundant, biocompatible, chemically robust and responsive to visible light, we anticipate that the photomemristive sensing platform presented herein opens up memristive and neuromorphic functions.

New concepts

We demonstrate a multimodal photomemristive sensing concept that bridges the field of Photo-Electrochemical (PEC) sensing and memristive organic electronics. The carbon nitride poly(heptazine imide) (K-PHI) is capable of "traditional" PEC sensing of a wide range of organic analytes and at the same time shows a characteristic bifunctionality of light absorption coupled to photocatalytic reactivity, and charge storage. Using these unique "optoionic" properties, the sensing information (*i.e.*, the stored charge) can be written onto the sensor and read out based on a number of physical quantities such as photovoltage or color change. This concept allows us to access new functionalities for sensors: memory of the analyte concentration information, tunable sensitivities and dynamic sensing ranges, as well as a diverse array of readout methods. Due to the facile sensor geometry – either as films or wireless particles – we circumvent conceptual and technical challenges of existing PEC- or memristive sensing concepts. This work underlines how functionalities from different fields (batteries, photocatalysts, memristors, sensors) can be merged to produce information storing devices with novel functionalities. While this concept accelerates the rapidly emerging research field of memristive sensors into a new direction, it also presents a toolkit to facilitate automated electronic signal processing.

8.1. Introduction

The trend towards digitization and automation necessitates novel sensing and information storage concepts. Sensors are of critical importance for medical applications, in smart healthcare systems and environmental monitoring.[1–3] Emerging neuromorphic sensing and monitoring concepts utilize memristive effects to enable exciting features such as memory sensing and low power data processing.[4–7]

The traditional path to application of memristive devices are non-volatile memory applications with many distinctly addressable states.[4] Artificial synapses are a class of bio-memristive devices which are cheap, offer biocompatibility and are investigated to develop synaptic electronics such as neural networks for neuromorphic computing.[4,8–11] However, memristors have further potential. Coupling photovoltaics with memristors or transistors can drastically reduce computational energy consumption with photonic- or photomemristive devices, which have been dubbed as "solar brains".[12] The memristive sensing approach presented in this work relies on such a photomemristive behavior. Most current memristive sensors are comprised of classical inorganic, memristive materials (*e.g.*, Si-nanowires) which are functionalized with a receptor and produce a voltage gap in their memristive behavior that can be linked to the analyte concentration.[6] However, those two-terminal memristor devices suffer from complex device geometries, as they do not have a straightforward pathway for biomolecules to approach the device.[13] To address this challenge, complex surface patterning[14] or nanowire[15] designs are necessary. While most memristive sensors so far have focused on the detection of complex biomolecules such as DNA aptamers,[16] cancer markers[17] or the ebola and dengue virus[18,19] sensing of easier biomolecules such as glucose was demonstrated but with a lack in both sensitivity (10 to 40 mM) and selectivity.[20]

Organic memristive devices have been designed with several different voltage thresholds or volatile switching mechanisms.[4,5,21–23] The common denominator is the writing and reading of different conductance states, which can be utilized for information storage. Redox-based switching uses electrochemical redox reactions of polymers (*e.g.*, PEDOT:PSS)[4,23] accompanied by ion diffusion, which modifies the conductance of the material.

Carbon nitrides are an interesting class of organic materials with potential applications in biosensing and memristive devices. They are layered molecular materials with one- (1D) or two-dimensional (2D) triazine- or heptazine backbones

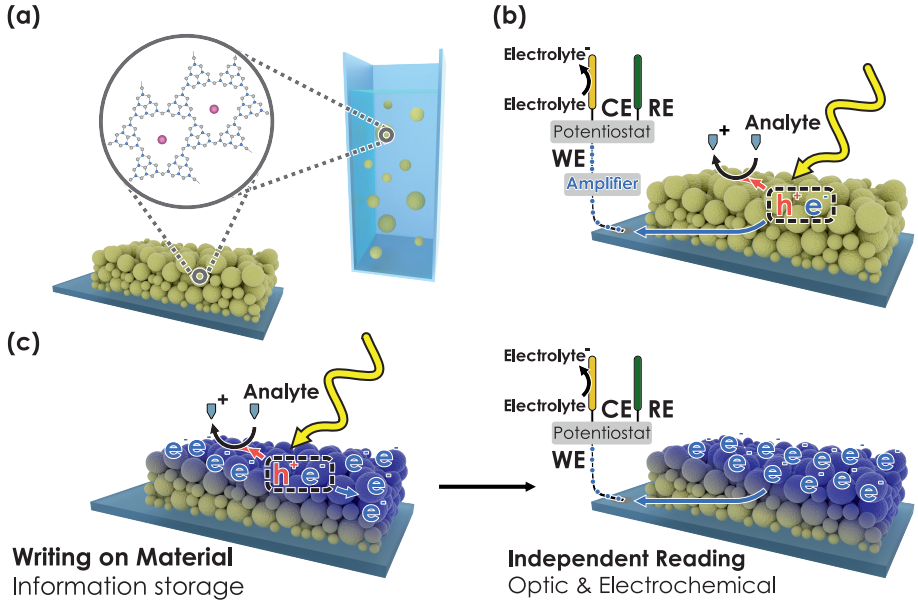

Figure 8.1. Concept of an oxidative (memristive) photo-electrochemical sensor. (a) The carbon nitride K-PHI can be deployed as nanosheets in a thin film on a conductive substrate or as nanoparticles in an aqueous suspension for wireless sensing. **(b)** Components of carbon nitride-based direct PEC sensors. Electron-hole pairs are generated upon illumination. The holes are extracted *via* oxidation of the analyte (*i.e.*, K-PHI acts as a receptor). The electrons generate a signal proportional to the analyte concentration (*i.e.*, K-PHI acts as a transducer). **(c)** In a photomemristive sensor, instead of generating a photocurrent directly, the electrons charge the sensor (writing) and thus, change the sensor's material properties as a function of the analyte concentration. This change is integrative due to accumulation of charge and modifies the material properties non-linearly (*i.e.*, K-PHI acts as memristive amplifier). Subsequently, the material properties can be accessed *via* electrochemical or optical techniques (readout).

and a visible-light bandgap. Carbon nitrides have lately attracted interest in various research areas including photocatalysis,[24–27] electrochemical and solar energy storage,[24,28,29] molecular machines,[30] environmental remediation,[31] and non-enzymatic or "nanozyme" sensing of *e.g.*, glucose.[3,32–35] Carbon nitride based sensors typically require heterostructures, mediators and/or redox indicator molecules. Potassium polyheptazine imide (K-PHI), a recently discovered 2D carbon nitride,[26,36,37] has remarkable optoelectronic and optoionic properties[38] that are derived from its dual functionality of both light harvesting and charge storage.[24,28,39,40] This versatile toolkit has led to the design of novel responsive and/or charge storing concepts, such as "dark photocatalysis"[24] and a solar battery anode.[28] K-PHI's large bandgap of $\sim$ 2.7 eV (see Figure C.1) corresponding to an absorption edge in the blue region

of the visible spectrum, together with the material's suitably positioned band edges ($+2.2$ and -0.5 V *vs.* NHE, for the valence band maximum and conduction band minimum, respectively), provides enough thermodynamic driving force for the oxidation and reduction of various chemical species,[41] while being chemically robust.

Herein, we exploit the abovementioned property modifications of K-PHI upon photocharging (Figure 8.1 (a)) and propose a refined photomemristive sensor beyond the commonly used two-terminal design. We show that K-PHI simultaneously acts as a receptor unit for glucose as a model analyte and a transducer, which is coupled to a memristive amplifier, thereby combining all sensing components in the same material. This compact design is complemented by various readout methods, which are based on different physical quantities that encode K-PHI's charging state. Our concept of sensing *via* charge storage comes with a novel set of combined features, such as an intrinsic memory function with writing and erasing procedures, tunable dynamic concentration ranges and adaptive sensitivities – properties which we explore, demonstrate and explain below. The manuscript is structured as follows: we first briefly show the direct PEC sensing ability of K-PHI (Figure 8.1 (b)) with different analytes to explain the interaction of the sensor with the analyte. This allows us to demonstrate in the following the K-PHI memsensing concept (Figure 8.1 (c)) *via* potentiometric, impedimetric and coulometric techniques that focus on the modified electronic material properties. Finally, we present a wireless, memristive sensing mode using optical readouts (colorimetric and fluorometric). Thus, we connect the field of memristive information storage to the well-established electrochemical sensor design by moving away from the more complex "classical" memristor design to a direct PEC sensor with built-in memristive functionalities. This is only possible due to the combination of a special set of photo-electrochemical properties of the carbon nitride K-PHI, namely light absorption, charge storage and a large oxidative driving force.

8.2. Results and discussion

8.2.1. PEC sensing interaction on K-PHI

The concept of PEC biosensors is briefly summarized above in Figure 8.1 (b).[42] To describe the direct memristive sensing mode discussed here, we start by summarizing the capability of K-PHI nanosheet films (see Figure 8.1 (a), Figure C.2, and Figure C.3 for details) to perform direct PEC amperometric sensing, *i.e.*, to si-

multaneously act as receptor and transducer while being illuminated in aqueous conditions (Figure 8.1 (b)). We use glucose as model analyte (see Section C.2), relating the analyte concentration to the photocurrent. Three linear concentration ranges are observed ($0-1$ mM, $1-10$ mM, and $10-50$ mM) and a limit of detection (LOD) of 11.4 µM (0.21 mg dL^{-1}) can be determined from the lower concentration range.[43] These observations are comparable to reported linear ranges and LOD's for metal-free amperometric carbon nitride glucose sensors (LOD of 11 µM and a linear range from 1 to 12 mM),[34] which additionally require the mediator H_2O_2 in convolution with the enzyme glucose oxidase (GOx) as the receptor. To confirm the broad applicability and generality of K-PHI as a PEC sensor, we have also tested other sugars, alcohols, the physiologically relevant molecules uric acid and ascorbic acid, as well as typical electron donor molecules, which are widely used as sacrificial agents in photocatalytic applications (Figure C.4 (d)). All these analytes show a strong photocurrent response and hence, can be detected with K-PHI sensors. At a concentration of 5 mmol, sugars produce photocurrents between ~ 0.6 and 1 µA cm^{-2} and the typical SED TEoA and 4-MBA show photocurrents of 7.5 and 23 µA cm^{-2}, respectively. The physiologically relevant molecules Ascorbic Acid (AA) and Uric Acid (UA) produce a photocurrent response of ~ 0.38 and 0.35 µA cm^{-2}, respectively, at a concentration of 0.1 mM, suggesting a viable monitoring strategy for these analytes as well. However, the strong oxidative driving force, which enables considerable photocurrents with many different species, makes it difficult to differentiate between organic substances in mixtures. Functionalization protocols for carbon nitrides developed by us[44] and others[45] are expected to further enhance the selectivity of K-PHI towards these analytes.

8.2.2. Photomemristive sensing with K-PHI films

Next, we demonstrate the photomemristive operation of the K-PHI sensor (Figure 8.1 (c)) based on the PEC sensing interaction outlined above. The necessary double functionality of charge storage and light absorption is illustrated in Figure 8.2 (a). Electric charging *via* cyclic voltammetry (CV) measurement shows the charging and subsequent discharging of the material occurring dominantly at potentials negative of -0.7 V *vs.* Ag/AgCl. Upon illumination with 1 Sun (AM1.5 G) at OCP and in the presence of an oxidizable analyte, a photopotential immediately develops due to electron accumulation in this potential range, which remains stable for ~ 1 h after 20 min of illumination (Figure 8.2 (a) right). The photopotential decay rate is very

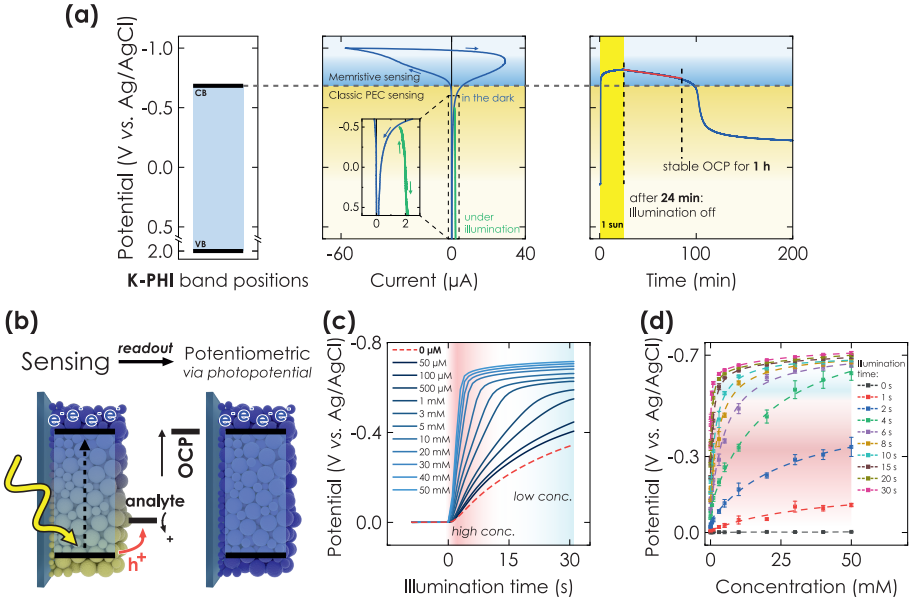

Figure 8.2. PEC properties of K-PHI and potentiometric memristive sensing *via* K-PHI films. (a) *Left:* VB and conduction band (CB) positions referenced to the Ag/AgCl reference electrode potential. *Middle:* Cyclic voltammetry (CV) measurement at $50\,\mathrm{mV\,s^{-1}}$, showing the behavior of K-PHI in the relevant potential window for sensing. At potentials more positive than $-0.7\,\mathrm{V}$ *vs.* Ag/AgCl, a constant photocurrent is observed (green), which is used for direct PEC sensing. Charge storage occurs at potentials more negative than $-0.7\,\mathrm{V}$ *vs.* Ag/AgCl. *Right:* evolution of K-PHI in the presence of glucose during illumination (photocharging) and its subsequent stability in the dark. **(b)** Scheme depicting memristive sensing and subsequent potentiometric readout *via* evaluation of the . **(c)** Increase of the during charging under illumination and in the presence of different glucose concentrations. With increasing concentrations, the shift becomes more pronounced due to faster charging. **(d)** Correlation of the photopotential to the concentration of glucose. This concentration can be extracted at different illumination times independently, which allows to tune the sensitivity range. Dashed lines are non-linear fits of the sensor response over the entire dynamic. Fitting is discussed in Section C.5.1.

8

slow ($1.21\,\mathrm{mV/min}$) and can be attributed to self-discharge *via* miniscule amounts of oxygen leaking into the reactor and being reduced by K-PHI (*e.g.*, ROS formation)[30,46] or the Fluorine doped Tin Oxide (FTO) substrate promoting water reduction, since charge storage on K-PHI occurs at potentials more negative than the hydrogen reduction potential (ca. $-0.61\,\mathrm{V}$ *vs.* Ag/AgCl at pH 7).[28] Different analyte concentrations produce a different shift in this (Figure 8.2 (c)). The inherent charge storage properties of K-PHI enable a quantitative comparison between the analyte concentration and the charging state of the material when the illumination time is fixed. The photomemristive behavior integrates the analyte oxidation current and

produces the stable change in the optoelectronic properties of K-PHI as the measurand. This accumulated charge is proportional to the charging current, which depends on both analyte concentration and illumination time. A longer illumination (or writing cycle) can improve the sensitivity for low analyte concentrations, as the system has more time to interact with the analyte and accumulate charges. In principle, there is no lower analyte detection limit in the absence of self-discharge (and other experimental limitations such as parasitic oxidation reactions due to a lack of selectivity), as the illumination time can be increased at will. On the other hand, a short light pulse allows for fast sensing of high analyte concentrations. Thus, K-PHI can act as receptor and transducer (as discussed in the previous paragraph) but also as a memristive amplifier due to its current integration mechanism, hence combining all sensor components on a single material. While related, it is important to contrast this sensing concept with persistent photoconductivity effects that have been reported in semiconductors like ZnO when exposed to gas molecules such as oxygen as the analyte.[47,48] Whereas hole-induced desorption of chemisorbed oxygen leads to the accumulation of photogenerated electrons in the conduction band and their subsequent re-trapping by surface-adsorbed oxygen, electron trapping in K-PHI is mediated by the photointercalation of electrolyte ions into the bulk of the material, and is hence akin to memristors.[38] The sole purpose of the analyte here is to act as a sacrificial electron donor (SED). In the following, three electrochemical readout methods of the sensor state are demonstrated and explained.

8.2.2.1. Potentiometric readout. Potentiometric sensing at open circuit condition (OCP) evaluates the photopotential that a given K-PHI nanosheet thin film reaches after illumination with a fixed duration and intensity (1 sun), in the presence of a specified analyte concentration (Figure 8.2 (b)). After activation of the sample (Section C.3), upon illumination and in presence of the glucose in different concentrations, the OCP shifts negatively over time (Figure 8.2 (c)), which shows that the sensor is being charged. With increasing analyte concentration, the OCP response becomes more pronounced (shifts faster and to more negative potentials). In all cases, we observe a nearly linear regime until approximately -0.7 V *vs.* Ag/AgCl, followed by a second and significantly slower saturation regime. The gradient of the OCP shift depends on the differential charge density or capacity of K-PHI (see CV in Figure 8.2 (a)), which is comparably small before reaching -0.7 V *vs.* Ag/AgCl and primarily due to surface capacitance,[28] followed by a faradaic response with a higher differential capacitance. The different charging kinetics can be exploited

by using different illumination times to sense different effective analyte concentration ranges, thereby adapting the material's response window and hence, relative sensitivity. This becomes more evident when looking at the OCP evolution with increasing illumination times (Figure 8.2 (d)): at short illumination times of $1-4$ s (red shading in Figure 8.2 (c and d)), higher glucose concentrations ($10-50$ mM) yield the most significant change in potential. Higher analyte concentrations can

Table 8.1. Summary of readout methods. A summary of recommended operation modes as well as key advantages that our memristive sensing concept provides in comparison to PEC amperometric sensing. Note that all memristive methods are tunable *via* illumination time (as demonstrated for potentiometric sensing) or illumination intensity. Furthermore, combining measurement methods allows to combine their advantages, minimize the errors and improve accuracy.

Method	Useful range (glucose sensitivity)	Illumination time	Readout time	Sensing characteristics
Amperometric	0.1 to 10 mM (11 µM)	Continuous	60 s	- Direct sensing
Potentiometric	0.05 to 50 mM (50 µM)	<1 mM: >10 s 1−10 mM: 4−10 s >10 mM: <4 s	Instant	- Non-invasive - Memory sensing
Impedimetric	0.05 to 20 mM (50 µM)	Only 200 s analyzed	<10−100 s	- Non-invasive - Memory sensing - No fitting required
Coulometric	5 to 50 mM (100 µM)	Only 200 s analyzed	<300 s	- Memory sensing - Sensor reset (invasive)
Colorimetric	0.2 to 50 mM (200 µM)	Only 200 s analyzed	<1 s	- Minimum-invasive - Memory sensing - Wireless sensing - Visible color change
Fluorometric	0.2 to 50 mM (200 µM)	Only 200 s analyzed	<1 s	- Minimum-invasive - Memory sensing - Wireless sensing

be measured more precisely as the OCP does not reach a value more negative than -0.7 V *vs.* Ag/AgCl, *i.e.*, no saturation occurs yet. When illuminating longer than 4 s (blue area in Figure 8.2 (c and d)), more charge accumulates over time at every concentration, which induces a stronger potential change. Hence, a steeper slope for small concentrations of $1-5$ mM can be seen in Figure 8.2 (d), which enables more accurate sensing of low analyte amounts due to the extended interaction and memristive integration times. The illumination time can be used as a parameter to adapt the sensitivity of this potentiometric sensor (see Table 8.1). In principle, similar adjustments are possible by changing the light intensity and hence, photon flux, which generates the photoresponse. To extract the sensing information, a relationship between the sensing signal (photopotential) and analyte concentration is required. We have performed both phenomenological non-linear fitting and linear fitting of the sensor's response. The non-linear fitting (see Section C.5.1) uses an equation that mimics the contributions of the charging mechanism including their saturation, without requiring dedicated input parameters for a given set of conditions. With this non-linear approach, extracting the response of all electrochemical and optical readout modes over the entire concentration range is easily possible, with a much better fitting quality compared to the linear fit. A detailed description of the fitting is given in Section C.5.1. The linear ranges are given in Table C.1 and the fit is shown in Figure C.9. The non-linear fit is shown in Figure 8.2 (d).

8.2.2.2. Impedimetric readout. Impedimetric sensing utilizes the Electrochemical Impedance Spectroscopy (EIS) to probe the change in impedance (resistance) of the charged state, which is equivalent to a direct readout of the memristive state. The measurements are performed after illumination with 1 Sun for 30 s at OCP by a 10 mV AC perturbation signal to extract the sensor's impedance. These measurements are non-invasive to the stored concentration information. When increasing the analyte concentration and hence, charge accumulation on K-PHI analogous to the potentiometric sensing discussed above (Figure 8.2 (c)), a decrease in magnitude of the impedance is measured and shown *via* a Bode plot in Figure 8.3 (a). We interpret this as the material becoming more conductive (less resistive) in response to charge accumulation of mobile charge carriers (photogenerated electrons and intercalated ions interacting with the backbone, equivalent to photodoping)[28,38,49] as a consequence of the interaction with the analyte. The resistance can be interpreted as direct measure of the memristance (RM) of the system as it directly and monotonously relates to the charged state. The systematic relationship between the

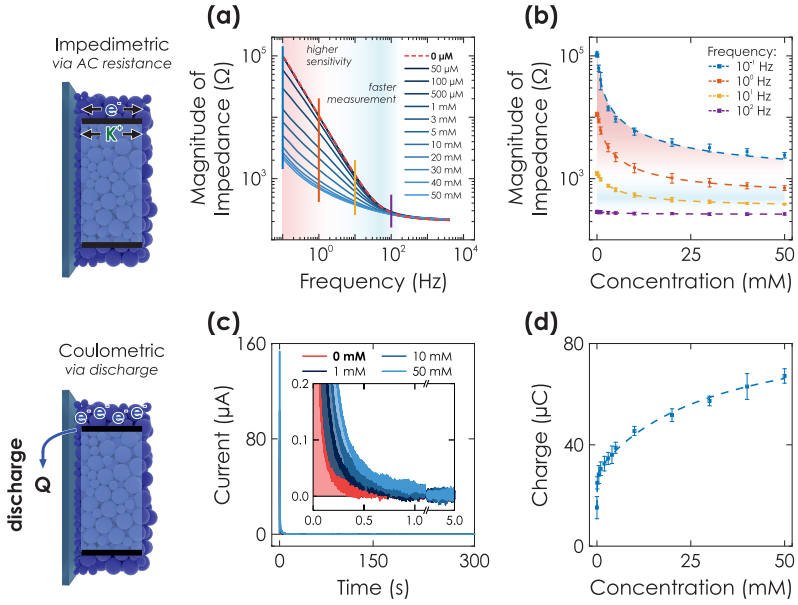

Figure 8.3. Further electrochemical readout methods *via* K-PHI thin films. (a) Impedimetric readout. Bode plot of the impedance response after illumination of the sensor for 60 s at OCP conditions and in presence of different glucose concentrations. **(b)** A change in magnitude of impedance can be correlated to the analyte concentration due to conductivity changes upon memristive charging. This effect has a varying signal amplitude at different time scales (*i.e.*, frequencies; shown with vertical lines in (a)) and concentrations. **(c)** Coulometric readout. Evolution of discharge current with time when applying a bias of $+0.2$ V *vs.* Ag/AgCl after illumination of the sensor for 60 s at OCP conditions and in presence of different glucose concentrations (inset shows a zoom of low currents). **(d)** The extracted charge Q correlates monotonously with the glucose concentration. Dashed lines in (b) and (d) are non-linear fits of the sensor response over the entire dynamic range. Fitting is discussed in Section C.5.2 and Section C.5.3.

magnitude of the impedance and analyte concentration at different frequencies is shown in Figure 8.3 (b). In the frequency region <100 Hz, a change in impedance is observed that contains the sensing information. At frequencies <1 Hz (red shading in Figure 8.3 (a and b)), the most pronounced shift with respect to the analyte concentration is observed, which causes a steeper slope for both small and large concentrations. We attribute this low frequency range to the comparably slow faradaic charge storage process being triggered. It is kinetically slower than the double layer capacitance and therefore more visible at lower frequencies. The advantage of measuring at moderately higher frequencies (1 to 100 Hz) is the shorter measurement time (blue shading in Figure 8.3 (a and b)). However, for large analyte concentrations the difference in magnitude of impedance for different concentra-

tions becomes less pronounced and is smaller than the measurement error, *i.e.*, it is not reliable. A realistic output can only be expected for <20 mM and frequencies of <10 Hz. Note that no impedance fitting is necessary as the concentration information can be extracted at a single frequency. Since the sensing interaction is analogous to potentiometric sensing discussed above, *i.e.*, charging under OCP conditions for a given time, sensitivity and dynamic concentration range can again be tuned by the illumination time and light intensity. Time delayed readout ("memory" sensing) is therefore possible as well.

We perform fitting of the relationship between impedance magnitude and analyte concentration with either a non-linear phenomenological fit over the entire dynamic range (Figure 8.3 (d) dashed lines and Figure C.10) or linear with two linear ranges ($0-1$ mM and $10-50$ mM, see Figure C.11), albeit with significantly reduced fitting quality. A detailed discussion of the fitting is given in Section C.5.2 and summarized in Table C.1.

8.2.2.3. Coulometric readout. Coulometric sensing quantifies the concentration of the analyte by discharging the sensor after charging it for a fixed time (here 60 s) after illuminating under OCP conditions in a degassed electrolyte containing a fixed glucose concentration. This readout should be distinguished from the others, as it is invasive, *i.e.*, it modifies the concentration information of the sensor during discharge. We perform the discharge by applying a constant potential of $+0.2$ V *vs.* Ag/AgCl and measuring the dark current. We observe an initial large current of up to ~ 150 µA, which rapidly decays and plateaus after approximately 60 s (Figure 8.3 (c)), at which already 96 % of the accumulated charges are discharged. We explain this fast decline with a decreasing amount of charge carriers available on the material and hence increasing resistance when discharging, a typical phenomenon for batteries,[50] and in-line with the discussed correlation between resistance (*i.e.*, magnitude of impedance) and amount of charging above for impedimetric sensing. After 300 s of discharge, the average current for all experiments (irrespective of analyte concentration) was below 10 nA, which indicates a near complete discharging process. By integrating the current over the entire 300 s, we obtain a measure of the total charge that was stored on the system. This charge contains the sensing information (Figure 8.3 (d)), as it mirrors the amount of charging and thus, glucose concentration which had led to charge accumulation on K-PHI at a fixed illumination time as discussed above for potentiometric sensing (Figure 8.2 (c)). The sensitivity can again be tuned by appropriately fixing the illumination time and/or intensity

during charging: short illuminations are beneficial for large concentration and long illuminations for low concentrations.

Note that this experiment also acts as a reset of the sensor for all memristive cases so that it can afterwards be reused for the next sensing experiment, *i.e.*, it deletes all previously stored information. This underlines that the change in memristive state is only dependent on the charged state and fully reversible, an important characteristic of a memristor.[51]

Combining this sensing method with a possible long charge retention time (when illuminating for 20 min, more than 1 h is possible; see Figure 8.2 (a)) allows us to demonstrate the delayed sensor readout, *i.e.*, "memory" sensing. When charging the sensor for 60 s and performing the discharge after delays of 60 and 300 s, a decrease in charge is observed when increasing the delay time (see Section C.6 for details). We attribute this to self-discharge *via* uncovered parts of the FTO substrate due to water reduction from the aqueous electrolyte and oxygen reduction from oxygen leaking into the reactor. This self-discharge is also responsible for larger error bars in the signal to concentration correlation compared to the other electrochemical readout methods as due to the integrating mechanism, small differences among samples such as coating degree and density play a much more significant role. However, since sensor fabrication can be scaled easily (dip coating) and sample batches can be calibrated with an offset factor, these effects are of little practical concern (see Section C.4).

Fitting of the measurement to extract the concentration information is done with the same fit function as for the potentiometric readout over the entire concentration range (Figure 8.3 (d) dashed line) or by a linear fit that requires two linear ranges ($0.1-5$ mM and $10-50$ mM, see Figure C.13) with a much reduced fit quality. The delay times for memory sensing produce a systematic feature by either changing fit contributions or an offset for non-linear and linear fitting, respectively. An offset factor can thus be calculated to account for the self-discharge losses. Details of the fitting are given in Section C.5.3 and Table C.1.

8.2.3. Photomemristive sensing with K-PHI wireless particles

Finally, we study the optical response of K-PHI nanoparticles suspended in an aqueous suspension. This sensing mode is more direct and its implementation is potentially simpler compared to the previous ones, as no wires or electrode substrates are needed for *in situ* probing. The memristive charge accumulation is caused by the

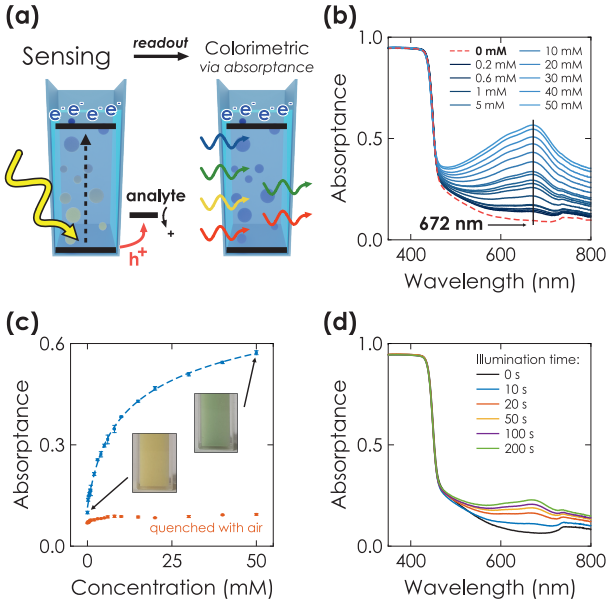

Figure 8.4. Colorimetric sensing *via* K-PHI wireless particles. **(a)** Scheme of memristive sensing and subsequent colorimetric readout. **(b)** Change of the absorptance at 672 nm after illuminating K-PHI particles suspended in an aqueous electrolyte for 200 s in presence of the example analyte glucose. With increasing concentrations, the absorption band with a maximum at 672 nm increases. **(c)** Correlation between the absorptance and glucose concentration. The red dots represent absorptance after quenching the respective charged state of K-PHI with air after the absorptance measurement. The color change is visible by eye (inset pictures). **(d)** Dependence of illumination time on change of absorptance at a fixed glucose concentration of 1 mM.

same light-induced oxidative charging process and reflects the accumulated sensing information *via* a change in photophysical properties.

8.2.3.1. Colorimetric readout. The most prominent change in the photophysical properties of K-PHI due to photocharging is a color change from yellow to blue, the so-called "blue state".[24,26,52] Measuring the K-PHI absorption after the sensing interaction allows to quantitatively relate the optical properties to the analyte concentration (Figure 8.4 (a)) in suspensions with a given concentration of K-PHI particles ($3\,\mathrm{mg\,mL^{-1}}$). After photocharging for 200 s in the absence of oxygen and in the presence of the analyte (here glucose), the absorptance of the suspension was measured from 800 to 350 nm (Figure 8.4 (b)). Note that for higher accuracy, absorptance and not absorbance is measured in an integrating sphere, to correct for scattering. With increasing analyte interaction, an additional absorption band with

a maximum at $\sim$670 nm appears and grows, which is characteristic for the "blue state".[24] Control experiments without glucose confirmed no absorptance at wavelengths above the optical bandgap of K-PHI ($\sim$450 nm). Plotting the value of the absorptance at this maximum against the analyte concentration reveals the colorimetric sensing ability (Figure 8.4 (c)). An increase in absorptance is detectable down to a glucose concentration of 200 µM for the chosen illumination time and K-PHI concentration. We have also investigated influences, which stem from the particle size. Although a slight offset could be observed (see Section C.7.1), no systematic change was found.

Similar to the above-discussed electrochemical readout methods, illumination time can be used to tune the response towards a more specific sensitivity range (Figure 8.4 (d) and Section C.7.2). Furthermore, a time-delayed readout of the sensing information is easily possible, with a signal decay of $\sim$30 % after a delay of 20 min (see Section C.7.3). This enables for example *in situ* measurements with *ex situ* readout in environments where *in situ* optical sensing is not possible. Note that the color change is also clearly visible by eye (Figure 8.4 (c), inset), which makes this readout method useful for label-free colorimetric applications and qualitative analysis even without instrumentation. In comparison to previously reported colorimetric carbon nitride sensors that rely on color changes of external species such as $3, 3', 5, 5'$-tetramethylbenzidine (TMB), our approach does not require any additional external signal molecules to achieve a visible color change, minimizing fabrication cost and time while simultaneously improving the design simplicity and recyclability.[33] The sensing information can be erased by opening the cuvette and enabling quenching of the reduced state by oxygen contained in air.[28,30] Notably, the quenched state always restores the initial absorptance value (Figure 8.4 (c), red dots) and no degradation of the material's optical properties was observed. This resetting method is more practical than washing the sensor to reset the concentration of external species (such as TMB). The relationships between absorptance signal and concentration can be fit analogous to the above discussed electrochemical readout methods. We find three linear ranges (0.2 to 2 mM, 3 to 10 mM, 15 to 50 mM, see Figure C.15) with a limited fitting quality. Phenomenological non-linear fitting works much better and over the entire dynamic concentration range (Figure 8.4 (c) dashed line and Figure C.14). A more detailed discussion of the fitting is given in Section C.5.4 and summarized in Table C.1.

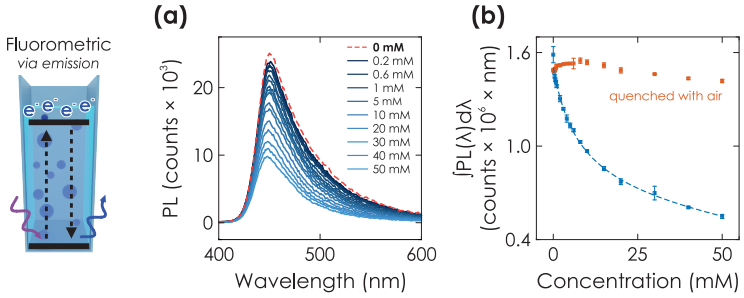

Figure 8.5. Further optical sensing method *via* K-PHI wireless particles. (a) Fluorometric readout. Photoluminescence spectroscopy (PL) emission when exciting the suspended K-PHI particles at a wavelength of 370 nm after illumination for 200 s in presence of different glucose concentrations. The PL quenching is caused by accumulated charges. **(b)** Integrated PL emission are shown with the blue dots. The red dots represent PL emission after quenching the respective charged state of K-PHI with air after the PL measurement.

8.2.3.2. Fluorometric readout. When exciting the characteristic and broad fluorescence emission of K-PHI at 370 nm, the emission signal with a maximum ∼450 nm can also be used to characterize the charged state, analogous to the colorimetric measurements. After illuminating the K-PHI nanoparticle suspension with different glucose concentrations for 200 s, we measured the emission spectrum from 400 to 600 nm (Figure 8.5 (a)). With linearly increasing glucose concentrations, we observed a fast-decreasing fluorescence activity (Figure 8.5 (b)). Since the absorption at the excitation wavelength (370 nm) remains unchanged (Figure 8.4 (b)), this decline is purely an emission property, which is caused by the accumulation of electrons, enabled by hole extraction due to glucose oxidation. We attribute the emission quenching to an increased recombination probability of photogenerated holes, which have more recombination partners with increasing amounts of electrons being stored on the material. This de-excitation, induced by accumulated charges, may be either radiative at frequencies out of our detection limits (>900 nm) or non-radiative. A schematic summary of this model together with a discussion of the negligible invasiveness of these measurements is given in Section C.7.4 and Section C.7.5. The glucose concentration cannot only be quantified by integrating the emission spectrum (Figure 8.5 (b)), but also by an emission intensity measurement at a single wavelength. By that, the measurement time can be significantly decreased (20 to 0.1 s). The sensitivity of the fluorometric readouts is comparable to the colorimetric readout, *i.e.*, a change in signal can be detected down to 200 µM for the chosen illumination time of 200 s. Emission from the quenched sensor (Figure 8.5 (b), red

dots) without washing the material or exchanging the electrolyte reveals a slight decay in the emission of the discharged state, which we attribute to slow particle agglomeration or surface clogging by oxidized donor species.[44] Both can be restored by washing away the analyte and its oxidation products, or by sonicating the material in order to fully restore the properties of the sensor material.[44] Besides, a slight dilution of K-PHI suspension due to the addition of glucose solution might also contribute to the signal decay. The relation between the analyte concentration and the signal can be fit analogous to the colorimetric readout, with three linear ranges (0.2 to 2 mM, 2 to 10 mM, 15 to 50 mM; see Figure C.17) or one non-linear fit over the entire dynamic concentration range (Figure 8.5 (b) dashed line and Figure C.16). A detailed discussion of the fitting is given in Section C.5.5 and Table C.1. Last and similar to before, the sensitivity ranges can be tuned by varying the illumination time (Figure C.20) or intensity and also by increasing the power of the laser for photoluminescence excitation. Besides, also time-delayed readout is possible with a signal loss of only $\sim$20 % after a delay of 1200 s (see Section C.7.3), caused by oxygen leaking or – in principle – other electron acceptors.[30,46] In principle, the wireless methods described here are applicable also to K-PHI particles immobilized on a thin film. However, the application of wireless K-PHI particles for sensing holds more promise for applications where environmental or biological conditions are studied in situ.[46]

8.3. Conclusion

We have introduced the biocompatible, environmentally friendly K-PHI as a photomemristive sensing platform enabling a multimodal analyte sensing. Building on the classical PEC amperometric sensing approach, in which an oxidative photocurrent can be correlated to the concentration of various analytes, we develop a photomemristive sensing concept, which utilizes the material's inherent bifunctionality of light absorption and charge storage to photo-oxidatively sense and quantify analytes by accumulating the generated electrons on the material. The change in the material's optoelectronic properties upon photocharging translates into various electrochemical and optical readout methods: (1) potentiometric and (2) impedimetric sensing (non-invasive), (3) coulometric sensing (invasive and method to reset), as well as (4) colorimetric and (5) fluorometric sensing (minimally invasive). The latter two optical methods enable wireless analyte quantification for in situ applications as particulate systems and a facile qualitative visual readout.[30,46,53] Contrary to most other sensors, the sensing methods are

all direct, *i.e.*, we combine receptor, transducer and current integrating memristive amplifier on the same material, while no additional intermediate species (*e.g.*, mediators) are required. In comparison to state-of-the-art memristive sensors requiring tailored nanostructures, the K-PHI sensor is simple (only a degassed standard electrochemical cell is required), flexible (nanosheet film electrodes or wireless sensing of nanoparticles) and easily scalable (cheap and easy material synthesis, film preparation *via* solution process). Moreover, the sensor can be reset and easily reused. Input parameters for sensing such as illumination time and intensity can be used to tune the sensitivity and measuring ranges. A time-delayed readout is possible. The main practical advantage of our sensing approach is its great flexibility for different applications, which enable fast (<1 s) and facile readout, as well as the combination of different techniques for adapting sensitivity ranges without modification of the sensor. A summary of the key advantages and measurement properties of the different analysis methods is given in Table 8.1. The organic nature of K-PHI with functionalizable groups at its edges was further shown to enable a targeted surface property engineering by chemical modifications, which can lead to much enhanced selectivity.[44] Similarly, the chemical attachment of dedicated receptors appears possible,[54] which would allow to engineer selectivity and responsivity further, according to the field of application. Besides sensing, the concepts described here are useful for evaluating SED strengths and thereby, to provide a better understanding of photocatalytic process parameters, while also being of interest as a characterization tool for light-driven charge storage properties of "solar battery" materials. At the same time, these novel sensing approaches can be applied to other photocatalytic and especially light-storing materials, including both organic and inorganic semiconductors. Since the memristive sensor generates an electrical signal upon charging (OCP), which can be used to drive a current by discharging (coulometric measurements), it can be coupled to other (bio)electronic devices in feedback loops, which can be triggered by using voltage or current thresholds. With this, true neuromorphic applications that facilitate automated electronic signal processing would be directly enabled.[4,5,12,55,56]

8.4. Experimental

Synthesis of the carbon nitride modification K-PHI as nanoparticles. The carbon nitride materials were synthesized as described in literature.[24,26,36] The precursor material melamine as well as potassium thiocyanate were acquired from

Sigma Aldrich in reagent grade purity. Exfoliation was carried out in 2-propanol (IPA) *via* sonication in an ice bath for 2 h (300 mg K-PHI in 100 mL IPA). Subsequently the nanosheets were separated *via* two centrifugation steps at 353 RCF for 20 min and 795 RCF for 40 min in a centrifuge (3–30k, Sigma) to ensure an uniform small particle size, akin to a reported procedure.[28] To reach the desired concentration, density was first evaluated by drying 1 mL of suspension and measuring the weight of the dried residue on a quartz crystal microbalance. To increase particle concentration to 0.2 mg mL^{-1} excess IPA was then removed using a rotary evaporator (HeiVap Value Digital G3B, Heidolph) at a pressure of 137 mbar and a water bath temperature of 50 °C.

Material characterization. ATR-IR spectra of the K-PHI bulk suspensions and nanosheets were collected with an IR spectrometer (UATR TWO, PerkinElmer), which was equipped with a diamond crystal. The optical bandgap of K-PHI bulk suspensions and nanosheets was characterized with an Ultraviolet Visible light (UV-VIS) spectrometer (Cary 5000, Agilent), equipped with an integrating sphere. Films were characterized *via* Atomic Force Microscopy (AFM) (MFP-3D, Asylum Research), Scanning Electron Microscopy (SEM) (ZEISS Merlin electron microscope), and Transmission Electron Microscopy (TEM) (CM 30 ST (300 kV, LaB6 cathode, Philips)).

Preparation of the sensor films and suspensions. Thin films of the K-PHI nanoparticles were deposited onto FTO substrates (Sigma Aldrich, surface resistivity of 7 Ω cm^{-2}) *via* dip coating with 400 dips, 100 mm/min extraction speed and 120 s drying time at ambient temperature between the dips (ND-R Rotary Dip Coater, Nadetech). A subsequent annealing at 70 °C for 2 days was performed to ensure removal of all leftover solvent. The sample was then cut into 10×12 mm and a small part of the film was scratched off for contacting. This was performed by gluing a wire to an uncovered part of the FTO using conductive silver paste (Silver Conductive RS 186-3600, RS-Pro). The contact was then sealed with epoxy glue (DP410, 3M Scotch-Weld) to provide a rigid connection and prevent both the silver paste and uncovered FTO to influence the measurements. Last, an electrochemical self-cleaning of the finished samples was performed according to a procedure described in Section C.3. For measurements, which utilize particles in a suspension, dried as synthesized bulk K-PHI was suspended in water (3 mg mL^{-1}) and vortexed for 120 s to ensure a proper distribution of particles.

Electrochemical measurements. Electrochemical measurements were performed in an aqueous electrolyte which contained a 10 mM KCl (Sigma Aldrich) background electrolyte. The electrolyte was purged with >99 % argon for at least 20 min through a porous glass frit before every measurement. An oxygen content of below 100 ppb during measurements was ensured by measuring trace oxygen with a trace optical oxygen meter (PSt6 sensor spot and Fibox 3 trace, Presens). All analytes (Sigma Aldrich) were dissolved in Deionized water (DI) water and added to the electrolyte in respective concentrations. An Ag/AgCl electrode with saturated KCl electrolyte (RE-1CP, ALS Japan) was used as the reference electrode and a gold foil (Sigma Aldrich) as counter electrode. Measurements were carried out with a multichannel potentiostat (Autolab M204, Metrohm) in a glass reactor equipped with a quartz window for illumination. Impedance measurements were carried out with a single-channel potentiostat (CompactStat, Ivium). Impedance fitting was performed with the RelaxIS 3 software, rhd Instruments.

Illumination (1 Sun) was generated by a calibrated Sciencetech LightLine A4 solar simulator, which provides simulated sunlight with class AAA quality (AM1.5G). Light was turned on and off using a ThorLabs SHB1T shutter.

Optical measurements. All optical measurements were performed in a quartz cuvette (Hellma Analytics). The suspension (K-PHI in DI water, $3\,\mathrm{mg\,mL^{-1}}$) was purged with >99 % argon before every measurement for 300 s and during charging illumination. Glucose (Sigma Aldrich) was dissolved in DI water and added into the cuvette in respective concentrations. The sample was illuminated (AM1.5G) using a solar simulator (IEC/JIS/ASTM, Newport). Fluorescence was measured using a spectrofluorometer (FLS980, Edinburgh Instruments). Absorptance spectra were measured using a spectrophotometer equipped with an integrating sphere (Cary 5000 UV-VIS, Agilent). The sample was positioned in the center of the sphere on an angle to obtain both total transmission and total reflection signals.

Acknowledgements

The authors acknowledge J. Kröger for insightful discussions. We thank L. Yao for SEM imaging and V. Duppel for TEM imaging. Financial support is gratefully acknowledged by the Max Planck Society, the European Research Council (ERC) under the European Union's Horizon 2020 Research and Innovation Program (grant agreement no. 639233, COFLeaf), the Deutsche Forschungsgemeinschaft (DFG) *via*

the cluster of excellence "e-conversion" (project number EXC2089/1-390776260) and by the Center for NanoScience (CENS). A. J. S. gratefully acknowledges a post-doctoral scholarship from the Max Planck Society. Open Access funding provided by the Max Planck Society.

Conflict of interest

The authors declare no conflict of interest.

8.5. References

(1) Wongkaew, N.; Simsek, M.; Griesche, C.; Baeumner, A. J. *Chem. Rev.* **2019**, *119*, 120–194.

(2) Teymourian, H.; Barfidokht, A.; Wang, J. *Chem. Soc. Rev.* **2020**, *49*, 7671–7709.

(3) Wei, M.; Qiao, Y.; Zhao, H.; Liang, J.; Li, T.; Luo, Y.; Lu, S.; Shi, X.; Lu, W.; Sun, X. *Chem. Commun.* **2020**, *56*, 14553–14569.

(4) Van de Burgt, Y.; Melianas, A.; Keene, S. T.; Malliaras, G.; Salleo, A. *Nat. Electron.* **2018**, *1*, 386–397.

(5) Van Doremaele, E. R. W.; Gkoupidenis, P.; van de Burgt, Y. *J. Mater. Chem. C* **2019**, *7*, 12754–12760.

(6) Carrara, S. *Ieee Sens. J.* **2021**, *21*, 12370–12378.

(7) Sun, K.; Chen, J.; Yan, X. *Adv. Funct. Mater.* **2021**, *31*, 2006773.

(8) Lu, K.; Li, X.; Sun, Q.; Pang, X.; Chen, J.; Minari, T.; Liu, X.; Song, Y. *Mater. Horiz.* **2021**, *8*, 447–470.

(9) Zhao, Y.-Y.; Sun, W.-J.; Wang, J.; He, J.-H.; Li, H.; Xu, Q.-F.; Li, N.-J.; Chen, D.-Y.; Lu, J.-M. *Adv. Funct. Mater.* **2020**, *30*, 2004245.

(10) Ling, H.; Koutsouras, D. A.; Kazemzadeh, S.; van de Burgt, Y.; Yan, F.; Gkoupidenis, P. *Appl. Phys. Rev.* **2020**, *7*, 011307.

(11) Park, Y.; Lee, J.-S. *ACS Nano* **2017**, *11*, 8962–8969.

(12) Pérez-Tomás, A. *Adv. Mater. Interfaces* **2019**, *6*, 1900471.

(13) Vahl, A.; Carstensen, J.; Kaps, S.; Lupan, O.; Strunskus, T.; Adelung, R.; Faupel, F. *Sci. Rep.* **2019**, *9*, 4361.

(14) Mohamad Hadis, N. S.; Manaf, A. A.; Herman, S. H. *Microsyst. Technol.* **2013**, *19*, 1889–1896.

(15) Tzouvadaki, I.; Madaboosi, N.; Taurino, I.; Chu, V.; Conde, J. P.; De Micheli, G.; Carrara, S. *J. Mater. Chem. B* **2016**, *4*, 2153–2162.

(16) Tzouvadaki, I.; Jolly, P.; Lu, X.; Ingebrandt, S.; de Micheli, G.; Estrela, P.; Carrara, S. *Nano Lett.* **2016**, *16*, 4472–4476.

(17) Tuoheti, A.; Pabois, A.; Pubbo, F.; Crespo, I.; Tzouvadaki, I.; Demarchi, D.; Delaloya, J. F.; Xenarios, I.; Carrara, S.; Doucey, M. A. *Columbia J. Cancer Res.* **2020**, *3*, 341–348.

(18) Ibarlucea, B.; Fawzul Akbar, T.; Kim, K.; Rim, T.; Baek, C.-K.; Ascoli, A.; Tetzlaff, R.; Baraban, L.; Cuniberti, G. *Nano Res.* **2018**, *11*, 1057–1068.

(19) Hadis, N. S. M.; Manaf, A. A.; Ngalim, S. H.; Herman, S. H.; Sawada, K.; Fauzi, N. A. In *2017 IEEE Asia Pacific Conference on Postgraduate Research in Microelectronics and Electronics (PrimeAsia)*, Kuala Lumpur, Malaysia, IEEE: 2017.

(20) Hadis, N. S. M.; Manaf, A. A.; Herman, S. H. In *2015 IEEE International Circuits and Systems Symposium (ICSyS)*, Langkawi, Malaysia, IEEE: 2015.

(21) Xiao, Z.; Huang, J. *Adv. Electron. Mater.* **2016**, *2*, 1600100.

(22) Wang, R.; Yang, J.-Q.; Mao, J.-Y.; Wang, Z.-P.; Wu, S.; Zhou, M.; Chen, T.; Zhou, Y.; Han, S.-T. *Adv. Intell. Syst.* **2020**, *2*, 2000055.

(23) Yuan, L.; Liu, S.; Chen, W.; Fan, F.; Liu, G. *Adv. Electron. Mater.* **2021**, *7*, 2100432.

(24) Lau, V. W.-h.; Klose, D.; Kasap, H.; Podjaski, F.; Pignié, M.-C.; Reisner, E.; Jeschke, G.; Lotsch, B. V. *Angew. Chem. Int. Ed.* **2017**, *56*, 510–514.

(25) Wang, X.; Maeda, K.; Thomas, A.; Takanabe, K.; Xin, G.; Carlsson, J. M.; Domen, K.; Antonietti, M. *Nat. Mater.* **2009**, *8*, 76–80.

(26) Schlomberg, H.; Kröger, J.; Savasci, G.; Terban, M. W.; Bette, S.; Moudrakovski, I.; Duppel, V.; Podjaski, F.; Siegel, R.; Senker, J.; Dinnebier, R. E.; Ochsenfeld, C.; Lotsch, B. V. *Chem. Mater.* **2019**, *31*, 7478–7486.

(27) Savateev, A.; Antonietti, M. *ChemCatChem* **2019**, *11*, 6166–6176.

(28) Podjaski, F.; Kröger, J.; Lotsch, B. V. *Adv. Mater.* **2018**, *30*, 1705477.

(29) Luo, Y.; Yan, Y.; Zheng, S.; Xue, H.; Pang, H. *J. Mater. Chem. A* **2019**, *7*, 901–924.

(30) Sridhar, V.; Podjaski, F.; Kröger, J.; Jiménez-Solano, A.; Park, B.-W.; Lotsch, B. V.; Sitti, M. *Proc. National Acad. Sci.* **2020**, *117*, 24748–24756.

(31) Cao, Q.; Barrio, J.; Antonietti, M.; Kumru, B.; Shalom, M.; Schmidt, B. V. K. J. *ACS Appl. Polym. Mater.* **2020**, *2*, 3346–3354.

(32) Xiong, M.; Rong, Q.; Meng, H.-m.; Zhang, X.-b. *Biosens. Bioelectron.* **2017**, *89*, 212–223.

(33) Zhang, P.; Sun, D.; Cho, A.; Weon, S.; Lee, S.; Lee, J.; Han, J. W.; Kim, D.-P.; Choi, W. *Nat. Commun.* **2019**, *10*, 940.

(34) Tian, J.; Liu, Q.; Ge, C.; Xing, Z.; Asiri, A. M.; Al-Youbi, A. O.; Sun, X. *Nanoscale* **2013**, *5*, 8921.

(35) Tian, J.; Liu, Q.; Asiri, A. M.; Al-Youbi, A. O.; Sun, X. *Anal. Chem.* **2013**, *85*, 5595–5599.

(36) Lau, V. W.-h.; Moudrakovski, I.; Botari, T.; Weinberger, S.; Mesch, M. B.; Duppel, V.; Senker, J.; Blum, V.; Lotsch, B. V. *Nat. Commun.* **2016**, *7*, 12165.

(37) Kröger, J.; Jiménez-Solano, A.; Savasci, G.; Lau, V. W. h.; Duppel, V.; Moudrakovski, I.; Küster, K.; Scholz, T.; Gouder, A.; Schreiber, M.-L.; Podjaski, F.; Ochsenfeld, C.; Lotsch, B. V. *Adv. Funct. Mater.* **2021**, *31*, 2102468.

(38) Podjaski, F.; Lotsch, B. V. *Adv. Energy Mater.* **2021**, *11*, 2003049.

(39) Kröger, J.; Podjaski, F.; Savasci, G.; Moudrakovski, I.; Jiménez-Solano, A.; Terban, M. W.; Bette, S.; Duppel, V.; Joos, M.; Senocrate, A.; Dinnebier, R.; Ochsenfeld, C.; Lotsch, B. V. *Adv. Mater.* **2022**, *34*, 2107061.

(40) Kasap, H.; Caputo, C. A.; Martindale, B. C. M.; Godin, R.; Lau, V. W.-h.; Lotsch, B. V.; Durrant, J. R.; Reisner, E. *J. Am. Chem. Soc.* **2016**, *138*, 9183–9192.

(41) Weinberg, N. L.; Weinberg, H. R. *Chem. Rev.* **1968**, *68*, 449–523.

(42) Devadoss, A.; Sudhagar, P.; Terashima, C.; Nakata, K.; Fujishima, A. *J. Photochem. Photobiol. C: Photochem. Rev.* **2015**, *24*, 43–63.

(43) Gauglitz, G. *Anal. Bioanal. Chem.* **2018**, *410*, 5–13.

(44) Kröger, J.; Jiménez-Solano, A.; Savasci, G.; Rovó, P.; Moudrakovski, I.; Küster, K.; Schlomberg, H.; Vignolo-González, H. A.; Duppel, V.; Grunenberg, L.; Dayan, C. B.; Sitti, M.; Podjaski, F.; Ochsenfeld, C.; Lotsch, B. V. *Adv. Energy Mater.* **2021**, *11*, 2003016.

(45) Fidan, T.; Torabfam, M.; Saleem, Q.; Wang, C.; Kurt, H.; Yüce, M.; Tang, J.; Bayazit, M. K. *Adv. Energy Sustainability Res.* **2021**, *2*, 2000073.

(46) Sridhar, V.; Podjaski, F.; Alapan, Y.; Kröger, J.; Grunenberg, L.; Kishore, V.; Lotsch, B. V.; Sitti, M. *Sci. Robot.* **2022**, *7*, 62.

(47) Hullavarad, S.; Hullavarad, N.; Look, D.; Claflin, B. *Nanoscale Res. Lett.* **2009**, *4*, 1421.

(48) Costa, I. M.; de Araújo, E. P.; Arantes, A. N.; Zaghete, M. A.; Chiquito, A. J. *Nanotechnology* **2021**, *32*, 015702.

(49) Adler, C.; Selim, S.; Krivtsov, I.; Li, C.; Mitoraj, D.; Dietzek, B.; Durrant, J. R.; Beranek, R. *Adv. Funct. Mater.* **2021**, *31*, 2105369.

(50) Costentin, C.; Savéant, J.-M. *Chem. Sci.* **2019**, *10*, 5656–5666.

(51) Pershin, Y. V.; Di Ventra, M. *J. Phys. D: Appl. Phys.* **2019**, *52*, 01LT01.

(52) Knorr, F. J.; Mercado, C. C.; McHale, J. L. *J. Phys. Chem. C* **2008**, *112*, 12786–12794.

(53) Tsang, A. C. H.; Demir, E.; Ding, Y.; Pak, O. S. *Adv. Intell. Syst.* **2020**, *2*, 1900137.

(54) Xavier, M. M.; Nair, P. R.; Mathew, S. *Anal.* **2019**, *144*, 1475–1491.

(55) Wang, Z. et al. *Nat. Electron.* **2018**, *1*, 137–145.

(56) Van de Burgt, Y.; Lubberman, E.; Fuller, E. J.; Keene, S. T.; Faria, G. C.; Agarwal, S.; Marinella, M. J.; Alec Talin, A.; Salleo, A. *Nat. Mater.* **2017**, *16*, 414–418.

Part IV

Concluding Remarks

9

Conclusion & Outlook

Novel material properties inspire new device concepts. However, the avenue to implementation is long and strenuous and consists of different stages of research, namely (1) observing and understanding a new property, (2) rationalizing its implications as well as deriving design guidelines, and (3) designing a proof-of-concept device. Recently, light induced processes have received attention not only in the context of more traditional optoelectronic applications such as photocatalysis or photovoltaics (Section 1.3),[1,2] but also for simultaneous light-induced ionic effects termed optoionics that we discuss in detail in Chapter 4.[3,4] Ionic effects are key for manifold energy storage devices and dictate performance (Section 1.4) – hence, optoionics may motivate light to enter the realms of batteries and capacitors. Coupled optoelectronic and optoionic features may go further: light energy may be used not only to assist carrier and ion motion, but also to be directly harvested by suitable integrated photoabsorbers.

As such, this thesis focuses on developing novel device concepts that integrate light absorption into devices, which operate traditionally in the dark – namely energy storage devices and sensors. We discuss the toolkit of optoionic effects to design such applications and the associated burgeoning research field in Chapter 4. Light induced ionic effects may lead to a larger ionic mobility or ion-interaction induced trapping of photogenerated charge carriers. In the perspective, we start by discussing light-ion interaction effects in a historical context (often also coined photoionics). We then proceed to explain our current understanding of the mechanism and then discuss a new concept of differentiating between short-range (SFE) and long-range (LFE) field effects that can occur intrinsic or extrinsic in either a single or two phases.

The field of solar batteries is novel and as such very rich and diverse in concepts as we elucidate in the second perspective in Chapter 5. Designs offer different levels of integration: Two-device designs separate light absorption and charge storage into

different devices and are currently widely employed. One-device designs can have three electrodes with distinct tasks (photoabsorption, battery anode, and battery cathode) or two electrodes with one electrode performing multiple tasks at once, either *via* bifunctional composite heterojunctions or bifunctional materials. We underline in the perspective (Chapter 5) that even though several different device concepts exist, they can be organized into two main categories: current efficient charging (IEC) or voltage efficient charging (VEC). By proposing this organization of the ensemble of solar battery concepts, we aim to pinpoint similar properties of devices from different origins. Especially in terms of applications, the implications may be very different: Whereas IEC devices might be beneficial for decentralized small-scale solar power plants or microdevices,[5–7] VEC systems could facilitate buffering DC devices with a variable power output. Current solar battery concepts provide several challenges that were recently summarized by Y. Wang *et. al.*:[8]

(i) the absence of general design principles,

(ii) photogenerated electrons/holes with significant reduction/oxidation power may decompose the electrolyte,

(iii) complex, not yet fully resolved operation mechanism complicates targeted optimization of solar battery devices,

(iv) short carrier diffusion distances dictate thin active layers, which in return reduces capacity of the photoactive layer.

By designing a novel solar battery concept based on K-PHI and with an internal charge transfer mechanism that is unprecedented for closed solar batteries with only solid-state electrodes, we aim to reach a new level of integration. We use the device as a case study to investigate several of the challenges listed above. As bifunctional photoanode material, we utilize the 2D polymeric carbon nitride K-PHI since it possesses a well-investigated toolkit of optoelectronic and optoionic features that enable both light absorption and electron storage in trap states.[9–12] We then use all-organic hole transport materials, which transfer the photogenerated hole to the hole storage material *via* a ladder-type redox transfer mechanism. The oxidative power of the hole is used as driving force for this process and as such may present a way to engineer challenge (2) mentioned above.

In the first research study discussed in Chapter 6, we design an optical model of the device to extract design guidelines, such as illumination geometry and required

thickness of the individual layers. We investigate where light absorption in the photoactive layer leads to a photocurrent (*i.e.*, where the IQE has a large value). We conclude that the photocurrent is generated only in a collection layer, which is located at the junction of K-PHI and the hole transporter. As such, illumination from the rear of the device produces a far larger photocharging current, since parasitic absorption of K-PHI outside of the collection layer is decreased. We propose different ideas to increase light absorption within the collection layer independent of changing the overall active layer thickness – a way to potentially circumvent the conceptional problem of thick active layers decreasing the photocurrent, when illuminated from the rear (challenge (iv)). We then continue to measure further photocurrent limitations *via* electrochemical measurements in half-cell configuration: Photochromic effects as well as charging-state dependent photocurrent (*i.e.*, reducing photocurrent when the device is charged more) – the latter being likely one of the most significant limitation of bifunctional materials for solar batteries.[13] All these calculations and measurements allowed us to design a model, which simulates the different shapes of *Ragone plots* for solar batteries – a key step to understand and engineer the operation principle and electrochemical signature of solar batteries (challenge (1) and (3)). While in a normal battery the *Ragone plot* reveals a line giving power and energy densities for different applied currents, solar batteries reveal an area which scales with illumination intensity. Interesting conclusions can be extracted: When discharging with an electric current that is in the range of the photocurrent generated *via* illumination, discharging will be much longer, which in return will significantly increase energy output (theoretically, when the photocurrent is larger than the electric discharging current, the device will never be discharged and operates like a solar cell). Hence, only minor light intensity variations may lead to major performance boosts, when tuning photocurrent and electric discharging current.

We proceed in the next study detailed in Chapter 7 to design a proof-of-concept device operating with this geometry. We show that the device can operate in different modes: solar cell, battery, and light assisted battery (that is, solar battery), the latter showing significantly enhanced energy and charge densities as well as electric coulombic efficiencies. Noteworthy, this work underlines the independent operation of different charging and discharging fluxes that we propose in Chapter 5 and simulate in Chapter 6. The overall current flux results from a cumulative combination of photocurrent and electric (dis)charging current that can charge the device completely independent of each other. We also provide an indication of the modified *Ragone plot* shape that we theoretically discuss in Chapter 6. This device is the

first demonstration of a full solar battery, which uses carbon nitrides as photoactive electrode and uses the internal hole transfer mechanism *via* interfacial ladder-type redox alignment.

The research avenue of this new sub-genre of solar batteries likely must focus on increasing photocurrent output of the device to become more competitive with classical solar cells. A good metric to give an idea of true performance of the device is the solar-to-output efficiency, which is for this device only $0.012\,\%$ when using the solar spectrum only above the bandgap – competitive when comparing the device to similar solar batteries (Table B.2), but definitely with a huge room of improvement when considering emerging solar cells with PCE values in the range of 10 to $20\,\%$. Strategies could include improving the K-PHI conductivity *via* heterojunctions with conductive additives such as reduced graphene oxide or even PEDOT:PSS.[14,15] Similar to organic solar cells, bulk heterojunctions should improve light absorption efficiency by reducing required exciton diffusion distances.[16] To reduce parasitic absorption of hole transport and hole storage materials in rear illumination geometry, several solar flow designs may be employed. Only a very thin liquid film would have to be on top of K-PHI, with the majority of catholyte residing in storage tanks next to the photoanode.[17,18]

The last research part of this thesis – Chapter 8 – uses K-PHI's bifunctionality in a different way. Photogenerated holes oxidize an analyte in the electrolyte and the resulting charging of K-PHI was detected *via* electrochemical (potentiometric, impedimetric, coulometric sensing) and optical (fluorometric, colorimetric sensing) techniques – the latter two being performed with K-PHI particle suspensions and thus in a wireless geometry. Besides proposing a sensing concept with K-PHI, this work underlines several key features: K-PHI can act as receptor for various organic molecules, transducer, and memristive amplifier. The amplification is a result of the "integrating photocurrent" mechanism of charge storage – a stronger detectable change of photophysical properties results from more extensive charging, *e.g.*, due to larger analyte concentrations, larger illumination intensities, or longer illumination times. This produces unique features of this sensing concept: Both LOD and sensitivity ranges are tunable by varying, *e.g.*, illumination conditions. The sensor can thus adapt to different sensitivity requirements. Furthermore, many different charging-states can be extracted, which is a feature of new resistive switching concepts that endeavor to engineer memory applications beyond the binary (that is, two distinct states) system.[19] We discuss writing, reading, and erasing procedures – the latter by adding a sacrificial electron acceptor to discharge K-PHI. As such, we

propose this concept as a photomemristive sensor, since photophysical properties result from sensing history.

Let us finish with some visionary concluding remarks. Manifold optoionic effects are present in our lives (just consider photolysis of silver halogenide (AgI, AgBr, etc.) as a key effect to enable early photography[20]), but only recently the field has received a huge research boost in understanding such effects. This fundamental research has already and will continue to enable a plethora of new device concepts, all of which capitalize on light ion motions.

K-PHI is positioned perfectly in this burgeoning research field, not only due to its optoionic properties, but also since it is earth-abundant, environmentally friendly and scalable in production – key ingredients for large-scale implementations (*e.g.*, a cheap light absorbing material for solar farms towards *solar battery farms* which don't require a large-scale battery anymore) not only in a more conventional implementation where solar panels are present (*e.g.*, rooftops), but also in decentralized solar energy conversion and storage settings (*e.g.*, *Internet-of-Things* microdevices) or even due to its translucent nature (light absorption only <450 nm) in places, where traditional solar panels cannot be implemented (*e.g.*, windows). In addition, K-PHI is biocompatible – this enables implementations for biological devices. While microswimmers for drug-delivery have already been demonstrated,[6] we have underlined with the photomemristive sensor a further possible application field in a medical context – sensing physiologically-relevant molecules such as ascorbic acid or dopamine.

Memory cells with not only one but manifold addressable states is a very important research field for artificial neural networks and neuromorphic computing.[21–26] Our photomemristive sensor indicates the applicability of K-PHI in this context. The huge analyte concentration range that can be stored and after a non-invasive readout deleted from the sensor indicates possibly many addressable states, which may also store different pieces of information, *i.e.*, act as a memory cell for neuromorphic computing. Noteworthy, one could also discuss such memory cells in the context of reducing our vast computing energy consumption by utilizing solar irradiation to assist writing/reading in memory cells, *i.e.*, towards a "solar brain".[23]

However, we can envisage even more application fields of K-PHIs exciting properties. Resistive switching has not only from a computational but also from a biological perspective huge potential.[19,27,28] Artificial synapses for instance may mimic part of signal transduction between neurons (*i.e.*, the synaptic function) and as such not only allow to design neural networks, but also to produce a neural interface. In a biohybrid artificial synapse, the dopamine recycling machinery within the synaptic cleft must be mimicked, as recently done by van der Burgt and coworkers with PEDOT:PSS.[29] K-PHI could find applicability here as well, since we have already underlined that the photomemristive K-PHI sensor may sense dopamine.

9.1. References

(1) Banerjee, T.; Podjaski, F.; Kröger, J.; Biswal, B. P.; Lotsch, B. V. *Nat. Rev. Mater.* **2020**, *6*, 168–190.

(2) Nayak, P. K.; Mahesh, S.; Snaith, H. J.; Cahen, D. *Nat. Rev. Mater.* **2019**, *4*, 269–285.

(3) Podjaski, F.; Lotsch, B. V. *Adv. Energy Mater.* **2021**, *11*, 2003049.

(4) Senocrate, A.; Maier, J. *J. Am. Chem. Soc.* **2019**, *141*, 8382–8396.

(5) Sridhar, V.; Podjaski, F.; Kröger, J.; Jiménez-Solano, A.; Park, B.-W.; Lotsch, B. V.; Sitti, M. *Proc. National Acad. Sci.* **2020**, *117*, 24748–24756.

(6) Sridhar, V.; Podjaski, F.; Alapan, Y.; Kröger, J.; Grunenberg, L.; Kishore, V.; Lotsch, B. V.; Sitti, M. *Sci. Robot.* **2022**, *7*, 62.

(7) Liu, R.; Wang, Z. L.; Fukuda, K.; Someya, T. *Nat. Rev. Mater.* **2022**, *7*, 870–886.

(8) Lv, J.; Xie, J.; Mohamed, A. G. A.; Zhang, X.; Wang, Y. *Chem. Soc. Rev.* **2022**, *51*, 1511–1528.

(9) Kröger, J.; Jiménez-Solano, A.; Savasci, G.; Lau, V. W. h.; Duppel, V.; Moudrakovski, I.; Küster, K.; Scholz, T.; Gouder, A.; Schreiber, M.-L.; Podjaski, F.; Ochsenfeld, C.; Lotsch, B. V. *Adv. Funct. Mater.* **2021**, *31*, 2102468.

(10) Lau, V. W.-h.; Klose, D.; Kasap, H.; Podjaski, F.; Pignié, M.-C.; Reisner, E.; Jeschke, G.; Lotsch, B. V. *Angew. Chem. Int. Ed.* **2017**, *56*, 510–514.

(11) Schlomberg, H.; Kröger, J.; Savasci, G.; Terban, M. W.; Bette, S.; Moudrakovski, I.; Duppel, V.; Podjaski, F.; Siegel, R.; Senker, J.; Dinnebier, R. E.; Ochsenfeld, C.; Lotsch, B. V. *Chem. Mater.* **2019**, *31*, 7478–7486.

(12) Kröger, J.; Jiménez-Solano, A.; Savasci, G.; Rovó, P.; Moudrakovski, I.; Küster, K.; Schlomberg, H.; Vignolo-González, H. A.; Duppel, V.; Grunenberg, L.; Dayan, C. B.; Sitti, M.; Podjaski, F.; Ochsenfeld, C.; Lotsch, B. V. *Adv. Energy Mater.* **2021**, *11*, 2003016.

(13) Savateev, O. *Adv. Energy Mater.* **2022**, *12*, 2200352.

(14) Savateev, A.; Markushyna, Y.; Schüßlbauer, C. M.; Ullrich, T.; Guldi, D. M.; Antonietti, M. *Angew. Chem. Int. Ed.* **2021**, *60*, 7436–7443.

(15) Zhao, P.; Jin, B.; Yan, J.; Peng, R. *Rsc Adv.* **2021**, *11*, 35147–35155.

(16) Proctor, C. M.; Kuik, M.; Nguyen, T.-Q. *Prog. Polym. Sci.* **2013**, *38*, 1941–1960.

(17) Wedege, K.; Bae, D.; Smith, W. A.; Mendes, A.; Bentien, A. *J. Phys. Chem. C* **2018**, *122*, 25729–25740.

(18) Sánchez-Díez, E.; Ventosa, E.; Guarnieri, M.; Trovò, A.; Flox, C.; Marcilla, R.; Soavi, F.; Mazur, P.; Aranzabe, E.; Ferret, R. *J. Power Sources* **2021**, *481*, 228804.

(19) Van de Burgt, Y.; Melianas, A.; Keene, S. T.; Malliaras, G.; Salleo, A. *Nat. Electron.* **2018**, *1*, 386–397.

(20) Senocrate, A.; Kotomin, E.; Maier, J. *Helvetica Chim. Acta* **2020**, *103*, e2000073.

(21) Sun, K.; Chen, J.; Yan, X. *Adv. Funct. Mater.* **2021**, *31*, 2006773.

(22) Gonzalez-Rosillo, J. C.; Balaish, M.; Hood, Z. D.; Nadkarni, N.; Fraggedakis, D.; Kim, K. J.; Mullin, K. M.; Pfenninger, R.; Bazant, M. Z.; Rupp, J. L. M. *Adv. Mater.* **2020**, *32*, 1907465.

(23) Pérez-Tomás, A. *Adv. Mater. Interfaces* **2019**, *6*, 1900471.

(24) Van Doremaele, E. R. W.; Gkoupidenis, P.; van de Burgt, Y. *J. Mater. Chem. C* **2019**, *7*, 12754–12760.

(25) Boybat, I.; Le Gallo, M.; Nandakumar, S. R.; Moraitis, T.; Parnell, T.; Tuma, T.; Rajendran, B.; Leblebici, Y.; Sebastian, A.; Eleftheriou, E. *Nat. Commun.* **2018**, *9*, 2514.

(26) Xiao, Z.; Huang, J. *Adv. Electron. Mater.* **2016**, *2*, 1600100.

(27) Park, Y.; Lee, J.-S. *ACS Nano* **2017**, *11*, 8962–8969.

(28) Van de Burgt, Y.; Lubberman, E.; Fuller, E. J.; Keene, S. T.; Faria, G. C.; Agarwal, S.; Marinella, M. J.; Alec Talin, A.; Salleo, A. *Nat. Mater.* **2017**, *16*, 414–418.

(29) Keene, S. T.; Lubrano, C.; Kazemzadeh, S.; Melianas, A.; Tuchman, Y.; Polino, G.; Scognamiglio, P.; Cinà, L.; Salleo, A.; van de Burgt, Y.; Santoro, F. *Nat. Mater.* **2020**, *19*, 969–973.

Part V

Appendix

A

Supporting Information to Chapter 6

Bridging the Gap between Solar Cells and Batteries: Optical Design of Bifunctional Solar Batteries based on 2D Carbon Nitrides

Contents

A.1. Optical Characterization of Materials 258

A.1.1. Absorption profile 258

A.1.2. Refractive Index 259

A.2. Optical simulation methods 259

A.3. Charge collection layer 260

A.4. Battery performance in the dark 262

A.5. Further optical and electrochemical considerations 264

A.5.1. Dependence of charging state on photocurrent 264

A.5.2. Electrochromic behavior 268

A.6. Simulating discharging 269

A.6.1. Influence of decaying photocurrent on charging time 271

A.6.2. Performance data normalization 271

A.6.3. Input data for simulations / calculations 272

A.7. References 276

A.1. Optical Characterization of Materials

A.1.1. Absorption profile

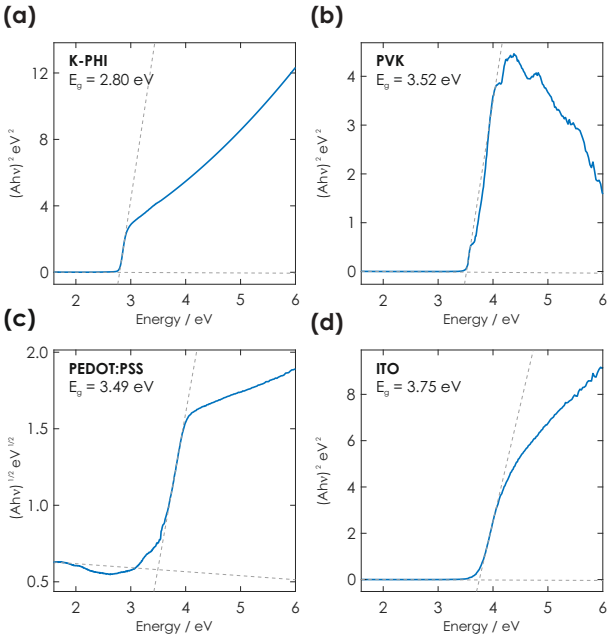

Figure A.1. The absorptance was measured for films of **(a)** K-PHI, **(b)** PVK, and **(c)** PEDOT:PSS deposited onto ITO, as well as **(d)** a pure ITO film. The Tauc plot was calculated either for a direct bandgap (K-PHI, ITO, PVK) or indirect bandgap (PEDOT:PSS) and bandgap values are in agreement with the literature.[1–4]

Measurements were performed with an UV-VIS capable to measure absorptance in an integrating sphere (Cary 5000, *Agilent Technologies*). For film preparation routines of ITO + K-PHI and ITO + PEDOT:PSS please check Section A.4. PVK was deposited onto ITO *via* spin coating (3000 rpm, 30 s) of a PVK solution (10 mg mL^{-1} in chloroform) onto a plasma cleaned ITO substrate (10 min, O_2 plasma) and subsequent annealing at 80 °C for 10 min. We can observe how ITO absorption becomes only relevant at wavelengths $<$350 nm. Furthermore, the absorption onset of K-PHI occurs at ca. 450 nm (Figure A.1 (a)), as expected for K-PHI with its bandgap of 2.7 eV. Note also that absorption at wavelengths larger than 450 nm occurs, as expected from the refractive index of K-PHI shown in Figure A.2. Both PEDOT:PSS and PVK show miniscule absorption at wavelengths between 350 and 800 nm (Figure A.1 (a) and (b), respectively), as discussed in the main text.

A.1.2. Refractive Index

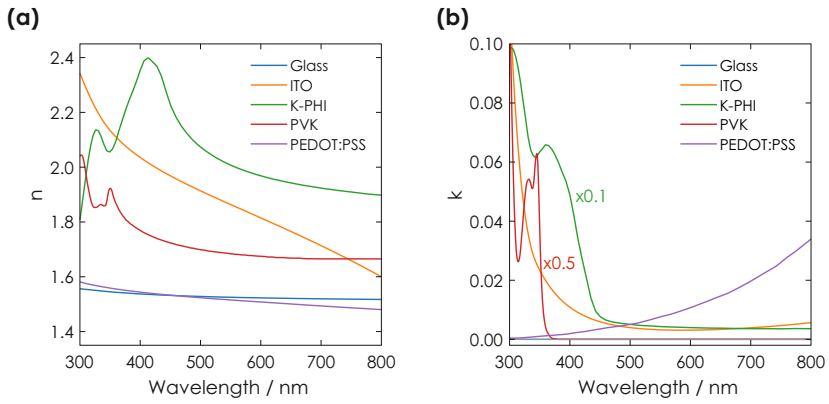

Figure A.2. Spectral dependence of the real **(a)** and imaginary **(b)** part of the complex refractive index ($n + i \cdot k$) of the materials employed in the calculations. The refractive index of glass, ITO, PVK, and PEDOT:PSS was extracted from the literature.[5–8] The refractive index of K-PHI was obtained from ellipsometry measurements performed on a pellet consisting of K-PHI powder.

Measurement of the refractive index of K-PHI is discussed in the following: A pellet of K-PHI powder (K-PHI synthesized as described by us previously.[1]) was pressed to dimensions of approx. 5 mm with up to 2 bar of uniaxial pressure. The refractive index was subsequently measured directly *via* Variable-Angle Spectroscopic Ellipsometer (VASE, *Woollam Co. Inc.*) at different angles of incidence (70, 75 and $80°$). Exemplary refractive index values are given in Table A.1.

A.2. Optical simulation methods

Utilizing the refractive index (Section A.1.2), the electric field intensity distribution and absorption maps were calculated *via* the transfer matrix method (TMM) as reported in the literature:[9–11]

$$A_j = 2\pi \int \frac{I\left(x_j, \lambda\right) \cdot 2 n_j k_j}{I_0\left(\lambda\right) \cdot \lambda} \mathrm{d}x_j \tag{A.1}$$

where j refers to the individual layers in the solar battery, λ gives the respective wavelength, and n_j and k_j give the respective real and imaginary part of the refractive index. Note that the integral extends over the entire volume of the solar battery. Due to the symmetry of the system, the volumes can be reduced to one

Table A.1. Exemplary values of real (n) and imaginary (k) part of the refractive index for materials utilized in this work. The refractive index of ITO, PVK, and PEDOT:PSS was extracted from the literature,[5–8] while the refractive index of K-PHI was measured as described above.

wave-length (nm)	K-PHI		PVK		PEDOT:PSS		ITO	
	n	***k***	***n***	***k***	***n***	***k***	***n***	***k***
300	1.81	9.89E-1	2.04	2.30E-1	1.58	4.30E-4	2.34	1.17E-1
400	2.35	4.89E-1	1.77	0	1.54	1.94E-3	2.04	1.09E-2
500	2.07	5.07E-2	1.67	0	1.52	5.06E-3	1.91	3.97E-3
600	1.97	3.98E-2	1.67	0	1.51	1.07E-2	1.81	3.11E-3
700	1.92	3.62E-2	1.67	0	1.49	1.97E-2	1.71	3.90E-3
800	1.90	3.60E-2	1.67	0	1.48	3.40E-2	1.60	5.67E-3

dimension (x_j). Calculations were performed using numerical calculations *via* a script designed in Matlab.

A.3. Charge collection layer

To evaluate how much the shape of the IQE governs the output of our simulations, we calculate two different functions, either a rectangular step function or a Gaussian with different values for HWHM (Figure A.3). Independent of function, the IQE within the collection layer is assumed to be $100\,\%$. To evaluate its influence on performance, we calculate the charging time required to fully charge the solar battery in dependence of K-PHI active layer thickness (Figure A.4). This metric depends on both width of K-PHI and PEDOT:PSS governing the electric capacity as well as the photocurrent that the active layer provides. The latter is governed by the collection layer and hence, charging time presents a metric which is fit to evaluate different

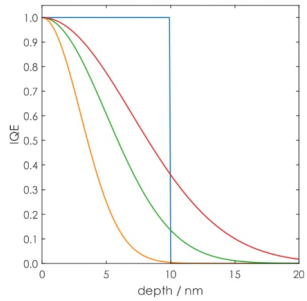

Figure A.3. Shapes of different charge collection layer functions, either rectangular with a decay of the IQE from 100 to 0 % (blue), or different Gaussian functions with different Half Width Half Maximum (HWHM) values (orange, green, blue with HWHM values of 3.5, 6.0 and 8.5 nm, respectively).

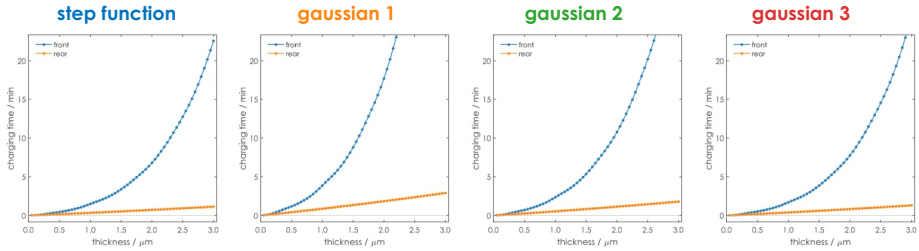

Figure A.4. Simulated charging time performance of solar battery samples using the charge collection layer functions shown in Figure A.3 as a function of K-PHI layer thickness and illumination through the front (blue) or the rear (orange). We define the charging time as the time that is required to fully charge the solar battery. A more detailed description of this performance metric is given in the main text in the main text in Section 6.2.2.

collection layer shapes. In the following, we will focus on front illumination since it shows a more dramatic influence on charging time. The step function is a rational choice due to its simplicity – analogous to the rationale behind the proposed step function when calculating the absorption edge by the Shockley-Queisser model.[12] A solar battery utilizing this function with a step width of 10 nm and a K-PHI active layer thickness of 2 µm would require 6.8 min to charge to its maximum capacity value governed by the layer thickness. We chose a Gaussian function as a very general second function, with HWHM values of 3.5, 6.0 and 8.5 nm leading to charging times of 17, 11 and 7.8 min, respectively. Thus, a monotonous increase in HWHM leads to a monotonous increase in charging time and similar HWHM values compared to step functions with the same width leads to similar charging times, when assuming a constant charging rate. Note that the curve shape of charging time in-

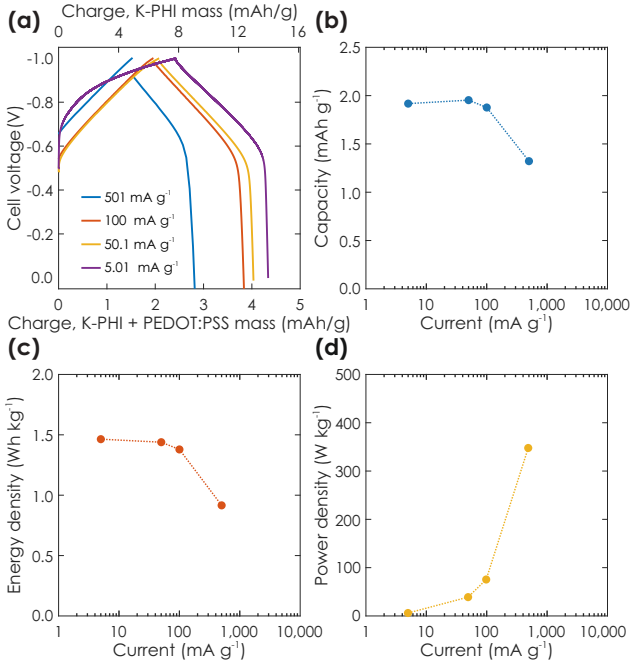

Figure A.5. Performance metrics of GCD measurements in the dark (voltage window of 1 V) with different currents. Extracted charge is normalized on either mass of both K-PHI anode and PEDOT:PSS cathode (bottom x-axis) or mass of only K-PHI (top x-axis). Mass of K-PHI is approximately 31 µg. **(a)** Charging and discharging cycles. **(b)** Extracted capacity during discharge, normalized on the mass of both K-PHI and PEDOT:PSS. **(c)** Energy density extracted during discharge. **(d)** Average power density during discharge. Extracted capacity, energy density, and power density is given in Table A.2.

A

crease with K-PHI active layer thickness (Figure A.4) looks very similar irrespective of collection layer function (Figure A.3), underlining that the shape of the collection layer function (*i.e.*, Gaussian with different HWHM or step function) influences the device performance far less than its thickness.

A.4. Battery performance in the dark

To complement the optical simulations presented in this work, we perform several facile electrochemical experiments on two samples: (1) K-PHI was synthesized as described by us previously *via* a salt-melt of melon and potassium thiocyanate.[1,13–15] Precursors melamine (for melon synthesis) and KSCN were purchased from *Sigma Aldrich* in reagent grade purity. K-PHI films on ITO substrates were fabricated as described by us previously by dip coating exfoliated K-PHI (2 h sonication in 2-

propanol (*Sigma Aldrich*) in an ice bath) in a 2-propanol suspension with a concentration of $3\,\mathrm{mg\,mL^{-1}}$.[1] Mass of the layer was determined by measuring the substrate pre and post K-PHI deposition. (2) A PEDOT:PSS layer deposited onto an ITO substrate, fabricated as follows: ITO substrates were treated with oxygen plasma for $10\,\mathrm{min}$. Subsequently, PEDOT:PSS (3-4 wt% aqueous suspension, *Sigma Aldrich*) was spin coated onto the ITO substrate ($2000\,\mathrm{rpm}$ for $30\,\mathrm{s}$) and annealed at $145\,^{\circ}\mathrm{C}$ in nitrogen atmosphere for $20\,\mathrm{min}$. Spin coating and annealing was repeated once to yield a thicker layer.

Electrochemical measurements were carried out in an aqueous electrolyte containing $100\,\mathrm{mM}$ KCl as background electrolyte. Prior to each measurement, oxygen was removed from the electrolyte by purging it with Argon ($>99\,\%$) for at least $20\,\mathrm{min}$. A gold foil was used as the counter electrode and for three-electrode measurements the potential was measured against an Ag/AgCl reference electrode with saturated KCl (RE-1CP, *ALS Japan*). Measurements were performed using a multichannel potentiostate (Autolab M204, *Metrohm*). The photo-electrochemical reactor was equipped with a quartz glass window for $1\,\mathrm{Sun}$ illumination, which was provided by a solar simulator calibrated to AM1.5 G standard with AAA quality (LightLine A4, *Sciencetech*).

To evaluate performance gains of the solar battery *via* illumination, we require an estimate of GCD performance in the dark. Thus, we design a facile two-electrode electrochemical experiment, consisting of two electrodes immersed in an electrochemical reactor ($0.1\,\mathrm{M}$ KCl, degassed with Ar): an electrode comprised of K-PHI

Table A.2. Resulting performance of characterization of a K-PHI anode and PEDOT:PSS cathode *via* GCD measurements in the dark shown in Figure A.5. Charge is normalized against mass of either only K-PHI anode (column marked with †), or total mass of both K-PHI anode and PEDOT:PSS cathode. GCD current, energy, and power density are all normalized against the total mass.

current ($\mathrm{mA\,g^{-1}}$)	Charge K-PHI† ($\mathrm{mAh\,g^{-1}}$)	Charge total ($\mathrm{mAh\,g^{-1}}$)	Energy density ($\mathrm{Wh\,kg^{-1}}$)	Power density ($\mathrm{W\,g^{-1}}$)
5.01	6.18	1.92	1.46	3.82
50.1	6.29	1.95	1.44	36.9
100	6.05	1.88	1.38	73.5
501	4.26	1.32	0.916	347

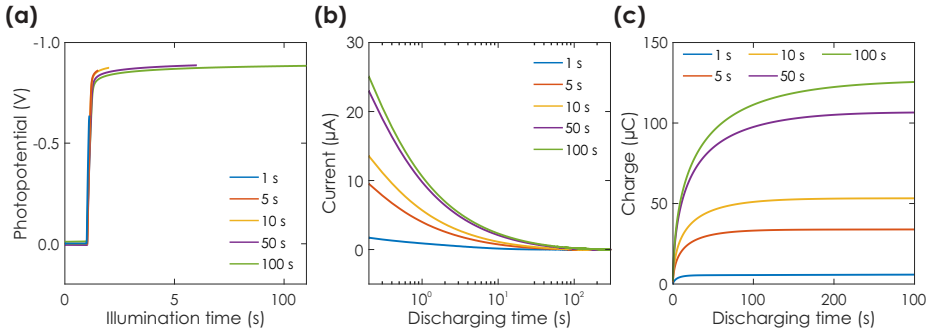

Figure A.6. **(a)** Photocharging of a K-PHI half-cell sample in a three electrode configuration *via* 1 Sun illumination under open circuit conditions and in presence of the SED 4-MBA. **(b)** Current and **(c)** charge generated during subsequent electric discharging in the dark *via* a bias of 0 V *vs.* Ag/AgCl.

deposited onto ITO (anode) and a second electrode comprised of PEDOT:PSS deposited onto ITO (cathode). GCD was performed with different currents. Performance parameters of this measurement are shown in Figure A.5. Ragone plots are shown in the main text in Figure 6.4.

A.5. Further optical and electrochemical considerations

A.5.1. Dependence of charging state on photocurrent

Solar batteries possess efficiency limitations beyond solar cells and batteries. We will discuss two of them in the following: It was shown that charge storage in K-PHI reduces its photocatalytic efficiency by increasing non-radiative recombination pathways *via* trapped electrons.[1,16,17] We expect a similar behavior for the solar battery, *i.e.*, a reducing photocurrent when the device is charging. To quantify this effect, we have designed an experiment comprising a K-PHI film deposited onto ITO, which is immersed into an electrochemical reactor. To extract the holes, we replace the HTM and HSM with two different SEDs, which possess different hole extraction efficiencies: MeOH and 4-MBA, the latter being much more efficient in extracting holes from K-PHI.[1]

The sample (preparation explained in Section A.4) was immersed into the reactor filled with a degassed aqueous 0.1 M KCl electrolyte with the SED. The sample was then illuminated for a set amount of time with 1 Sun under open circuit conditions,

i.e., no external current was applied (Figure A.6 (a)). Note that for longer illumination times >5 s the charging photopotential remains nearly constant independent of illumination time. This behavior results from a slow photocharging rate coupled to a very large density of states at the photopotential, *i.e.*, the potential where photogenerated electrons are stored (here approx. -0.8 V *vs.* Ag/AgCl). Thus, during the light charging process the potential does not change significantly, but the extracted charge increases as a function of the illumination time.[18] Subsequently, a bias potential of 0 V *vs.* Ag/AgCl was immediately applied in the dark for 300 s to extract the photogenerated charge (Figure A.6 (b)).

Resulting charge as a function of illumination time is shown in Figure A.7 (a). With increasing illumination times more charge can be extracted, until for very long illumination time the charge saturates at a capacity which roughly correlates to the capacity of the sample. We utilize a fitting function, which describes the charging behavior of K-PHI:[1]

$$C\left(t\right) = \frac{b_1 \cdot t}{b_2 + t} + \frac{c_1 \cdot t}{c_2 + t} \tag{A.2}$$

where $C\left(t\right)$ gives the charge as a function of illumination time t. The equation comprises two terms (b_1, b_2 and c_1, c_2), which correspond to capacitive charging and faradaic charging, respectively.[1] Table A.3 gives the fitting coefficients for 4-MBA and MeOH.

A

Table A.3. Resulting fitting coefficients of photocharging depending on illumination time shown in Figure A.6 (a). Equation A.2 was used for the fitting.

donor	b_1	b_2	c_1	c_2
MeOH	23.51	5.033	119.1	339.1
4-MBA	7.822E-3	18.13	142.9	16.89

With Equation A.2, we can roughly extrapolate a maximum charge of $4.60\,\mathrm{C\,g^{-1}}$ (or $1.28\,\mathrm{mA\,h\,g^{-1}}$) for 4-MBA and $4.59\,\mathrm{C\,g^{-1}}$ ($1.28\,\mathrm{mA\,h\,g^{-1}}$) for MeOH (grey dashed line in Figure A.7 (a)):

$$C_{max} = \lim_{t\to\infty}\left(\frac{b_1 \cdot t}{b_2 + t} + \frac{c_1 \cdot t}{c_2 + t}\right) = b_1 + c_1 \tag{A.3}$$

Note that this charge is substantially smaller than the capacity of K-PHI reached after 6000 s of photocharging in our previous work ($43\,\mathrm{C\,g^{-1}}$).[19] This deviation may

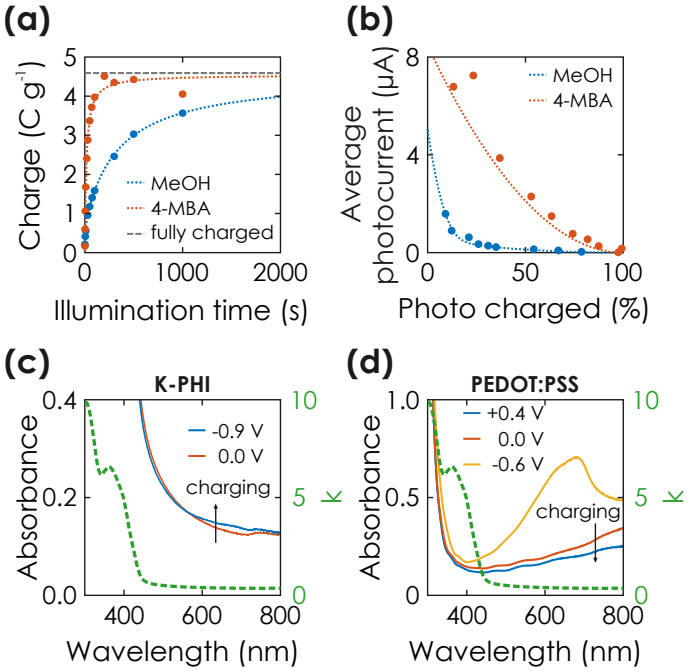

Figure A.7. How does charge storage influence electrochemical and optical properties. (a) Charge which can be extracted from a K-PHI sample by applying a bias potential of 0 V *vs.* Ag/AgCl after illumination with 1 Sun under OCP conditions (illuminated from the K-PHI side, which corresponds to back-side illumination in the solar battery device). Two different donors are used to quench the holes very efficiently (4-MBA) and less efficiently (MeOH). The maximum charge can be extracted from the fitting. **(b)** The average photocharging current extracted from the derivative of (a) is plotted against the charging state of K-PHI. **(c-d)** Change in absorbance of the electron storage material K-PHI and hole storage material PEDOT:PSS when charged. Absorption >450 nm increases for K-PHI (the so-called blue state). Absorption >350 nm decreases for PEDOT:PSS, underling its suitability as a HSM when the solar battery is operated in rear illumination mode. The green dashed line shows the refractive index of K-PHI. Its very low value for wavelengths above 450 to 500 nm underlines that the impact of enhanced absorption at this wavelength should not significantly impact absorption in K-PHI.

A

be due to changes in sample preparation and a shorter photocharging time (1000 s here *vs.* 6000 s in our previous work), a different discharging method (potentiostatic here *vs.* galvanostatic in our previous work) that potentially reduces the measured capacity due to kinetic limitations even stronger,[19] and a thicker sample (around 31 µg here prepared *via* dip coating *vs.* 10 µg in our previous work prepared *via* drop casting). All of these effects are the likely cause of different discharge kinetics in the bulk of the K-PHI film, which results in different extracted charge values. Furthermore, while using SED to extract holes allows to focus on light absorption

and electron storage dynamics of K-PHI (provided that the SED is present in sufficiently high concentration[16]), one has to compare this case with a solar battery with solid HTM carefully since hole transport kinetics may be very different in a solid-solid junction. Note though that the analysis here is more of qualitative nature to underline further limitations of bifunctional solar batteries in general.

As expected, charging *via* the SED 4-MBA is faster, as evidenced by the steeper fit function (Equation A.2) in Figure A.7 (a). Note that irrespective of the SED, both fit functions approach a similar capacity value asymptotically. Utilizing this capacity C ($4.60\,\mathrm{C\,g^{-1}}$ for 4-MBA and $4.59\,\mathrm{C\,g^{-1}}$ for MeOH), we can now calculate an average photocurrent (derivative of Equation A.2) as a function of the charging state of the solar battery, as shown in Figure A.7 (b):

$$I_{avg}\left(t\right) = \frac{\mathrm{d}C\left(t\right)}{\mathrm{d}t} = \frac{b_1 \cdot b_2}{\left(b_2 + t\right)^2} + \frac{c_1 \cdot c_2}{\left(c_2 + t\right)^2} \tag{A.4}$$

where I_{avg} gives the average photocurrent as a function of illumination time t. The concomitant decrease of photocurrent with increasing charging state becomes evident. When fully charged, the photogeneration current is reduced to zero. Note that this effect is weaker for the more efficient SED 4-MBA, underlining the importance of efficient hole extraction. To correlate the average photocurrent to the charging state ch, we first have to normalize the extracted charge (divide Equation A.2 with Equation A.3):

$$ch\left(t\right) = \frac{C\left(t\right)}{C_{max}} = \frac{t}{b_1 + c_1} \cdot \left(\frac{b_1}{b_2 + t} + \frac{c_1}{c_2 + t}\right) \tag{A.5}$$

By plotting Equation A.4 against Equation A.5, we obtain the average photocurrent depending on the charging state (Figure A.7 (b), solid lines). We can observe from the plot that the charging state influences the photocurrent quite significantly (when $50\,\%$ charged, only $26\,\%$ (4-MBA) or $3\,\%$ (MeOH) of the initial photocurrent remains), which thus has to be considered in the simulations presented in this work.

We will discuss implementation into the simulations in the following: First, we assume and propose efficient hole extraction and thus, utilize fitting parameters of the 4-MBA fitting to govern the shape of the photocurrent decrease. Since initial photocurrent I_0 depends on illumination intensity in the simulations discussed in the main text, we have to normalize Equation A.4 to this initial photocurrent I_0 to

give us the normalized average photocurrent $I_{avg,norm}$:

$$I_{avg,norm}\left(t, I_0\right) = \frac{I_0}{\frac{b_1}{b_2} + \frac{c_1}{c_2}} \cdot I_{avg}\left(t\right) \tag{A.6}$$

Solving Equation A.6 to utilize charging state, (*i.e.*, Equation A.5) as an input instead of illumination time requires to first invert Equation A.5:

$$\begin{aligned} t\left(ch\right) = ch^{-1}\left(t\right) = \frac{1}{2 \cdot \left(ch-1\right) \cdot \left(b_1 + c_1\right)} \\ \cdot \Big(- \sqrt{\left(ch \cdot \left(b_1 + c_1\right) \cdot \left(b_2 + c_2\right) - \left(b_1 c_2 + b_2 c_1\right)\right)^2 - 4 \cdot ch \cdot \left(ch-1\right) \cdot \left(b_1 + c_1\right)} \\ \overline{\cdot \left(b_1 b_2 c_2 + b_2 c_1 c_2\right)} - ch \cdot \left(b_1 b_2 + b_1 c_2 + b_2 c_1 + c_1 c_2\right) + b_1 c_2 + b_2 c_1 \Big) \end{aligned} \tag{A.7}$$

From Equation A.6 and Equation A.7 we obtain a function, which we can utilize as an input in our simulations to describe how photocurrent $I_{avg,normP}$ behaves with charging state:

$$I_{avg,normP}\left(ch, I_0\right) = I_{avg,norm}\left(t\left(ch\right), I_0\right) \tag{A.8}$$

We use this equation as an input for subsequent simulations of the increase of photocurrent whilst discharging (see Section A.6).

A

A.5.2. Electrochromic behavior

Besides a modified charging rate with charging state, the charge storage materials show electrochromic behavior, *i.e.*, change their absorptance as a function of amount of charging. For K-PHI, charging increases the absorptance >450 nm (see Figure A.7 (c)) – the so-called blue state absorptance.[1,13]

While for the single junction device architecture used herein this is not a problem since absorption of K-PHI producing a photocurrent only occurs at <450 nm, potential further multi-junction devices utilizing additional active layers which absorb at larger wavelengths to maximize efficiency have to take this into account. Conversely, upon charging PEDOT:PSS shows a reduced absorption at wavelengths >350 nm (see Figure A.7 (d)),[20] increasing transmission of light to the collection layer, thus once more underlining why it is a good HSM candidate material for a solar battery when operating in rear illumination mode.

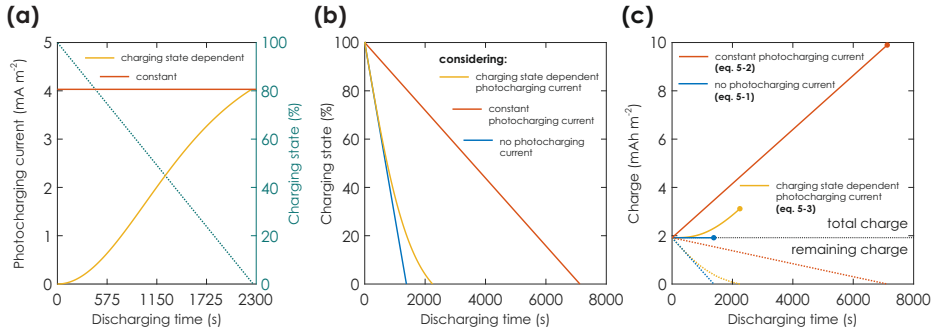

Figure A.8. Simulating photoassisted discharge, calculated for a GCD experiment at 5.01 mA g^{-1} discharge current and under 1 Sun illumination. **(a)** Linear decreasing charging state (turquoise, dashed line), as assumed in the main text for simulations of discharging time (Figure 6.2). The constant photocurrent (main text Equation 6.1) is shown in red and the charging state dependent photocurrent (Equation A.8) is shown in yellow. **(b)** Charging state of iterative solution of Equation A.11, showing a linear decreasing charging state for dark, (*i.e.*, no photocurrent; blue) and constant photocurrent (red; compare to (a): slope governed by photocurrent) and a non-linear decrease for the charging state dependent photocurrent (yellow). **(c)** Resulting charge from (b). The solid lines show the overall extracted charge during discharging, and the dashed lines show the remaining charge.

A.6. Simulating discharging

The charge C_{remain}, which remains on a battery during galvanostatic discharging (*i.e.*, *via* constant current I_{dch}) at a time during discharging t_{dch}, is defined as

$$C_{remain}\,(t_{dch}) = C_0 - I_{dch} \cdot t_{dch} \tag{A.9}$$

where C_0 gives the charge on the battery when fully charged (*i.e.*, capacity). Here and in the following, green parts of the equation describe charging contributions and red parts discharging contributions. Note that this equation requires a constant discharging current I_{dch}, which for batteries is ensured with galvanostatic discharging. While this equation can be used to describe discharging of a solar battery operated in the dark, during illumination a photocharging current I_{ph} is generated which modifies the charging state. We obtain I_{ph} from simulations discussed in the main text in Figure 6.2. Note that while these simulations propose a linear increase of photocurrent generation with illumination intensity, scaling of decrease of photocatalysis performance with smaller illumination intensities was reported for K-PHI albeit with no description of the type of scaling.[16]

We will explain calculations by first discussing a constant photocurrent, and then

implement the charging state dependent photocurrent discussed in Section A.5.1. For a constant photocurrent I_{ph} during discharging, we can adapt Equation A.9:

$$C_{remain}\left(t_{dch}\right) = C_0 + \eta_c \cdot \int I_{ph}\,\mathrm{d}t_{dch} - I_{dch} \cdot t_{dch} \tag{A.10}$$

The solar-to-output efficiency η_c describes how efficiently the photocurrent is generated and charges the battery. It is calculated by dividing the output energy with the energy of the incoming light.[21] We utilize it to link the simulated photocurrent to the current which charges the battery *via* light (*i.e.*, photocharging efficiency) and term the resulting current henceforth as photocharging current. For an exemplary solar battery being discharged with a current of $5.01\,\mathrm{mA\,g^{-1}}$ and under 1 Sun illumination (the photocurrent is calculated with simulations as explained in the main text), the constant photocurrent I_{ph} as a function of discharging time is shown in Figure A.8 (a) red line. Note that the charging state decreases linearly as shown by the turquoise dashed line.

However, as we elaborate in detail in Section A.5, the photocurrent depends significantly on the charging state of the solar battery: The more the solar battery is charged, the smaller the current gets – as expected and reported in literature.[17] We describe this behavior with Equation A.8, which gives $I_{avg,normP}$ as photocurrent. We have to modify Equation A.10 as follows:

$$C_{remain}\left(t_{dch}\right) = C_0 + \eta_c \cdot \int I_{avg,normP}\left(\frac{C_{remain}\left(t_{dch}\right)}{C_0}, I_{ph}\right)\mathrm{d}t_{dch} - I_{dch} \cdot t_{dch} \tag{A.11}$$

The iterative solution is shown in Figure A.8 (b) and (c). Note that the equation requires the charging state as an input to govern the photocharging, since the charging state is modified non-linearly. This becomes evident in Figure A.8 (b): compare linearly decreasing charging state for constant photocurrent (red) and non-linear decrease for charging state dependent photocurrent according to Equation A.8 (yellow). The influence on extracted charge and discharging time is also significant, as shown in Figure A.8 (c): While discharging in the dark yields the smallest extracted charge and discharging time ($1.92\,\mathrm{A\,h\,kg^{-1}}$ and 1379 s, blue line), assuming a charging state dependent photocurrent increases the performance significantly ($3.09\,\mathrm{A\,h\,kg^{-1}}$ and 2223 s, yellow line). While the theoretical assumption of a constant photocurrent shows by far the biggest increase in performance ($9.55\,\mathrm{A\,h\,kg^{-1}}$ and 6867 s, red line), it is quite artificial as discussed in Section A.5.1 due to charge accumulation induced recombination effects.[17]

A

We calculate overall charge and energy density as follows:

$$C_{total}\left(t_{dch}\right) = C_0 + \eta_c \cdot \int I_{avg,normP}\left(\frac{C_{total}\left(t_{dch}\right)}{C_0}, I_{ph}\right) \mathrm{d}t_{dch} \tag{A.12}$$

$$E_{total} = C_{total} \cdot V_{ph} \tag{A.13}$$

with V_{ph} being the photopotential that is assumed to be constant at $0.8\,\mathrm{V}$ during discharging. Note that it slightly drops over the discharge procedure, as shown in Figure A.5 (a) and recently evidenced experimentally.[18]

A.6.1. Influence of decaying photocurrent on charging time

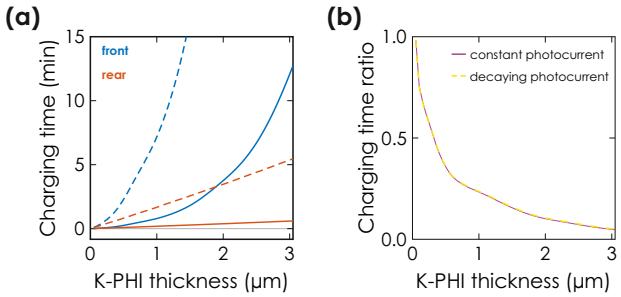

Figure A.9. Influence of decaying photocurrent on charging time. (a) Solid lines show charging time, when a constant photocurrent is assumed. The figure is a reproduction of Figure 6.2 (d). Dashed lines show the charging time, when charging the device to 90 % and using a decay photocurrent according to Equation A.12. **(b)** Charging time ratio for a constant and decaying photocurrent. No difference occurs, as both front and rear decaying photocurrents are affected in a similar manner.

A.6.2. Performance data normalization

A challenge for solar batteries is the issue of normalization, since battery performance scales with mass and solar cell performance scales with area. We face this challenge when comparing performance of our measurements (Section A.4) with simulated photocurrent (main text Section 6.2.1 & Section 6.2.2) and literature devices (main text Figure 6.4 (b) and (c)). The issue arises since mass and illumination area are independent variables and depend on the geometry of the device (*i.e.*, a given mass does not result in a specific illumination area). Hence, to account for the device geometry we have to introduce a fofa, which describes how the device's

mass m [g] or active layer thickness x_{al} [cm] changes with illumination area:

$$fofa = \frac{\mathrm{d}m}{\mathrm{d}a_{ill}} = \rho \cdot \left(a_{ill} \cdot \frac{\mathrm{d}x_{al}}{\mathrm{d}a_{ill}} + x_{al} \right) \tag{A.14}$$

where $\rho \left[\mathrm{g\,cm^{-3}}\right]$ is the active layer density and $a_{ill} \left[\mathrm{cm^{-2}}\right]$ gives the illumination area. We utilize the fofa to normalize photocurrent in main text Figure 6.4 (b) and additional extracted charge *via* illumination in main text Figure 6.4 (c).

A.6.3. Input data for simulations / calculations

To facilitate understanding of the simulations presented in this work, we have elaborated Table A.4 showing the different simulation steps as chronologically presented in the manuscript. This includes a summary of the input data for the calculations described in Section A.5.1 and Section A.6.

Table A.4. Summary of all simulations performed in this work. (1 of 2)

Simulation	Steps	Assumptions
Simulation 1: Calculate solar cell performance **Section 6.2.1** **Section 6.2.2**	**1:** Calculate absorption profile of device by simulating the absorptance. **Input:** Refractive index of individual layers; Layer thickness (Figure 6.1 (b)). **Output:** Absorptance profile (Figure 6.1 (d)) as a function of active layer thickness and illumination direction. See Equation A.1 in Section A.2.	- Capacity of K-PHI anode (active layer) and PEDOT:PSS cathode scales linearly with thickness, when <3 µm.
	2: Calculate the photocurrent **Input:** Absorptance profile. **Output:** Photocurrent as a function of active layer (Figure 6.2 (c)) and collection layer thickness. See Equation 6.1. Charging time (Figure 6.2 (d)) and charging time ratio (Figure 6.2 (e)).	- Variable collection layer thickness. - IQE in collection layer is 100 % - For charging time: Constant photocurrent. - Fix illumination area to 1 µm*.

∗: Values extracted from measurements discussed in Section A.4 and our recently published proof-of-concept device.[18]

Table A.4. Summary of all simulations performed in this work. (2 of 2)

Simulation	Steps	Assumptions
Simulation 2: Calculate solar battery performance **Section 6.2.4**	**1:** Calculate the photocharging current. **Input:** Photocurrent (Table A.6). Utilize input of measured decaying photocurrent (Section A.5.1) to analyze dependence between photocurrent and charging state. **Output:** Photocharging current in dependence of initial photocurrent and charging state. See Equation A.8 in Section A.5.1.	- Fixed collection layer thickness to 10 nm - Fixed active layer thickness to 500 nm, HSM thickness to 119 nm, and device mass to 100 µg.* - Solar-to-output efficiency of 0.1 %†
	2: Simulate discharge to extract solar battery performance parameters *via* iterative solution of Equation A.12 simulating discharge.# **Input:** Photocharging current. Dark performance measured *via* electrochemical GCD experiments of a separated full-cell (Section A.4). See Table A.5. **Output:** Improved coulomb efficiency (see Equation A.12 in Section A.6) and round-trip efficiencies (see Equation 6.3 and Equation A.13 in Section A.6).	- Normalization *via* fofa (Section A.6.1).

∗: Values extracted from measurements discussed in Section A.4 and our recently published proof-of-concept device.[18]

†: A solar-to-output efficiency of 0.1 % was utilized, a common value for two-electrode bifunctional solar batteries.[21]

#: We calculate the iterative solution of Equation A.12 by using steps of 0.1 s and illumination intensities of 0.1 to 2 Sun in steps of 0.1 Sun (see Table A.6). In cases where the photocurrent exceeded the electric discharging current (occurred at illumination times >1.3 Sun), simulated discharging was aborted after 3 h.

Table A.5. Summary of performance measured *via* dark GCD measurements, which was used as an input for simulated discharging. Reproduced from Table A.2.

current (A kg^{-1})	extracted electric charge (Ah kg^{-1})
5.01	1.92
50.1	1.95
100	1.88
501	1.32

Photocurrent input was simulated as a function of illumination intensity, as discussed in Section A.2 and main text Section 6.2.1 and Section 6.2.2. Exemplary photocurrent values for rear side illumination are given in Table A.6.

Table A.6. Summary of illumination intensity and respective calculated photocurrent, which was used as an input for simulated discharging. Calculated for a device with a K-PHI and PEDOT:PSS respective thickness of 500 and 119 nm, illumination area of 1 cm^2, and illumination mode from the rear. See Table A.4 for further details on the calculation.

Illumination intensity (Sun)	Photocurrent rear illumination (A m^{-2}) (in brackets: (mA cm^{-2}))
0.1	0.403 (0.0403)
0.2	0.806 (0.0806)
0.3	1.21 (0.121)
0.4	1.61 (0.161)
0.5	2.02 (0.202)
0.6	2.42 (0.242)
0.7	2.82 (0.282)
0.8	3.23 (0.323)
0.9	3.63 (0.363)
1.0	4.03 (0.403)
1.1	4.43 (0.443)
1.2	4.84 (0.484)
1.3	5.24 (0.524)
1.4	5.64 (0.564)
1.5	6.05 (0.605)
1.6	6.45 (0.645)
1.7	6.85 (0.685)
1.8	7.26 (0.726)
1.9	7.66 (0.766)
2.0	8.06 (0.806)

A.7. References

(1) Gouder, A.; Jiménez-Solano, A.; Vargas-Barbosa, N. M.; Podjaski, F.; Lotsch, B. V. *Mater. Horiz.* **2022**, *9*, 1866–1877.

(2) Azizi, S.; Belhaj, M.; Zargouni, S.; Dridi, C. *Appl. Phys. A* **2017**, *123*, 475.

(3) Singh, V.; Kumar, T. *J. Sci. Adv. Mater. Devices* **2019**, *4*, 538–543.

(4) Weiher, R. L.; Ley, R. P. *J. Appl. Phys.* **1966**, *37*, 299–302.

(5) Chang, J.-F.; Huang, Y.-S.; Chen, P.-T.; Kao, R.-L.; Lai, X.-Y.; Chen, C.-C.; Lee, C.-C. *Opt. Express* **2015**, *23*, 14695.

(6) Chen, C.-W.; Hsiao, S.-Y.; Chen, C.-Y.; Kang, H.-W.; Huang, Z.-Y.; Lin, H.-W. *J. Mater. Chem. A* **2015**, *3*, 9152–9159.

(7) König, T. A. F.; Ledin, P. A.; Kerszulis, J.; Mahmoud, M. A.; El-Sayed, M. A.; Reynolds, J. R.; Tsukruk, V. V. *ACS Nano* **2014**, *8*, 6182–6192.

(8) Rubin, M. *Sol. Energy Mater.* **1985**, *12*, 275–288.

(9) Jiménez-Solano, A.; Galisteo-López, J. F.; Míguez, H. *Adv. Opt. Mater.* **2018**, *6*, 1700560.

(10) Szendrei-Temesi, K.; Jiménez-Solano, A.; Lotsch, B. V. *Adv. Mater.* **2018**, *30*, 1803730.

(11) Szendrei, K.; Jiménez-Solano, A.; Lozano, G.; Lotsch, B. V.; Míguez, H. *Adv. Opt. Mater.* **2017**, *5*, 1700663.

(12) Nayak, P. K.; Mahesh, S.; Snaith, H. J.; Cahen, D. *Nat. Rev. Mater.* **2019**, *4*, 269–285.

(13) Lau, V. W.-h.; Klose, D.; Kasap, H.; Podjaski, F.; Pignié, M.-C.; Reisner, E.; Jeschke, G.; Lotsch, B. V. *Angew. Chem. Int. Ed.* **2017**, *56*, 510–514.

(14) Lau, V. W.-h.; Moudrakovski, I.; Botari, T.; Weinberger, S.; Mesch, M. B.; Duppel, V.; Senker, J.; Blum, V.; Lotsch, B. V. *Nat. Commun.* **2016**, *7*, 12165.

(15) Schlomberg, H.; Kröger, J.; Savasci, G.; Terban, M. W.; Bette, S.; Moudrakovski, I.; Duppel, V.; Podjaski, F.; Siegel, R.; Senker, J.; Dinnebier, R. E.; Ochsenfeld, C.; Lotsch, B. V. *Chem. Mater.* **2019**, *31*, 7478–7486.

(16) Yang, W.; Godin, R.; Kasap, H.; Moss, B.; Dong, Y.; Hillman, S. A. J.; Steier, L.; Reisner, E.; Durrant, J. R. *J. Am. Chem. Soc.* **2019**, *141*, 11219–11229.

(17) Savateev, O. *Adv. Energy Mater.* **2022**, *12*, 2200352.

(18) Gouder, A.; Podjaski, F.; Jiménez-Solano, A.; Kröger, J.; Wang, Y.; Lotsch, B. V. *Energy Environ. Sci.* **2023**, DOI: 10.1039/d2ee03409c.

(19) Podjaski, F.; Kröger, J.; Lotsch, B. V. *Adv. Mater.* **2018**, *30*, 1705477.

(20) Sonmez, G. *Chem. Commun.* **2005**, 5251.

(21) Lv, J.; Xie, J.; Mohamed, A. G. A.; Zhang, X.; Wang, Y. *Chem. Soc. Rev.* **2022**, *51*, 1511–1528.

B

Supporting Information to Chapter 7

An Integrated Solar Battery based on a Charge Storing 2D Carbon Nitride

Contents

B.1. Morphological characterization 280
B.2. Electrochemical study of HTM materials 280
B.3. Activation & reset of solar battery samples 281
B.4. Kinetic analysis of charge storage mechanism 283
B.5. Additional analysis: Light charging and electric discharging 285
B.6. Additional analysis: Scaling of Power and Energy with Discharge Current 287
B.7. Shape of GCD measurements & chosen voltage window 288
B.8. Charge retention for delayed discharge 290
B.9. Solar cell performance comparison 1 sun & 365 nm LED 292
B.10.Comparison of solar battery performance with literature 294
B.11.References 295

B.1. Morphological characterization

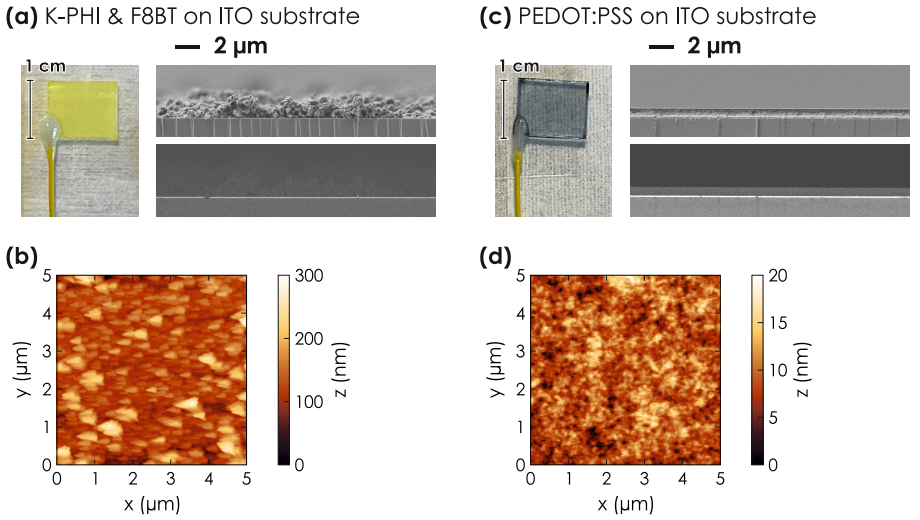

Figure B.1. Morphological characterization of films *via* SEM and AFM. (a) Characterization of the K-PHI film functionalized with F8BT (picture of a sample on the left) *via* SEM of a cross section. Secondary electron detector (right, top) and backscattered electron detector (ESB) (right, bottom) images are recorded, showing a rough surface with an average film thickness of ca. 1 µm. **(b)** AFM image of the film shown in (a). A Rough Mean Square (RMS) roughness of 35.8 nm is calculated. **(c)** Characterization of the PEDOT:PSS film *via* SEM of a cross section. Secondary electron detector (right, top) and ESB (right, bottom) images are recorded, showing a smooth surface with an average film thickness of ca. 0.6 µm. **(d)** AFM image of the film shown in (c). A RMS roughness of 2.59 nm is calculated.

B

B.2. Electrochemical study of HTM materials

The list of suitable hole transport materials (HTM) is vast, both for small molecule HTMs and conductive polymer HTMs. We chose multiple candidates based on their suitably positioned valence band potential and other desirable characteristics, such as conductivity, size or other functionalities (*e.g.*, a band gap, which could allow them HTM to participate as active material). Conductive polymers P3HT, PTB7TH, PVK, F8BT, and small molecule TPD, TCP, or TCTA HTMs were chosen and deposited onto K-PHI films (on a transparent conductive substrate (here ITO) *via* dip coating) *via* spin coating. A solution of HTM in chloroform (1 mg mL^{-1}) was prepared, spin coated at 2000 rpm for 30 s and subsequently annealed for 10 min at 80 °C on a hot plate.

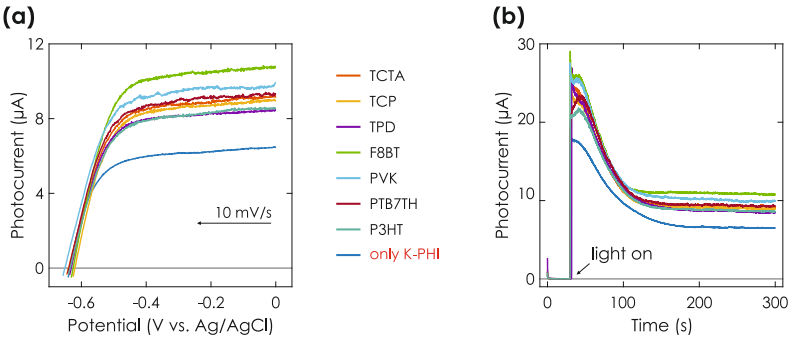

Figure B.2. Electrochemical characterization of K-PHI samples with different HTMs. (a) LSV measurements of K-PHI with respective HTMs in a 3-electrode configuration and under illumination. All HTM materials show a larger photocurrent than the K-PHI sample alone, with F8BT showing the largest improvement. **(b)** Photocurrent output, when applying a bias voltage of 0 V to the device. An initial large photocurrent is observed, which stabilizes after ca. 100 s onto a "steady state" photocurrent.

To evaluate the performance of HTM materials, the photocurrent at different potentials was evaluated in a 3-electrode CV measurement, in the presence of a sacrificial electron donor to replace the HSM and under illumination with 1 Sun. In Figure B.2 (a), the IV curves of the sample with different HTMs are shown. The potential is swept into the negative direction at a scan rate of $10\,\mathrm{mV\,s^{-1}}$. From 0 to about -0.4 V *vs.* Ag/AgCl, the photocurrent is very slowly decreasing due to a reducing driving force of the electron extraction from K-PHI. Subsequently, an open circuit potential (OCP) of approx. -0.65 V *vs.* Ag/AgCl can be measured for all samples. F8BT shows the largest photocurrents and has thus been chosen for the further development of the device.

B.3. Activation & reset of solar battery samples

Prior to each solar battery measurement, an activation measurement was performed to ensure comparability between different samples. An exemplary measurement routine is shown in Figure B.3.

First, a bias voltage of 0 V was applied under illumination for 5 min. This ensures that possible organic contaminations are oxidized by K-PHI. Subsequently, a CV was measured under illumination between 0 V and the OCP, (*i.e.*, as soon as a cathodic current is observed). The idea behind this measurement is to control whether the sample shows the typical IV curve and is not short circuited (e.g., through accidental pinhole formation during sample preparation). Finally another CV measurement

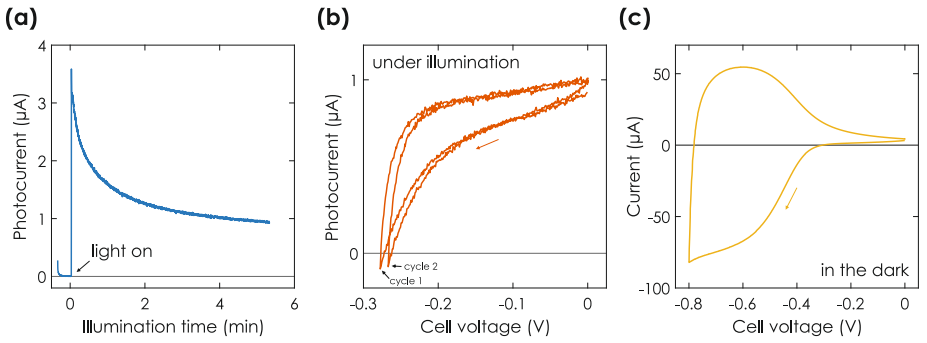

Figure B.3. Activation measurement routine. (a) Photocurrent when applying a bias voltage of $0\,\mathrm{V}$ to the solar battery device. The bias was applied for $5\,\mathrm{min}$. **(b)** CV under illumination and between $0\,\mathrm{V}$ and OCP, cycled twice with a scan rate of $10\,\mathrm{mV\,s^{-1}}$. **(c)** CV in the dark, cycled once with a scan rate of $50\,\mathrm{mV\,s^{-1}}$.

was carried out in the dark between 0 and $-0.8\,\mathrm{V}$ to check that both K-PHI and PEDOT:PSS work as intended when charged electrically in the dark.

Subsequently, a reset measurement was performed to remove all charges left on the device, *i.e.*, electrons from K-PHI and holes from PEDOT:PSS, and to ensure that the sample was in a state that is comparable to other samples at different stages of the measurement. This measurement was performed both after the activation discussed in the paragraph above and after GCD measurements. An exemplary measurement is shown in Figure B.4.

The concept behind this measurement is to remove unwanted charges from the electrodes individually, *i.e.*, first remove holes from PEDOT:PSS, then electrons from K-PHI. It ensures that the charge state (or "oxidation state") of K-PHI and PEDOT:PSS is in balance prior to each measurement. For this, only one electrode was connected as working electrode, and a bias potential of $0\,\mathrm{V}$ *vs.* Ag/AgCl was applied against a reference electrode and a counter electrode which were immersed in the same electrolyte as the sample. The potential was applied until the current reached a value of $<50\,\mathrm{nA}$. This measurement was first done for PEDOT:PSS and then for K-PHI.

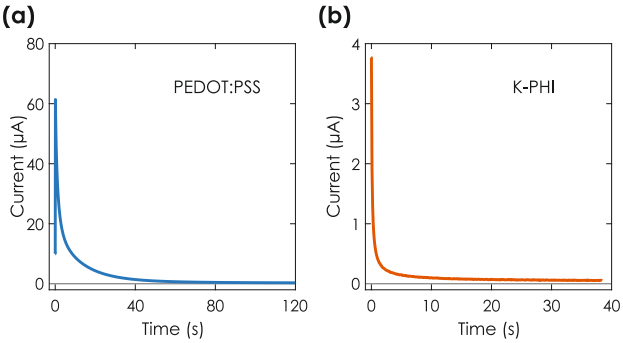

Figure B.4. Reset measurement routine. An exemplary reset measurement is shown for PEDOT:PSS **(a)** and subsequently K-PHI **(b)**. A bias potential was applied to the respective electrodes of the device and a bias potential of 0.1 V *vs.* Ag/AgCl (PEDOT:PSS) and 0 V *vs.* Ag/AgCl (K-PHI) was applied. The measurement was stopped as soon as the current reached a value <50 nA.

B.4. Kinetic analysis of charge storage mechanism

In this section, we present a more detailed kinetic analysis of the charge storage mechanism of the two half-cells, (*i.e.*, K-PHI and PEDOT:PSS; measured in a 3 - electrode setup in a degassed 0.1 M KCl electrolyte against an Ag/AgCl reference electrode and Au counter electrode) as well as the full-cell *via* a scan rate dependent CV analysis. Results are shown in Figure B.5.

We will first discuss the half-cells. K-PHI shows its very specific CV shape (Figure B.5 (a), the curve at more negative potentials). When extracting the current at the anodic sweep peak and plotting it against the scan rate, the data can be fitted according to the equation in the inset of Figure B.5 (c). The exponent b of 0.65 unveils largely faradaic or pseudocapacitive charge storage kinetics,[1,2] in line with our previously reported results.[3] On the other hand, when extracting current of the PEDOT:PSS measurement at a potential of 0 V *vs.* Ag/AgCl, the fit reveals a much more linear dependence of current with scan rate (b value of 0.98). Since this is more reminiscent of a capacitive kinetic signature,[4] but the charge storage mechanism of PEDOT:PSS is known to be faradaic, we link the kinetic behavior to pseudocapacitive charge storage,[1,2,5,6] as widely reported for PEDOT:PSS.[7–10]

Next, when looking at the scan rate dependence of peak current of the full-cell (Figure B.5 (b)) and fitting the data (Figure B.5 (c)), a b value of 0.62 can be calculated, indicating a faradaic or pseudocapacitive charge storage mechanism. Note that this value is similar to the K-PHI half-cell, suggesting that the kinetics of charge storage of the full-cell is dominated by K-PHI photoanode, which thus also limits the

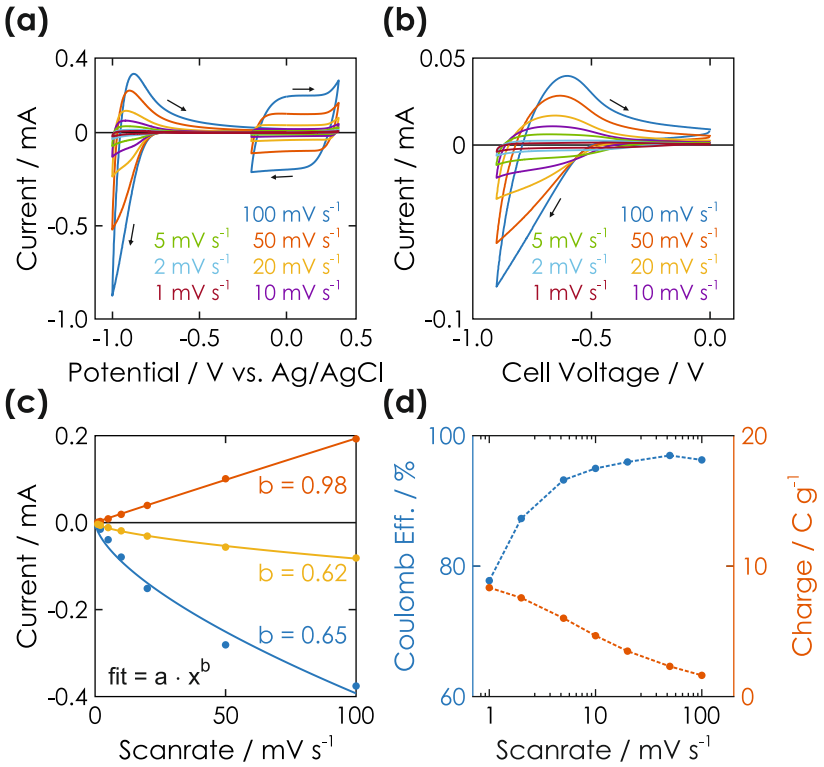

Figure B.5. Kinetic study *via* CV and with different scan rates. (a) Study of K-PHI between 0.0 and $-1.0\,\mathrm{V}$ *vs.* Ag/AgCl, and PEDOT:PSS between 0.5 and $-0.1\,\mathrm{V}$ *vs.* Ag/AgCl for different scan rates. **(b)** Study of a full-cell solar battery sample between 0.0 and $0.9\,\mathrm{V}$ *vs.* Ag/AgCl for different scan rates. **(c)** Extracted current of half-cells ((a): K-PHI in blue, extracted at $-0.9\,\mathrm{V}$ *vs.* Ag/AgCl; PEDOT:PSS in red, extracted at $0\,\mathrm{V}$ *vs.* Ag/AgCl) and full-cell ((b), at $-0.9\,\mathrm{V}$, yellow) in dependence of the scan rate. A fit was calculated using the formula in the inset.[1] **(d)** Extracted charge and coulombic efficiencies from CV full-cell measurements shown in (b). Normalized onto mass of K-PHI, HTM, and PEDOT:PSS.

performance of the device. When looking at the extracted charge (Figure B.5 (d)) as a function of scan rate, we observe that with slower scan rates more charge can be extracted. This indicates that the amount of charge is limited by the charging kinetics, *i.e.*, a very slow charging and discharging process maximizes the effective capacity – analogous to GCD measurements discussed in the main text in Figure 7.3 (d). When looking at the coulombic efficiency as a function of scan rate of the full-cell (Figure B.5 (d)), we see a maximum of $90\,\%$ at a scan rate of $50\,\mathrm{mV\,s^{-1}}$. For both larger and smaller scan rates the coulombic efficiency decreases. We explain this with the existence of an optimum scan rate determined by kinetic limitations for

larger scan rates and increased self-discharge for smaller scan rates, as previously reported for the K-PHI half-cell.[3]

B.5. Additional analysis: Light charging and electric discharging

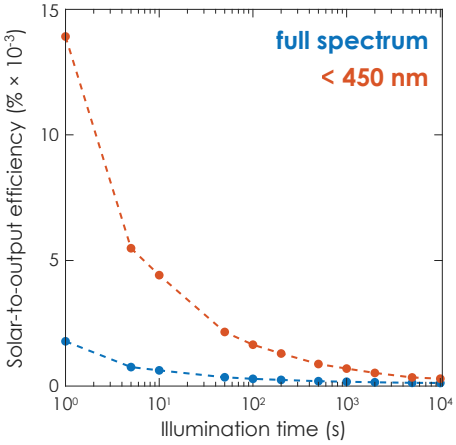

Figure B.6. Calculated solar-to-output efficiency. The solar-to-output efficiency was calculated from light charging and electric discharging measurements shown in Figure B.7 as a function of illumination time. The light energy was calculated according to AM1.5 G 1 Sun illumination, with either the full spectrum or only wavelengths below the bandgap (2.7 eV, corresponding to 450 nm).

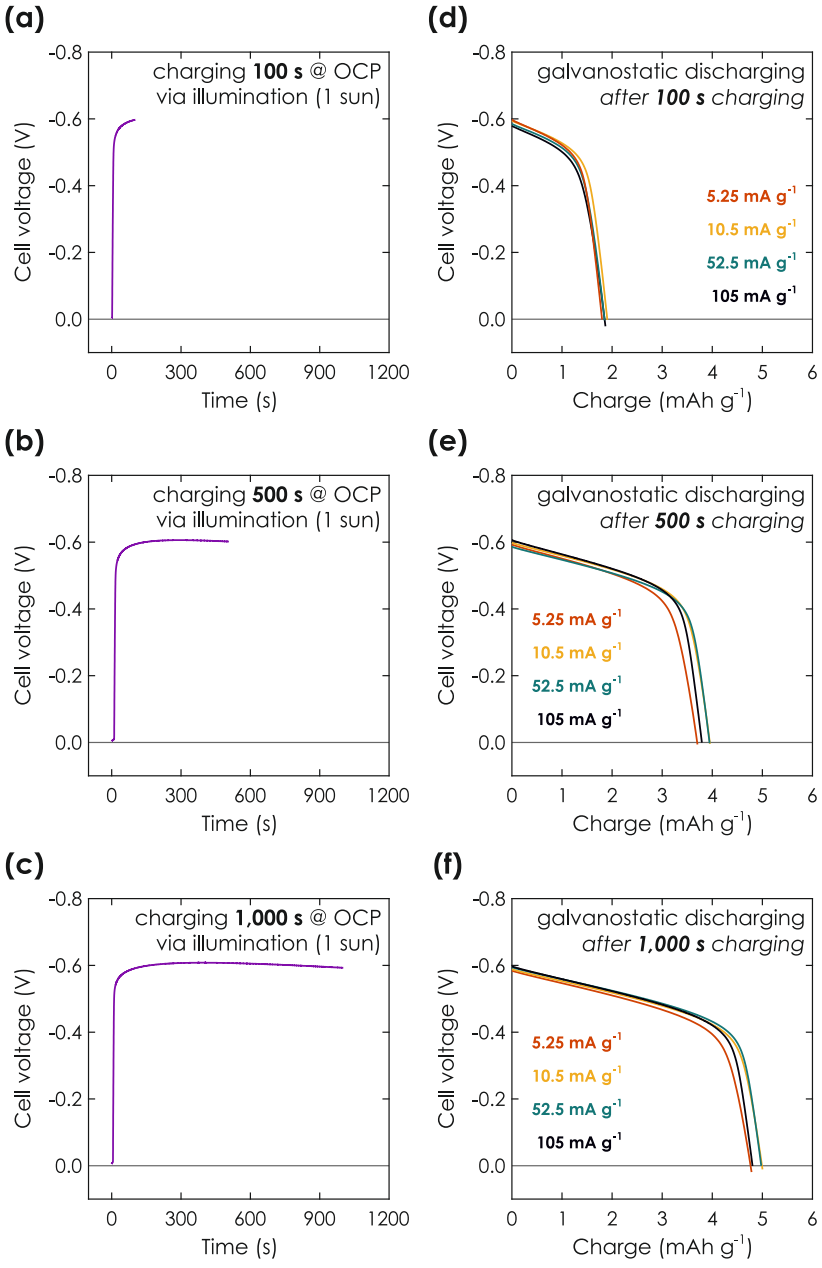

Figure B.7. Kinetic study of light charging and subsequent immediate electric discharging, discussed in the main text in Section 7.2.2.2. (a) to **(c)** Charging of a solar battery sample *via* 1 Sun illumination for three different illumination times. The solar battery sample is kept under OCP conditions to prevent any electric current during the light charging process. A photopotential of $-0.6\,\mathrm{V}$ develops for all illumination times. **(d)** to **(f)** Respective electric discharging in the dark and with different currents given in the legend.

B.6. Additional analysis: Scaling of Power and Energy with Discharge Current

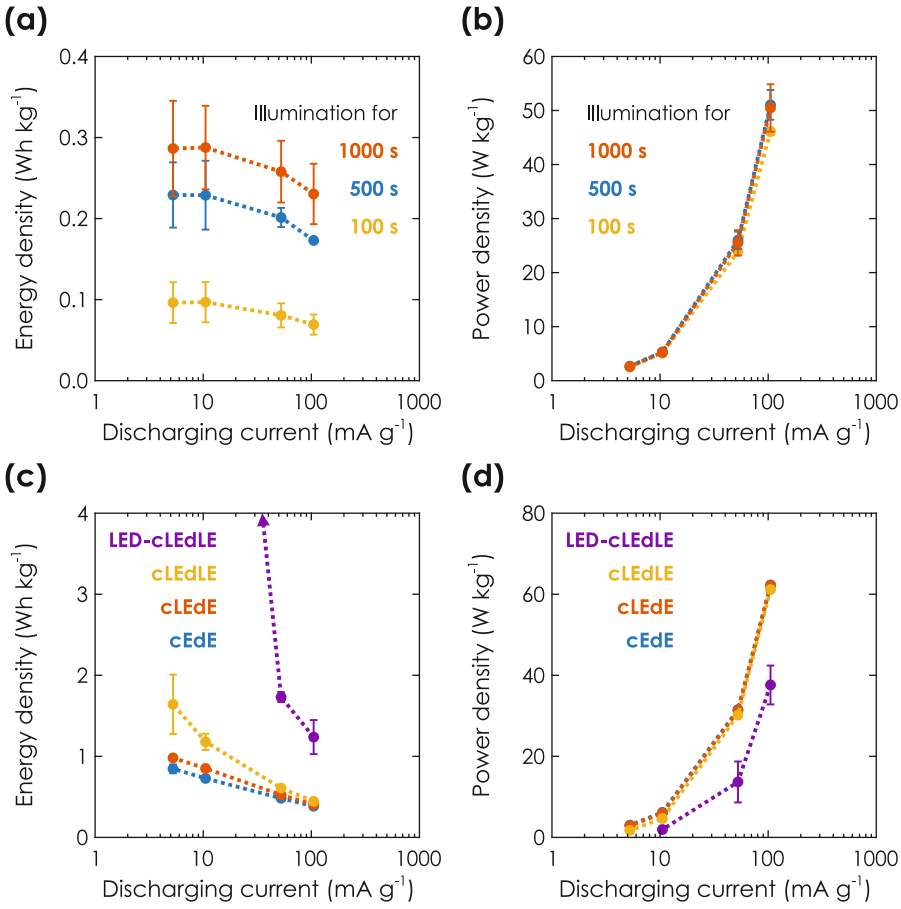

Figure B.8. Additional analysis to main text Figure 7.2 & Figure 7.3. (a) and **(b)** Charging of a solar battery sample *via* 1 Sun illumination and subsequent electric discharging in the dark at different discharging currents. Scaling of energy (a) and average power (b) with discharging current. The corresponding Ragone plot is shown in the main text in Figure 7.2 (f). **(c)** and **(d)** Charging of a solar battery sample *via* GCD in the dark (cEdE), charging under illumination (cLEdE) or both charging and discharging under illumination (cLEdLE when illuminated with the solar simulator and 1 Sun ($100\,\mathrm{mW\,cm^{-2}}$), or LED-cLEdLE when illuminated with an LED at 365 nm ($100\,\mathrm{mW\,cm^{-2}}$)). Scaling of energy (a) and Power (b) with discharging current. The corresponding Ragone plot is shown in the main text in Figure 7.3 (f).

B.7. Shape of GCD measurements & chosen voltage window

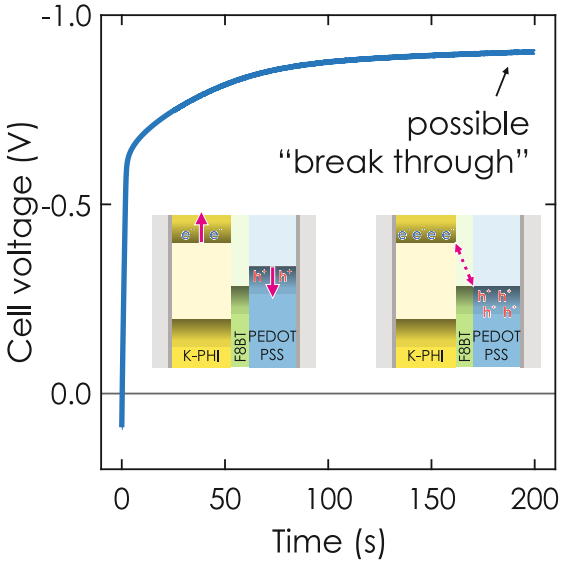

Figure B.9. Analysis of shape of GCD curve during charging. GCD measured under analogous conditions as electric and light assisted electric GCD performance analysis discussed in the main text in Section 7.2.2.3 and shown in Figure 7.3. The only difference is that the abort condition of charging is not the upper voltage vertex of 0.8 V. Instead, the measurement is stopped after 200 s. Inset shows normal charging (left) and a proposed short circuit or "breakthrough" mechanism (right).

B

In the following we will discuss the rationale behind the chosen GCD voltage window. The shape of the charging curve for a typical battery shows an initial fast increase to a relatively flat plateau in which the battery experiences charging. Subsequently after reaching a fully charged state, the potential increases rapidly again.[1,4] Conversely, in our solar battery device we do not observe this second rapid increase. Instead, the plateau seems to flatten out (Figure B.9). We propose a possible mechanism for this behavior in the inset in Figure B.9: Electrons from K-PHI can reach holes from PEDOT:PSS, a process that is normally inhibited by the HTM F8BT and termed by us as "breakthrough" voltage. This is possible as soon as the potential of hole storage in PEDOT:PSS (*i.e.*, the valence band of PEDOT:PSS) gets more negative than the valence band of F8BT. Consequently, holes are being injected from PEDOT:PSS into F8BT and can then recombine with electrons from K-PHI.

Note also that while photocharging of the solar battery occurs at a potential of

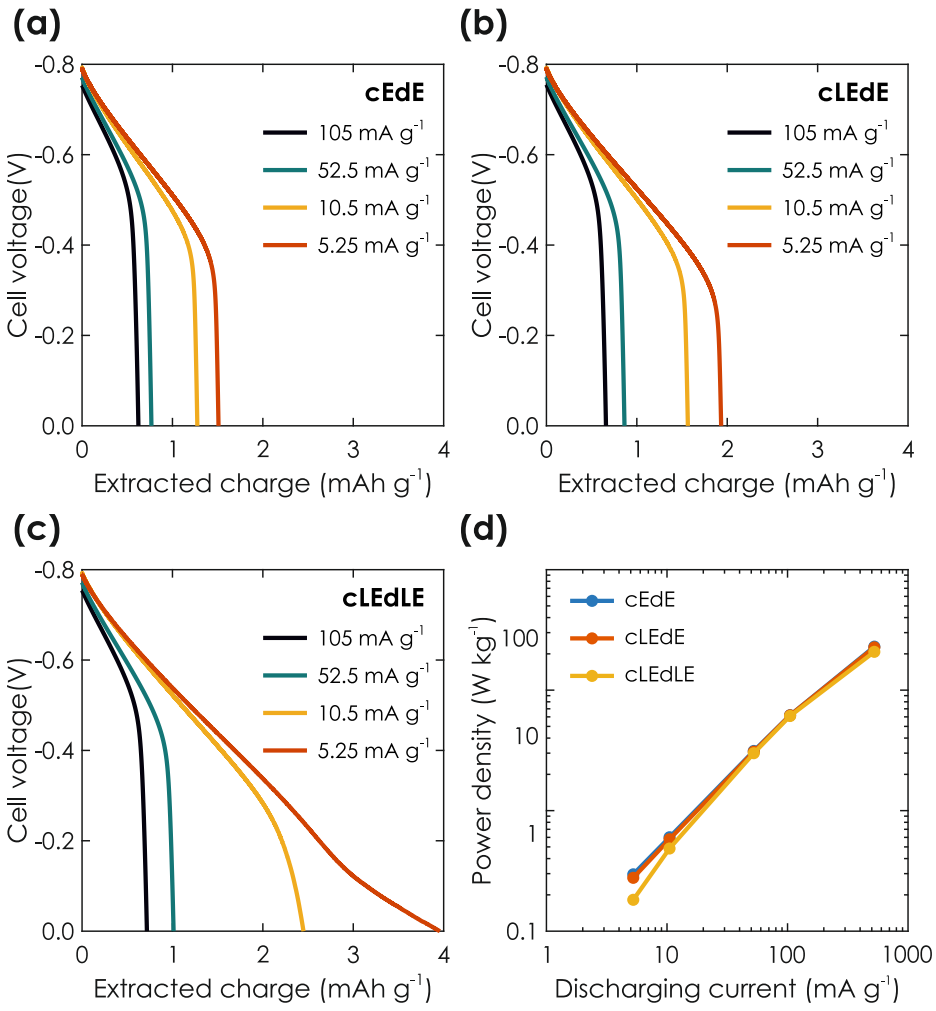

Figure B.10. Analysis of shape of GCD curve during discharging. (a) to **(c)** GCD discharge profiles with different discharge currents and in the dark (cEdE) (a), illuminated during only charging (cLEdE) (b) or illuminated during both charging and discharging (cLEdLE) (c), measured in analogous conditions than measurements shown in the main text in Figure 7.3 (d), (e), (f). **(d)** Power density of solar battery samples when GCD is performed in cEdE (blue; extracted from (a); hidden behind red curve), cLEdE (red; extracted from (b)), or cLEdLE (yellow; extracted from (c)). Power output reproduced from the main text Figure 7.3 (f).

0.6 V (see main text Figure 7.2 (b) and (c)), we reach a higher voltage of 0.8 V before the "break-through" voltage is reached. We explain this by the different charging mechanisms of light charging *via* an "internal" photocurrent and electric charging *via* applying the "external" charging current. While the first charges the K-PHI film

most likely more in the bulk and close to the junction to the HTM, the latter charges the film *via* the substrate. The low conductivity of K-PHI produces an iR drop across the film, which in return reduces the voltage at which the device is charged and subsequently discharged. This means: K-PHI charging starts at 0.6 V, and charges can be theoretically stored on the device until it reaches the "break-through" voltage. However, while electric charging with a very small current should in theory stay at a similar potential than light charging and yield a similar capacity (note the bend in the cell voltage at ca. 0.6 V, when charged electrically as shown in Figure B.9), this current would produce a much smaller power output. Hence, we chose 0.8 V as a compromise for electric charging, which – while charging the device unevenly, (*i.e.*, the parts of K-PHI close to the substrate are charged more than the bulk) – produces a reasonably high power and energy output at currents between 5.25 and 105 mA g^{-1}. Note that in theory the capacity of K-PHI is thus underestimated in this work.

Next, we will address the shape of GCD discharge curves under different illumination conditions as shown in Figure B.10 (a-c). Conditions are analogous to measurements shown for GCD in the main text in Figure 7.3 (d)-(f). Note that for cLEdLE and slower currents after discharging the plateau, the cell voltage does not rapidly decrease to zero but rather shows a tail. This is due to the photocurrent generated during illumination which simultaneously charges the device during electric discharging. It affects small electric discharging currents more since they are in the range of the photocurrent, as discussed in the main text. The power density output is thus affected and decreases for small discharging currents when discharged under illumination (Figure B.10 (d)).

B.8. Charge retention for delayed discharge

An important feature of solar battery device is its charge retention time, *i.e.*, how fast the solar battery self-discharges. To analyze this, we perform a measurement analogous to light charging and electric discharging measurements discussed in the main text in Section 7.2.2.2, but fix the illumination time onto 1000 s and instead delay dark discharging (10.5 mA g^{-1}). The resulting charge is shown in Figure B.11 (a) blue data points. The charging state describing how much charge is left after the delayed discharging is shown in Figure B.11 (b). We observe an initial fast decay of the charging state which subsequently levels out. After 500 and 1000 s, a respective 63 and 55 % of the initial charge was left on the device. We also analyze de-

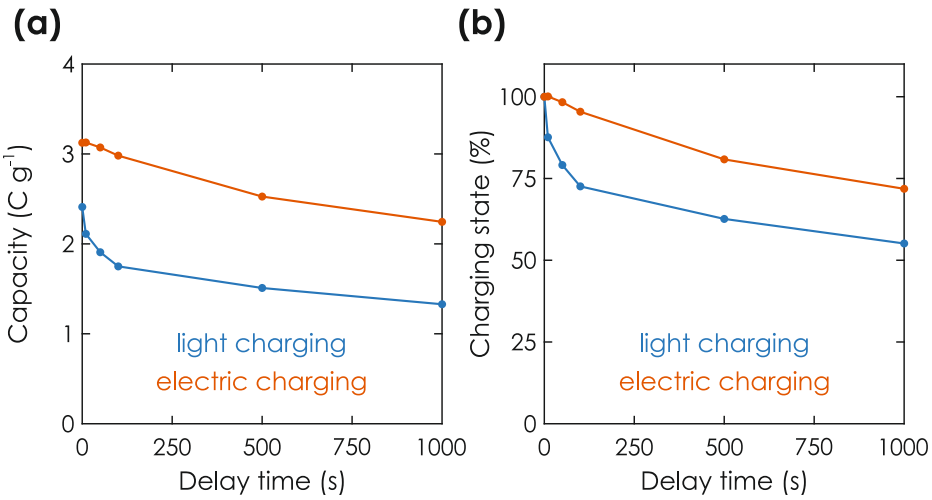

Figure B.11. Analysis of charge retention. **(a)** Extracted charge from a solar battery, which was charged *via* illumination at OCP and discharged in the dark with $10.5\,\mathrm{mA\,g^{-1}}$ (blue), or charged and discharged in the dark (between a cell voltage of 0 V (discharged) and 0.8 V (charged)) with $10.5\,\mathrm{mA\,g^{-1}}$ (red). The subsequent electric discharge in the dark ($10.5\,\mathrm{mA\,g^{-1}}$) was delayed as shown in the Figure. **(b)** Extracted charge retention from (a), normalized against the extracted charge without any time delay before the discharge.

layed discharge when charged not with light but with an electric charging current ($10.5\,\mathrm{mA\,g^{-1}}$) in the dark (Figure B.11 (a) and (b) red data points). Interestingly, while under the chosen conditions a larger initial charge was present on the device ($3.12\,\mathrm{C\,g^{-1}}$ for electric charging *vs.* $2.41\,\mathrm{C\,g^{-1}}$ for light charging), a delayed discharge decreases the charge output less than for light charging (after 500 and 1000 s, a respective 81 and 72 % of the initial charge was left on the device).

We rationalize the self-discharge with issues arising from sample preparation, such as pinholes, or more generally, insufficiently charge selective HTM performance to separate charges from the cathode and anode efficiently. Electrons and holes can thus slowly recombine *via* the internal layer, and discharge the system from the inside, *i.e.*, by the electrode material adjacent to the HTM. The faster self-discharge from light charging can be explained with light charging occurring more in the bulk of K-PHI and electric charging occurring more close to the junction to the substrate. Since the former charges K-PHI closer to the junction of the HTM and due to the low conductivity of K-PHI, light charging produces a slightly faster self-discharge. In the electrically charged case, however, the material adjacent to the contact is charged first, thus hindering charge recombination through the material in device volume.

B.9. Solar cell performance comparison 1 sun & 365 nm LED

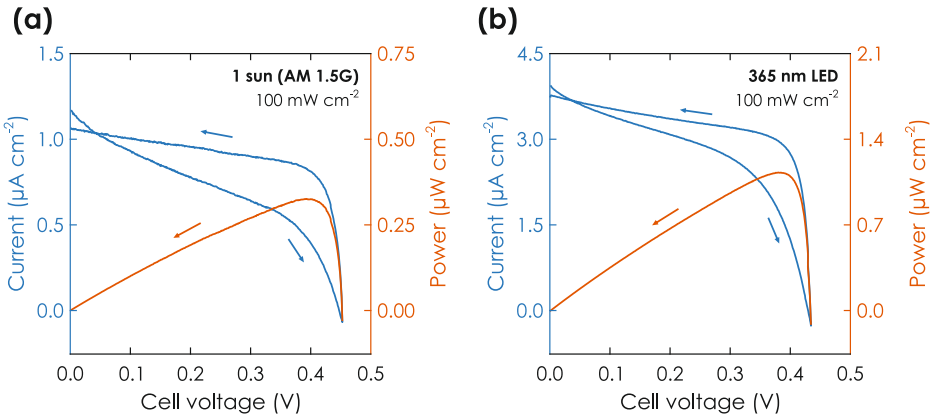

Figure B.12. Comparison of IV curves with different light sources. (a) Current-voltage (blue) and power (red) curves ($10\,\mathrm{mV\,s^{-1}}$) of a solar battery sample in solar cell mode, illuminated with 1 Sun. Reproduced from main text Figure 7.2 (a). **(b)** Current-voltage (blue) and power (red) curves ($10\,\mathrm{mV\,s^{-1}}$) of a solar battery sample in solar cell mode, illuminated with a 365 nm LED ($100\,\mathrm{mW\,cm^{-2}}$; bandwidth of ca. 10 nm).

We discuss operation of the solar battery device in solar cell mode extensively in main text Section 7.2.2.1. Two different illumination sources are utilized for measurements presented in this work: Either artificial sunlight (1 Sun) with AM 1.5 G standard (see Section 7.4 for details) to provide real-world illumination conditions for operation of the solar battery, or an 365 nm LED (ca. 360 to 375 nm) to provide light which is below the bandgap of K-PHI (450 nm). Both light sources were operated at the same power setting ($100\,\mathrm{mW\,cm^{-2}}$). IV and power curves are shown in Figure B.12 and performance parameters are summarized in Table B.1. Notably, the shape of IV and power curves looks very alike and open-circuit potential, potential at which maximum power is provided as well as the *FF* are very similar. However, as expected short-circuit current is significantly higher when operated with the LED (277 %) and the device produces much more power (248 %).

Table B.1. Performance parameter of IV curves. Summary of performance parameters of current-voltage and power curves of the solar battery, when illuminated either with artificial sunlight or a 365 nm LED. The *FF* is calculated *via* the backward sweep (OCP to 0 V) from open circuit potential (U_{OCP}), short circuit current (I_{sc}), and potential (U_{Pmax}) as well as current (I_{Pmax}) at which the device produces maximum power (P_{max}). IV curves are shown in Figure B.12.

Illumination mode	U_{OCP} (V)	U_{Pmax} (V)	I_{sc} (µA cm^{-2})	I_{Pmax} (µA cm^{-2})	P_{max} (µW cm^{-2})	FF
1 Sun (100 mW cm^{-2})	0.45	0.39	1.07	0.828	0.326	0.68
365 nm LED (100 mW cm^{-2})	0.43	0.38	3.78	2.98	1.13	0.69

B.10. Comparison of solar battery performance with literature

Table B.2. Comparison of performance of several different solar battery materials. $\eta_{conv.}$ gives the solar-to-output efficiency defined as light energy input divided by energy from electric discharging, and $\eta_{roundt.}$ gives the additional roundtrip efficiency upon illumination, defined as energy from electric charging (under illumination) divided by energy from electric discharging.

Photo electrode	Counter electrode	Electrolyte	Battery type	$\eta_{conv.}$ (%)	η_{roundt} (%)	Cycling stability	Year Ref
Photoanode design							
K-PHI anode	PEDOT:PSS cathode	F8BT solid	battery	0.012*	94.1	50	*This work*
F8BT anode	ITO	Na_2SO_4/PVA gel	super capacitor	0.0017	-	-	2021 [11]
Na_xMoO_3 anode	MnO_2 cathode	Na_2SO_4 aqueous	half flow battery	-	-	8	2017 [12]
TiO_2@WO_3 anode#	I^-/I_3^- Pt cathode	I^-/I_3^- propylene carbonate	half flow battery#	-	-	-	2019 [13]
TiO_2@carbon nitride anode	I^-/I_3^- cathode	I^-/I_3^- acetonitrile	half flow battery#	-	-	-	2021 [14]
Photocathode design							
Perovskite† cathode	Li metal anode	$LiPF_6$	Li-ion battery	0.034	-	10	2018 [15]
TiO_2/Fe_2O_3 cathode	Li metal anode	$LiCF_3SO_3$ in TEGDME	Li-O_2 battery	-	86	100	2020 [16]
V_2O_3/P3HT/rGO cathode	Li metal anode	LiTFSI	Li-ion battery	0.22	57	35	2021 [17]
V_2O_3/P3HT/rGO cathode	Zn metal anode	$Zn(CF_3SO_3)_2$ aqueous	Zn-ion battery	1.2	-	25	2020 [18]

*: for illumination with AM1.5 G, when only taking light below the bandgap into account (<450 nm). For full AM1.5 G spectrum: 0.002 %. See Section B.5 for details.

#: bifunctional composite electrode. Half flow battery means that the cathopde is not a solid electrode but rather an electrolyte.

†: $(C_6H_9C_2H_4NH_3)_2PbI_4$ 2D perovskite, abbreviated as CHPI.

B.11. References

(1) Fleischmann, S.; Mitchell, J. B.; Wang, R.; Zhan, C.; Jiang, D.-e.; Presser, V.; Augustyn, V. *Chem. Rev.* **2020**, *120*, 6738–6782.

(2) Augustyn, V.; Simon, P.; Dunn, B. *Energy Environ. Sci.* **2014**, *7*, 1597.

(3) Podjaski, F.; Kröger, J.; Lotsch, B. V. *Adv. Mater.* **2018**, *30*, 1705477.

(4) Shao, Y.; El-Kady, M. F.; Sun, J.; Li, Y.; Zhang, Q.; Zhu, M.; Wang, H.; Dunn, B.; Kaner, R. B. *Chem. Rev.* **2018**, *118*, 9233–9280.

(5) Costentin, C.; Savéant, J.-M. *Chem. Sci.* **2019**, *10*, 5656–5666.

(6) Costentin, C.; Porter, T. R.; Savéant, J.-M. *ACS Appl. Mater. Interfaces* **2017**, *9*, 8649–8658.

(7) Sun, K.; Zhang, S.; Li, P.; Xia, Y.; Zhang, X.; Du, D.; Isikgor, F. H.; Ouyang, J. *J. Mater. Sci. Mater. Electron.* **2015**, *26*, 4438–4462.

(8) Bryan, A. M.; Santino, L. M.; Lu, Y.; Acharya, S.; D'Arcy, J. M. *Chem. Mater.* **2016**, *28*, 5989–5998.

(9) Volkov, A. V.; Wijeratne, K.; Mitraka, E.; Ail, U.; Zhao, D.; Tybrandt, K.; Andreasen, J. W.; Berggren, M.; Crispin, X.; Zozoulenko, I. V. *Adv. Funct. Mater.* **2017**, *27*, 1700329.

(10) Sellam, N.; Hashmi, S. A. *ACS Appl. Mater. Interfaces* **2013**, *5*, 3875–3883.

(11) Dong, W. J.; Cho, W. S.; Lee, J.-L. *ACS Appl. Mater. Interfaces* **2021**, *13*, 22676–22683.

(12) Lou, S. N.; Sharma, N.; Goonetilleke, D.; Saputera, W. H.; Leoni, T. M.; Brockbank, P.; Lim, S.; Wang, D.-W.; Scott, J.; Amal, R.; Ng, Y. H. *Adv. Energy Mater.* **2017**, *7*, 1700545.

(13) Wang, Z.; Chiu, H.-C.; Paolella, A.; Zaghib, K.; Demopoulos, G. P. *ChemSusChem* **2019**, *12*, 2220–2230.

(14) He, L.; Tang, X.; Li, Y.; Zhang, L.; Cao, G. *Adv. Energy Sustainability Res.* **2021**, *2*, 2100111.

(15) Ahmad, S.; George, C.; Beesley, D. J.; Baumberg, J. J.; De Volder, M. *Nano Lett.* **2018**, *18*, 1856–1862.

(16) Li, M.; Wang, X.; Li, F.; Zheng, L.; Xu, J.; Yu, J. *Adv. Mater.* **2020**, *32*, 1907098.

(17) Boruah, B. D.; Wen, B.; De Volder, M. *Nano Lett.* **2021**, *21*, 3527–3532.

(18) Boruah, B. D.; Mathieson, A.; Wen, B.; Feldmann, S.; Dose, W. M.; De Volder, M. *Energy Environ. Sci.* **2020**, *13*, 2414–2421.

C

Supporting Information to Chapter 8

Photomemristive sensing via charge storage in 2D carbon nitrides

Contents

C.1. Material and thin film analysis . . . 298

C.1.1. Molecular structure and optical analysis . . . 298

C.1.2. Structure Analysis of K-PHI Films . . . 299

C.2. K-PHI as a direct amperometric PEC sensor . . . 301

C.3. Electrochemical self-cleaning of thin films . . . 303

C.4. Normalizing coulometric readout measurements . . . 304

C.5. Fitting of the sensor curves . . . 305

C.5.1. Potentiometric fitting . . . 308

C.5.2. Impedimetric fitting . . . 312

C.5.3. Coulometric fitting . . . 315

C.5.4. Colorimetric fitting . . . 318

C.5.5. Fluorometric fitting . . . 320

C.6. Additional electrochemical analysis of memristive properties of K-PHI films . . . 323

C.7. Additional optical analysis of memristive properties of K-PHI particles . 324

C.7.1. Influence of particle size . . . 324

C.7.2. Dependence on illumination time . . . 327

C.7.3. Delayed sensor information readout . . . 327

C.7.4. Negligible invasive nature of the memristive state readout . . . 328

C.7.5. Schematic representation of the PL characterization process by the quenched PL emission 329
C.8. References 330

C.1. Material and thin film analysis

C.1.1. Molecular structure and optical analysis

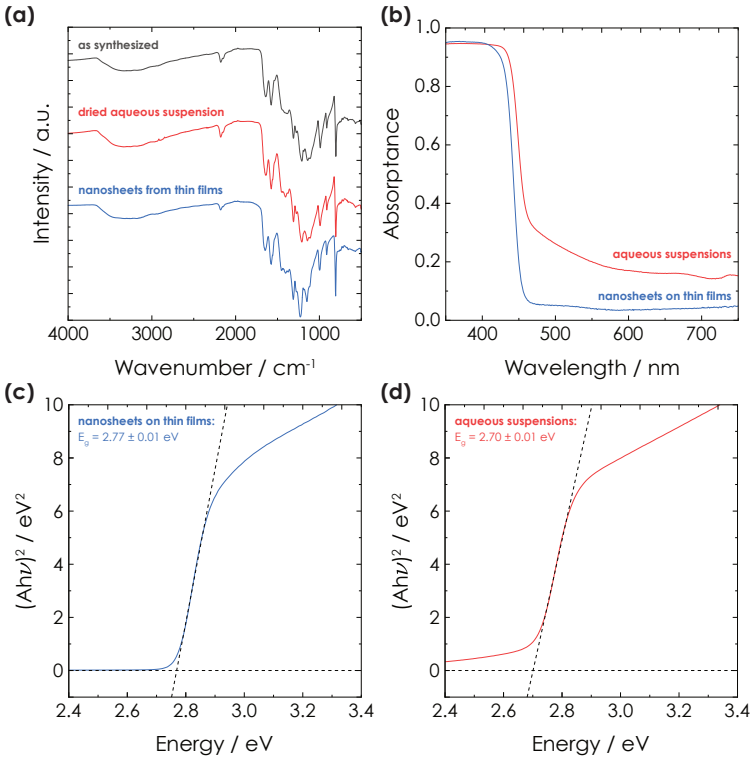

Figure C.1. Structural and optical characterization. (a) Fourier Transformed Infrared spectroscopy (FT-IR) characterization of K-PHI as-prepared, as dried nanosheets from aqueous suspension and scratched off from K-PHI nanosheet films on FTO. The spectra are normalized to the characteristic heptazine vibration at $815\,\mathrm{cm}^{-1}$. No significant changes in the structure of the material are observed. The characteristic NCN-stretching-signal indicating possible hydrolysis at $2180\,\mathrm{cm}^{-1}$ for K-PHI does not change significantly.[1] **(b)** Absorptance spectra of K-PHI as nanosheets deposited onto FTO and aqueous suspensions ($3\,\mathrm{mg\,mL}^{-1}$). **(c)** and **(d)** Tauc plot of K-PHI nanosheets deposited onto a FTO film (c) and in an aqueous suspension (d). It is in agreement with the reported literature bandgap value of K-PHI.[2]

C

C.1.2. Structure Analysis of K-PHI Films

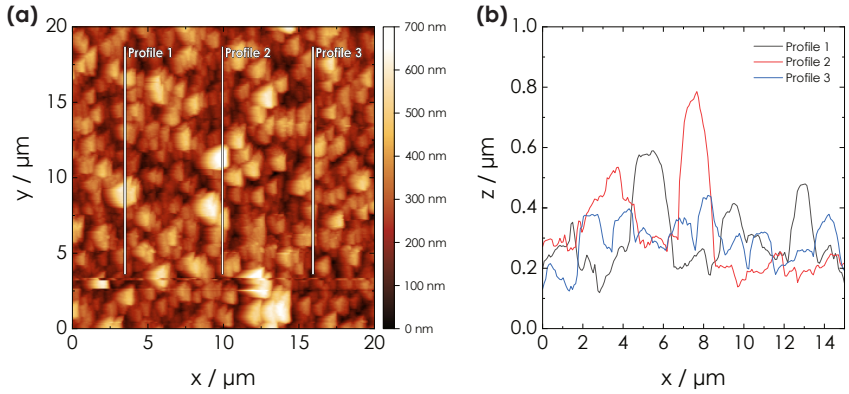

Figure C.2. AFM characterization of thin films. (a) AFM image for a K-PHI thin film sensor. The surface has a rather large roughness with a RMS roughness of 110 nm. Three profiles were extracted for further analysis along the lines shown within the picture. **(b)** Height profiles alongside the lines shown in (a).

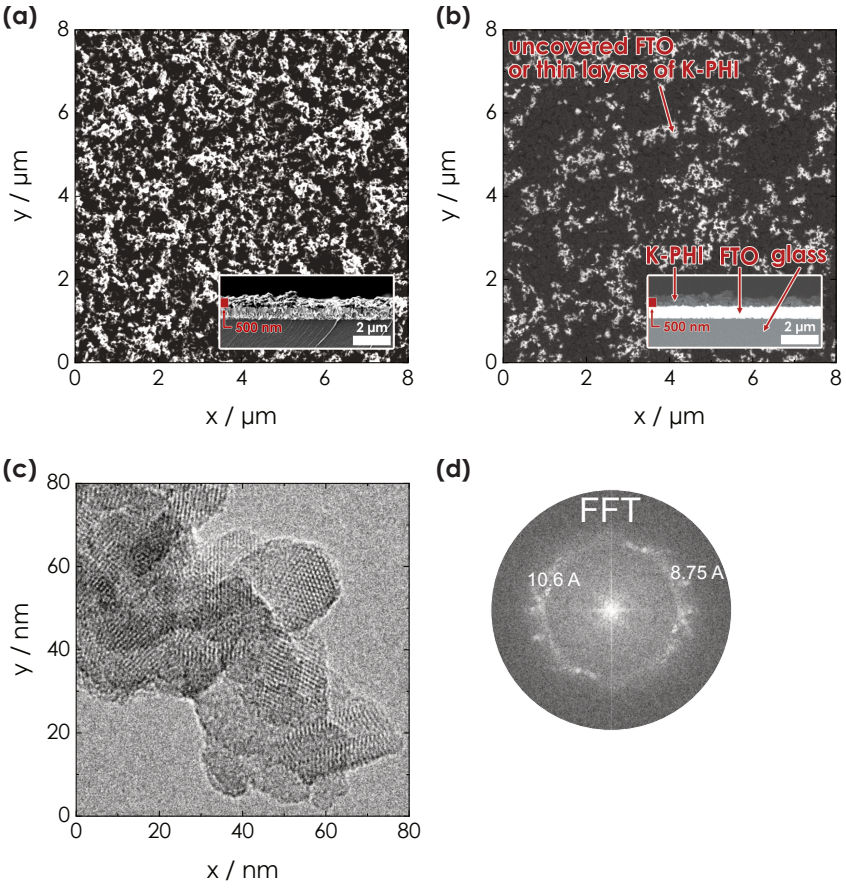

Figure C.3. SEM and TEM characterization. (a) SEM images for a K-PHI thin film sensor *via* the secondary electron detector showing irregular surface morphology below the µm-scale. The inset shows the cross section of the film *via* the same detector. **(b)** SEM image of the same spot shown in (a) visualized by the ESB. The bright parts correspond to either uncovered FTO parts or thin layers of K-PHI through which the FTO is still visible, and the dark parts correspond to thicker layer areas. The inset shows again the cross section of the film (ESB detector). The FTO layer on top of the glass is clearly visible. The dark layer deposited on top of the FTO represents K-PHI. **(c)** TEM images of K-PHI particles, showing the contours of crystalline nanoparticles with lateral dimensions ranging from 20 to 60 nm. **(d)** FFT image of K-PHI particles shown in (c).

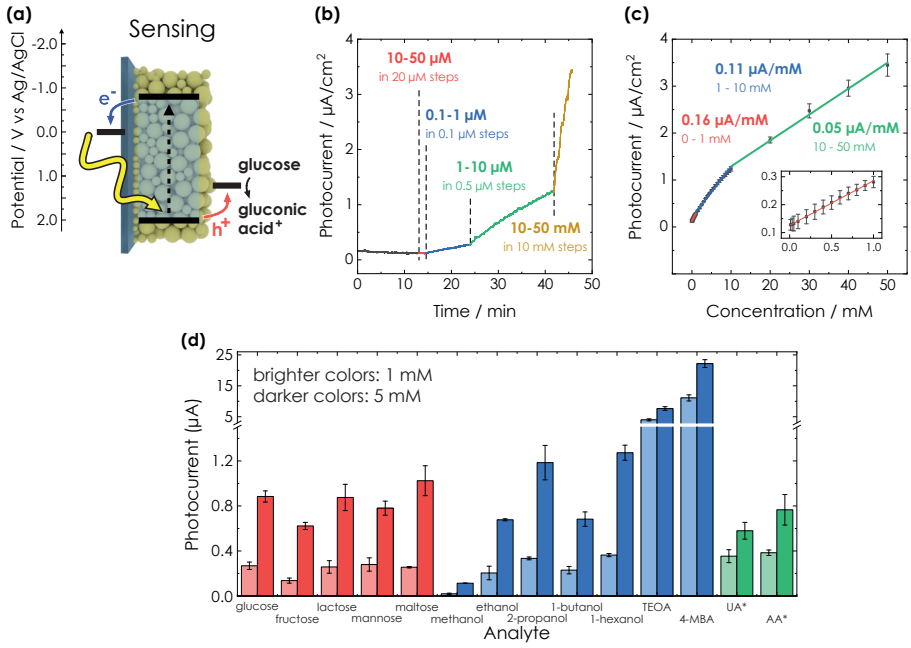

Figure C.4. K-PHI as a direct amperometric PEC sensor. (a) Scheme of a classic oxidative PEC sensor, in which photoexcited charges generate current. Holes oxidize the analyte, the electrons are extracted continuously, mirroring the reaction rate. **(b)** Photocurrent of a K-PHI sensor under continuous illumination at a bias of 0 V *vs.* Ag/AgCl in a degassed 10 mM KCl solution with stepwise increasing glucose concentrations. **(c)** Relationship between photocurrent and concentration of glucose. Three linear ranges with a $R^2 > 0.99$ are fitted to the two glucose concentration ranges 0 to 1 mM (inset, red), 1 to 10 mM (blue) and 10 to 50 mM (green). The limit of detection (LOD), 11.4 µM, was calculated *via* the smallest red concentration range (inset). **(d)** Photocurrent of a direct amperometric K-PHI sensor for different sugars (red), alcohols (blue) and the physiologically relevant molecules AA and UA (green). Measurements are performed at a concentration of 1 and 5 mM for sugars and alcohols, and 0.1 and 0.5 mM for UA and AA with a bias of 0 V *vs.* Ag/AgCl, highlighting the versatility of K-PHI sensors.

C.2. K-PHI as a direct amperometric PEC sensor

We have investigated the ability of K-PHI thin films to perform direct photoelectrochemical amperometric sensing *via* the case study of glucose. The sample was immersed into a degassed aqueous electrolyte and activated (see Section C.3 for details). Degassing is necessary to prevent charge losses due to side reactions such as the formation of reactive oxygen species (ROS).[3] A potential of 0 V *vs.* Ag/AgCl is applied to provide a driving force for electron extraction. While glucose is added in stepwise increasing concentrations from 10 to 50 µM in 1 min cycles, the aver-

age photocurrent over the last $10\,\mathrm{s}$ (*i.e.*, after initial stabilization) of each cycle is measured (Figure C.4 (b)).[4] We observe a linear scaling of the photocurrent with glucose concentration for three distinct concentration ranges: $0-1\,\mathrm{mM}$, $1-10\,\mathrm{mM}$, and $10-50\,\mathrm{mM}$, with average slopes of 0.16, 0.11 and $0.05\,\mu\mathrm{A\,mM^{-1}}$, respectively (Figure C.4 (c)). In the regime between 0 and $1\,\mathrm{mM}$, a limit of detection (LOD) of $11.4\,\mu\mathrm{M}$ ($0.21\,\mathrm{mg\,dL^{-1}}$) can be determined.[5] Note that in the main text we do not discuss the last largest slope, since the measurement errors are too large to gain an useful sensing information. To underline the versatility of K-PHI amperometric sensors as a sensing platform, we have investigated other analytes, such as sugars (Figure C.4 (c), red bars), alcohols (Figure C.4 (c), blue bars) and other physiologically relevant molecules (Figure C.4 (c), green bars). At a concentration of $5\,\mathrm{mM}$, the mono- and disaccharide sugars (Figure 8.1 (a), red) produce photocurrents between ~ 0.6 and $1\,\mu\mathrm{A\,cm^{-2}}$. By far the strongest response is observed for TEoA and 4-MBA – both typical sacrificial electron donors for photocatalytic studies[2,6–8] – with photocurrents of 7.5 and $23\,\mu\mathrm{A\,cm^{-2}}$, respectively. The physiologically relevant molecules AA and UA were measured at lower concentrations of 0.1 and $0.5\,\mathrm{mM}$, as usually found in blood serum.[9] A significant photocurrent response of 0.38 and $0.35\,\mu\mathrm{A\,cm^{-2}}$ is observed already at a concentration of $0.1\,\mathrm{mM}$ for AA and UA, respectively.

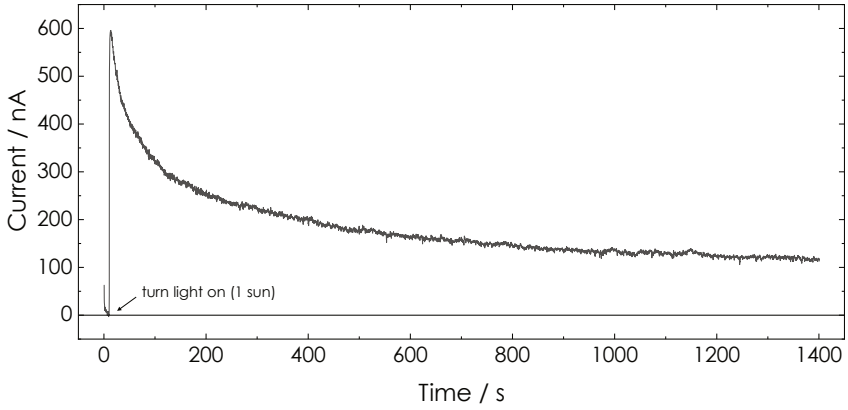

Figure C.5. Pretreatment of K-PHI thin films by self-cleaning. Self-cleaning of a fresh K-PHI thin film in 10 mM KCl. A bias potential of 0 V *vs.* Ag/AgCl is applied and after 10 s the sample is illuminated with 1 Sun (AM 1.5G) until a current of 120 nA is reached.

C.3. Electrochemical self-cleaning of thin films

The K-PHI thin films are very sensitive to organic contaminations as well as for charging through ambient light – *per se* beneficial properties for a sensor. However, it is essential to remove any unwanted potential sources of charges before starting the sensing experiments. Otherwise, those charges could influence the sensor output as they would contribute to the memristive change in material properties. Thin films of K-PHI for potentiometric and impedimetric sensing were thus first immersed into a degassed reactor without any analyte and a bias potential of 0 V *vs.* Ag/AgCl was applied. Subsequently, the sample was illuminated until a current of <120 nA was reached. The required illumination time to achieve this varied between 30 and 120 min. An exemplary measurement is shown in Figure C.5. The initial peak in the dark is caused by electrons stored onto the K-PHI film prior to applying a bias. The photocurrent that develops initially during the very first illumination could be linked to organic contaminations either from the reactor or the K-PHI thin film (*e.g.*, residues of IPA from the thin film deposition). When those miniscule organic contaminations are oxidized and thus consumed, the photocurrent slowly decreases.

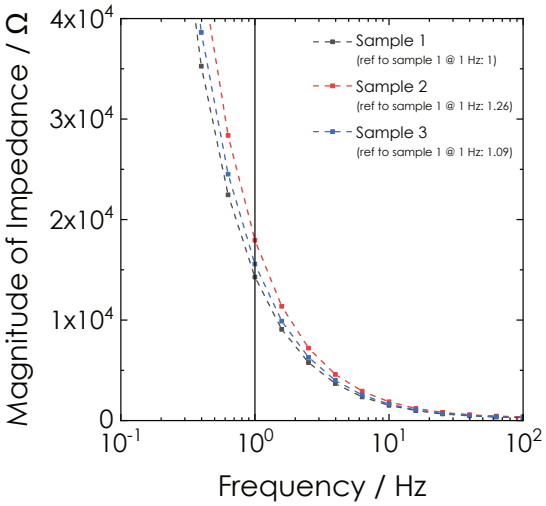

Figure C.6. Reference impedance measurements for coulometric readout. Bode plot of the magnitude of impedance from the impedance measurement of the samples used for coulometric sensing after the sensing measurements. To calculate a correction factor for better comparison of the different samples, the magnitude of each sample at 1 Hz (vertical line) was normalized to the first sample. The correction factors are given in the legend.

C.4. Normalizing coulometric readout measurements

As stated in Section 8.2.2.3, this method is very sensitive on K-PHI thin film properties such as size and film thickness as the readout is the integration of the current over the entire 5 min of discharging. Thus, to allow a better comparison between samples, an impedance measurement was carried out after each measurement. This measurement is shown in Figure C.6 for three samples for coulometric sensing. A small variation in magnitude of the impedance can be observed. To reference the measurements to each other, a correction factor was calculated and multiplied to the respective coulometric measurements. To do that, the magnitude of impedance of the impedance measurements at 1 Hz was normalized to the first sample. Thus, the correction factors for coulometric sensor samples discussed in the main text (denoted herein as sample 1, 2 and 3) are 1.00, 1.26 and 1.09, respectively (see legend in Figure C.6).

C.5. Fitting of the sensor curves

For an application of our sensor, a fitting function has to be found that gives a numeric relation between concentration of glucose and the sensor output. In this section, we will discuss both linear and non-linear fitting of our different sensor methods. In Table C.1, the results of all the fits in their respective ranges are summarized.

LINEAR FITTING. Linear fitting allows a very easy and straightforward relationship between analyte concentration and sensor signal and is therefore typically used to fit sensors.[5,10] We have chosen linear ranges so that they reach a fit quality of $R^2 > 0.9$ (with two exceptions of $R^2 > 0.8$ as discussed below). The slope of the linear range is a measure for how accurate the sensor can measure: With a steeper slope and hence, larger response factor, the measurand error (*e.g.*, OCP for potentiometric sensing) has a smaller

NON-LINEAR FITTING. The sensor signal is not linear over its whole dynamic range, which is partially due to the non-linear charge storage characteristics.[11] Thus, either linearization of the sensor output *via*, *e.g.*, an external circuit or nonlinear fitting can improve the accuracy of the sensor's signal.[5,10,12] Non-linear monotonous signal fitting can be adapted better to the sensor mechanism, thereby extending the dynamic sensing range. A biosensor system where the sensing response is governed by adsorption, can be fitted with the function:[13]

$$signal\,(x) = A_1 + \frac{B_1 \cdot x}{B_2 + x} \tag{C.1}$$

where $signal\,(x)$ is the measured sensor signal, x the analyte concentration and A_1, B_1, and B_2 are the fitting parameters. While A_1 gives the offset of the sensor signal when no analyte is present, B_1 takes into account the signal when all sensing sites on the sensor are occupied with the analyte.[13] B_2 relates to the dissociation constant of the analyte from the sensor.13 Phenomenologically, this equation can approximate any linear behavior ($B_2 \gg x$) and well approximate exponential type behaviors (*e.g.*, isotherms).

In case of our memristive sensor, we have both non-linear diffusion controlled (analyte diffusion to the sensor, faradaic charging process), linear (capacitive charging of the sensor), adsorption (sensor clogging) as well as other processes (*e.g.*, conductivity limitations (especially when not charged), self-discharge). Furthermore,

faradaic charging only occurs at potentials <-0.7 V *vs.* Ag/AgCl (see Figure 8.2 (b)). Thus, it is difficult to assign specialized equations to specific processes. We therefore modified the very general Equation C.1 to account for all above-described processes to perform a phenomenological, which allows to extract the analyte concentration information from the sensing signal over the entire dynamic range.

We separate the description of the charging behavior into two major contributions: (1): A process which is governed by the diffusion of analyte to the sensor and capacitive charging. The latter only occurs at potentials >-0.7 V *vs.* Ag/AgCl. (2): A process which consists mainly of the faradaic charging and therefore, only possesses a major contribution at potentials <-0.7 V *vs.* Ag/AgCl. Sensor clogging as well as conductivity limitations influence both processes. Hence, Equation C.1 is modified accordingly:

$$signal\,(x,t) = A_1\,(t) + \frac{B_1\,(t)\cdot x}{B_2\,(t)+x} + \frac{C_1\,(t)\cdot x}{C_2\,(t)+x} \tag{C.2}$$

The process described with the coefficient B_1 and B_2 describe the capacitive charging and the process with C_1 and C_2 the faradaic charging. A_1 gives the offset of the blind current when no analyte is present. All processes depend on the illumination time t. Furthermore, to correct for the nonlinear distribution of measurement points at different analyte concentrations, the derivative of concentrations (difference to the two neighboring analyte concentration values) was chosen as a weight for all fitting points.

Table C.1. Summary of sensor fitting results. Two different fittings where performed for all sensor readout methods: Linear fitting and non-linear fitting according to Equation C.2. Results of ranges as well as the fitting error R^2 is given. The † sign marks values which are tunable *via* illumination time (as with potentiometric) or illumination intensity (herein everything measured with 1 Sun).

Method	Illumination time	Linear ranges	Non-linear ranges
Amperometric	constant	$0.1-10$ mM	none
Potentiometric	$1-2$ s†	$0.05-50$ mM† ($R^2 > 0.93$)	50 µM† $-$ 50 mM† (for >1 s: $R^2 > 0.98$)
	>2 s†	4 s: 0.05† $-$ 20 and $30-50$ mM $6-8$ s: $0.05-10$ and $20-50$ mM 10 s: $0.05-5$ and $10-50$ mM >15 s: $0.05-1$ and $10-50$ mM† (all $R^2 > 0.83$)	
Impedimetric	30 s†	$0.05-1$ mM† ($R^2 > 0.97$) $10-50$ mM† ($R^2 > 0.82$)	50 µM† $-$ 50 mM† ($R^2 = 0.99$)
Coulometric		$0.1-5$ mM† ($R^2 > 0.93$) $10-50$ mM† ($R^2 > 0.97$)	100 µM† $-$ 50 mM† ($R^2 > 0.99$)
Colorimetric	200 s†	$0.2-2$ mM† ($R^2 = 0.97$) $2-10$ mM ($R^2 = 0.98$) $20-50$ mM† ($R^2 = 0.99$)	200 µM† $-$ 50 mM† ($R^2 = 0.99$)
Fluorometric		$0.2-2$ mM† ($R^2 = 0.99$) $2-10$ mM ($R^2 = 0.99$) $15-50$ mM† ($R^2 = 0.98$)	200 µM† $-$ 50 mM† ($R^2 = 0.99$)

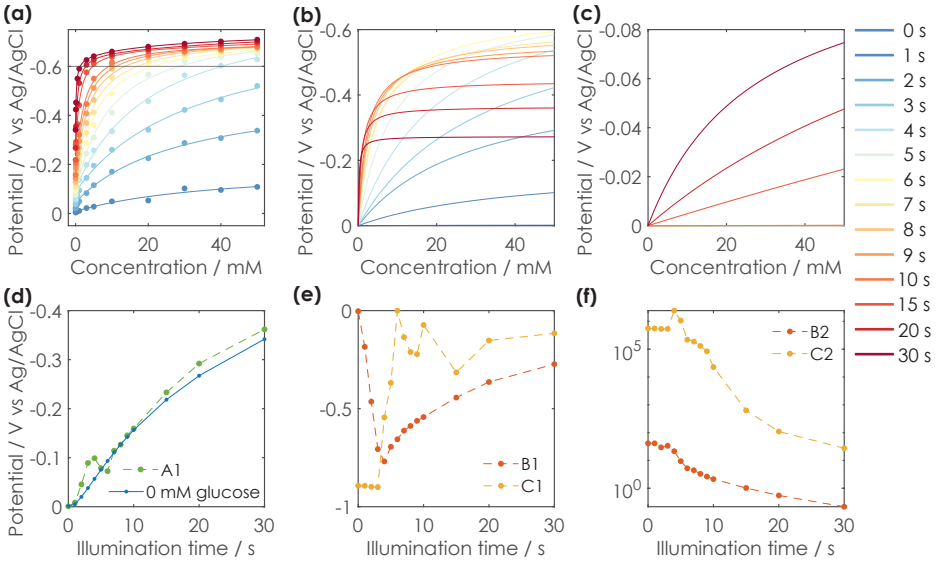

Figure C.7. Non-linear fitting of the potentiometric sensing measurement. (a) The OCP change with glucose concentration is plotted after different illumination times. This measurement is discussed in Section 8.2.2.1. Fitting of the results was performed according to Equation C.2. This Figure is a reproduction of Figure 8.3 (c). **(b)** and **(c)** The individual contributions of the two terms of Equation C.2 are plotted for all illumination times. The capacitive charging contribution (B_1, B_2) is shown in (b) and the faradaic charging contribution (C_1, C_2) in (c). **(d)**, **(e)**, and **(f)** Values for the fitting parameters at different illumination times.

C.5.1. Potentiometric fitting

NON-LINEAR FITTING. In potentiometric sensing, we observe different slopes for different illumination times and the potential reaches a minimum value of approx. -0.7 V *vs.* Ag/AgCl. Thus, both above-described charging processes govern the signal response and Equation C.2 is used for fitting. The longest illumination time (30 s) is fitted first and the fitting parameters are used as starting parameters for next smaller illumination time. The result of the fitting is shown in Figure C.7 (a). The contributions of the capacitive charging term (B_1, B_2) and faradaic charging term (C_1, C_2) are shown in Figure C.7 (b) and (c), respectively. When looking at the contributions of terms including the offset of A_1 at different illumination times (Figure C.8), it becomes evident that the B_1, B_2 term never reaches a potential <-0.7 V *vs.* Ag/AgCl, as expect for capacitive charging. Only at longer illumination times >10 s, the C_1, C_2 term starts to play a significant role. The parameter A_1 fits the measured photopotential when no glucose was present (see Figure C.6 (d)). It is

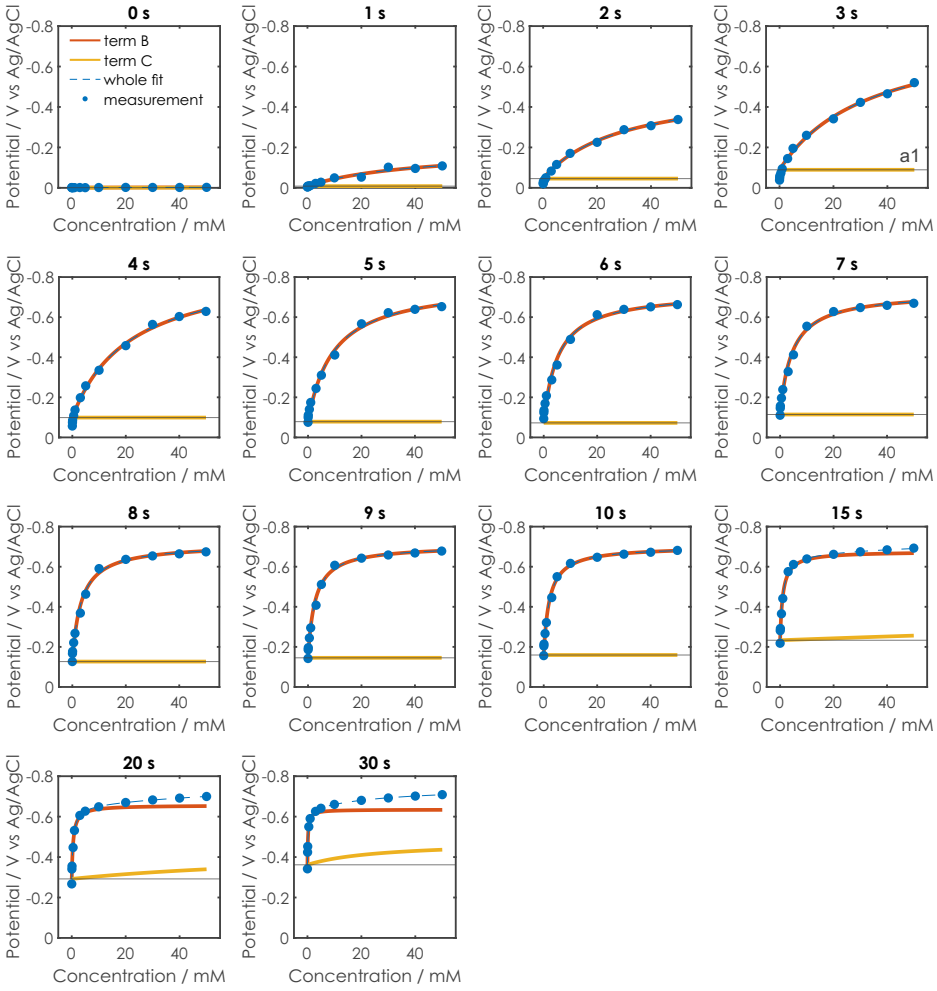

Figure C.8. Individual contributions to non-linear fitting of the potentiometric sensing measurement. Comparison of measurement data (blue dots) to the whole fit (blue dashed line) and contributions of terms of B_1, B_2 (capacitive charging, red line) and C_1, C_2 (faradaic charging, yellow line) at all analyzed illumination times.

difficult to interpret the trend of parameters B_1, B_2 and C_1, C_2 (Figure C.7)(e) and f) as the response of the term is always a convolution of both parameters. However, the parameters do show a trend.

Depending on the illumination time, contributions of capacitive and faradaic charging change as follows: At short times, no or not a lot of faradaic charging occurs. Thus, the charging kinetic is governed mainly by capacitive charging and analyte diffusion. The longer the illumination time, the more the sensor is charged and

therefore a more significant influence of the faradaic charging to the overall diffusion process is observed. Note also that only at times longer than 10 s, a saturation of the OCP during illumination occurs (see Figure C.7 (a)), pointing towards a strong light charging of the sensor in the non-linear, faradaic charge storage regime.[11]

In summary, longer illumination times improve the sensitivity for low analyte concentrations. For measurement times between 10 and 30 s, the slope for the range from 0 to 1 mM is much larger than from 10 to 50 mM (see Figure C.7 (a)). For longer illumination times, the sensor works more accurately for low concentrations. This fits nicely with the enhanced sensitivity in this range and underlines that our sensor works best at these measurement conditions. Large glucose concentrations are measured more accurately at short illumination times below 4 s. Measurement and suitable fitting ranges are summarized in Table C.1.

LINEAR FITTING. Here, we look at potentiometric sensing in which the OCP change can be linked to the glucose concentration (see Section 8.2.2.1). Depending on the illumination time, different slopes can be observed in different glucose concentration regimes. We have fitted linear regressions to different suitable concentration ranges. The respective ranges were chosen so that the fitting error of the linear regression $R^2 > 0.9$. Results of this analysis are shown in Figure C.9 and Table C.2. When looking at the OCP increase with the concentration (Figure C.9 (a) and Figure 8.3 (c)), we can observe a roughly linear increase of the OCP over the entire measured concentration range for the first 2 s. For longer illumination times, a saturation of the OCP at large concentrations occurs at potentials <-0.7 V *vs.* Ag/AgCl, which corresponds to the charge storage potential of K-PHI.[11] A second linear range develops with a far smaller slope. Thus, the first linear range can be attributed to the surface capacitive contribution of the OCP up to the charge storage potential of K-PHI and the second linear range to the faradaic charging of K-PHI, which causes a constantly smaller rise of the OCP. At potentials more negative -0.7 V *vs.* Ag/AgCl, faradaic charging becomes the dominant kinetic process compared to the capacitive charging.

As explained in the main text, longer illumination times improve the sensitivity for low analyte concentrations. For measurement times between 10 and 30 s, the slope for the linear range from 0 to 1 mM is much larger than from 10 to 50 mM (compare Figure C.9 (b) and (c)). This means that for longer illumination times, the sensor works more accurate for low concentrations. This fits nicely with the enhanced sensitivity in this range discussed in the main text. On the other hand,

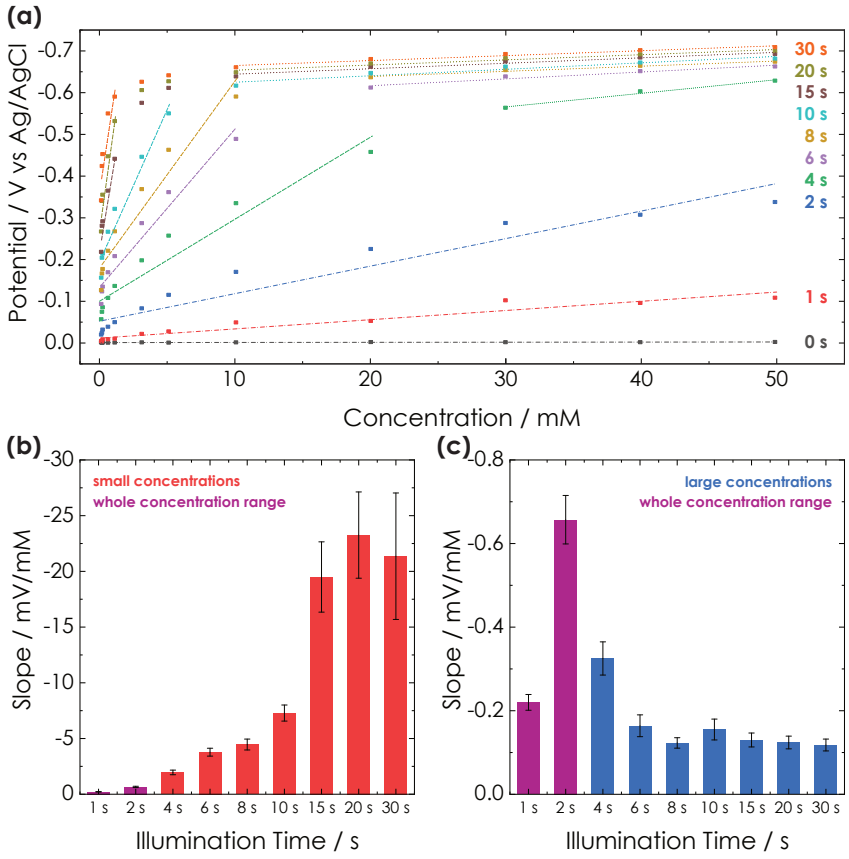

Figure C.9. Linear ranges in the potentiometric sensing measurement. (a) The OCP change with glucose concentration is plotted after different illumination times. This measurement is discussed in Section 8.2.2.1. Linear ranges that fulfill the fitting quality requirement of $R^2 > 0.9$ can be found. Linear ranges for small concentrations are plotted with dash lines, linear ranges for large concentrations with dot lines and linear ranges over the entire concentration range with dash-dot lines. **(b)** Slopes of linear fits for small concentrations at different illumination times. **(c)** Slopes of linear fits for large concentrations at different illumination times. Errors in (b) and (c) have been calculated from the linear regression.

large glucose concentrations are measured more accurately at short illumination times <4 s, were the slope of the linear range for large concentrations from 10 to 50 mM is larger. This is also in line with the upper sensitivity limit discussed in the main text and allows us to define the optimal measurement settings for our sensor *via* potentiometric readout, which is given in Table C.1.

C.5.2. Impedimetric fitting

NON-LINEAR FITTING. Fitting of the impedimetric readout works different to the other readout methods, since not only the charging governs the readout but also the frequency at which the sensor readout is probed. When performing sensing *via* impedance readout, all samples were illuminated for 30 s (see Section 8.2.2.2). When looking at the potential reached after 30 s of illumination (Figure C.7), except of the very small concentration value it is always <0.7 V *vs.* Ag/AgCl. Hence, all processes which govern the kinetics of the system participate. However, the processes have different time constants in impedance which complicates the fitting. We found that Equation C.1 is sufficient to phenomenologically describe the behavior reasonably well with $R^2 > 0.99$ for frequencies <100 Hz. The fitting and fit coefficients

Table C.2. Linear ranges of potentiometric sensing. The linear range and fitting error R^2 of the linear ranges, which were fitted to the OCP change with concentration shown in Figure C.9.

Illumination time	Linear range		R^2
1 s	whole range	0.05 to 50 mM	0.93
2 s	whole range	0.05 to 50 mM	0.93
4 s	small concentrations	0.05 to 20 mM	0.93
	large concentrations	30 to 50 mM	0.99
6 s	small concentrations	0.05 to 10 mM	0.95
	large concentrations	20 to 50 mM	0.95
8 s	small concentrations	0.05 to 1 mM	0.93
	large concentrations	20 to 50 mM	0.98
10 s	small concentrations	0.05 to 5 mM	0.95
	large concentrations	10 to 50 mM	0.93
15 s	small concentrations	0.05 to 1 mM	0.93
	large concentrations	10 to 50 mM	0.95
20 s	small concentrations	0.05 to 1 mM	0.92
	large concentrations	10 to 50 mM	0.96
30 s	small concentrations	0.05 to 1 mM	0.83
	large concentrations	10 to 50 mM	0.96

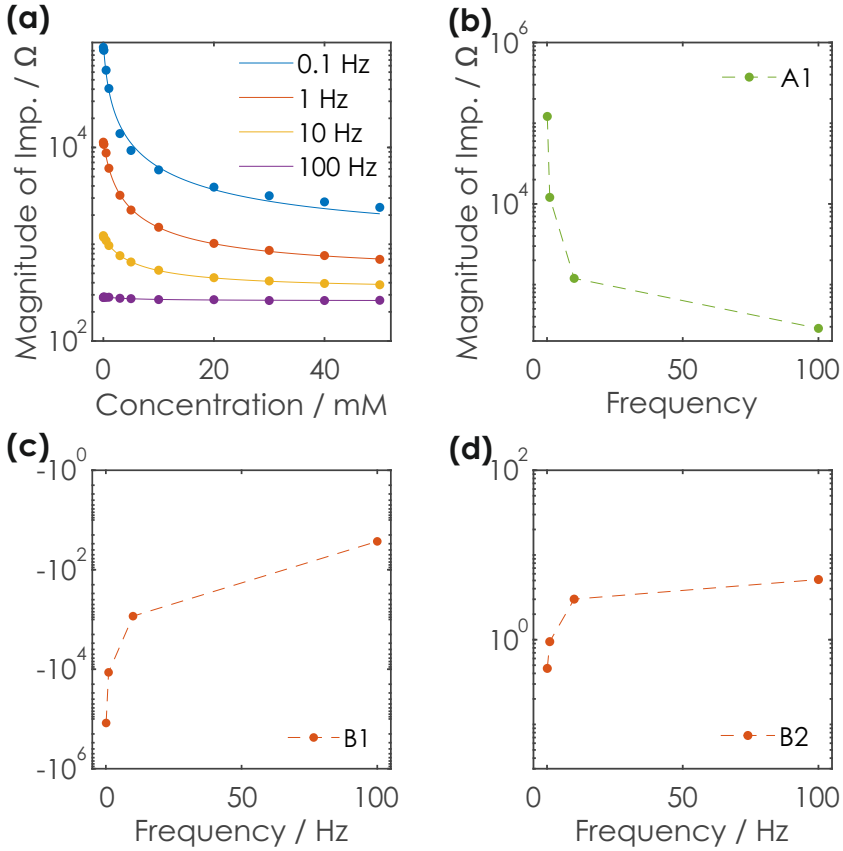

Figure C.10. Non-linear fitting of the impedimetric sensing measurement. (a) Fitting of the magnitude of impedance was performed according to Equation C.2. The fits possess an error R^2 of 0.993, 0.997, 0.992 and 0.943 for frequencies of 0.1, 1, 10 and 100 Hz, respectively. Illumination time is fixed to 30 s. **(b)**, **(c)**, and **(d)** Fitting coefficients of the fit.

are shown in Figure C.10.

At low frequencies <10 Hz, we have observed a much steeper slope for small concentrations <1 mM. Measurements in this range can thus be performed with a better accuracy. The good fit quality for this frequency range ($R^2 = 0.99$) allows the most reliable readout of the sensing information. The loss in sensitivity at faster frequencies, discussed in the main text, is also accompanied by a loss in measurement accuracy. This suggests that impedance measurements at frequencies >100 Hz are less accurate for determination of the analyte concentration. In fact, the change in magnitude of impedance is much smaller than the measurement error over the entire concentration range already for 100 Hz and measurements should be performed

<10 Hz. To summarize, with slower frequencies a better sensitivity and accuracy is achieved for both slow and large concentration. However, large concentrations can not be measured well for any frequency due to the very small slope. This result is represented in Table C.1.

LINEAR FITTING. The impedance sensing measurements that are discussed in Section 8.2.2.2 were fitted with two linear ranges. The fitting and respective slopes are shown in Figure C.11 and fitting ranges as well as fitting errors are given in Table C.3. At low frequencies <10 Hz, we have observed a much steeper slope for small concentrations <1 mM than for large concentrations. Measurements in this range can thus be performed with a better accuracy. The loss in sensitivity at faster frequencies discussed in the main text is also accompanied by a loss in measurement accuracy. The very small R^2 values for those measurements (red numbers in Table C.3) are caused by the very small slope and thus, those frequencies are not useful to extract the sensing information accurately. The slopes for large concentrations >10 mM show a similar behavior of larger slopes for slower frequencies. Note that they are three orders of magnitude smaller and thus much less accurate than for small concentrations. To summarize, with slower frequencies a better sensitivity and accuracy is achieved for both slow and large concentrations. However, the

Table C.3. Linear ranges of impedance sensing. The linear range and fitting error R^2 of the linear ranges, which were fitted to the impedance change with concentration shown in Figure C.11.

Frequency	Linear range		R^2
0.1 Hz	small concentrations	0.05 to 1 mM	0.97
	large concentrations	10 to 50 mM	0.85
1 Hz	small concentrations	0.05 to 1 mM	0.99
	large concentrations	10 to 50 mM	0.82
10 Hz	small concentrations	0.05 to 1 mM	0.99
	large concentrations	10 to 50 mM	0.84
100 Hz	small concentrations	0.05 to 1 mM	0.04
	large concentrations	10 to 50 mM	0.61
1000 Hz	small concentrations	0.05 to 1 mM	0.54
	large concentrations	10 to 50 mM	0.68

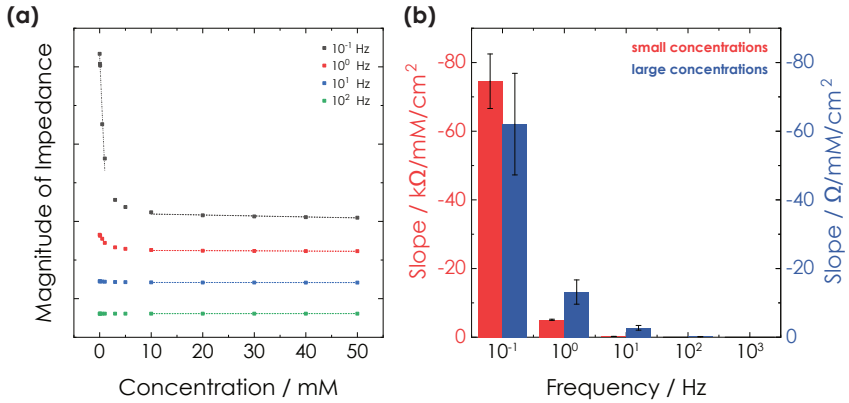

Figure C.11. Linear ranges in impedance sensing. (a) The magnitude of the impedance was measured for different glucose concentrations and discussed in Section 8.2.2.2. Two linear regressions for two different concentration ranges were performed: 0 to 1 mM (dash-dot lines) and 10 to 50 mM (dash lines). **(b)** Slope extracted from the linear regressions of the concentration ranges, plotted for every frequency. Errors were calculated from the linear regression.

fitting quality especially for larger frequencies is still much worse than non-linear fitting which is discussed above and should be used instead for readout. Note that non linear fitting also works over the entire concentration range. These results are summarized in Table C.1.

C.5.3. Coulometric fitting

NON-LINEAR FITTING. For coulometric sensing, the sensor was illuminated for 120 s. From potentiometric sensing discussed in Section C.5.1, we know that after already 30 s the potential reached values <-0.7 V *vs.* Ag/AgCl for nearly all analyte concentrations and both capacitive as well as faradic charging contributed to the charging process. Both processes should thus also influence charging in the coulometric measurements and we have therefore, used Equation C.2 to fit the sensor response. Note that for longer illumination times, the charge should increase even more.

The fit for different delay times is shown in Figure C.12 (a)-(c). The shape of the two fitting terms B_1, B_2 and C_1, C_2 looks similar to the potentiometric fitting shown in Figure C.8. With longer delay times, mainly term B_1, B_2 decreases due to the slow self-discharge discussed in the main text. For small analyte concentrations there is nearly no charge left after the delay of 300 s, term B_1, B_2 gets very small. Term C_1, C_2, which contributes to the faradaic capacity, does not decrease that much or

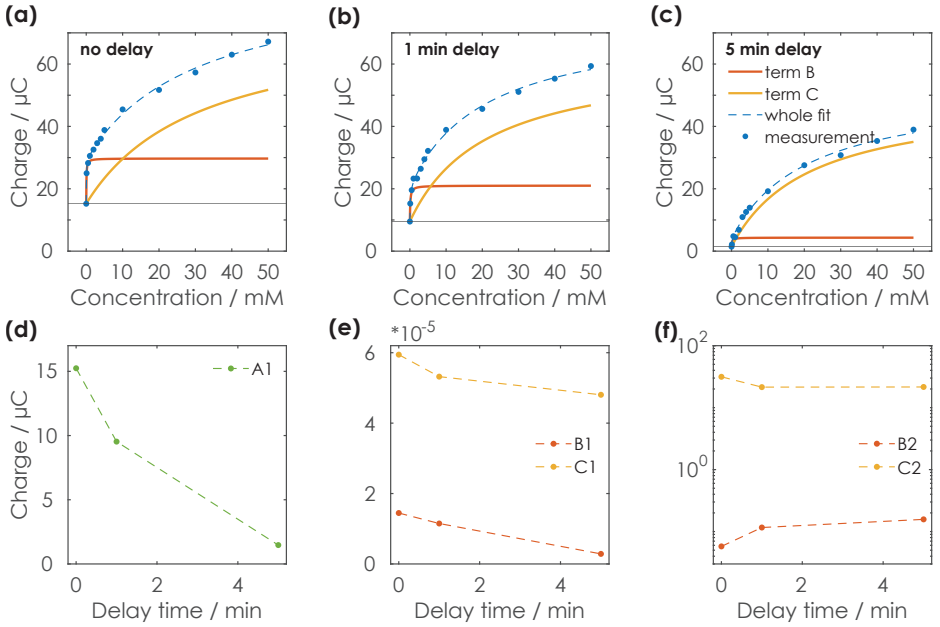

Figure C.12. Non-linear fitting of the coulometric sensing measurement. (a), **(b)**, and **(c)** Fitting of the extracted charge after the sensing interaction, *i.e.*, coulometric sensing was performed according to Equation C.2. The fits possess an R^2 of 0.997, 0.996 and 0.997 for delay times of 0, 1 and 5 min, respectively. **(d)**, **(e)**, and **(f)** Fitting coefficients of the fits at different delay times.

change a lot in shape. Thus, we can calculate a parameter to correct for delayed discharging from the decrease of term B_1, B_2. Fitting parameters are given in Figure C.12 (d)-(f). The very good fit quality ($R^2 > 0.996$) hints that a reliable and accurate readout of the sensing information is possible throughout the entire measured analyte concentration range. A summary of fitting results is given in Table C.1.

LINEAR FITTING. The link between extracted charge after charging the sensor and glucose concentration is discussed in Section 8.2.2.3. The results of fitting linear ranges to this data and their slopes are shown in Figure C.13. Concentration ranges as well as the fitting error R^2 are given in Table C.4. Two linear ranges were attributed, one for small concentrations (0.1 to 5 mM) and one for large concentrations (10 to 50 mM). The slope for smaller concentrations is steeper, which gives it a better sensing accuracy. An advantage of this method in comparison to potentiometric and impedimetric sensing is the larger linear concentration range up to 5 mM compared to 1 mM for small concentrations. Similar to potentiometric and impedimetric sensing, non-linear fitting again works much better than linear fitting in

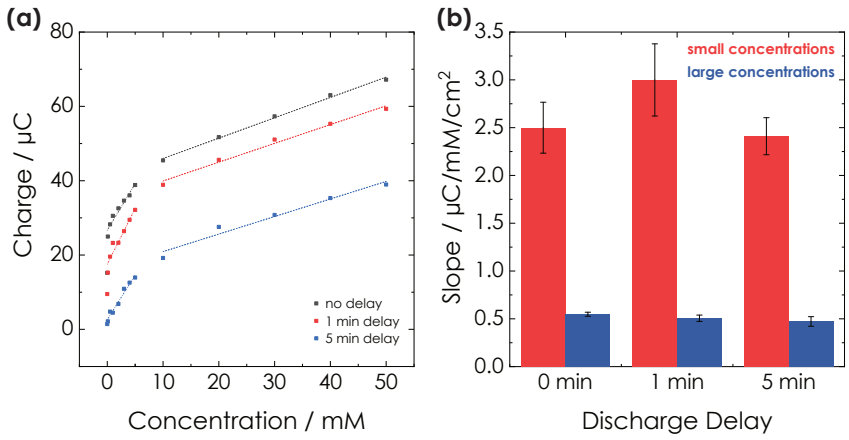

Figure C.13. Linear ranges in coulometric sensing. (a) The extracted charge after illumination was measured for different glucose concentrations and discussed in Section 8.2.2.3. Two linear regressions for two different concentration ranges were performed: 0.1 to 5 mM (dash-dot-dot lines) and 10 to 50 mM (dash lines). **(b)** Slope extracted from the linear regressions of the two concentration ranges, plotted for every frequency. Errors were calculated from the linear regression.

regard to the fitting error and also works over the entire concentration range. The best sensing conditions are given in Table C.1.

The delay times of 60 and 300 s do not alter these slopes significantly. Mean and standard deviation of the linear fits of both concentration ranges calculated from all delay times are given in Table C.5. This means that memory sensing does not influence accuracy of the linear fitting significantly.

Table C.4. Linear ranges of coulometric sensing. The linear range and fitting error R^2 of the linear ranges, which were fitted to the charge change with concentration shown in Figure C.13.

Delay time	Linear range		R^2
0 s	small concentrations	0.1 to 5 mM	0.95
	large concentrations	10 to 50 mM	1.00
60 s	small concentrations	0.1 to 5 mM	0.93
	large concentrations	10 to 50 mM	0.99
300 s	small concentrations	0.1 to 5 mM	0.97
	large concentrations	10 to 50 mM	0.97

Table C.5. Slopes of linear fits. The mean and standard deviation calculated from the linear fits of 0, 60 and 300 s delayed discharge.

Value	small concentration (0.1 to 5 mM) (µC mM^{-1})	large concentration (10 to 50 mM) (µC mM^{-1})
mean	2.83	0.509
standard deviation	0.288	0.0377

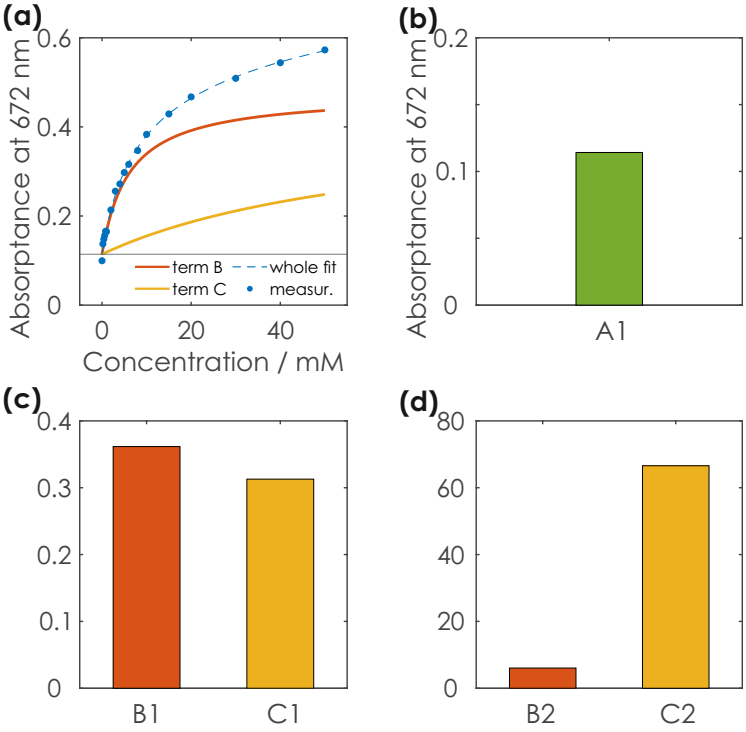

Figure C.14. Non-linear fitting of the colorimetric sensing measurement. (a) Contributions of term B_1, B_2 and C_1, C_2 of Equation C.2 to the fitting of the absorptance signal at a wavelength of 672 nm after illumination. The fit possesses a fitting error R^2 of 0.999. **(b)**, **(c)**, and **(d)** Corresponding fit coefficients.

C.5.4. Colorimetric fitting

NON-LINEAR FITTING. Fitting of the optical sensor readout methods works analogous to fitting of the electrochemical potentiometric and coulometric sensing with Equation C.2, as the charging mechanism of the wireless particles is similar. Since the sample was illuminated for 200 s, both capacitive and faradaic charge storage

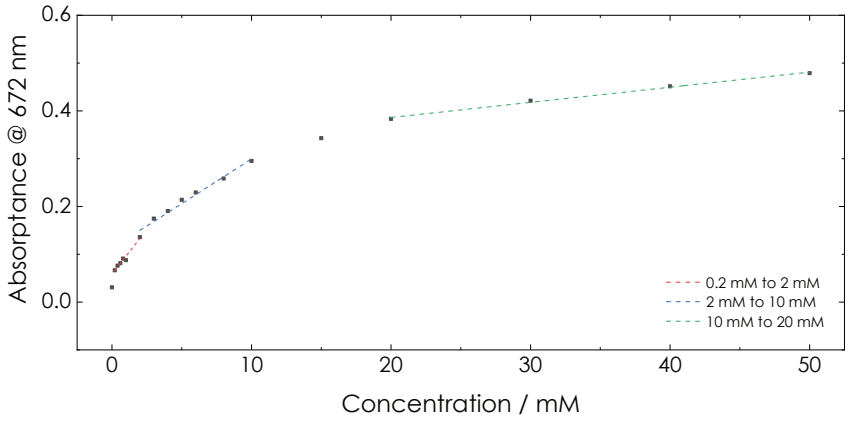

Figure C.15. Linear ranges in colorimetric sensing. The absorptance signal at a wavelength of 672 nm after illumination was measured for different glucose concentrations, as described in Section 8.2.3.1. Three linear regressions for different concentration ranges were performed.

mechanisms contribute to the charging (see Figure C.8: For illumination times of 30 s, nearly all concentration measurements reach a potential <-0.7 V *vs.* Ag/AgCl), in agreement with the potentiometric fitting. The fitting is shown in Figure C.14. The shape of the two terms B_1, B_2 and C_1, C_2 looks similar to the potentiometric sensor fitting for long illumination times (Figure C.8). Term B_1, B_2 relates to the capacitive charging and term C_1, C_2 to the faradaic charging. Fit coefficients are shown in Figure C.14 (b)-(d). The very good fit quality ($R^2 = 0.999$) allows a reliable readout of the analyte concentration over the entire measured concentration range. Best sensing conditions are summarized in Table C.1.

LINEAR FITTING. Analogous to fitting linear ranges to electrochemical sensor readout methods described above, we have fitted three linear ranges to concentration ranges of the absorptance signal, which was measured of a K-PHI suspension after charging and is described in Section 8.2.3.1. Ranges were chosen so that the fit quality criterion ($R^2 > 0.9$) is fulfilled. The fits are shown in Figure C.15. Three different concentration ranges can be observed, slopes are given in Table C.6. The slope of the fit decreases with increasing analyte concentration. Therefore, with larger analyte concentrations the sensing accuracy decreases. Note that non-linear fitting discussed above works better than linear fitting in regard to the fitting error and also works over the entire concentration range. Best sensing conditions are summarized in Table C.1.

Table C.6. Fitting parameters for linear ranges of coulometric sensing. The linear range and fitting error R^2 of the linear ranges, which were fitted to the absorptance change at a wavelength of 672 nm with concentration shown in Figure C.15.

Linear range	Slope (absorptance mM^{-1})	R^{-1}
0.2 to 2 mM	0.037 ± 0.003	0.97
2 to 10 mM	0.019 ± 0.001	0.98
20 to 50 mM	0.003 ± 0.000	0.99

C.5.5. Fluorometric fitting

NON-LINEAR FITTING. The fitting of the fluorometric sensor readout works analogous to the colorimetric sensor discussed in Section C.5.4 *via* Equation C.2. The terms B_1, B_2 and C_1, C_2 of the fitting are shown in Figure C.16 (a) and show a similar behavior to the colorimetric readout (Figure C.14 (a)) and potentiometric as well as coulometric readout (Figure C.8 and Figure C.12 (a)). Both capacitive and faradaic charge storage plays a role since the illumination time during the charging is 200 s, as discussed for the colorimetric sensor in Section C.5.4. Fitting coefficients are shown in Figure C.16 (b)-(d). Due to the very good fitting quality ($R^2 = 0.998$), a reliable concentration readout throughout the entire measured analyte concentration range is possible. In Table C.1, the best sensing conditions are summarized.

LINEAR FITTING. Analogous to the linear fitting of the colorimetric sensor discussed above, we have fitted three linear ranges to concentration ranges of the integrated PL signal, which was measured of a K-PHI suspension after charging and is described in Section 8.2.3.2. Ranges were chosen so that the fit quality criterion ($R^2 > 0.9$) is fulfilled. The fits are shown in Figure C.17. Three different concentration ranges can be observed and their slopes are given in Table C.7. With larger analyte concentrations, the slopes get smaller and thus, the sensing accuracy decreases. Similar to colorimetric sensing, the non-linear fitting works again better than the linear fitting in regards to the fitting error. It also works over the entire concentration range and should therefore be used. Sensing conditions are summarized in Table C.1.

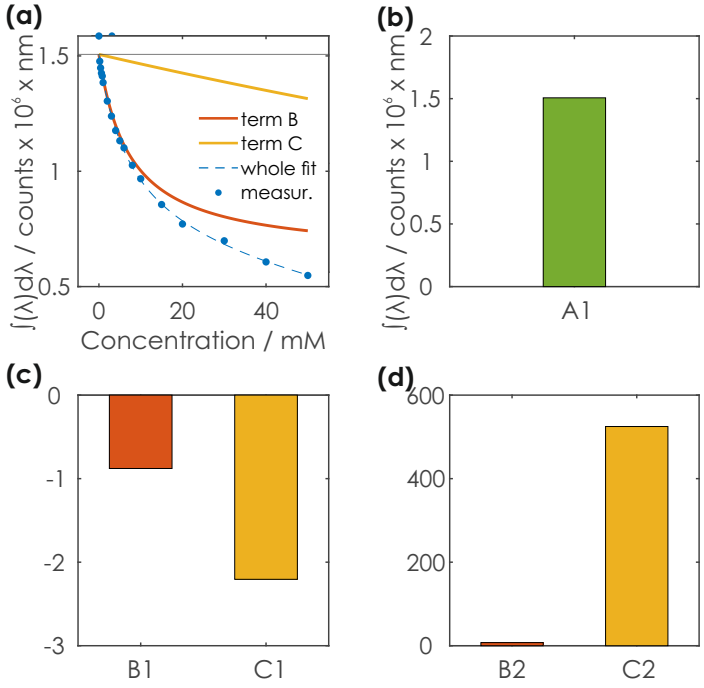

Figure C.16. Non-linear fitting of the fluorometric sensing measurement. (a) Contributions of term B_1, B_2 and C_1, C_2 of Equation C.2 to the fitting of the absorptance signal at a wavelength of $672\,\text{nm}$ after illumination. The fit possesses a fitting error R^2 of 0.998. **(b)**, **(c)**, and **(d)** Corresponding fitting coefficients.

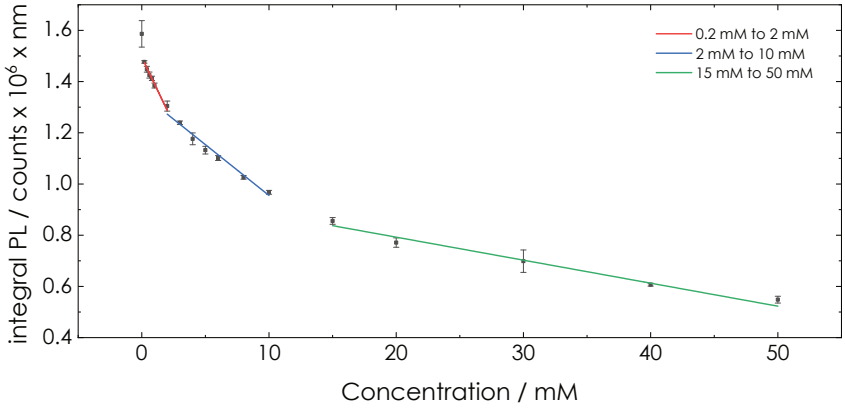

Figure C.17. Linear ranges in fluorometric sensing. The PL signal after illumination was measured for different glucose concentrations and integrated, as described in Section 8.2.3.2. Three linear regressions for three different concentration ranges were performed.

Table C.7. Fitting parameters for linear ranges of fluorometric sensing. The linear range and fitting error R^2 of the linear ranges, which were fitted to the integrated PL signal change with concentration shown in Figure C.17.

Linear range	Slope (counts $\times$ 10^6 mM^{-1})	R^{-1}
0.2 to 2 mM	-0.104 ± 0.006	0.99
2 to 10 mM	-0.040 ± 0.002	0.99
15 to 50 mM	-0.009 ± 0.0007	0.98

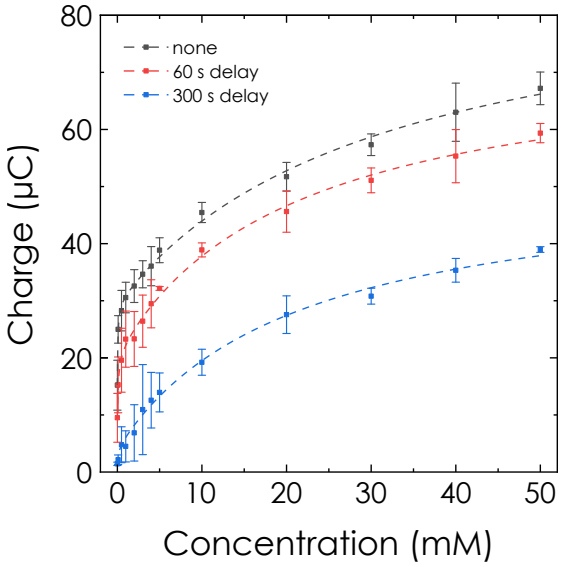

Figure C.18. Analysis of delay times for memory sensing. Charge extracted from the sensor *via* coulometric readout after a delay of 0, 60 and 300 s (black, red and blue points, respectively). The dashed lines show the phenomenological non linear fit discussed in Section C.5.3. The measurement with no delay is also shown in Figure 8.3

C.6. Additional electrochemical analysis of memristive properties of K-PHI films

In Section 8.2.2.3, a time delayed readout of memristive properties is discussed for coulometric readout. After charging the sensor during sensing, the readout *via* discharging is delayed by 60 and 300 s. Results are shown in Figure C.18. A decrease in extracted charge for all analyzed concentrations can be observed, which we explain with self-discharge *via* water reduction or oxygen leaking into the reactor (see Section 8.2.2.3 for more details). This decrease produces a systematic offset for fitting (see Section C.5.3) and a correction parameter becomes necessary to still allow a readout. The signal decay was calculated *via* the measurement at a concentration of 50 mM. Results are shown in Table C.8.

Table C.8. Impact of delayed readout on signal intensity. Coulometric sensing charge signal loss after the delayed readout compared to the measurement with no delay. Measurement shown in Figure C.18.

Delay time (s)	Signal loss in charge (%)
60	11.7
300	42.0

C.7. Additional optical analysis of memristive properties of K-PHI particles

C.7.1. Influence of particle size

To evaluate influence of particle size on the sensing response, we perform sensing experiments with particle suspensions, which have different particle sizes. As described in Section 8.4, we use different centrifugation steps to separate the nanosheets from the bulk material. Here, we use the different particle fractions from the individual centrifugation steps to yield particles sizes in the range of 1200 nm (P1), 250 nm (P2), and 150 nm (P3) – as reported in our previous work.[11,14] Dynamic light scattering measurements (DLS) of the different particle sizes are shown in Figure C.19 (a). We performed colorimetric and fluorometric sensing measurements in analogous conditions to the measurements presented in Figure 8.4 and Figure 8.5 (glucose concentrations of 1, 10 and 100 mM), but with a slightly smaller concentration of the K-PHI suspension of 2 mg mL^{-1}, since it is difficult to obtain a very dense P3 suspension. Results are shown in Figure C.19 (b) and (c).

The largest particles P1 show slightly increased absorptance and integrated emission signals (Figure C.19 (a) and (b)). For the colorimetric measurement, P3 shows a larger absorptance than P2 for large concentrations of 100 mM (Figure C.19 (b)). In comparison, the lowest PL integrated emission signal results from P3 (Figure C.19 (c)). To conclude, P1 works best for colorimetric sensing *via* absorptance, but at the same time shows the smallest sensing response for fluorometric sensing since the integrated emission is the largest (Figure C.19 (c)). Thus, colorimetric sensing and fluorometric sensing seem to show opposite trends. To elucidate on the cause of this behavior, we show absorptance and emission spectra of the K-PHI suspension prior to the measurements (Figure C.19 (d) and (e)). While absorptance at 672 nm

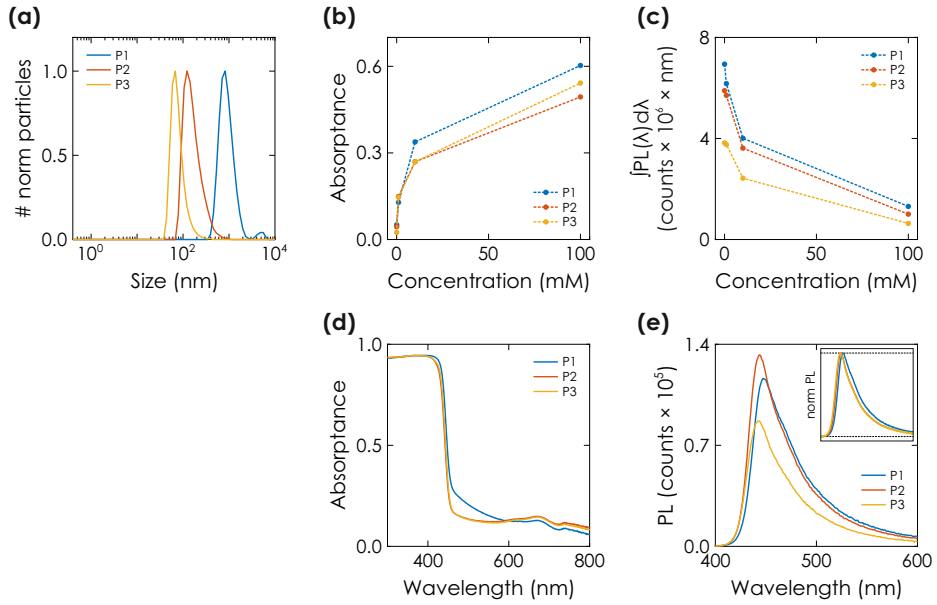

Figure C.19. Influence of particle morphology on sensing efficiency. (a) Particle size distributions after centrifugation of fractions P1, P2, and P3, achieved by exfoliating as-synthesized and washed K-PHI *via* sonication for 2 h in an ice bath and subsequent exfoliation at 2000 rpm for 25 min, 3000 rpm for 40 min, and 24 000 rpm for 90 min, respectively. Sensing is performed under analogous conditions as measurements shown in the main text (Figure 8.4 and Figure 8.5), but at a lower particle concentration of 2 mg mL^{-1}. **(b)** Output of colorimetric sensing comparing the suspensions containing particles P1, P2, and P3 *via* change in absorptance at a wavelength of 672 nm (compare to Figure 8.4 (c)). **(c)** Output of fluorometric sensing with particles P1, P2, and P3 *via* integrated PL emission signal (compare to Figure 8.5 (b)). **(d)** Absorptance of particle suspensions P1, P2, and P3 before the sensing experiment. **(e)** PL emission of particle suspensions P1, P2, and P3 (excitation at 370 nm) before the sensing experiment (inset show the PL spectra normalized to P1).

remains mainly unaffected by different particle sizes, the emission shows major differences in intensity (intensity: P2 > P1 » P3). We explain this deviation with differences in the optical density of suspensions: When preparing the suspensions, we ensured that they have the similar particle concentration of 2 mg mL^{-1}. While suspension density is the same, optical density affecting the overall PL quantum yield is according to Figure C.19 (e) not the same. Other deviations influencing the PL emission intensity in Figure C.19 (e) are also possible, such as partial particle sedimentation for large P1 particles or a different scattering behavior occurring during the measurement. Thus, colorimetric readout seems to be the more precise method to gauge particle size effects, suggesting that P1 particles actually give the largest

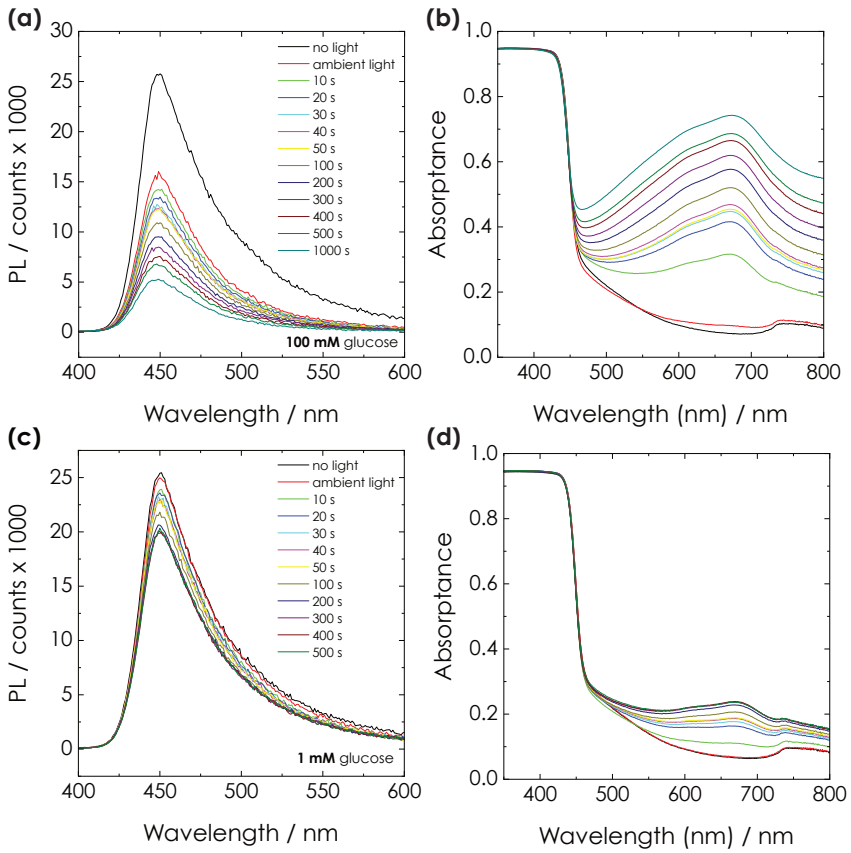

Figure C.20. Evolution of optical properties with increasing the illumination time. (a) and **(b)** PL emission (a) and absorptance (b) after charging the K-PHI autonomous sensing particles in presence of 100 mM glucose with different illumination times. **(c)** and **(d)** PL emission (c) and absorptance (d) of an autonomous, not wired K-PHI sensor (K-PHI particles in an aqueous suspension) in presence of 1 mM glucose after charging it by different illumination times.

sensing signal. This aligns with observations of influence of particle size effects on photocatalytic measurements.[14] Note that since these particles are too large to deposit onto substrates, we chose the smallest particles for the photoelectrochemical sensor measurements presented herein.

Overall, the trends described in the manuscript remain unaffected by particle size, and can be regarded as small fluctuations, which do not play a role after calibration of a given sensor batch. Thus, this underlines that other particle sizes can be used with same trends, but slightly different absolute signal intensities, since suspension stability, scattering, and intrinsic photophysical properties enabling charge accumulation are not fundamentally different when modifying the particle size.[14]

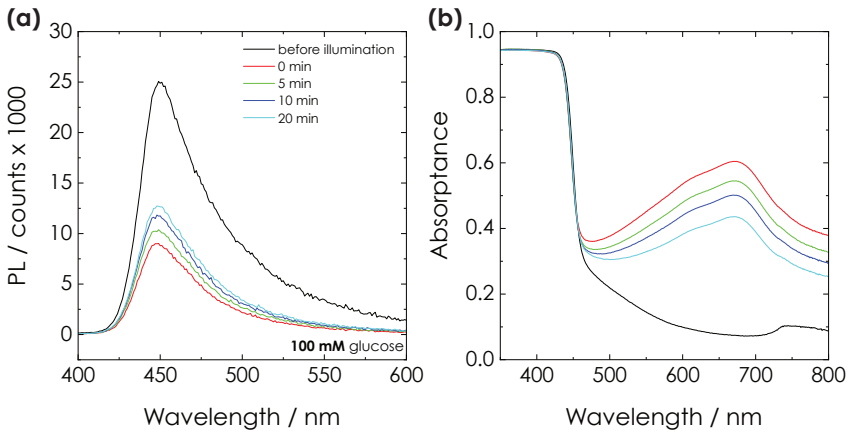

Figure C.21. Analysis of delay times for memory sensing. (a) Emission and **(b)** absorptance of a K-PHI sensor after illuminating it for 200 s and waiting for several different delay times.

C.7.2. Dependence on illumination time

As discussed in Section 8.2, the amount of charging of the K-PHI sensor depends on both, the glucose concentration and illumination time. In Figure C.20, this illumination time is varied from 0 to 1000 s for two different glucose concentrations (1 and 100 mM). With increasing illumination time, the emission is decreasing and absorptance is increasing. Thus, the sensitivity can be tuned by varying the illumination time. For the main text measurements, a charging time of 200 s was chosen because it represents a good compromise between signal intensity and measurement time.

C.7.3. Delayed sensor information readout

In Section C.6, a time delayed readout of memristive properties is discussed for coulometric readout. Here, we show that this is also possible for the optic measurement methods. A K-PHI suspension which contained 100 mM was measured under similar conditions as discussed in Section 8.2.3. However, the optic readout after illumination was delayed by 5, 10 and 20 min. The measurement is shown in Figure C.21. While the signal decays with longer illumination times, a readout of the optic properties is still measurable. Note that for 5 min delay, the signal loss is much less than in the wired case (42 %). The signal decay is given in Table C.9. A delayed readout is therefore well possible if the decay is corrected. We attribute the signal decay to oxygen slowly leaking into the cuvette and quenching the excited state of K-PHI. The water reduction reaction can be excluded as mechanism here, since energy

storage on K-PHI is stable at potentials negative of the RHE[11] and is only mediated by contact to conductive substrates like FTO. However, other electron accepting reactants that affect the electron storage on K-PHI and act as electron acceptors, such as oxygen in particular, should be avoided for efficient and long term charge accumulation.[3,11,15]

Table C.9. Impact of delayed readout on signal intensity. Optic sensing property signal loss after the delayed readout compared to the measurement with no delay. Measurement shown in Figure C.21.

Delay time (min)	Signal loss in emission (%)	Signal loss in absorptance (%)
5	8.1	11.2
10	15.5	19.4
20	21.1	31.8

C.7.4. Negligible invasive nature of the memristive state readout

To proof the negligible invasiveness of the optical characterization shown in the main text, a kinetic (continuous) photoluminescence experiment was performed for 100 s to study the influence of the excitation source on the photocharging properties. This experiment was carried out under the same conditions as the PL measurements. Figure C.22 show the photoluminescence remains almost constant for the quenched with air (orange curve) and for the charged (blue curve) suspensions under these illumination conditions for much longer times (100 s) than that necessary for the characterization itself (20 s). Note that it is not necessary to measure the entire emission spectrum to extract the sensing information, since the readout of the memristive state can also be extracted at a single wavelength. Thus, the measurement time can be reduced to below 1 s (*e.g.*, when measuring at 450 ± 2 nm), further minimizing the little disturbance of the system by its PL analysis.

In the absorption experiments case, no invasiveness is expected since the measurement is carried out by sweeping the excitation monochromator from low to high energies, hence beginning below the band gap of K-PHI. The charged state of the sensor would be modified as soon as it is illuminated with light with an energy above the bandgap (for K-PHI: $\lambda < 450$ nm), which is after the sensor information is read out ($\lambda = 672$ nm).

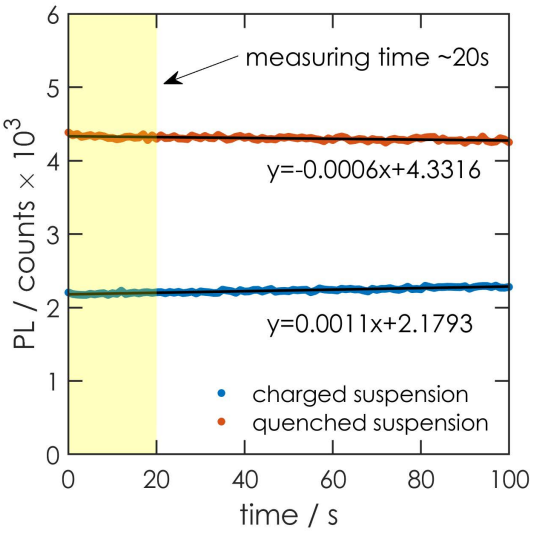

Figure C.22. Kinetic photoluminescence study. Photoluminescence emission intensity ($\lambda = 450$ nm) under continuous excitation ($\lambda = 370$ nm) for the quenched with air (orange) and charged (blue) suspensions. Linear fittings, together with their corresponding equations, are shown as solid black lines and the equations given in the graph. The yellow rectangle indicates the time required to collect each PL spectrum shown in Figure 8.4 (b).

C.7.5. Schematic representation of the PL characterization process by the quenched PL emission

As mentioned in the main text, we attribute the PL intensity decline in the charged state to an either radiative at frequencies out of our detection limits (>900 nm) or non-radiative recombination rate between photogenerated charge carriers (*i.e.*, the holes) required for the PL measurement and increased amounts of previously trapped electrons that increase the recombination probability. Figure C.23 summarizes the measurement process for the quenched (Figure C.23 (a)) and the charged (Figure C.23 (b)) suspensions.

When illuminating the suspension during the PL experiment which was quenched with oxygen after a sensor experiment (Figure C.23 (a)), an excited electron originating from the PL measurement (I, II, III and IV) can decay to the VB with an energy E_2 either in a non-radiative (I and II) or in a radiative way (III and IV). The presence of oxygen in the suspension prevents the decay of these electrons to the IB. Therefore, the initial and final states of the sample under study must be similar.

In the "charged" samples case (Figure C.23 (b)), *i.e.*, with electrons trapped in the

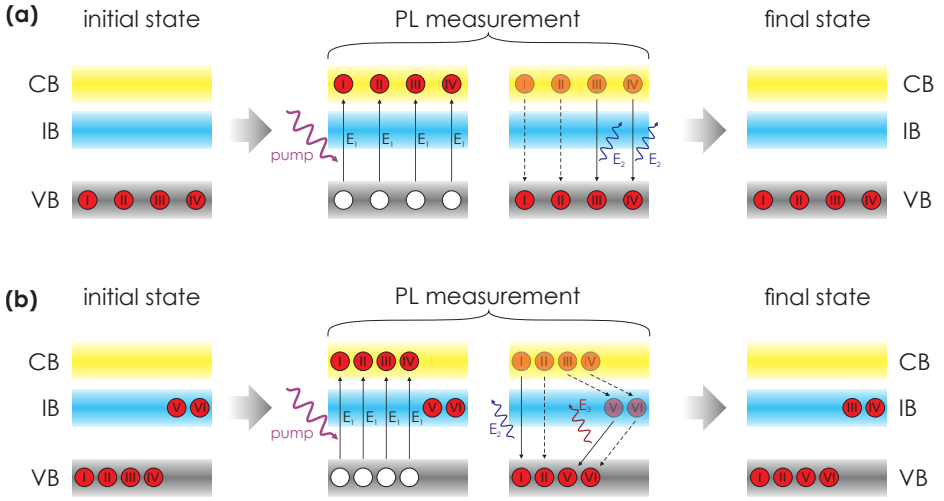

Figure C.23. Proposed PL decay mechanism and its potential modification due to photocharging. Schematic representation of the PL characterization of with oxygen quenched **(a)** and charged **(b)** K-PHI suspensions in presence of glucose. Red circles represent electrons, white circles holes and the roman numbers help to visualize the path of excited electrons. The valence band (VB), conduction band (CB) and Intercalation Band (IB) are shown in gray, yellow and blue, respectively.

IB (V and VI), a new recombination pathway opens between them and holes created by the PL measurement pumping (white circles). This process with energy E_3 is either non-radiative (VI) or emits beyond our detection limit (V, >900 nm). Thus, less electrons relax from CB into VB, the emission with energy E_2 declines. An increased charge recombination of photoexcited electrons in charged carbon nitride photocatalysts due to much faster recombination kinetics ($\sim$400 fold) was also reported by J. R. Durrant *et al.*, in line with this proposed mechanism.[16]

C.8. References

(1) Schlomberg, H.; Kröger, J.; Savasci, G.; Terban, M. W.; Bette, S.; Moudrakovski, I.; Duppel, V.; Podjaski, F.; Siegel, R.; Senker, J.; Dinnebier, R. E.; Ochsenfeld, C.; Lotsch, B. V. *Chem. Mater.* **2019**, *31*, 7478–7486.

(2) Lau, V. W.-h.; Klose, D.; Kasap, H.; Podjaski, F.; Pignié, M.-C.; Reisner, E.; Jeschke, G.; Lotsch, B. V. *Angew. Chem. Int. Ed.* **2017**, *56*, 510–514.

(3) Sridhar, V.; Podjaski, F.; Kröger, J.; Jiménez-Solano, A.; Park, B.-W.; Lotsch, B. V.; Sitti, M. *Proc. National Acad. Sci.* **2020**, *117*, 24748–24756.

(4) Mayer, F.; Müller, V. In Springer Berlin Heidelberg: 2013, pp 122–129.

(5) Gauglitz, G. *Anal. Bioanal. Chem.* **2018**, *410*, 5–13.

(6) Lau, V. W.-h.; Moudrakovski, I.; Botari, T.; Weinberger, S.; Mesch, M. B.; Duppel, V.; Senker, J.; Blum, V.; Lotsch, B. V. *Nat. Commun.* **2016**, *7*, 12165.

(7) Wang, X.; Maeda, K.; Thomas, A.; Takanabe, K.; Xin, G.; Carlsson, J. M.; Domen, K.; Antonietti, M. *Nat. Mater.* **2009**, *8*, 76–80.

(8) Banerjee, T.; Podjaski, F.; Kröger, J.; Biswal, B. P.; Lotsch, B. V. *Nat. Rev. Mater.* **2020**, *6*, 168–190.

(9) Krebs, H. A. *Annu. Rev. Biochem.* **1950**, *19*, 409–430.

(10) Göpel, W.; Jones, T. A.; Kleitz, M.; Lundstrom, J.; Seiyama, T., *Sensors, Chemical and Biochemical Sensors*; Wiley: 1991; Vol. 2, pp 1–701.

(11) Podjaski, F.; Kröger, J.; Lotsch, B. V. *Adv. Mater.* **2018**, *30*, 1705477.

(12) Islam, T.; Mukhopadhyay, S. C. *Int. J. On Smart Sens. Intell. Syst.* **2019**, *12*, 1–21.

(13) De Vico, L.; Sørensen, M. H.; Iversen, L.; Rogers, D. M.; Sørensen, B. S.; Brandbyge, M.; Nygård, J.; Martinez, K. L.; Jensen, J. H. *Nanoscale* **2011**, *3*, 706–717.

(14) Kröger, J.; Jiménez-Solano, A.; Savasci, G.; Lau, V. W. h.; Duppel, V.; Moudrakovski, I.; Küster, K.; Scholz, T.; Gouder, A.; Schreiber, M.-L.; Podjaski, F.; Ochsenfeld, C.; Lotsch, B. V. *Adv. Funct. Mater.* **2021**, *31*, 2102468.

(15) Sridhar, V.; Podjaski, F.; Alapan, Y.; Kröger, J.; Grunenberg, L.; Kishore, V.; Lotsch, B. V.; Sitti, M. *Sci. Robot.* **2022**, *7*, 62.

(16) Yang, W.; Godin, R.; Kasap, H.; Moss, B.; Dong, Y.; Hillman, S. A. J.; Steier, L.; Reisner, E.; Durrant, J. R. *J. Am. Chem. Soc.* **2019**, *141*, 11219–11229.

List of Publications

Publications that are part of this thesis

(i) **Title:** An Integrated Solar Battery based on a Charge Storing 2D Carbon Nitride.

Authors: Andreas Gouder, Filip Podjaski, Alberto Jiménez-Solano, Julia Kröger, Yang Wang, and Bettina V. Lotsch.

Published in: *Energy & Environmental Science* **2023**.
doi: 10.1039/D2EE03409C

(ii) **Title:** Bridging the Gap between Solar Cells and Batteries: Optical Design of Bifunctional Solar Batteries based on 2D Carbon Nitrides.

Authors: Andreas Gouder, Liang Yao, Yang Wang, Filip Podjaski, Ksenia S. Rabinovich Alberto Jiménez-Solano, and Bettina V. Lotsch.

Submitted to: *Advanced Energy Materials* (2nd review round).

(iii) **Title:** Photomemristive sensing *via* charge storage in 2D carbon nitrides.

Authors: Andreas Gouder, Alberto Jiménez-Solano, Nella M. Vargas-Barbosa, Filip Podjaski, and Bettina V. Lotsch.

Published in: *Materials Horizons* **2022**, 9, 1866-1877.
doi: 10.1039/D2MH00069E

(iv) **Title:** Integrated Solar Batteries: Design and Device Concepts.

Authors: Andreas Gouder and Bettina V. Lotsch.

Submitted to: *ACS Energy Letters* as a perspective.

(v) **Title:** Optoionics: A Toolkit to Drive Light Assisted Applications.

Authors: Andreas Gouder and Bettina V. Lotsch.

In preparation for: *Journal of Materials Chemistry B* as a perspective.

Publications that are not part of this thesis

(i) **Title:** Morphology Matters: 0D/2D WO3 Nanoparticle-Ruthenium Oxide Nanosheet Composites for Enhanced Photocatalytic Oxygen Evolution Reaction Rates.

Authors: Hugo A. Vignolo-González, Andreas Gouder, Sourav Laha, Viola Duppel, Sol Carretero-Palacios, Alberto Jiménez-Solano, Takayoshi Oshima, Peter Schützendübe, and Bettina V. Lotsch.

Published in: *Advanced Energy Materials* **2022**, 13, 2203315.
doi: 10.1002/aenm.202203315

(ii) **Title:** The Weyl Semimetals $MIrTe_4$ (M = Nb, Ta) as Efficient Catalysts for Dye-sensitized Hydrogen Evolution.

Authors: Manisha Samanta, Hengxin Tan, Sourav Laha, Hugo A. Vignolo-González, Lars Grunenberg, Sebastian Bette, Viola Duppel, Peter Schützendüble, Andreas Gouder, Binghai Yan, and Bettina V. Lotsch.

Submitted to: *Advanced Energy Materials*. 2nd review round.

(iii) **Title:** Crystal structure and spectral characterization of $La_2(CO_3)_3 \cdot 5\,H_2O$ - an industrially relevant lanthanide carbonate.

Authors: Esengül Çiftçi, Filip Podjaski, Andreas Gouder, Bettina V. Lotsch, Robert E. Dinnebier, and Sebastian Bette.

Published in: *Zeitschrift für Anorganische und Allgemeine Chemie* **2022**, 648, e202200218.
doi: 10.1002/zaac.202200218

(iv) **Title:** Morphology Control in 2D Carbon Nitrides: Impact of Particle Size on Optoelectronic Properties and Photocatalysis.

Authors: Julia Kröger, Alberto Jiménez-Solano, Gökcen Savasci, Vincent W. h. Lau, Viola Duppel, Igor Moudrakovski, Kathrin Küster, Tanja Scholz, Andreas Gouder, Marie-Luise Schreiber, Filip Podjaski, Christian Ochsenfeld, and Bettina V. Lotsch.

Published in: *Advanced Functional Materials* **2021**, 31, 2102468. doi: 10.1002/adfm.202102468

(v) **Patent Title:** Electrochemical device, batteries, method for harvesting light and storing electrical energy, and detection methods.

Authors: Bettina V. Lotsch, Filip Podjaski, Julia Kröger, Andreas Gouder, and Hendrik Schlomberg.

Published as: *worldwide application* **2019**, WO2020143912A1.

List of Figures

1.1. Global warming. 11
1.2. Sustainable energy research. 13
1.3. Potential of solar irradiation as renewable energy source. 14
1.4. Germany's energy mix in 2022. 16
1.5. Structural analogs and synthesis cascade of key carbon nitrides. . . . 19
1.6. Light absorption and photocharging of carbon nitrides. 21
1.7. Emerging applications of carbon nitrides. 24
1.8. Progress in solar cell technology. 29
1.9. Operation and energy loss mechanism in DSSCs. 31
1.10. HTMs as redox shuttle for solid-state DSSCs. 32
1.11. Concepts of OSC devices. 36
1.12. The effect of electric field distribution in BHJ OSC devices governed by SCLC. 39
1.13. Solar cell performance and efficiency. 42
1.14. Capacitor energy storage. 46
1.15. Pseudocapacitance. 50
1.16. Battery energy storage and intercalation. 55
1.17. Memristors and resistance switching devices. 61

2.1. Fundamental semiconductor properties. 83
2.2. Developing p-n junction. 85
2.3. Illumination of a crystalline Si semiconductor. 86
2.4. Fundamental concepts of electrochemistry. 88
2.5. Interfacial reactions. 91
2.6. Effect of applied potential. 93
2.7. Impact of diffusion on an electrochemical reaction. 95
2.8. Concept of scanning voltammetry measurements. 97
2.9. LSV measurements (IV curves) in solar cells. 99
2.10. CV measurements in energy storage devices. 101
2.11. CV measurements in memristors and resistance switching devices. . 103

2.12. GCD measurements in energy storage devices. 105
2.13. From half-cell to full-cell. 108

3.1. Summary of the progress of this thesis. 114

4.1. Literature overview of reported light-ion interactions. 123
4.2. Extending optoionic concepts to 2-phase K-PHI systems. 127

5.1. Operation mechanism of a solar battery. 140
5.2. Three-electrode solar battery designs during photocharging. 142
5.3. Two-electrode solar battery designs during photocharging, which employ bifunctional heterojunction electrodes. 145
5.4. Two-electrode solar battery designs during photocharging, which employ bifunctional materials. 149
5.5. Charging and discharging during solar battery operation. 152
5.6. GCD measurements of IEC and VEC devices. 155

6.1. Description and optical challenges that a solid-state solar battery based on K-PHI and PEDOT:PSS provides. 169
6.2. Optical design of the solar battery based on the ESM K-PHI and HSM PEDOT:PSS. 173
6.3. Proposed strategies for light harvesting efficiency increase in the collection layer without tuning the active layer thickness. 176
6.4. Performance enhancement of a solar battery *via* illumination compared to other energy conversion and storage devices. 180

7.1. Concept and requirements of a solar battery device. 196
7.2. Solar battery characterization of light charging process. 199
7.3. Solar battery characterization of electric and light-assisted electric charging process. 203
7.4. Performance summary of operation modes of the solar battery. . . . 208

8.1. Concept of an oxidative (memristive) photo-electrochemical sensor. 223
8.2. PEC properties of K-PHI and potentiometric memristive sensing *via* K-PHI films. 226
8.3. Further electrochemical readout methods *via* K-PHI thin films. 230

8.4. Colorimetric sensing *via* K-PHI wireless particles. 233
8.5. Further optical sensing method *via* K-PHI wireless particles. 235

A.1. Absorptance of K-PHI, PVK, PEDOT:PSS, and ITO as films. 258
A.2. Real and imaginary part of refractive index of glass, ITO, PVK, PEDOT:PSS, and K-PHI. 259
A.3. Charge collection layer functions. 261
A.4. Simulated charging time with different collection layer functions. . . 261
A.5. GCD measurements in the dark of separated full-cells with K-PHI and PEDOT:PSS. 262
A.6. K-PHI photocharging with and without SED. 264
A.7. How does charge storage influence electrochemical and optical properties. 266
A.8. Simulating photoassisted discharge. 269
A.9. Influence of decaying photocurrent on charging time. 271

B.1. Morphological characterization of films *via* SEM and AFM. 280
B.2. Electrochemical characterization of K-PHI samples with different HTMs.281
B.3. Activation measurement routine. 282
B.4. Reset measurement routine. 283
B.5. Kinetic study *via* CV and with different scan rates. 284
B.6. Calculated solar-to-output efficiency. 285
B.7. Kinetic study of light charging and subsequent immediate electric discharging, discussed in the main text in subsubsection 7.2.2.2. . . . 286
B.8. Additional analysis to main text Figure 7.2 & Figure 7.3. 287
B.9. Analysis of shape of GCD curve during charging. 288
B.10. Analysis of shape of GCD curve during discharging. 289
B.11. Analysis of charge retention. 291
B.12. Comparison of IV curves with different light sources. 292

C.1. Structural and optical characterization. 298
C.2. AFM characterization of thin films. 299
C.3. SEM and TEM characterization. 300
C.4. K-PHI as a direct amperometric PEC sensor. 301

C.5. Pretreatment of K-PHI thin films by self-cleaning. 303
C.6. Reference impedance measurements for coulometric readout. 304
C.7. Non-linear fitting of the potentiometric sensing measurement. 308
C.8. Individual contributions to non-linear fitting of the potentiometric sensing measurement. 309
C.9. Linear ranges in the potentiometric sensing measurement. 311
C.10. Non-linear fitting of the impedimetric sensing measurement. 313
C.11. Linear ranges in impedance sensing. 315
C.12. Non-linear fitting of the coulometric sensing measurement. 316
C.13. Linear ranges in coulometric sensing. 317
C.14. Non-linear fitting of the colorimetric sensing measurement. 318
C.15. Linear ranges in colorimetric sensing. 319
C.16. Non-linear fitting of the fluorometric sensing measurement. 321
C.17. Linear ranges in fluorometric sensing. 321
C.18. Analysis of delay times for memory sensing. 323
C.19. Influence of particle morphology on sensing efficiency. 325
C.20. Evolution of optical properties with increasing the illumination time. 326
C.21. Analysis of delay times for memory sensing. 327
C.22. Kinetic photoluminescence study. 329
C.23. Proposed PL decay mechanism and its potential modification due to photocharging. 330

List of Acronyms

AA Ascorbic Acid

AC Alternating Current

AFM Atomic Force Microscopy

AQE Apparent Quantum Efficiency

BAH Bifunctional Anode Heterojunction

BAM Bifunctional Anode Material

BCH Bifunctional Cathode Heterojunction

BCM Bifunctional Cathode Material

BHJ Bulk Heterojunction

CB Conduction Band

CE Counter Electrode

cE charging Electric

cEdE charging Electric, discharging Electric

ch Charging State

cL charging Light

cLdE charging Light, discharging Electric

cLE charging Light Electric

cLEdE charging Light Electric, discharging Electric

cLEdLE charging Light Electric, discharging Light Electric

COF Covalent Organic Framework

COP Covalent Organic Polymer

CSS Charge Separated State

CT Charge Transfer State

CV Cyclic Voltammetry

DC Direct Current

DFT Density Functional Theory

DI Deionized water

dLE discharging Light Electric

DOS Density Of States

DSSC Dye Sensitized Solar Cell

eCE electric Coulombic Efficiency

EDL Electric (Electrolyte) Double Layer

EDLC Electrolyte Double Layer Capacitor

EIS Electrochemical Impedance Spectroscopy

EQE External Quantum Efficiency

ESB backscattered electron detector

ESM Electron Storage Material

ESW Electrolyte (Electrochemically) Stable Window

ETM Electron Transport Material

FF Fill Factor

fofa Form Factor

FT-IR Fourier Transformed Infrared spectroscopy

FTO Fluorine doped Tin Oxide

GCD Galvanostatic Charging and Discharging

HOMO Highest Occupied Molecular Orbital

HSM Hole Storage Material

HTM Hole Transport Material

HWHM Half Width Half Maximum

IB Intercalation Band

IEC Current Efficient Charging

IQE Internal Quantum Efficiency

ITO Indium Tin Oxide

IV Current Voltage (measurement)

LFE Long-range Field Effect

LiB Lithium Battery

LOD Limit Of Detection

LSV Linear Scanning Voltammetry

LUMO Lowest Unoccupied Molecular Orbital

MCI Mixed Conducting Interphase

MIEC Mixed Electronic-Ionic Conductor

MOF Metal Organic Framework

MPP Maximum Power Point

NFA Non Fullerene Acceptor

NMC $LiNiMnCoO_2$ (battery cathode material)

NP Nanoparticle

OCP Open Circuit Potential

OER Oxygen Evolution Reaction

ORR Oxygen Evolution Reaction

OSC Organic Solar Cell

PCE Power Conversion Efficiency

PEC Photo-Electrochemical

PET Photoinduced Electron Transfer

PHJ Planar Heterojunction

PL Photoluminescence spectroscopy

PSU Power Supply

PV Photo Voltaic

RE Reference Electrode

rGO reduced Graphene Oxide

RMS Rough Mean Square

RRAM Random Access Memory

SCLC Space Charge Limited Current

SEA Sacrificial Electron Acceptor

SED Sacrificial Electron Donor

SEI Solid Electrolyte Interface

SEM Scanning Electron Microscopy

SFB Solar Flow Battery

SFE Short-range Field Effect

SQ Shockley Queisser

TEM Transmission Electron Microscopy

UA Uric Acid

UV-VIS Ultraviolet Visible light

VB Valence Band

VEC Voltage Efficient Charging

WE Working Electrode

WF Work Function

Chemical Glossary

4-MBA 4-Methylbenzyl alcohol

Ag/AgCl Silver/Silver Chloride Reference Electrode

F8BT poly(99,9-dioctyfluorene-alt-benzothiadiazole)

g-C_3N_4 graphitic polymeric carbon nitride

H-PHI protonated poly(heptazine imide)

K-PHI potassium poly(heptazine imide)

LCO $LiCoO_2$ (battery cathode material)

LFP $LiFeO_2$ (battery cathode material)

LMO $LiMn_2O_4$ (battery cathode material)

MAPI Methylammonium Lead Iodide

MeOH Methanol

MXene $M_{n+1}X_nT_x$, where M is a transition metal, X is carbon or nitrogen, and T is the surface termination group

NHE Normal Hydrogen Reference Electrode

P3HT poly(3-hexylthiophen-2.5-diyl)

PANI Polyaniline

PCBM [6,6]-Phenyl-C61-butyric acid methyl ester

PEDOT poly(3,4-ethylenedioxythiophene)

PEDOT:PSS poly(3,4-ethylenedioxythiophene) polystyrene sulfonate

PHI poly(heptazine imide)

PPY polypyrrole

PTB7TH poly[4,8-bis(5-(2-ethylhexyl)thiophen-2-yl)benzo[1,2-b;4,5b']dithio- phene-2,6-diyl-alt-(4-(2-ethylhexyl)-3-fluorothieno[3,4-b]thiophene-)-2-carboxylate-2,6-diyl)

PVK Polyvinylcarbazole

TCP 1,3,5-Tris(N-carbazolyl)benzene

TCTA Tris-(4-carbazoyl-9-yl-phenyl)-amin

TEoA Triethanol amine

TPD N,N'-Bis(3-methylphenyl)-N,N'-diphenyl- benzidine